Towards the Detection of Core-Collapse Supernovae Burst Neutrinos with the 3-inch PMT System of the JUNO Detector

Victor Lebrin

▶ **To cite this version:**

Victor Lebrin. Towards the Detection of Core-Collapse Supernovae Burst Neutrinos with the 3-inch PMT System of the JUNO Detector. Atomic Physics [physics.atom-ph]. Nantes Université, 2022. English. NNT : 2022NANU4080 . tel-04098003

HAL Id: tel-04098003

https://theses.hal.science/tel-04098003v1

Submitted on 15 May 2023

HAL is a multi-disciplinary open access archive for the deposit and dissemination of scientific research documents, whether they are published or not. The documents may come from teaching and research institutions in France or abroad, or from public or private research centers.

L'archive ouverte pluridisciplinaire **HAL**, est destinée au dépôt et à la diffusion de documents scientifiques de niveau recherche, publiés ou non, émanant des établissements d'enseignement et de recherche français ou étrangers, des laboratoires publics ou privés.

DOCTORAT MATIERE BRETAGNE MOLECULES LOIRE ET MATERIAUX

Nantes Université

THÈSE DE DOCTORAT DE

NANTES UNIVERSITÉ

ÉCOLE DOCTORALE N° 596
Matière, Molécules, Matériaux
Spécialité : *Physique Subatomique et Instrumentation Nucléaire*

Par
Victor Lebrin

Towards the Detection of Core-Collapse Supernovae Burst Neutrinos with the 3-inch PMT System of the JUNO Detector

Thèse présentée et soutenue à Nantes, le 05/09/2022
Unité de recherche : Laboratoire Subatech, UMR 6457

Rapporteurs avant soutenance :

Christine Marquet	Directrice de Recherche, CNRS-IN2P3
Juan-Pedro Ochoa-Ricoux	Associate Professor, UCI Department of Physics

Composition du Jury :

Président :	Pol-Bernard Gossiaux	Professeur, IMT Atlantique
Examinateurs :	Christine Marquet	Directrice de Recherche, CNRS-IN2P3
	Juan-Pedro Ochoa-Ricoux	Associate Professor, UCI Department of Physics
	Barbara Erazmus	Directrice de Recherche, CNRS-IN2P3
	Jacob Lamblin	Maître de Conférence, Université Grenoble Alpes
	François Montanet	Professeur, Université Grenoble Alpes
Dir. de thèse :	Mariangela Settimo	Chargée de Recherche, CNRS-IN2P3
Co-dir. de thèse :	Frederic Yermia	Maître de Conférence, Nantes Université

A mes parents,

Table of Contents

Remerciements

Il y a un grand nombre de personnes que je souhaiterais remercier, sans qui cette thèse n'aurait pas pu se faire, ou simplement sans qui elle n'aurait pas eu la même saveur.

Mes premiers remerciements vont à mes encadrants de thèse, Mariangela Settimo et Frederic Yermia. Ca m'embête de devoir écrire le nom de l'un avant celui de l'autre dans ce paragraphe, tant leur encadrement a été équitable et complémentaire durant ces 3 ans. Je m'en remets donc à l'ordre alphabétique. Merci pour les réponses que vous avez apporteés à toutes mes questions concernant la thèse, toujours avec pertinence, bienveillance et respect. Merci de vous être rendus si disponibles, dès que j'en avais besoin. Je comprends aussi qu'une thèse, c'est donnant-donnant. Mes travaux ont aussi permis à l'équipe Neutrino de Subatech de contribuer au developpement de JUNO. Pourtant, j'ai le sentiment d'être celui qui tire le plus profit de ces 3 ans, avec la formation que je reçu grâce à vous et votre encadrement. Merci, je vous souhaite bonne continuation, je sais déjà que vous me manquerez.

D'une manière plus générale, je souhaiterais remercier le Centre National de la Recherche Scientifique (CNRS) ainsi que le Laboratoire Subatech. Le premier d'avoir financé ma thèse et le second de m'avoir accueilli pendant ces 3 ans. Il y a plusieurs personnes au sein de Subatech avec qui j'ai eu l'occasion de travailler ou qui m'ont aidé, je les mentionne dans ce paragprahe. Merci à Gines Martinez; Directeur de Subatech, d'être passé régulièrement dans les couloirs de Subatech, même dans les périodes les plus intenses de la crise Covid, pour nous demander à nous, étudiants en thèse, si tout se passait bien malgré les difficultés du moment, et cela toujours avec bienveillance. Merci à Farah Alibay, pour les quelques (nombreuses?) heures passées à préparer et à participer à la Fête de La Science et la Nuit Blanche des Chercheurs. Je suis heureux de t'avoir rencontré, je ne suis pas près d'oublier ton rire tonitruant et unique qu'on entend et reconnait probablement depuis l'autre bout de la Terre. Comme quoi c'est pas parce qu'on est "haut comme 3 pommes" qu'on passe inaperçu (tmtc). Merci aussi aux autres personnes du Service Administration de Subatech pour l'aide précieuse que vous m'avez apportée lorsque j'en avais besoin pour les missions, la soutenance de thèse, la paperasse administrative etc. Tanja Pierret, Sophie De Peindray D'Ambelle, Severine Gadeyne, Véronique Ansquer, Isabelle Ollitrault, Sandrine Benac... Merci ! Je voudrais aussi remercier certains chercheurs qui travaillent à Subatech, avec qui je n'ai pas travaillé dirèctement mais qui m'ont apporté une aide précieuse. Merci à Mathieu Bongrand et à Benoit Viaud pour les quelques discussions que nous avons pu avoir lors de mes trois années de thèse et aussi pour votre aide lors de la préparation de la soutenance, qui m'a permis d'être plus à l'aise le jour-J et d'éclaircir mon propos le plus possible. Merci aussi à Nicolas Thiollière pour les quelques discussions que nous avons pu avoir sur mon projet professionnel après cet thèse. C'était comme une bouffée d'air de pouvoir avoir ces discussions alors que j'étais pris dans les turbulences de la thèse. Je souhaite aussi remercier des chercheurs externes à Subatech: Joao Pedro Athayade Marcondes De Andre, Cédric Cerna, Frederic Perrot, Cécile Jollet,

Clément Bordereau et Anataël Cabrera que j'ai pu rencontrer au début de ma thèse et avec qui j'ai eu l'occasion de travailler ou simplement discuter. Merci pour votre aide lorsque je suis arrivé dans JUNO, elle m'a permis de m'intégrer de la meilleure manière possible dans la collaboration. Je vous souhaite une bonne continuation. Merci aussi à Thiago Sogo Bezerra qui a été mon encadrant de stage de Master 1 et avec qui j'ai découvert la Physique des Neutrinos dans l'expérience Double Chooz. Je considère aujourd'hui que ces 2 mois de stage ont joué un rôle important dans mon choix de faire une thèse dans ce domaine.

Je garderai aussi de ma thèse de nombreux souvenirs des moments passés avec mes camarades doctorants... Il y aurait tellement à dire, mais j'en ai un peu marre d'écrire et je pense que, typiquement, Grégoire Pihan ne vaut pas la peine que je perde trop de temps sur son cas. Alors je vais essayer d'être concis. Johannès... Pour le coup c'est un peu plus qu'une simple thèse qu'on vient de faire ensemble, c'est carrément 11 années de notre vie scolaire, professionnelle et amicale. Depuis 2011, jusqu'à cette année 2022. Comme tu l'as dit toi-même, ce sont 11 années inoubliables, et je sais que même si on va s'éloigner pour un petit temps, on aura aucun mal à rendre la suite de cette amitié inoubliable elle aussi. Merci pour tout, toute l'écoute que tu m'as offerte, tous les moments de rire, de pleures, tous les délires, les match de badminton, les bouffes (certaines interminables, par ta faute lol) tant au RU qu'au restaurant, toutes les dicussions sur la Physique, sur la Musique, sur l'Actualité, sur nos histoires repectives et enfin merci pour ta confiance. Maxime... On en est à combien de Pina Colada déjà ? Merci à toi pour toutes ces discussions sur la Physique, pour ce nombre infini de thés que tu m'as offert, pour ta disponibilité, ta gentillesse. Je te souhaite le meilleur, je n'ai aucun doute sur le fait que tu arriveras à obtenir ce que tu veux dans ta vie professionnelle. A très vite pour une Pina Colada, ou un thé. "C'est pas le tout mais...". Merci aussi à toi Vincent, pour ta gentillesse et toutes nos discussions sur le réchauffement climatique et ses conséquences, merci aussi pour le sport et désolé de pas t'avoir suivi tous les midis (enfin sauf quand il pleuvait, là j'avais aucun scrupule à te laisser aller courir seul). Bon Grégoire, je vais quand même faire un petit effort pour toi... Merci d'être toi tout simplement, tellement gentil, drôle et sincère, surtout quand on parle maternité. J'espère qu'on continuera de parler musique notamment, je pense que t'as encore un bon million de groupes chelous à me fare découvrir. Arthur, ravi de t'avoir rencontré au début de cette thèse, merci pour ta gentillesse et le soutien sans condition que tu m'as apporté lorsque tu voyais que j'avais un coup de mou... En revanche, pas merci pour tes retards et les galères pour s'organiser quand on voulait aller boire un verre ensemble. Vivement la prochaine fois. Merci aussi à toi Claudia pour tout ces TikTok que tu m'as montrés et qui m'ont fait rire, j'aimais vraiment ceux avec les petits chats. Plus sérieusement, merci pour ta gentillesse, ta simplicité et aussi pour les 2-3 délires un peu bizarres qu'on a pu avoir pendant ces 3 ans (blblblbl !!!! LLLet's play a gaaaame !!!). Léonard, je te souhaite une bonne continuation dans JUNO, heureusement qu'on peut compter sur toi pour la reconstruction des évènements, sinon le groupe SPMT aurait vraiment été mal. Je te souhaite le meilleur pour les 2 ans de thèse qu'il te reste, je sais déjà que ça se passera bien. Et biensur, on se boit un verre bientôt ! Je souhaite aussi le meilleur à David F, David H, Eamonn, Gabriel, Guillaume, Hanna, Johan, Mahbobeh, Micheal, Nadège, Nadiya, Nathan, Nico, Ophélie, Rita, Roland, Stéphane, Tobie, Yohannes... Bonne continuation à vous tous, vous me manquerez... Au plaisir de se recroiser un jour !

Une mention spéciale à tout ces artistes musicaux que j'ai passé d'innombrables heures à écouter pendant ces 3 ans. Merci James Blake, Tame Impala, Kendrick Lamar, Odezenne, FKA Twigs, Fontaines D.C, MNNQNS, Radiohead, Massive Attack et j'en passe... Merci

aussi à mes 2 compères avec qui je faisais de la musique le Dimanche et avec qui j'espère continuer d'en faire encore longtemps: Baptiste, Edgar, merci. Toutes ces répet' m'étaient particulièrement précieuses.

Merci aussi à ma famille. Merci Papa et Maman, je vous dédie ce manuscrit. Merci pour tout le soutien que vous m'avez toujours apporté, à n'importe quel moment de ma scolarité et plus généralement dans ma vie. Je suis certain que je vous dois à peu près tout ce qui m'arrive de bien aujourd'hui, merci infiniment. Merci aussi à mes frères et soeurs, Marie, Gaelle, Gwenn, à leur compagnons respectifs, Fabien, Laurent et Oriane ainsi qu'à leurs enfants, Almah, Aubin, Jules, Mathéo, Merlin et Mila. J'ai beaucoup de chance de vous avoir près de moi.

Pour terminer, je souhaiterais te remercier Pauline. Nous nous sommes rencontré il y a maintenant un peu plus d'un an et demi, alors que j'étais en plein mileu de cette thèse, et j'ai presque envie de dire: "heureusement que tu étais là !". Je sais qu'on est pas trop d'accord là-dessus, mais là c'est moi qui écrit alors je le dis... :)
Merci pour ton soutien indéfectible et pour cette paix que tu m'as apportée durant cette année et demi. Le fait de rentrer chez nous, après la journée de travail, dans un endroit ou l'insouciance et la simplicité étaient de mise, était particulièrement précieux à mes yeux... Il y aurait beaucoup à dire, mais il est temps que cette section se termine et en plus, tu sais déjà tout. Je t'aime.

Introduction

The first reflections on the nature of the matter that constitutes our universe dates back – at least – to six centuries before the Common Era. They were mainly conducted by groups of philosophers following different schools of thoughts, notably ionnian and eleastics. These reflections led to the *atomism*, a philosophy of nature according to which the universe is made of fundamental invisible components known as *atoms*. It was only in the 19^{th} century that these reflections were formalised and theories were constructed. The concept of *nuclear physics* and *particle physics* were born in the 20^{th} century with the progress on the understanding of nuclear fission as well as the beginnings of quantum physics. Together with the tremendous technical progress of the time, including the construction of the first particle colliders and detectors, the development of the quantum field theory led to the elaboration of the Standard Model (SM) of particle physics, referred to as Standard Model (SM) in the following. Nowadays, the particle physics is notably studied for its strong implications for the understanding of the origin of the universe.

The neutrino is an elementary particle of the SM. It was first predicted in 1930 by W. Pauli and detected for the first time in 1956. After several decades of experimental studies, the *neutrino flavor oscillation* – or *neutrino oscillation* – was discovered at the very end of the 20^{th} century. Thus, the last two decades have been dedicated to the measurement of the neutrino oscillation *parameters*: three mixing angles (θ_{12}, θ_{13} and θ_{23}), three mass splittings (Δm^2_{21}, Δm^2_{31} and Δm^2_{32}) and a Charge-Parity (CP) symmetry violating phase (δ). Even though most of them are today known with a precision of a few percent, the CP violating phase remains undetermined and the sign of Δm^2_{31} is still unkown which is also referred to as the Neutrino Mass Ordering (NMO) problem. In addition, the neutrino absolute mass and its Dirac or Majorana nature are yet to be determined. All these unanswered questions make neutrino physics among the most active topics in particle physics today. The observation of neutrino flavour mixing implies a extension in the Standard Model in order to take into account flavour mixing in the lepton sector as well as massive neutrinos, it opens the potentiality to explore new physics.
The neutrino is also a valuable messenger for astrophysics, it is notably known to play a crucial role in the Core-Collapse Supernova (CCSN) process, gigantic explosion of a massive star at the end of its life, during which 99% of the binding energy is emitted in neutrinos with energies of $\mathcal{O}$(10 MeV). In the upcoming years, the emergence of low-threshold $\mathcal{O}$(MeV) and large-scale neutrino detectors first and foremost dedicated to the study of neutrino oscillation will also open a new era in the study of CCSN with the possibility to detect several hundreds or thousands of neutrinos from the next nearby (1-100 kpc) one. The low rate of CCSN in the galaxy (of the order of 1 or 2 per century) makes the next event a once-in-a-lifetime opportunity to understand in more details the collapse and explosion mechanisms and to study nuclear and particle physics in extreme conditions.

This PhD thesis takes place within the framework of the Jiangmen Underground Neutrino Observatory (JUNO) experiment. JUNO is a multipurpose Liquid Scintillator (LS)

neutrino detector to be completed by the end of 2023. It primarily aims to determine the NMO and to perform a sub-percent measurement of three of the neutrino oscillation parameters (θ_{12}, Δm^2_{21} and Δm^2_{31}) as well as access to the measurement of θ_{13}. This will be done by detecting the disappearance of electron antineutrinos ($\bar{\nu_e}$) from the Yangjiang and Taishan nuclear power plants at an average baseline of 52.5 km. The NMO will be extracted from the fine structures of the $\bar{\nu_e}$ energy spectrum at the 3σ significance in 6 years of data taking. Consequently, such a measurement requires an unprecedent energy resolution – for a LS detector – of 3% at 1 MeV. The $\bar{\nu_e}$ detection will be based on the Inverse Beta Decay (IBD) whose resulting positron signal will be used to retrieve the incident $\bar{\nu_e}$ energy. The light emitted through the positron interaction with the LS will be collected by means of Photomultiplier Tube (PMT). Whereas ∼18,000 20" PMTs (LPMTs) will ensure the collection of a large amount of scintillation light and then small statistical fluctuations, ∼26,000 3" PMTs (SPMTs) have been proposed as an additional system to ensure a better control of the systematic uncertainties of the energy resolution. The huge detection volume of JUNO naturally extends its physics program. Thus, it will be sensitive to the next galactic CCSN burst neutrinos, Diffuse Supernovae Neutrino Background (DSNB)[1], solar neutrinos, atmospheric neutrinos, geo-neutrinos and will also allow to search for proton decay. With APC laboratory, Subatech was one the laboratories that proposed integrating the SPMT system to the JUNO detector. As a separate readout system, the SPMTs will constitute the centrepiece of the Dual Calorimetry technique for instrumental non-linearity calibration. It will also allow to perform semi-independent physics analyses. It is notably planned to be used to measure two oscillation parameters (θ_{12} and Δm^2_{21}) – Subatech notably worked to the estimation of the system sensitvity by deploying one of the two oscillation fit frameworks for the SPMT system – to study the proton decay as well as the next galactic CCSN neutrino burst. The latter topic is the core of this PhD thesis. During the burst, the event rate in the detector is expected to sharply increase and will range between the kHz and the MHz following the distance to the CCSN. The small size of the SPMTs provides a fast response and smaller saturation effects which will surely constitute assets, especially for nearby CCSN.

Since the SPMT system proposal came in a second stage of the JUNO conception (after 2016), at the beginning of this PhD thesis the simulation of the SPMTs was only partly developed (the electronics readout response was not included) and the event reconstruction with the SPMTs was not developed. Moreover, many activities were ongoing on the hardware side, notably for the electronics, the SPMTs testing and characterisation etc. Thus, the work presented in this manuscript was done in a context which allowed me to participate to the hardware part – related to the SPMTs readout and Data Acquisition (DAQ) which were among the Subatech contributions to the SPMT system – and to the reconstruction and analysis part. Even though these developments were done to address the challenges related to the specific case of a CCSN, they are valid for any physics case of JUNO. Thus, this manuscript presents a study of the capabilities of the SPMT system as a standalone detection system for CCSN burst neutrinos. It is divided into five chapters. Chapter 1 sets the context of neutrino physics at the time of this PhD thesis with a summary of the history of the neutrino, including the measurement of the neutrino oscillation parameters performed during the last two decades. This chapter also introduces the CCSN process with the role neutrinos play into it and therefore what they can teach us about this phenomenon. Chapter 2 presents the physics program of JUNO as well as the detector design. In Chapter 3, a study on the performance of the SPMT

[1] All along this manuscript, *CCSN neutrinos* refer to the *burst of neutrinos* that is emitted during a CCSN and not to the Diffuse Supernovae Neutrino Background (DSNB), a small but constant neutrino flux that is generated by the rate of CCSN in the observable universe.

system readout electronics during a CCSN is presented. In Chapter 4, the developed vertex and energy reconstruction algorithms are presented and their performance is evaluated. Finally, Chapter 5 is dedicated to the CCSN neutrino event selection and energy spectra reconstruction with the SPMT system.

Chapter 1

Neutrino physics and Core-Collapse Supernovae Neutrinos

Contents

1.1 Neutrino, a brief summary

The branch of physics that studies the elementary particles that make up the Universe is called *particle physics* [1, 2]. Together with cosmology, the study of particle physics aims to improve our understanding of the Universe and its origin. It notably classifies the fundamental particles into different families and investigates the laws governing their interactions. Nowadays, the model that describes the most accurately and with the best consistency the elementary particles and their dynamics is called the Standard Model (SM) of particle physics. Figure 1.1 lists the elementary particles of the SM. They can be shared into two categories, the **fermions** – that constitute de matter and that include *quarks* and *leptons* – and the **bosons** that mediate the interactions between the fermions. Each fermion has its own antiparticle, the latter are not indicated in Figure 1.1.

The *neutrino* belongs to the lepton family which is divided into three *flavors*, named after three particles: the electron (e), the muon (μ) and the tau (τ). Thus, there exists three types of neutrinos: ν_e, ν_μ, ν_τ. Since the hypothesis of its existence (1930), the comprehension of the neutrino nature has mobilised important resources, notably on the experimental side. After the discovery of the *neutrino oscillation*[1], efforts to understand the neutrino properties have increased further to the point of becoming one of the major issues in particle physics. These efforts keep on going today. Thanks to the current and future neutrino experiments, more progress are expected which could have implications not

[1] Nobel Prize in Physics 2015 shared by T. Kajita and A. B. McDonald for their early pioneering observations of these oscillations.

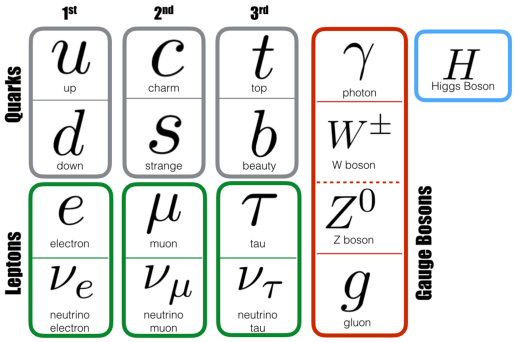

Figure 1.1: *List of the elementary particles of the Standard Model. The antiparticles, when exist, are not displayed.*

only for the understanding of neutrino physics, but also for the discovery of physics beyond the SM. The first part of this chapter is constructed as follows: The section 1.1.1 briefly introduces the neutrino interaction with matter, a summary of the neutrino history is given in section 1.1.2, the principle of neutrino oscillation is recalled and the main experimental measurements on this topic are listed in section 1.1.3, finally the open questions that remain in neutrino physics are listed in section 1.1.4.

1.1.1 Neutrino interaction with matter

The elementary particles of the SM interact with each other *via* three different fundamental interactions: the *electromagnetic* interaction, the *strong* interaction and the *weak* interaction. The fourth known one – the *gravitational* interaction – is not described by the SM. All the elementary particles are not sensitive to each of the three interactions. More precisely, there is a nesting structure between the latter (Figure 1.2). Thus, the (anti)quarks are sensitive to the three interactions while the e, μ and τ are sensitive to the electromagnetic and weak interactions only. Finally, the (anti)neutrinos only couple to the weak interaction. The interaction between the elementary particles always involves the exchange of a boson. The gluons (g) mediate the strong interaction, a virtual photon (γ) mediates the electromagnetic interaction and the Z^0 and $W^{\pm}$ bosons mediate the weak interaction. The Higgs boson (H^0) – or quantum of the Higgs field – does not mediate any interaction but confers mass to the fermions and weak bosons.

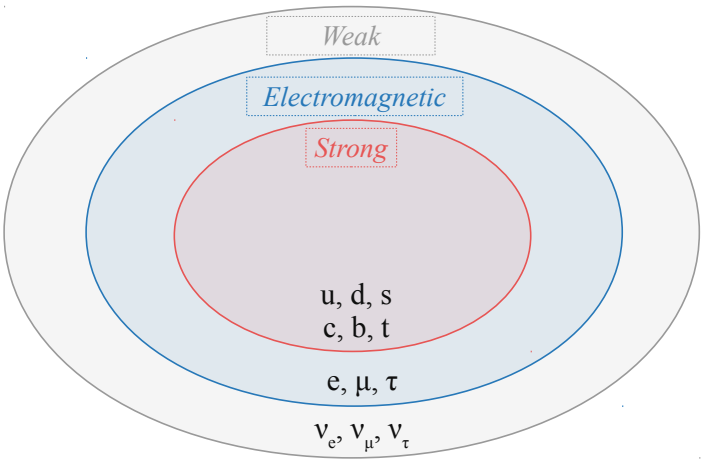

Figure 1.2: *Three of the four fundamental interactions described by the SM. They have a nesting structure. All fermions are not sensitive to the three of them.*

As the name suggests, the *weak* interaction results in a very small probability of particle interaction compared to the electromagnetic and strong ones, hence the fact that neutrinos are often defined as *elusive* particles. Compared to that of the gravitational one, the relative strength of the strong, electromagnetic and weak interactions are 10^{38}, 10^{36} and 10^{25}, respectively. Also, their respective ranges are 10^{-15} m, infinity, and 10^{-18} m.

There exist two ways of interacting for the particles that couple to the weak force, the Neutral Current (NC) and the Charged Current (CC). The first one involves the exchange of a Z^0 boson that transfers momentum, spin and energy but does not change the quantum numbers (e.g. the charge) of the interacting particles. The second one involves the exchange of a W^+ or a W^- boson and therefore the transfer of an electric charge in addition to the momentum, spin and energy. During a CC interaction, the neutrino can swap itself into the lepton corresponding to its flavor. Figure 1.3 shows an example of two physics processes involving neutrinos. The left one is a NC interaction and the right one is a CC interaction.

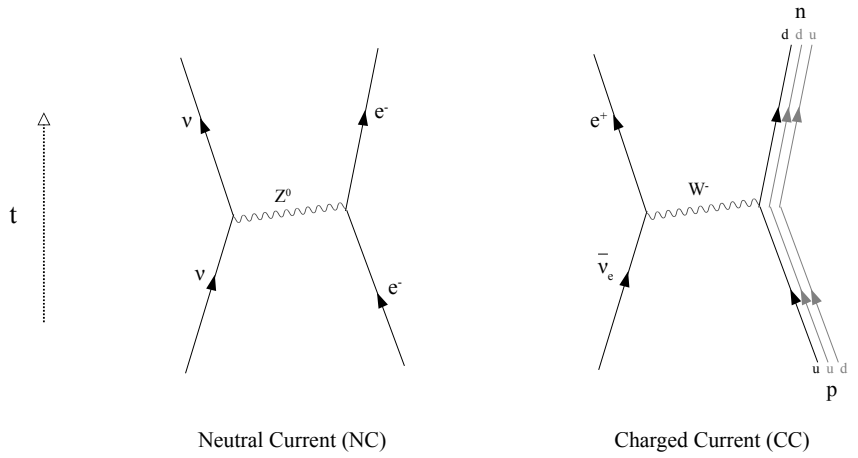

Figure 1.3: *Example of NC and CC interactions represented by Feynman diagrams [3]. The left one is a Neutrino-Electron Elastic Scattering (νeES) (ν stands for all (anti)neutrino flavors) and the right one is an Inverse Beta Decay (IBD). The time line is upward going.*

The interaction *cross-section* characterises the probability of a physics process between two fermions to occur. It is often denoted as σ and expressed in units of area. The most common unit is the barn[2]. In neutrino physics, knowledge of the interaction cross sections involving neutrinos is very important. For example, it can be used to predict the number of neutrino interactions in a detector, notably to optimise its design for a given physics goal. The cross-section of a process depends on the properties of the particles, including their energy, charge, mass etc. The cross-sections of numerous processes involving neutrinos, including some that are relevant for this PhD thesis, are reviewed in Refs. [4, 5].

1.1.2 From the research to the study

[2] 1 barn = 10^{-28} m^2

1.1.2.1 Discovery

The end of the 19^{th} century was marked by the discovery of radioactivity by Henri Becquerel. It happened in 1896, by chance, while he was studying the phosphorescence of uranium ore [6]. It was Marie-Curie who gave her name to radioactivity two years later, when she demonstrated that several chemical elements emit their own radiation [7]. During the years that followed this discovery, many physicists studied the different types of radiation (α, β, γ) emitted by various chemical elements. In 1914, James Chadwick observed for the first time the *continuous* energy spectrum of electrons from the β-decay [8], a measurement that was confirmed 13 years later by Charles Drummond Ellis and William Alfred Wooster [9]. At that time, the β-decay was considered as a two-body reaction such as:

$$ {}^{A}_{Z}X \rightarrow {}^{A}_{Z+1}Y + \beta^{-} \tag{1.1} $$

where ${}^{A}_{Z}X$ denotes a radioactive isotope called the *father nucleus* and ${}^{A}_{Z+1}Y$ denotes the *daughter nucleus* that can be radioactive or not. Thus, according to the law of energy conservation, the electron shall be emitted with a fixed kinetic energy that would only depend on the father and daughter nuclei masses. The *a priori* incomprehensibility of Chadwick, Ellis and Wooster's observation has disrupted the physicists for several years. In 1930, Wolfgang Ernst Pauli put forward the existence of a third particle in the β-decay in order to explain the continuous spectrum observed [10]. This particle had to be light, neutral and interact weakly with matter: he named it "neutron". After the discovery of the nowadays neutron by James Chadwick in 1932 [11] – here the proton mate in the atom nucleus – Pauli's neutron was renamed as "neutrino" by Enrico Fermi. The β-decay was then considered as a three-body reaction such as:

$$ {}^{A}_{Z}X \rightarrow {}^{A}_{Z+1}Y + \beta^{-} + \nu \tag{1.2} $$

The first direct observation of a neutrino was made in 1956 by a collaboration lead by Frederick Reines and Clyde Cowan [12, 13]. The neutrino source was a nuclear reactor and the detection medium was a liquid scintillator whose scintillation light was collected by means of Photomultiplier Tube (PMT)s (see Chapter 2). The detection channel was the Inverse Beta Decay (IBD), as proposed in 1934 by Enrico Fermi in its theory of β-decay [14]:

$$ \bar{\nu} + p \rightarrow e^{+} + n \tag{1.3} $$

The observation of neutrinos in 1956 was followed by the establishment of many experiments whose objective was to learn more about this mysterious particle and its interaction with matter. In the next sub-section, the discoveries that have marked the study of the neutrino are presented, building on what has been done in Ref. [15].

1.1.2.2 Milestones and anomalies

One of the most important steps of the history of neutrino physics is the discovery of today's muon neutrino in 1961 by a collaboration lead by Leon Lederman, Melvin Schwartz and Jack Steinberg. The experiment consisted in creating a proton beam that slammed a Beryllium (Be) target producing a large number of pions decaying such as:

$$ \pi \rightarrow \mu + \nu \tag{1.4} $$

The produced neutrinos then passed through an Aluminium (Al) target. In addition to be the first experiment that managed producing an actual *neutrino beam*, it demonstrated

that only muons were produced through the neutrinos induced reactions in Al [16], suggesting that their nature was different from that of reactor neutrinos discovered 5 years earlier.

The Homestake experiment was built during the late 1960s'. It aimed to detect solar neutrinos in order to study the proton-proton fusion cycle in the Sun. The detection was based on the following channel:

$$\nu + {}^{37}Cl \rightarrow e^{-} + {}^{37}Ar \tag{1.5}$$

The ^{37}Ar production rate was used to estimate the neutrino interaction rate into the detector [17]. Unexpectedely, Homestake reported a deficit – by a factor of $\sim$3 – in the measured solar neutrino flux compared to the Solar Standard Model predictions [18]. Many experiments confirmed this observation during the years that followed [19–23]. This first anomaly, referred to as the *solar neutrino problem*, remained unexplained until the neutrino oscillation was theorised and proven. The latter was first proposed by Bruno Pontecorvo, in 1957 [24, 25]. He suggested that neutrinos could oscillate such as $\nu \leftrightarrow \bar{\nu}$ like the already known neutral kaon oscillation $K_0 \leftrightarrow \bar{K_0}$. No experimental evidences were found for such oscillation. In 1962, Maki et. al suggested that the neutrino oscillation happens between two lepton flavor states (ν_e and ν_μ) constituting the birth of today's neutrino oscillation theory [26]. In 1976, the τ lepton was discovered [27]. The existence of the associated third neutrino flavor (ν_τ) was deduced and experimentally confirmed by the DONUT collaboration in 2001 [28, 29]. The neutrino oscillation was then extended to a three-flavor oscillation.

As for the solar neutrinos, the first measurement of the atmospheric neutrino flux in the early 1990s' led to the identification of an anomaly that was reported by the Kamiokande [30, 31], IMB [32, 33] and Soudan [34] collaborations. Indeed, given the atmospheric neutrino production modes (decay of charged pions), twice as many ν_μ as ν_e events were expected to be detected. However, the observed ratio was closer to one, constituting the *atmospheric neutrino anomaly*. Even if the solar and atmospheric anomalies were first experimental hints for the neutrino oscillation, the first unambiguous evidence was reported in 1997 by the Super-Kamiokande (SK) collaboration. Indeed, the SK data displayed a zenithal angle dependance in the number of atmospheric ν_μ detected. The upward going ν_μ – that travelled an extra 12,000 km (Earth diameter) before interacting into the detector – were actually less numerous than the downward going ones. The discrepancy was consistent with the two flavor $\nu_\mu \leftrightarrow \nu_\tau$ oscillation [35, 36], constituting the very first proof that the neutrinos oscillate as conceptualised by Maki et. al. Later on, the solar anomaly was somehow solved by the results from the Subdury Neutrino Observatory (SNO) collaboration in 2002. In contrary to the Homestake experiment, their detector was sensitive to *all* neutrino flavors, hence the total solar neutrino flux measured by SNO was consistent with the Solar Standard Model. Furthermore, the fraction of ν_e and non-ν_e events detected provided evidence for the ν_e flavor swap.

The twenty last years saw the development of multiple experiments that aim to measure the parameters of the neutrino oscillation theory by detecting neutrinos from multiple sources, they are summed-up in section 1.1.3.2. Before, the basics of the neutrino oscillation theory are brielfy recalled in section 1.1.3.1.

1.1.3 Neutrino oscillation

1.1.3.1 Oscillation probability

In quantum mechanics, *quantum states* – referred to as *states* in the following – are associated to particles. These states are mathematical objects that give access to the probability distribution of measuring a value for a physical quantity (position, energy, momentum...). According to the neutrino oscillation theory, there exist three *flavor states* for the neutrino that can be denoted as $|\nu_e\rangle$, $|\nu_\mu\rangle$ and $|\nu_\tau\rangle$ in the "bra/ket" Dirac notation [37]. To these flavor states can be associated three *mass states* denoted as $|\nu_1\rangle$, $|\nu_2\rangle$ and $|\nu_3\rangle$. The *transition amplitude* between the neutrino flavor states are not zero so that a state can transform into another one like for example: $|\nu_\mu\rangle \leftrightarrow |\nu_e\rangle$. The transition probabilities are proportional to the transition amplitudes:

$$P = t.t^* \tag{1.6}$$

where P is the transition probability and t and t^* are the transition amplitude and its complex conjugate. In addition, the non-zero transition amplitude implies that the flavor states are a linear combination of several mass eigenstates such as:

$$\begin{pmatrix} |\nu_e\rangle \\ |\nu_\mu\rangle \\ |\nu_\tau\rangle \end{pmatrix} = \mathrm{U_{PMNS}} \begin{pmatrix} |\nu_1\rangle \\ |\nu_2\rangle \\ |\nu_3\rangle \end{pmatrix} \tag{1.7}$$

where $\mathrm{U_{PMNS}}$ is the Pontecorvo-Maki-Nakagawa-Sakata matrix [26] that is *considered to be unitary*.[3] It can be written as a 3×3 matrix such as:

$$\mathrm{U_{PMNS}} = \begin{pmatrix} U_{e1} & U_{e2} & U_{e3} \\ U_{\mu 1} & U_{\mu 2} & U_{\mu 3} \\ U_{\tau 1} & U_{\tau 2} & U_{\tau 3} \end{pmatrix} \tag{1.8}$$

Considering that the flavor states are a linear combination of the mass states and that $\mathrm{U_{PMNS}}$ is unitary, it is possible to write:

$$|\nu_\alpha\rangle = \sum_{i=1}^{3} U^*_{\alpha,i} |\nu_i\rangle \quad \text{and} \quad |\nu_i\rangle = \sum_{\alpha=e,\mu,\tau} U^*_{\alpha,i} |\nu_\alpha\rangle \tag{1.9}$$

where α denotes one of the three flavor states, i denotes one of the three mass states and $U^*_{\alpha i}$ represents the PMNS matrix. For a neutrino produced as $|\nu_\alpha\rangle$ and that propagates over a distance x during a time t, the Shrödinger equation [40, 41] can be written as:

$$|\nu_\alpha(x,t)\rangle = \sum_{i=1}^{3} U^*_{\alpha,i} e^{-i(E_i t - p_i x)} |\nu_i\rangle \tag{1.10}$$

where E_i and p_i stand for the energy and momentum of the neutrino mass states, respectively. Injecting equation 1.9 (right) in the previous equation, it becomes:

$$|\nu_\alpha(x,t)\rangle = \sum_{\beta=e,\mu,\tau} \left(\sum_{i=1}^{3} U^*_{\alpha,i} e^{-i(E_i t - p_i x)} U_{\beta,i} \right) |\nu_\beta\rangle \tag{1.11}$$

[3] This assumption still needs to be experimentally corroborated [38, 39]. It is analogue to the Cabibbo–Kobayashi–Maskawa (CKM) matrix which contains information on the quark flavor oscillation from the weak interaction.

Thus, a neutrino produced as a ν_α evolves as a linear superposition of the three flavor states. The mass of neutrinos being very small, they always travel ultrarelativistically ($E \sim p >> m$). Using natural units ($c = \hbar = 1$):

$$E_i = \sqrt{p^2 + m_i^2} \simeq p + \frac{m_i^2}{2p} \simeq E + \frac{m_i^2}{2E} \tag{1.12}$$

Then, it is possible to write the probability for a neutrino to be detected in a state $|\nu_\beta\rangle$ while it was produced in a state $|\nu_\alpha\rangle$ such as:

$$P_{\nu_\alpha \to \nu_\beta} = |\langle \nu_\beta | | \nu_\alpha \rangle|^2 = \sum_{i,j=1}^{3} U^*_{\alpha,i} U_{\beta,i} U^*_{\alpha,j} U_{\beta,j} e^{-i(\frac{\Delta m^2_{ij} L}{2E})} \tag{1.13}$$

where L is the distance between the neutrino source and the interaction point, E is the neutrino energy and Δm^2_{ji} are called *mass splittings* and correspond to the difference between the square of the eigenvalues of two mass states:

$$\Delta m^2_{21} = m_2^2 - m_1^2 \quad \text{and} \quad \Delta m^2_{31} = m_3^2 - m_1^2 \quad \text{and} \quad \Delta m^2_{32} = m_3^2 - m_2^2 \tag{1.14}$$

They obey to the following relationship:

$$\Delta m^2_{21} + \Delta m^2_{32} - \Delta m^2_{31} = 0 \tag{1.15}$$

More details on the previous calculation can be found in Ref. [15]. For convenience – especially in an experimental context – the PMNS matrix can be parametrised and developed in terms of three rotation matrices such as:

$$\mathrm{U_{PMNS}} = \begin{pmatrix} 1 & 0 & 0 \\ 0 & \cos\theta_{23} & \sin\theta_{23} \\ 0 & -\sin\theta_{23} & \cos\theta_{23} \end{pmatrix} \begin{pmatrix} \cos\theta_{13} & 0 & \sin\theta_{13} e^{-i\delta} \\ 0 & 1 & 0 \\ -\sin\theta_{13} e^{i\delta} & 0 & \cos\theta_{13} \end{pmatrix} \begin{pmatrix} \cos\theta_{12} & \sin\theta_{12} & 0 \\ -\sin\theta_{12} & \cos\theta_{12} & 0 \\ 0 & 0 & 1 \end{pmatrix}$$

where θ_{12}, θ_{23} and θ_{13} are called *mixing angles* and δ is a Charge-Parity (CP) violation phase that characterises the matter-antimatter asymmetry in the leptonic sector. The three matrices are attached to three different "sectors" whose names arise from the sources which have been historically used to measure the corresponding parameters. Thus, the *atmospheric sector* corresponds to the leftmost matrix, the *reactor sector* corresponds to the center one and the *solar sector* corresponds to the rightmost one. Thus, the neutrino oscillation includes seven parameters in total: the three mixing angles (θ_{12}, θ_{23} and θ_{13}), the three mass splittings (Δm^2_{21}, Δm^2_{31} and Δm^2_{32}) and the CP violation phase δ.

In some experiments, the neutrino oscillation can be simplified to a two-flavor case. Thus, in vaccum, the probability for a neutrino to remain in the same flavor state during its propagation can be generally expressed as:

$$P_{\nu_\alpha \to \nu_\alpha} = 1 - \sin^2(2\theta) \sin^2[1.27 \left(\frac{\Delta m^2 L}{E} \right)] \tag{1.16}$$

Figure 1.4 shows the value of $P_{\nu_\alpha \to \nu_\alpha}$ as a function of the ratio L/E for fixed values of θ and Δm^2. The amplitude of the oscillation depends on θ while its frequency depends on Δm^2.

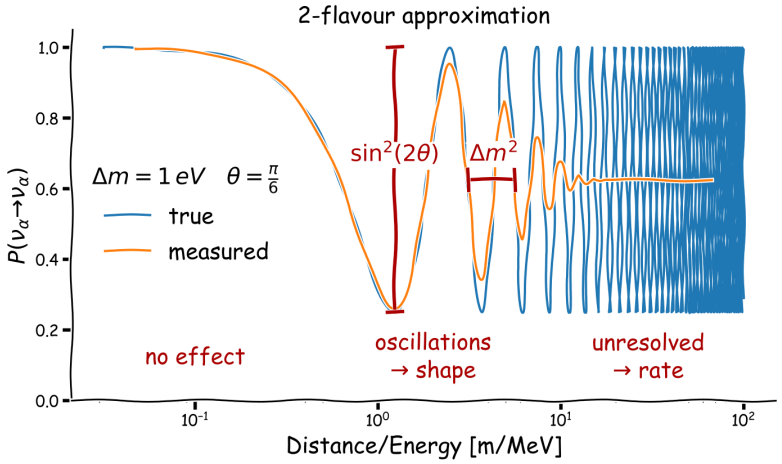

Figure 1.4: *Example of the neutrino oscillation probability as a function of the ratio L/E in the two-flavor case. The oscillation pattern shown in orange assumes that the measurement is done with a neutrino detector having a finite energy resolution.*

Even though neutrinos interact weakly with matter, the latter can have a non-negligible effect on the oscillation pattern of those travelling through a large amount of it. These so-called *matter effects* were pointed out for the first time in 1978 by Lincoln Wolfenstein, Stanislav Mikheyev and Alexei Smirnov and are thus also referred to as the MSW effect [42]. They explain the aforementioned large solar neutrino deficit (section 1.1.2.2) and have notably been used to determine that $m_1 < m_2$. It is also plan to be used by future neutrino experiments to determine the Neutrino Mass Ordering (NMO) (i.e. $\mathbf{m_1 < m_2 < m_3}$ (Normal Ordering (NO)) or $\mathbf{m_3 < m_1 < m_2}$ (Inverted Ordering (IO))).

The measurement of the oscillation parameters is done by experiments that can be split into two categories: the *disappearance experiments* that search for a lack in the number of expected neutrinos $|\nu_\alpha\rangle$ from a source producing $|\nu_\alpha\rangle$, and the *appearance experiments* that search for an excess in the number of neutrinos $|\nu_\alpha\rangle$ from a source producing $|\nu_\beta\rangle$. By placing themselves at different distances – also referred to as *baselines* – from a source producing neutrinos of greater or lesser energies, they are more or less sensitive to specific parameters. In the next section, a brief status of the neutrino oscillation parameters measurements is given. Also, the remaining questions in neutrino oscillation and more generally in neutrino physics are listed.

1.1.3.2 Oscillation parameter measurement

Reactor sector (θ_{13})

Three reactor neutrino experiments have determined the value of θ_{13} by detecting nuclear reactor $\bar{\nu_e}$ at relatively short baselines (∼km): Double Chooz [43, 44], RENO [45, 46] and Daya Bay [47, 48]. They have the best precision on θ_{13} to date. The left plot of Figure 1.5 shows the $\bar{\nu_e}$ survival probability as a function of the distance travelled by 3 MeV neutrino in the two flavor case. The latest results from the three experiments are represented in Figure 1.5 (right). The T2K experiment has also performed a measurement of θ_{13} that is not competitive with the reactor neutrino experiments in terms of precision [49]. According to the NuFit global fit [50]:

$$\mathbf{\sin^2\theta_{13} = 0.02221^{+0.00068}_{-0.00062}}$$

68% CL, Normal Ordering, without SK atmospheric data.

It is worth pointing out that, here and in the following paragraphs, the values and uncertainties of the oscillation parameters can slighlty change assuming a specific NMO. The inclusion or non-inclusion of SK atmospheric data also has an impact [51].

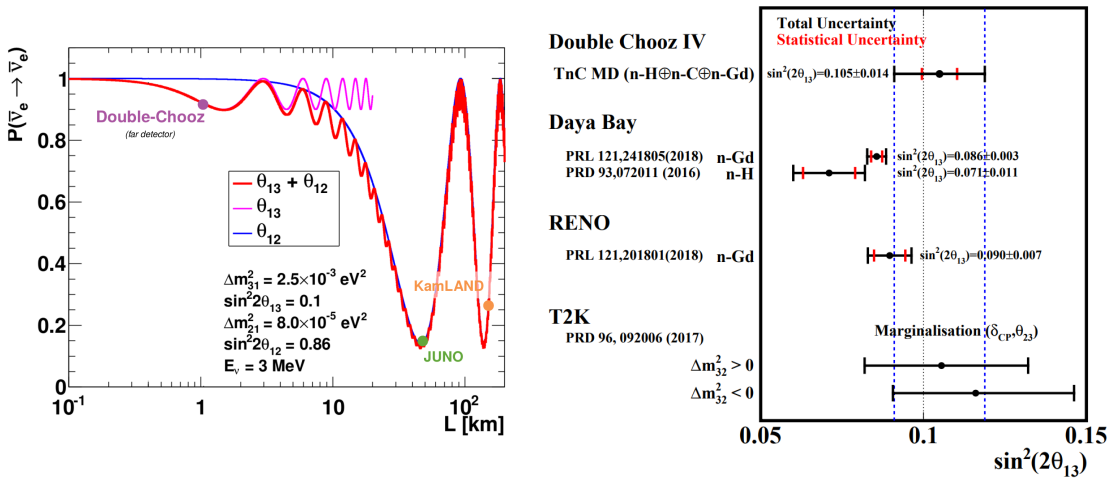

Figure 1.5: ***Left**: $\bar{\nu}_e$ survival probability as a function of the baseline. The $\bar{\nu}_e$ energy is fixed at 3 MeV. At a baseline of a few kilometers, the effect of θ_{13} is dominant. The baselines of JUNO and KamLAND (see next paragraph on the solar sector) are also indicated. Adapted from Ref. [52].* **Right**: The latest measurements of $\sin^2(2\theta_{13})$ from Double Chooz, RENO, Daya Bay and T2K. From Ref. [44]

Solar sector (θ_{12}, Δm^2_{21})

The determination of θ_{12} and Δm^2_{21} has been done in two different ways. The first one by combining the data from the solar neutrino experiments [19–23] and by including them in the NuFit global fit. The second one by extracting the parameters from the reactor $\bar{\nu}_e$ spectrum, as done by the KamLAND collaboration. The experiment aimed to detect neutrinos from 55 nuclear reactors at an average baseline of ∼180 km [53]. The results from both solar data and KamLAND experiment are shown in Figure 1.6. In addition, it is worth mentioning that it is the results from the solar neutrino experiments that allowed to determine that $m_1 < m_2$, by using the aforementioned MSW effect. According to the NuFit global fit [51]:

$$\mathbf{\sin^2\theta_{12} = 0.304^{+0.013}_{-0.012}}$$
$$\mathbf{\Delta m^2_{12} = 7.42^{+0.21}_{-0.22} \cdot 10^{-5} eV^{-2}}$$

68% CL, Normal Ordering, without SK atmospheric data.

Atmospheric sector (θ_{23}, $|\Delta m^2_{32}|$) and δ_{CP}

The measurement of θ_{23} and $|\Delta m^2_{32}|$ has been performed by experiments detecting atmospheric neutrinos with energies ranging from the GeV to the hundred of GeV (SK [36, 55], IceCube-DeepCore [56, 57], MINOS [58, 59] and ANTARES [60, 61]) and experiments detecting accelerator neutrinos, also referred to as LBνB experiments (K2K [62], MINOS [63], MINOS+ [64], T2K [49, 65], NOνA [66]). The LBνB experiments observe (anti)neutrinos that are produced *via* pion decays generated at accelerator facilities. Their typical energy is at the GeV level. The baselines are of the order of a few hundreds of kilometers

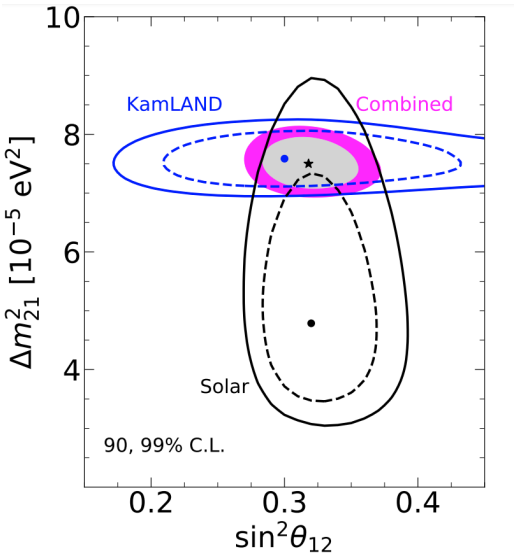

Figure 1.6: *Allowed regions for the solar parameters – 90% and 99% Confidence Level (CL) – from the solar data (black full/dashed lines + black dot), KamLAND data (blue full/dashed lines + blue point) and NuFit results (colored regions + black star). The value of θ_{13} was fixed according the latest measurements from the reactor neutrino experiments [51]. From Ref. [54]*

(see for example K2K whose baseline was ∼250 km or MINOS whose baseline was ∼735 km). The results of all these experiments are generally consistent with each other, the measurements of those that obtained the best precision are summarised on the left plot of Figure 1.7. The T2K experiment has the best precision to date. The T2K and NOνA experiments also reported their favored region of δ_{CP}. The results are shown on the right plot of Figure 1.7. According to the NuFit global fit [51]:

$$\mathbf{\sin^2\theta_{23} = 0.570^{+0.018}_{-0.024}}$$
$$\mathbf{|\Delta m^2_{32}| = 2.514^{+0.028}_{-0.027} \cdot 10^{-3} eV^{-2}}$$
$$\mathbf{\delta_{CP} = 195^{+51}_{-25}\ deg}$$
68% CL, Normal Ordering, without SK atmospheric data.

1.1.4 Open questions

The efforts invested over the last 20 years have led to significant progress in neutrino physics and in particular in the comprehension of the neutrino oscillation. However, some questions remain unanswered. They are briefly reviewed in the following.

1. All the fermions of the SM are known to be *Dirac particles* (i.e. particles and anti-particles are two distinct entities) and the neutrino oscillation theory has been developed in this scope. However, in 1937, Ettore Majorana reviewed the Dirac equation and developed a theory that implies that neutrinos could be their own antiparticles [68, 69]. This theory has not been disproved yet. Thus, **the Dirac or Majorana-nature of the neutrino is yet to be determined**. According to the Majorana theory, the Neutrinoless Double Beta Decay ($0\nu\beta\beta$) is an actual physics process. Experiments are currently under operation or development to detect the $0\nu\beta\beta$ of isotopes that represent good candidates like for example ^{48}Ga, ^{76}Ge, ^{136}Xe etc. The theory of $0\nu\beta\beta$ as well as the most up-to-date experimental results are reviewed in Ref. [70, 71].

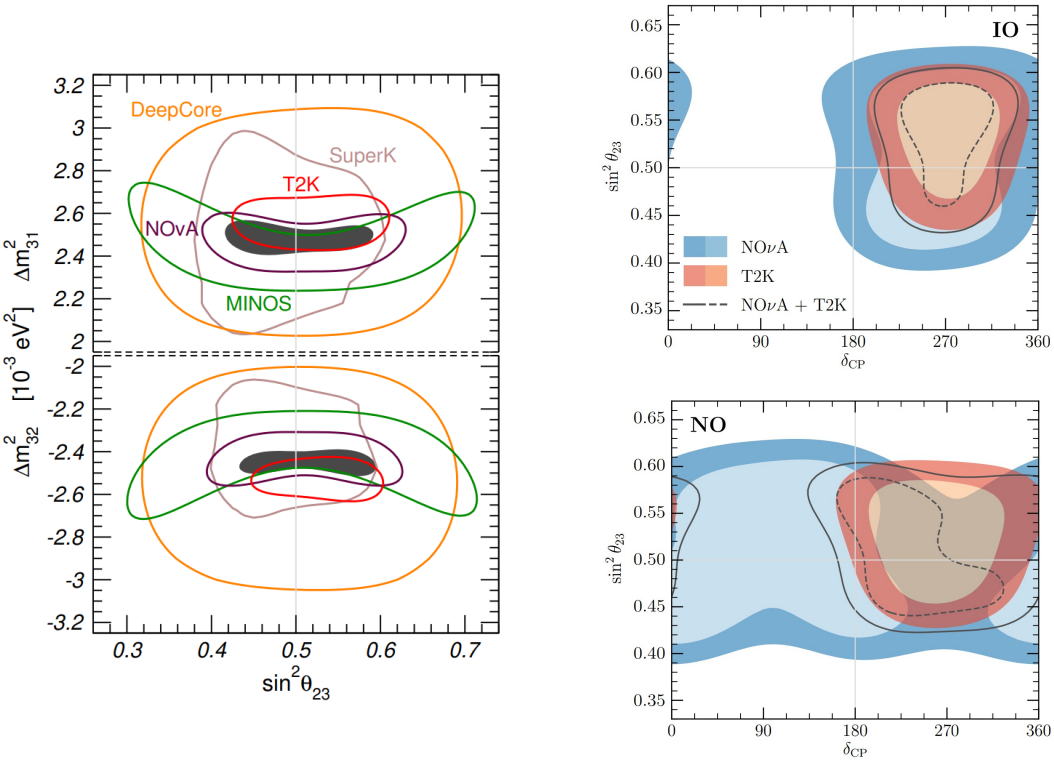

Figure 1.7: ***Left**: Allowed regions for θ_{23} and $\Delta m^2_{31(2)}$ – 95% CL – from IceCube-DeepCore (orange), SK (grey), MINOS (green), NOνA (purple) and T2K (red) assuming NO (top panel) and IO (bottom panel). The black area represents the combination of all these results (NuFIT). From [67]. **Right**: Allowed regions for δ_{CP} – 68% and 95% CL – as measured by NOνA (red) and T2K (blue). The combination (NuFIT) of the two results is displayed with a black curves. From Ref. [51]*

2. The measurement of the neutrino oscillation parameters only gives access to the differences between the three neutrino mass eigenvalues, **the absolute neutrino mass scale is not accessible and remains unknown**. There exist two main ways to constrain the absolute neutrino mass scale. The first one consists in studying the β decay of specific isotopes as done by the Karlsruhe Tritium Neutrino experiment (KATRIN) experiment [72]. This experiment aims to determine the upper bound of the mass scale by studying the end-point of the Tritium (^{3}H) β-decay spectrum. The limit can be derived using kinematics. The second way consists in studying the $0\nu\beta\beta$ process whose half-life can be used to constrain the neutrino mass [70, 71].

3. In the neutrino oscillation theory, the neutrino has three mass states ($|\nu_1\rangle$, $|\nu_2\rangle$ and $|\nu_3\rangle$) that have different eigenvalues (m_1, m_2, and m_3). We have seen that the solar neutrino experiments results allowed to determine that $m_1 < m_2$. **None of the currently running experiments allow to determine – with enough significance – whether $\mathbf{m_1 < m_2 < m_3}$ (NO) or $\mathbf{m_3 < m_1 < m_2}$ (IO). This question is referred to as the Neutrino Mass Ordering (NMO) problem** (Figure 1.8). The NMO determination has several implications:

   - It will contribute to determine the lower limit of the absolute neutrino mass scale.
   - It will help determining the target sensitivity of the $0\nu\beta\beta$ experiments [71]. Indeed if the NMO is inverted, most of the currently running $0\nu\beta\beta$ experiments have not enough sensitivity to detect this theoritical process.
   - It has also an impact on the CP violation measurement by current LBνB experiments (T2K and NOνA).
   - More generally, it has implications for the understanding of the neutrino mass generation as well as in cosmology [73, 74].

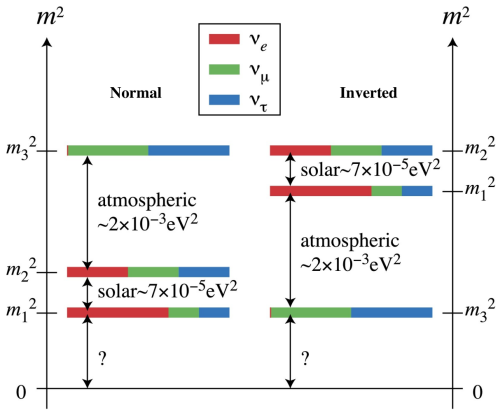

Figure 1.8: *Sketch illustrating the NMO problem and the unkown neutrino mass scale. From Ref. [75]*

Experiments that will allow to resolve the NMO by detecting neutrinos from different sources at different baselines and with or without matter effects are currently under development. The main ones are: Jiangmen Underground Neutrino Observatory (JUNO) that will extract the NMO from the energy spectrum of reactor $\bar{\nu_e}$ at a baseline of ∼52.5 km [76] (see Chapter 2), it is the only experiment that plans to measure the NMO with neutrino vaccum-oscillations; DUNE that will determine the NMO by detecting neutrinos from the Fermilab accelerator [77]; ORCA and Hyper-Kamiokande (HK) that will determine the NMO by detecting atmospheric

neutrinos [78, 79]. Note that the NMO could also be infered from the next galactic Core-Collapse Supernova (CCSN) neutrino burst detection [80, 81].

4. The latest NuFit results suggest two solutions for θ_{23}, **one in the lower octant ($\theta_{23} > \frac{\pi}{4}$) and one in the upper octant ($\theta_{23} < \frac{\pi}{4}$)**. This is yet to be determined. The octant of θ_{23} has implications for the theory of neutrino masses and mixing [82], it will be determined thanks to future neutrino experiments like DUNE [83] and HK [84].
5. The Charge-Parity (CP) symmetry implies that a particle and its antiparticle behave the same in a "mirror space" (opposite spatial coordinates). **The CP symmetry violation in the baryon sector was discovered in 1964 [85]. However, such violation has not been observed – if it indeed exists – in the lepton sector yet**. The precise measurement of δ by future neutrino experiments (DUNE [77] and HK [86, 87]) will allow to resolve whether the CP symmetry is violated in the lepton sector or not, having strong implications on the understanding of the matter-antimatter asymmetry in the universe.
6. Several experiments reported anomalies in their data that cannot be explained by the current formulation of the neutrino oscillation theory [88, 89]. **The existence of additional light (eV scale) neutrino flavors – referred to as *sterile* neutrinos – could explain the discrepancies observed [90, 91]**. Other explanations for these anomalies, like for example a lack of knowledge of the neutrino sources, are also currently being explored.

The transition to the next section is a somewhat abrupt jump from particle physics to astrophysics. No worries, neutrinos are good strings to hang on to. We will see that they play an important role in CCSN and that although the aforementioned experiments are dedicated to the study of the neutrino as a particle, some of them can also serve astrophysics.

1.2 Core-Collapse Supernovae neutrinos

In the history of stargazing, there are many reports of the "sudden appearance of stars in the sky" [92]. One such report was made in 1006 by many observers accross several countries of the North hemisphere. They described a glow that lasted for several months before slowly fading away. A similar phenomenon was observed in 1572 notably by Tycho Brahe, a Danish astronomer that detailed the evolution of the brightness of this "star" in a book that he named *De Stella Nova*. The origin of these observations is nowadays well known, it was in fact *Supernovae (SN)* which basically consists in the powerful and luminous *explosion* of a star. This term was first proposed in 1934 by W. Baade and F. Zwicky [93]. The remnants – i.e. the structures resulting from the explosions – of SN1006 and SN1572 still emit electromagnetic radiations and have been identified for example in [94, 95].

This PhD thesis takes as a starting point a specific kind of SN, the so-called Core-Collapse Supernovae (CCSN) that only concern the massive stars (i.e. $M > 8\ M_\odot$[4]) and that is one of the most powerful and violent astrophysical phenomenon identified so far. CCSN have been observed for a long time and on many occasions by detecting their electromagnetic radiations, providing valuable information on the process. However, it remains impossible to probe the deep interior of the collapsing star since the light cannot escape from there. The electromagnetic radiations and the kinetic energy of the ejected matter

[4] $M_\odot$ = solar mass

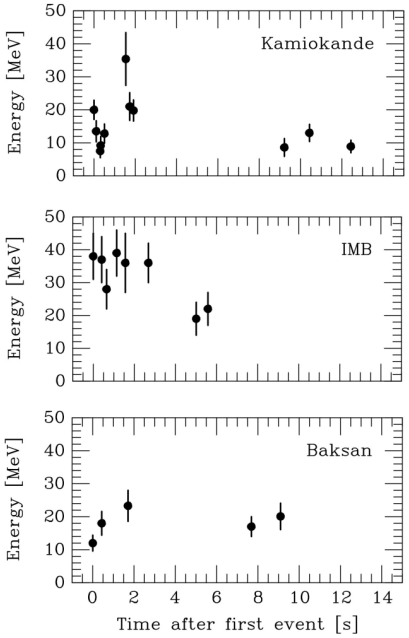

Figure 1.9: *Neutrino events recorded by the Kamiokande, IMB and Baksan detectors. The plots show the energy deposited and the arrival time of positrons from the IBD of $\bar{\nu}_e$. The detectors clocks have unkown relative offsets and the uncertainty on the time of the events of each experiments is of the order of several tens of seconds so in each of the plots, the time of the first event is used as a reference (t = 0). From Ref. [105]*

actually represent ∼0.01% and ∼1% of the total energy released, respectively, while the remaining ∼99% are carried away by $\mathcal{O}$(10 MeV) neutrinos [96] emitted up to several hours before the electromagnetic radiations. Although neutrinos interact only weakly with matter, they are known to play a crucial role in the dynamics of the collapse and explosion [97]. During the last 50 years, significant efforts have been made in order to develop end-to-end simulations of the phenomenon based on fundamental principles of nuclear physics and particle physics. In 1987, the detection of two dozens of neutrinos over a time of about 12 seconds from the SN1987A[5] by the Kamiokande [98], IMB [99] and Baksan [100] detectors (Figure 1.9) allowed to confirm the role of neutrinos in the CCSN process [101, 102] and marked the beginning of a new era in the study of CCSN notably with the opporunity to probe the interior of dying stars. However, questions about the fine mechanisms that govern the explosion remain and/or need to be experimentally corroborated. This thesis is set in a specific context in the particle physics field. Indeed, several large-scale neutrino detectors are currently being developed or constructed. These detectors – JUNO included – have the potential to detect a large number of neutrinos from the next galactic CCSN, allowing for a more accurate probing of the explosion mechanisms. One of the latest estimation of the CCSN rate in the Milky Way predicts 1.63 ± 0.46 (100 yr^{-1}) [103], making the next galactic CCSN a once-in-a-life-time opportunity. Section 1.2.1 gives an overview of the neutrino production and their role in the collapse and explosion of the star (which is fully reviewed in Refs. [97, 104, 105]). Section 1.2.2 summarises what can be learnt from the detection of the next galactic CCSN neutrino burst and section 1.2.3 reviews the future experiments that will have the sensitivity to detect these neutrinos.

1.2.1 From the progenitor star to the explosion

1.2.1.1 Stellar nucleosynthesis

The creation of chemical elements by the nuclear fusions occuring into the stars is called the *stellar nucleosynthesis*. For example, the Hydrogen fusion forms Helium-4 ($^4_2$He) – through the so-called *pp*-chain and the *CNO*-cycle [106] – and is the dominant process occuring in all stars during their early life. Each fusion releases energy and the sum of all

[5]Nobel Prize in Physics 2002 awarded to R. Davis Jr and M. Koshiba for their pioneering work in the field of astrophysics, in particular for the detection of cosmic neutrinos.

of them generates thermal pressure that compensates for the gravitational force that tends to make the stars collapse (Figure 1.10, left). The Helium nuclei generated gradually form a core at the center of the star. At some point, the core reaches temperature and pressure conditions that allow to ignit Helium fusion which creates heavier chemical elements, and so on. Only the massive stars reach the most advanced stages of the stellar nucleosynthesis and can end-up as CCSN. The different chemical elements are then distributed in layers and the star can be represented schematically as the right sketch of Figure 1.10.

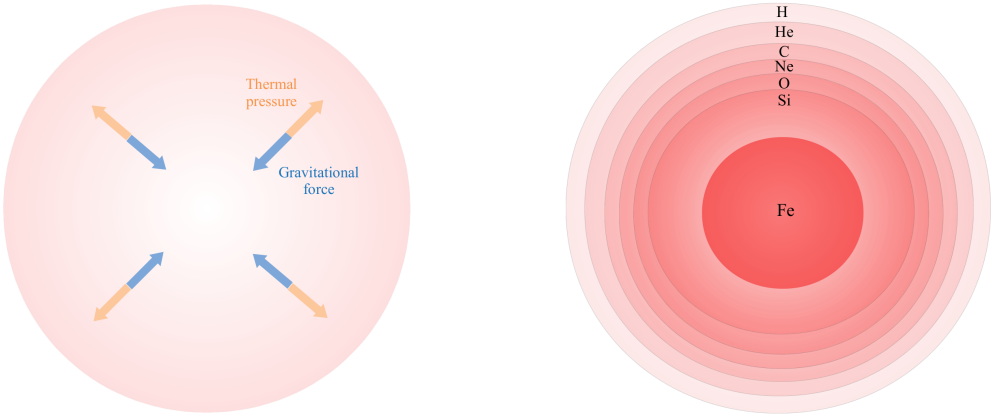

Figure 1.10: ***Left**: During the different stages of the stellar nucleosynthesis, the fusion of the chemical elements releases energy whose resulting thermal pressure compensates for the gravitationnal force.* ***Right**: Simplified schematic of the onion-like structure of an evolved massive star just before the collapse. The layers are not to scale.*

Reactions occuring during the Silicon (Si) shell burning (notably e^+e^- annihilation and $e^{\pm}$ captures) produce a significant number of neutrinos (moslty ν_e and $\bar{\nu_e}$) that are referred to as *pre-SN neutrinos* [107]. Since these neutrinos are emitted up to several days before the explosion [108, 109] (Figure 1.11), they are very useful objects for early warnings in the scope of multimessenger astronomy [110]. They also represent probes to study the latest stages of the stellar evolution. It is worth mentioning that the expected flux is about 100 times smaller than that emitted during a CCSN. In addition, the average energy of the pre-SN neutrinos is $\sim$1 MeV. Thus, very few detectors (JUNO is one of them) will be sensitive to pre-SN neutrinos and only close-by progenitors ($<$ 1 kpc) can be detected using them.

1.2.1.2 Core-collapse

Before the collapse, the diameter of the Iron (Fe) core is of a few thousands of kilometers. In contrast to lighter elements, iron fusion consumes more energy than it produces and then tends to cool the core temperature down, the thermal pressure gradually drops. While the nuclear fusion keeps on going in the Si layer, the iron core mass grows. For a while, the electron degeneracy pressure[6] compensates for the gravitational force and the core does not collapse. At this point, the density of the core is $\rho \sim 10^9$ g·cm^{-3}. The density keeps increasing with time and the electrons start to be captured on heavy nuclei as well as on free protons, heavy nuclei are also photodisintegrated by gammas. As a consequence, the electron degeneracy pressure drops and the collapse begins. The capture of electron on free protons produces electron neutrinos (ν_e) (equation 1.17) that start escaping the core.

$$e^- + p \rightarrow \nu_e + n \tag{1.17}$$

[6]The electron degeneracy pressure [112] is a consequence of Pauli's exclusion principle [113].

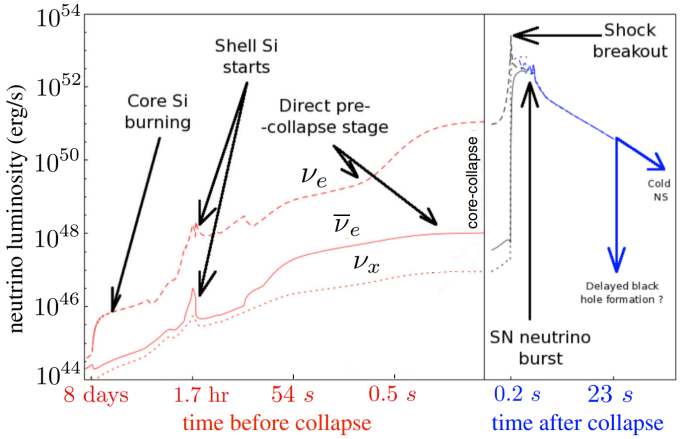

Figure 1.11: *Example of the evolution of the neutrino luminosity (energy radiated under the form of neutrinos, 1 erg = 10^{-7} J) as a function of time for ν_e (dashed), $\bar{\nu}_e$ (full), ν_x and $\bar{\nu}_x$ (dotted). The plot focuses on the pre-SN neutrino luminosities (red curves) from the Si shell burning. From Ref. [111].*

It is worth mentioning that there exist three other known processes that lead to the collapse of massive stars core, namely the *electron capture in degenerated Oxygen-Neon-Magnesium core*, the *pair instability* and the *photodisintegration*. The first one occurs in stars with M $\simeq$ 9 $M_\odot$ while the two others concern stars with M $>$ 150 $M_\odot$ [114]. The studies carried-out during this PhD only concern iron core-collapse SN as described in this section.

The sudden core collapse creates a "vaccum" at its boundaries and the stellar matter of the upper layers falls toward the center of the dying star. The collapsing core density regularly increases to reach $\rho \sim 10^{12}$ g·cm^{-3} and the ν_e (equation 1.17) get trapped in a region with a radius that is roughly R$\sim$100 km. Then, an equilibrium between the electron capture on free protons and the ν_e capture on neutron is reached. The deepest regions of the collapsing core density finally reaches the nuclear density saturation $\rho_0 \sim 2.6 \cdot 10^{14}$ g·cm^{-3}. Because of the repulsive nuclear force, the incompressibility suddenly rises and further compression is impossible: the core bounces back (R_{bounce} $\sim$10 km) and an outwarding shockwave is formed. The shockwave propagates within the outer layers of the collapsing core. The trapped ν_e are suddenly released producing a **ν_e-burst**. The brutal drop of the electron-lepton number in the matter – due to the ν_e-burst – generates large concentrations of positrons and pair-production processes start to produce heavy-flavor (anti)neutrinos as well as $\bar{\nu}_e$ [115] notably *via* the following processes:

$$e^- + e^+ \rightarrow \nu + \bar{\nu} \quad \text{and} \quad \nu_e + \bar{\nu}_e \rightarrow \nu + \bar{\nu} \tag{1.18}$$

where ν refers to neutrinos of all flavors. At the level of the dense core, a so-called *neutrinosphere* (R_ν $\sim$50 km) – whose radius actually slightly depends on the neutrino flavor – is formed and corresponds to a very dense region where the neutrinos are strongly coupled to matter and from where they hardly escape. In the mean time, the shockwave propagation is counteracted by the stellar matter that still falls down toward the center and eventually stalls at a radius R_{shock} $\sim$150 kilometers, approximately 100 miliseconds after the bounce. The area that separates the densest region of the collapsing star – the so-called Proto-Neutron Star (PNS)[7] – and the stalled shock radius consists of two parts:

[7]Note that depending on the progenitor star mass and metallicity, the dense core can also turn into

- The cooling layer from where ν_e and $\bar{\nu_e}$ are produced.
- The heating layer where significant convective movements of matter take place and through which neutrinos emitted by the inner regions of the dying star pass.

In the mean time, the stellar matter from the upper layers has kept accreting onto the PNS feeding the heating and cooling layers and maintaining the emission of ν_e and $\bar{\nu_e}$ by the latter. This process is the ***Accretion phase*** of the neutrino signal. Figure 1.12 shows a snapshot of the CCSN at the moment of the shockwave stalling.

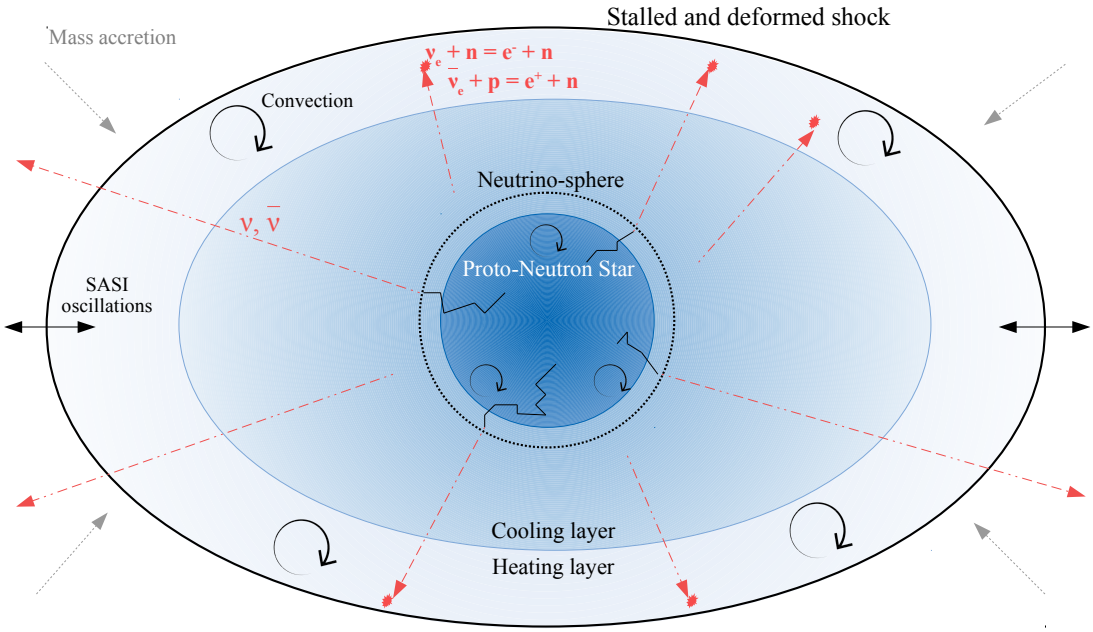

Figure 1.12: *Sketch illustrating the neutrino heating mechanism. Inspired from Ref. [119]*

The origin of the shock revival that causes the final explosion remains a subject of active research [120–122]. The most promising mechanism is the so-called *neutrino heating*. It was mentioned for the first time in 1982 by J.R. Wilson during a conference at the University of Illinois and then more detailed in a dedicated paper by H.A. Bethe and J.R. Wilson himself [123]. In brief, the principle is that the ν_e and $\bar{\nu_e}$ produced in the PNS and in the cooling layer deposit energy *behind* the stalling shock (Figure 1.12) *via* the following reactions:

$$\nu_e + n \rightarrow e^- + p \quad \text{and} \quad \bar{\nu_e} + p \rightarrow e^+ + n \tag{1.19}$$

The total energy deposited re-accelerates the shock. Note that other mechanisms such as non-radial hydrodynamic instabilities (see Standing Accretion Shock Instabilities (SASI) [124]) and convection movements could also have a determining role in the onset of the explosion, which still needs to be experimentally corroborated. Note that the aforementioned accretion phase does not necessarily stops after the explosion starts, it can last several hundreds of miliseconds depending on the progenitor star. Finally, when the accretion phase terminates, the PNS enters in a ***Cooling phase*** during which (anti)neutrinos of all flavors keep being emitted. Their flux slowly decreases over several seconds. Figure 1.13 shows an example of the luminosities and mean energy of the different neutrino

a black hole [116] which notably translates into a sharp decrease of the neutrino luminosities [117, 118]

flavors during the three main neutrino emission phases from the simulation of a 27 $M_\odot$ progenitor star. The neutrino energy spectra as well as their evolution against time can also be predicted (Figure 1.14).

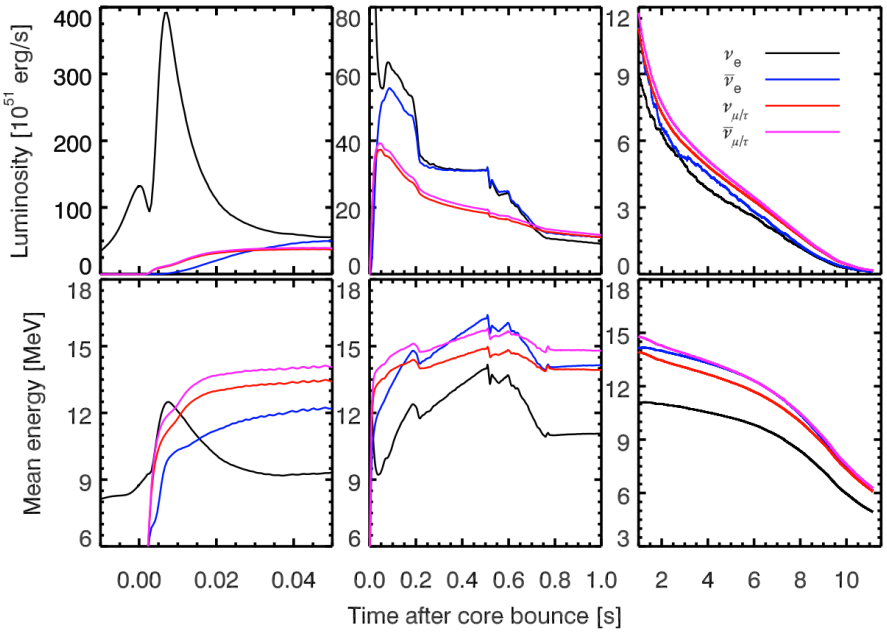

Figure 1.13: *Neutrino luminosities (top) and mean energies (bottom) from a 27 $M_\odot$ star. The black line corresponds to ν_e, the blue line corresponds to $\bar{\nu_e}$, the red line corresponds to the ν_μ and ν_τ and the pink line corresponds to $\bar{\nu_\mu}$ and $\bar{\nu_\tau}$. The left panel shows the ν_e-burst emission phase, the middle panel shows the accretion phase and the right panel shows the PNS cooling phase. From [125].*

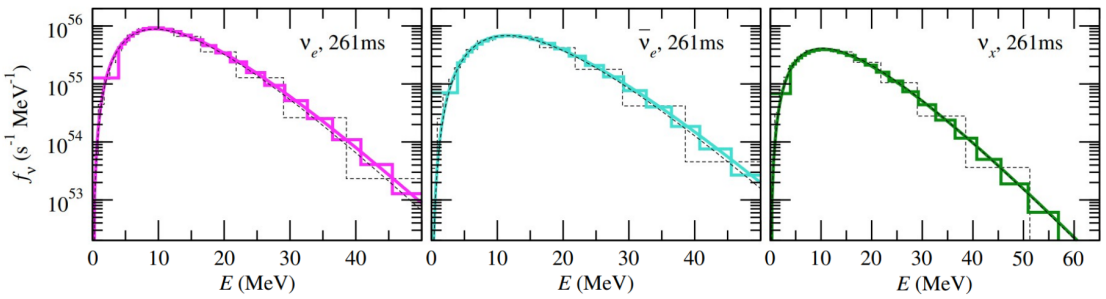

Figure 1.14: *An example of the neutrino energy spectra of ν_e (left), $\bar{\nu_e}$ (middle) and ν_μ, $\bar{\nu_\mu}$, ν_τ, $\bar{\nu_\tau}$ (right) 261 miliseconds after the core bounce. The step functions corresponds to simulation data with higher (coloured) or lower (thin black) resolutions. The continuous line is a fit with a quasi-thermal spectrum function. From [126].*

The simulation of CCSN requires to take into account many different physics phenomena, from the dynamics of nuclear matter to the production of neutrinos, their transport etc. Thus, the end-to-end simulations are often limited by the computing power available which notably led to the development of 1D and 2D modelisations of the CCSN that allowed to highly reduce it. Furthermore, because of the lack of knowledge on the process ongoing in the extreme conditions of the dying star, modelling groups make different approximations and assumptionss [127–131]. For these two reasons, strong differences in the time-dependent neutrino luminosities and energy spectra predictions can be observed

from one model to another. Since the work realised during this PhD thesis focused on the *detection* of CCSN neutrino burst, no dedicated study has been carried-out on the different existing models and their characteristics. The two models that have been used to generate the neutrino interactions in a simulated JUNO detector are introduced in more details in Chapter 3.

1.2.2 What can neutrinos teach us about the CCSN

In the previous section, we have seen that the neutrino signal is modulated following the different steps of the star death. In addition, they are produced in different regions – including the most central ones – *via* different physical processes. Thus, the detection of CCSN neutrinos represents an excellent opportunity to track one-by-one the phases of the collapse and explosion and to constrain various parameters of the PNS and accretion flow as well as the progenitor star properties. The two main observables that can be extracted by the detectors are the time-dependent neutrino luminosities (L) as well as their energy spectra. The main ways these observables can be used to probe the CCSN features are listed below and are fully reported in Ref. [132]. It is worth pointing out that the distance to the CCSN [133, 134] and the isotropy (or anisotropy) of the neutrino emission during the explosion will have strong impact on the number of detected events. Moreover, the signal flavor content can be alterated due to the collective neutrino oscillation that occurs in very dense neutrino media like a CCSN [135]. Thus, if the next galactic CCSN is too far and/or if the collective neutrino oscillation alterates too much the flavor content, the information extractable from the signal could be limited even with nowadays detection and analysis techniques. Below are listed the main characteristics of the progenitor star and the subsequent CCSN that might be extracted from the detected neutrino signal:

1. As mentioned in the end of the previous section, distinguish which CCSN model will describe the best the future data constitutes a milestone in the comprehension of the explosion mechanism. Examples of such works using simulation data are given in Refs. [136, 137].

2. In the PNS region, the neutrino electron-flavor and heavy-flavor luminosities strongly depend on the temperature and radius of the neutrinosphere. Particularly, the heavy-flavor luminosity is well described by a grey-body emission law $L_{\nu_x} = 4\pi\phi\sigma_f R^2 T^4$ where ϕ is the greyness factor, σ_f is the radiation constant for massless fermion and R and T are the radius and temperature of the neutrinosphere, respectively. Thus, the determination of these luminositites give a direct access to some of the neutrinosphere parameters.

3. A very large fraction of the neutrino electron-flavor luminosity arises from the accretion region (cooling+heating layer) and the total flux, comprising both PNS and accretion contributions, is well described by the following formula: $L_{\nu_e} + L_{\bar{\nu_e}} = 2\beta_1 L_{\nu_x} + \beta_2 \frac{GM\dot{M}}{R}$ where G is the gravitational constant, $\beta_{1,2}$ are non-dimensional parameters [138], $\dot{M}$ is the mass accretion rate and M and R are the PNS mass and radius, respectively. Thus, such a formula can also be used to constrain the PNS parameters.

4. Related to the previous point, quantify how the electron flavor luminosity is shared between ν_e and $\bar{\nu_e}$ allows to probe the neutrino interaction rates in the medium (for example study the effect of nucleon potentials on the Charged Current (CC) rate) [139]

5. The determination of the neutrino electron-flavor energy spectra might help constraining the PNS thermodynamic properties, especially the thermodynamic equilibrium as reported in Ref. [140].

6. According to Ref. [141], the determination of the $\bar{\nu_e}$ average energy can be used to constrain the PNS mass during the accretion phase thanks to the following formula: $\langle E_{\bar{\nu_e}} \rangle \simeq a \times \frac{M}{M_\odot}$ MeV. However, a depends on the nuclear matter equation of state, as well as on the progenitors so that the uncertainty on the extracted M would be large.

7. The ν_e and $\bar{\nu_e}$ luminosities brutaly drop during the accretion phase, at about 250 miliseconds (see the top-middle panel in Figure 1.13). This is due to the decrease of $\dot{M}$ after the accretion of the Si/O shell. The precise timing of this drop in luminosity might give access to the radius and mass of the Si/O shell before the collapse and then on the internal structure of the progenitor star:

$$t_{if} = \sqrt{\frac{\pi^2 r_{if}}{3 G m_{if}}} \tag{1.20}$$

   where r_{if} is the shell pre-collapse radius and m_{if} is the shell mass.

8. As reported in Ref. [142], the correlation between the total energy emitted in $\bar{\nu_e}$ and the progenitor compactness could be used to estimate the latter.

As an example, an analysis of the $\bar{\nu_e}$ SN1987A events (energy spectra, time-dependence and even incidence angle) allowed to extract several parameters including the neutrinosphere radius, the accretion phase duration as well as the total energy emitted in neutrinos [143].

1.2.3 Preparing for the next galactic CCSN

From the two previous sections, it is clear that the precise measurement of the flavor and time-dependent neutrino luminosities as well as the energy spectra is the key to maximise the amount of extractable information about the CCSN. Thanks to their unprecendently large detection volume, the present and future neutrino detectors (JUNO, HK, DUNE, KM3NeT, IceCube etc.) represent excellent candidates to this purpose. However, one shall keep in mind that getting the most of the next burst will also involve a pooling of data from these experiments (see for example the impoved analyis of the neutrino burst from SN1987A using the data from the Kamiokande, IMB and Baksan detectors in Ref. [143]). As a matter of fact, detectors with different target media favor different interaction channels and are then more or less sensitive to specific (anti)neutrino flavors. This section briefly lists the potential of some current and future neutrino detectors for the CCSN neutrino detection with particular emphasis on the advantage they have over others, building on what has been done in Ref. [144]. Given that the Earth is located ∼10 kpc from the center of the Milky Way and that it is the most active star forming region of the galaxy, the most probable distance to the next galactic CCSN is ∼10 kpc [133, 134]. For this reason, such distance is taken as reference in the following.

CCSN neutrino interactions

The knowledge of the neutrino interaction cross-sections are of paramount importance to retrieve the actual neutrino luminosities and spectra after the burst detection. The dominant interaction channels at future large-scale neutrino detectors are the Inverse Beta Decay (IBD) [145] ($\bar{\nu_e}$), the Neutrino-Electron Elastic Scattering (νeES) [146] (mostly ν_e

$+ \bar{\nu_e}$) and the Neutrino-Proton Elastic Scattering (νpES) [147] (mostly $\nu_x + \bar{\nu_x}$). The cross sections of these processes have been calculated, notably in Refs. [146–149] but have been only marginally constrained experimentally in the tens of MeV range. Furthermore, although the neutrino-nuclei interaction cross-sections are generally smaller, a non-negligible number of events are expected in some detectors: even less experimental measurements exist for these. Thus, it is worth pointing out that idependent measurements of relevant cross-sections might be necessary to enhance the precision on the extracted flux and energy spectra. Figure 1.15 shows the cross-sections of interaction channels expected in various detectors during the next galactic CCSN neutrino burst.

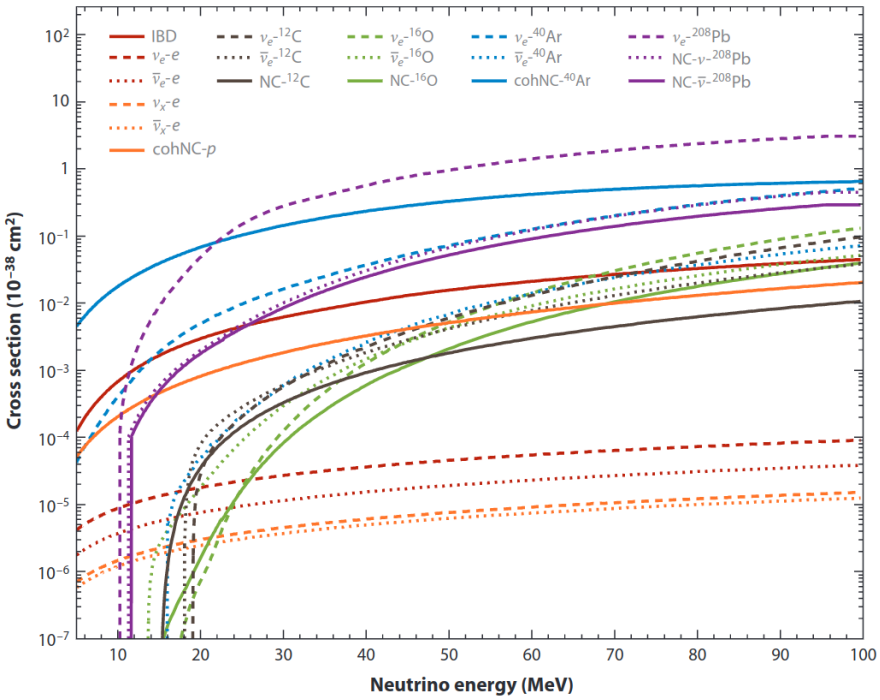

Figure 1.15: *Neutrino interaction cross-sections for different targets in the tens of MeV energy range, ν_x stands for the μ and τ lepton flavors, cohNC corresponds to coherent neutrino elastic scatterings. From [144].*

Water Cherenkov detectors

The ultra-pure water Cherenkov technology has been used for several decades by a large number of experiment (IMB, Kamiokande, SK) and has a proven track record. The relatively low cost of the detection medium and the good command of the technology allow to build the largest "closed environment" detectors in the world as will be HK with its ∼500 ktons of ultra-pure water. The abundance of free protons in water makes HK particularly sensitive to the IBD detection channel, it would actually provide an unbeatable $\bar{\nu_e}$ sampling compared to other detectors (several tens of thousands). With a smaller but still large detection volume (∼50 ktons), SK would also detect a significant number of IBDs (several thousands). The second great advantage of water cherenkov detectors is their capability to locate the CCSN. This can be done with the νeES events (several hundreds and thousands of events expected in SK and HK, respectively), using the direction of the cherenkov ring of the scattered electron. This is particularly useful to warn astronomers so that the telescopes point toward the right direction to optmise the detection of the CCSN electromagnetic radiations. Although they are not designed to measure $\mathcal{O}$(10 MeV) neutrinos, the "open environment" cherenkov detectors like IceCube

and KM3NeT would also be sensitive to CCSN neutrinos thanks to their gigantic detection volumes [150, 151].

Liquid Scintillator detectors

As the water cherenkov detectors, Liquid Scintillator (LS) detectors (Daya Bay, KamLAND, Borexino...) have been used for a long time and also allowed to perform great achievement in neutrino physics. A LS detector is predominantly composed of protons (∼85-90%) so that the IBD would also be the dominant detection channel (several thousands of events). Also, thanks to the high photon yield, these detectors presents two advantages: 1) a better energy resolution with respect to water chrenkov detectors, which ensures a high resolution energy spectra reconstruction 2) they can have a lower threshold so that a significant number of νpES can be detected and used to probe the heavy neutrino flavors. In particular, the future JUNO detector (E_{res} ∼3% at 1 MeV) will contain 20 kton of LS and is expected to detect several thousand of IBD and νpES. More details are provided in Chapter 2.

Liquid Argon Time Projection Chamber

The Liquid Argon Time Projection Chamber (LArTPC) detectors have a unique sensitivity to the ν_e mainly thanks to the CC interaction $\nu_e + {}^{40}\mathrm{Ar} \rightarrow \mathrm{e}^- + {}^{40}\mathrm{K}^*$, both e^- and γ from the excited potassium being observable to tag such events. The future DUNE detector (four 10 kton LArTPC modules) is expected to see several thousands of these events. The detector being designed to observe accelerator neutrinos interactions (∼GeV), it is not optimal for a precise reconstruction of the CCSN neutrino spectra and would predominantly contribute to a precise timing of the ν_e signal.

Xenon dark matter detectors

The Liquid Xenon Time Projection Chamber (LXeTPC) detectors such as XENON1T [152], XENONnT [153] and the future DARWIN [154] are made of several tons (even several tens of tons for the latter that is still under development) of liquid Xenon as target material. They present the unique advantage to detect the CCSN neutrinos via Coherent Elastic Neutrino-Nuclei Scatterings (CEνNS), making them sensitive to the three (anti)neutrino flavors. With 5 kton of liquid Xenon, the DARWIN detector is expected to detect several hundreds of events. Thanks to an energy resolution of the order of a few percent at 1 MeV combined to a precise timing resolution, DARWIN would precisely contribute for both energy spectrum and signal timing reconstruction.

Finally, it is important to mention the Supernova Early Warning System (SNEWS) [155], a network of active neutrino detectors that aims to give early warnings to astronomers in case a CCSN occurs in the Milky Way, or in a nearby galaxy such as the Large Magellanic Cloud. Indeed, as mentioned before, neutrinos from CCSN can be detected up to several days before the electromagnetic counterpart. Such a warning would allow to point the telescopes towards the expected direction before the explosion. Currently, seven neutrino detectors integrated the network: Borexino, Daya Bay, KamLAND, HALO, IceCube, LVD, and SK. The JUNO detector entry into this network is in progress.

Chapter 2

The JUNO experiment

Contents

The idea of a JUNO-like experiment was first put forward in 2008, when it was demonstrated that the Neutrino Mass Ordering (NMO) could be determined with a reactor neutrino detector at an intermediate baseline if the mixing angle $\sin^2(2\theta_{13}) > 0.02$ and even $\sin^2(2\theta_{13}) > 0.005$ [156, 157]. The requirements concerned the energy resolution and energy precision of the detector, the baseline and the event statistics [158]. The relevance and feasibility of such an experiment was indeed confirmed in 2012, after the Daya Bay [159], Double Chooz [160] and RENO [161] experiments measured $\sin^2(2\theta_{13})$ to be > 0.02. Thus, the JUNO experiment has been conceptualised and optimised for the NMO measurement (section 2.1.1). The experimental site is located near the Jiangmen city (Guangdong province, China), at equal distances ($\sim$52.5 $\pm$ 0.5 km) from the Yangjiang and Taishan Nuclear Power Plant (NPP) (Figure. 2.1, left). The civil construction, including the experimental site (Figure. 2.1, right) and the underground laboratories construction started in 2015 and finished in December 2021. The detector assembly started in early 2022 and will be finished in 2023. The status of each component of the detector is summarised in the next sections. The JUNO collaboration gathers $\sim$ 700 people including researchers, post-doctoral students, PhD students, engineers and technicians from 76 different institutes around the world.

Figure 2.1: ***Left**: The JUNO location, in southern China. **Right**: Bird view of the JUNO experimental site.*

2.1 Neutrino Physics with JUNO

Even if the design of the JUNO detector (section 2.2) was optimised for the determination of the NMO, its large detection volume, excellent energy resolution and background level requirements naturally extend its physics programme and will notably allow to measure three of the neutrino oscillation parameters with an unprecedent precision. This section first details the strategy of JUNO for determining the NMO and reviews the different physics topics to which JUNO will contribute in the coming years.

2.1.1 Neutrino Mass Ordering Determination

2.1.1.1 Reactor $\bar{\nu}_e$ disappearance and experimental requirements

Previous works [156, 157] demonstrated that the NMO can be extracted from the reactor $\bar{\nu}_e$ energy spectrum, by studying their disappearance in vacuum with a detector placed at an intermediate baseline (40-60 km). Indeed, the detected $\bar{\nu}_e$ energy spectrum can be expressed such as:

$$F(L/E) = \phi(E)\sigma(E)P_{\bar{\nu}_e\to\bar{\nu}_e}(L/E) \tag{2.1}$$

where $F(L/E)$ is the $\bar{\nu}_e$ spectrum, $\phi(E)$ denotes the $\bar{\nu}_e$ flux from a nuclear reactor, $\sigma(E)$ corresponds to their interaction cross section with matter, $P_{\bar{\nu}_e\to\bar{\nu}_e}(L/E)$ corresponds to their survival probability, L is the distance between the source and the detector in km (also referred to as "baseline") and E the $\bar{\nu}_e$ energy in MeV. In the three-neutrino framework, $P_{\bar{\nu}_e\to\bar{\nu}_e}(L/E)$ can be described by the following formula:

$$\begin{aligned} P_{\bar{\nu}_e\to\bar{\nu}_e} &= 1 - P_{21} - P_{31} - P_{32} \\ P_{21} &= \cos^4\theta_{13}\sin^2 2\theta_{12}\sin^2\Delta_{21} \\ P_{31} &= \sin^2 2\theta_{13}\cos^2\theta_{12}\sin^2\Delta_{31} \\ P_{32} &= \sin^2 2\theta_{13}\sin^2\theta_{12}\sin^2\Delta_{32} \end{aligned} \tag{2.2}$$

where Δ_{ij} is defined as:

$$\Delta_{ij} = 1.27\Delta m^2_{ij} L/(4E) \tag{2.3}$$

and where θ_{ij} are the neutrino oscillation mixing angles, Δm^2_{ij} are the neutrino oscillation mass splittings in eV^2 and i, j runs over the three mass eigenstates. The Eq. 2.2 can also be rewritten such as:

$$\begin{aligned} P_{\bar{\nu_e}\to\bar{\nu_e}} = 1 &- \cos^4\theta_{13}\sin^2 2\theta_{12}\sin^2\Delta_{21} \\ &- \sin^2 2\theta_{13}\sin^2(|\Delta_{32}|) \\ &- \cos^2\theta_{12}\sin^2 2\theta_{13}\sin^2(\Delta_{21})\cos(|2\Delta_{32}|) \\ &- [\pm\frac{1}{2}\cos^2\theta_{12}\sin^2 2\theta_{13}\sin(2\Delta_{21})\sin(|2\Delta_{32}|)] \end{aligned} \tag{2.4}$$

where the "±" in the last term symbolises the Normal Ordering (NO) (+) or the Inverted Ordering (IO) (-), hence the oscillation pattern is different following the NMO. Each of the three P_{ij} terms of Eq. 2.2 contains one of the three mass splitting terms, that drive the oscillation frequency. The terms containing Δm^2_{31} and Δm^2_{32} are the ones sensitive to the NMO. However, these terms are highly suppressed due to the small value of $\sin^2(2\theta_{13})$, making these measurements very challenging.

The ability of JUNO to infer the NMO will thus mainly rely on its capability to precisely reconstruct the reactor $\bar{\nu_e}$ energy spectrum. The experimental requirements necessary to resolve the NMO are reported in Ref. [158]. The most sensitive parameters are the baseline, energy resolution (necessary to distinguish the fine structures of the spectrum), the energy precision (in order not to err on the position of the oscillation pattern), and the event statistics (necessary to limit the spectrum distortion due to the statistical error). The requirements are the following:

- Baseline: 53 ± 0.5 km
- Energy resolution: 3% at 1 MeV (visible energy)
- Energy precision: 1%
- Total number of events: ∼100,000

Figure 2.2 shows the expected $\bar{\nu_e}$ energy spectrum – considering a perfect energy resolution – assuming the NMO is normal (blue) or inverted (red). In order to evaluate the sensitivity of JUNO to the NMO with such a spectrum, a least squared method is employed and a χ^2 function is constructed such as:

$$\chi^2 = \sum_{i=1}^{N_{bin}} \frac{[M_i - T_i(1+\sum_k \alpha_{ik}\epsilon_k)]^2}{M_i} + \sum_k \frac{\epsilon_k^2}{\sigma_k^2} \tag{2.5}$$

where i is the i^{th} bin of the $\bar{\nu_e}$ energy spectrum, M_i and T_i are the number of neutrino events measured and predicted (with oscillation), respectively. The second sum runs other a set of pull parameters (ϵ_k) used to implement the systematics uncertainties (σ_k). Finally, α_{ik} is the fraction of neutrino events contribution to the k-th pull parameter in the i-th energy bin.

The $\bar{\nu_e}$ spectrum is fitted twice with the Eq. 2.4. Once assuming the NO - for which the minimum is defined as $\chi_{min}(NO)$ - and once assuming the IO - for which the minimum obtained is defined as $\chi_{min}(IO)$. The difference between the two minima:

$$\Delta\chi^2_{MO} = |\chi_{min}(NO) - \chi_{min}(IO)| \tag{2.6}$$

gives the sentivity in units of σ as $\sqrt{\Delta\chi^2_{MO}}$ (significance). With the assumptions that are fully detailed in Refs. [76], JUNO is expected to resolve the NMO at 3σ ($\Delta\chi^2_{MO} \sim$

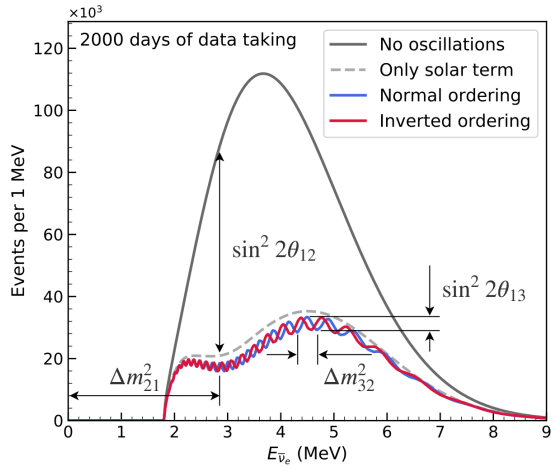

Figure 2.2: *The expected $\bar{\nu}_e$ energy spectrum at JUNO after 2000 days (∼6 years) of data taking, assuming a perfect energy resolution, with and without oscillation. The dependance on four oscillation parameters is shown.*

9) with ∼100,000 events or ∼6 years of data taking. Note that the sensitivity of JUNO *alone* could be enhanced to $\sim 4\sigma$ thanks to the precision measurement of $\Delta m^2_{\mu\mu}$ from atmospheric muon (anti)neutrino disappearance[162]. The aforementioned works [156, 157] showed that the Normal Ordering (NO) or Inverted Ordering (IO) can also be extracted from the Fourier transform of the energy spectrum, which brings to light particular structures. Indeed, after the Fourier transform is applied, one can observe symmetries in the shape of the obtained power spectra of P_{21} and P_{32}. This symmetry is broken in different ways whether the NMO is normal or inverted. Finally, synergies between JUNO and other experiments JUNO+ORCA [163], JUNO +IceCubeUpgrade [164]) and finally JUNO+T2K+NOνA [165] will boost its sensitivity to the NMO with a potential 5σ significance. The latter combination should lead to such a sensitivity by 2030.

2.1.1.2 Reactor $\bar{\nu}_e$ flux

A precise knowledge of the reactor $\bar{\nu}_e$ energy spectrum is of great importance for any experiment measuring neutrino oscillation parameters using nuclear reactors as a source. The Yangjiang and Taishan Nuclear Power Plant (NPP) ($\bar{\nu}_e$ source of JUNO) are commercial reactors from which $> 99.5\%$ of the $\bar{\nu}_e$ are produced *via* the β decays of fission products from four main isotopes: $^{235}_{92}$U, $^{238}_{92}$U, $^{239}_{94}$Pu and $^{241}_{94}$Pu. The $\bar{\nu}_e$ energy spectrum can be expressed as:

$$\phi_{\bar{\nu}_e}(E) = \int_{t_0}^{t} \frac{P_{th}(t)}{\sum_k \alpha_k(t)\langle E_k\rangle} \sum_k \alpha_k(t)\phi_k(E)dt \tag{2.7}$$

where $\phi_{\bar{\nu}_e}(E)$ denotes the total $\bar{\nu}_e$ energy spectrum – that is time-dependent since the multiple fissions that occur in the reactor core evolve the fuel composition over time –, P_{th} is the thermal power of the reactor, the index k corresponds to the $^{235}_{92}$U, $^{238}_{92}$U, $^{239}_{94}$Pu and $^{241}_{94}$Pu, $\langle E_k\rangle$ is the mean energy per fission weighted by the fraction of the kth isotope in the core, and ϕ_k is the $\bar{\nu}_e$ energy spectrum of the kth isotope. Two different methods are generally used to compute the $\bar{\nu}_e$ spectrum from reactor cores:

- The *conversion method* that is based on experimental measurements that have been performed in the 1980s at the Institut Laue-Langevin (ILL) in Grenoble. The experiment consisted in irradiating – with neutrons – targets made either of $^{239}_{94}$Pu, $^{239}_{92}$Pu or $^{235}_{92}$U (it was not possible to do it for $^{238}_{92}$U) and to measure the resulting

β spectrum, that actually includes the spectra of all the fission products [166–168]. The β spectra were then converted into $\bar{\nu}_e$ spectra and can be used to predict that from a given reactor.

- The *summation method* (also named *ab-initio method*) that sums the $\bar{\nu}_e$ spectra of all fission products using the nuclear database (see for example Evaluated Nuclear Structure Data File (ENSDF) [169]) and then predicts the total spectrum. This method implies to have a good knowledge of the production rate of the fission products in the reactor core, their branching ratio etc.

In the last decade, the Double-Chooz, Daya Bay and RENO experiments reported strong deviations in both measured rate and shape of the spectrum with respect to the predictions from the summation method[44, 46, 48], this is the so-called *reactor anomaly*. This anomaly is still under investigation today by searching for the existence of light sterile neutrinos [90] and by updating the nuclear data bases with new experimental results [170]. The Taishan Neutrino Observatory (TAO) detector (a satellite experiment of JUNO, see section 2.2.6) will be placed at ∼30 m of one of the cores of the Taishan nuclear power plant. It will measure the $\bar{\nu}_e$ spectrum which will notably serve as benchmark measurements to test nuclear databases.

2.1.1.3 Detection of $\bar{\nu}_e$

The detection of $\bar{\nu}_e$ will be based on the Inverse Beta Decay (IBD), which consists in a Charged Current (CC) interaction between a $\bar{\nu}_e$ and a proton (p). The proton target is provided by the LS. As shown in Eq. 2.8, two particles are produced through this reaction, a positron (e^+) and a neutron (n).

$$\bar{\nu}_e + p \longrightarrow e^+ + n \tag{2.8}$$

The IBD cross section [148] follows the following formula (at the first order):

$$\sigma_{IBD} = \frac{2\pi^2}{m_{e^+}^5 f \tau_n} p_{e^+} E_{e^+} \tag{2.9}$$

where τ_n is the measured neutron lifetime, f is a phase space factor [148] and m_{e^+}, p_{e^+} and E_{e^+} are the mass, momentum and kinetic energy of the positron, respectively. The uncertainty on σ_{IBD} is ∼1% [145]. The interaction cross-section of the IBD increases with the $\bar{\nu}_e$ energy, while the $\bar{\nu}_e$ flux decreases with it. This results in a detected spectrum as shown in Figure 2.3.

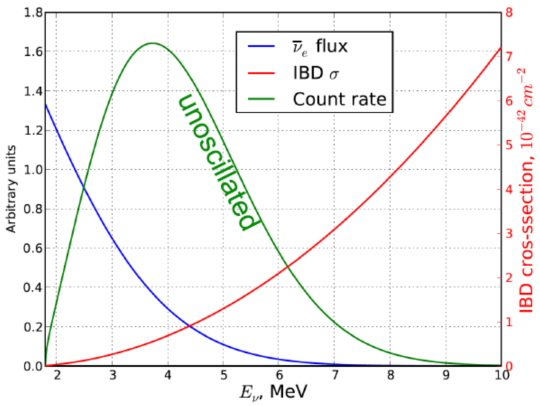

Figure 2.3: *The multiplication of the IBD cross section (red line) with the reactor neutrino flux (blue line) reasults in an expected detected spectrum (green line).*

The IBD detection principle is pictured in Figure 2.4. The positron deposits its kinetic energy in the LS within a few hundred of ps (a few ns at most if a positronium is formed [171, 172]) and then annihilates with an electron. Two 0.511 MeV gammas are created and deposit their energy by Compton diffusion or photoelectric effect within a similar timescale than the positron. This is called the *prompt* signal. As for the neutron, it will thermalise by doing multiple elastic scatterings on the LS protons before being captured by an hydrogen nucleus ($^1_1$H) – in $>$ 99% of the cases – or by a Carbon-12 nucleus ($^{12}_6$C) – in less than 1% of the cases. The neutron capture by an $^1_1$H will induce the emission of a single 2.2 MeV gamma while several gammas with a total energy of 4.95 MeV will be produced if it is captured by a $^{12}_6$C. These gammas produce a second signal that occurs on average ∼220 μs after the prompt signal, which roughly correspond to the neutron thermalisation time in the JUNO LS. For this reason, the neutron-induced signal is called *delayed*. The prompt and delayed signals are also spatially correlated, with an average distance of ∼14 cm.

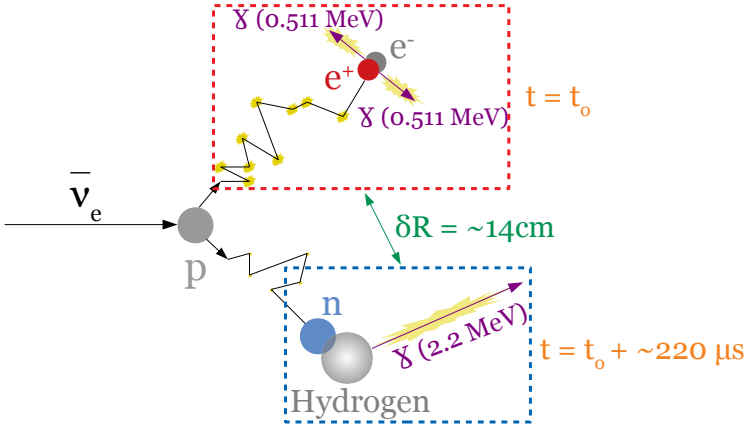

Figure 2.4: *Schematic of an Inverse Beta Decay. In this example, the neutron is captured by an Hydrogen, producing a 2.2 MeV gamma.*

The temporal and spatial coincidences between the prompt and the delayed signals as well as the fixed energy of the delayed signal represent powerful criteria to identify the IBD and discriminate the $\bar{\nu_e}$ from the background events. In addition, the incident energy of the $\bar{\nu_e}$ can be retrieved from the prompt signal since the positron carries most of the $\bar{\nu_e}$ energy (the neutron carries only ∼10 keV in case of an IBD from reactor $\bar{\nu_e}$). Indeed, if the mass of the neutrino is neglected compared to that of the target proton and assuming that the latter is at rest during the reaction, the $\bar{\nu_e}$ energy can be written as:

$$E_{\overline{\nu_e}} = E_{e^+} + (m_n - m_p) = E_{e^+} + 1.293 \ [MeV] \tag{2.10}$$

where E_{e^+} is the positron energy (mass + kinetic) and m_n and m_p are the neutron and proton rest mass, respectively. This equation implies that the minimum energy required for a $\bar{\nu_e}$ to do an IBD is 1.804 MeV. Furthermore, let's define the visible energy (E_{vis}) as the prompt signal energy where will sum up the positron kinetic energy and the energy of the two annihilation gammas:

$$E_{vis} \approx E_{e^+} + 0.511 \ [MeV] \tag{2.11}$$

Finally, by injecting Eq. 2.11 in Eq. 2.10, it comes:

$$E_{\bar{\nu_e}} \approx E_{vis} + 0.782 \ [MeV] \tag{2.12}$$

Thus, the reconstruction of the prompt signal energy of an IBD gives a direct access to the $\bar{\nu_e}$ energy.

2.1.1.4 Backgrounds

As seen in the previous section, the detection of the IBD is based on the spatial and temporal coincidence between the prompt and the delayed signals. This signature allows to significantly reduce the backgrounds, i.e. events that can mimic the IBD. In this section, the sources and characteristics of two-event coincidences that can mimic an IBD in the JUNO detector are listed. They have to be comprehensively studied in order to reject them effectively when selecting the IBD candidate events.

Accidental Background.

It can happen that two random energy deposition (from the natural radioactivity, cosmogenic isotopes, spallation neutrons etc.) occur in spatial and temporal coincidence. This type of coincidence is called accidental background. The majority of random energy deposition will come from the natural radioactivity of the JUNO detector components [173], or from its surrounding environment. Given the setup of the detector (detailed in section 2.2), these events will mainly occur at the detector edges. An efficient way to reject them is to apply a Fiducial Volume (FV) cut throughout the IBD candidate selection. The FV cut foreseen to be used in the NMO analysis is currently R = 17.2 m [76] (corresponding to a volume of ∼21,314 m^3) while the radius of the sphere is 17.7 m (corresponding to a volume of 23,227 m^3). See Section 2.2 for more details on the detector geometry.

Muon-induced background.

The detector will be constantly crossed by cosmic muons. The rate, integrated over the full detector volume, will be ∼3 Hz and the average energy of the muons will be ∼207 GeV. They will represent the most important sources of background for the NMO analysis. The different muon-induced background are listed below:

- A muon which enters the detector can interact with the Carbon nucleus of the LS molecules. Long life time (∼10-100 ms) isotopes (also called "cosmogenics") like Lithium 9 ($^9_3$Li) and Helium 8 ($^8_2$He) can be created. These two isotopes undergo β-n decay, as described in Eq.2.13. The electron and neutron will mimic the prompt and delayed signals.

$$
\begin{aligned}
&^8_2He \xrightarrow{84\%} \bar{\nu_e} + e^- + ^8_3Li \\
&^8_2He \xrightarrow{16\%} \bar{\nu_e} + e^- + n + ^7_3Li \\
&^9_3Li \xrightarrow{49.2\%} \bar{\nu_e} + e^- + ^9_4Be \\
&^9_3Li \xrightarrow{50.8\%} \bar{\nu_e} + e^- + n + ^8_4Be
\end{aligned}
\tag{2.13}
$$

  These backgrounds can be rejected by vetoing (i.e. ignoring the data during a given period of time) the part of the detector around the muon track for a period of time equal to the lifetime of the cosmogenics.

- Passing through the cavern rocks surrounding the detector, a muon can interact by an electromagnetic spallation process (violent shock between the muon and a nucleus where some fragments of the latter are ejected), producing fast neutrons (with a kinetic energy of $E_{kin} \simeq$ MeV). Some of these neutrons can enter the detector,

thermalise in the LS and eventually be captured. Here, the proton recoil mimics the prompt signal while the neutron capture mimics the delayed one. If the muon is tagged, this background can also be rejected by vetoing all the detector volume.

Even it is not a background as such, it is important to mention that muons can deposit a great amount of energy in the detector and flood the nearby PMTs. As a consequence, these PMTs won't be able to correctly detect events – including the IBDs – for a given time.

$^{13}_{6}C(\alpha,n)^{16}_{8}O$ background.

The Uranium-238 ($^{238}_{92}$U) and Thorium-232 ($^{232}_{90}$Th) radioactive isotopes present in the LS undergo alpha decays. The alphas can interact with Carbon-13 ($^{13}_{6}$C) nuclei that compounds the LS generating a neutron and an Oxygen-16 ($^{16}_{8}$O). The neutron can scatter on the LS protons (prompt signal mimicking) before thermalising and being captured (delayed signal mimicking). If the $^{16}_{8}$O nucleus is produced in an excited state, it emits a gamma which also contributes to the prompt signal.

Geo-Neutrinos

The β-decays of various $_{92}$U and $_{90}$Th isotopes in the Earth crust will produce a non-negligible flux of $\bar{\nu_e}$ with an energy ranging from 0 to 3 MeV (∼1.5 event per day expected), overlapping with the reactor $\bar{\nu_e}$ (∼83 events per day expected). Just like that from the reactors, these $\bar{\nu_e}$ will interact through IBD in the detector. Since JUNO will be able to measure the geo-neutrino flux, the corresponding spectrum will be removed from the reactor spectrum.

2.1.1.5 IBD candidate selection

The IBD from actual reactor $\bar{\nu_e}$ will have to be selected among the backgrounds listed above. As mentioned below, part of them will be identified thanks to the sub-detectors of JUNO, that are described in section 2.2. Based on the estimation of each background components, a set of selection criteria has been determined [76]:

- Fiducial Volume: R < 17.2 [m]
- Prompt signal energy cut: $0.7 < E_{vis} < 12$ [MeV]
- Delayed signal energy cut: $1.9 < E_{vis} < 2.5$ [MeV]
- Time interval between prompt and delayed: $\Delta T < 1.0$ [ms]
- Distance between prompt and delayed: $R_{p-d} < 1.5$ [m]
- Muon veto criteria:
  - Muons tagged by the Water Cherenkov Detector (WCD) and/or the Top Tracker (TT) (see section 2.2): All the LS volume is vetoed for 1.5 ms
  - Muons that are well-tracked in the Central Detector (CD) (see section 2.2): A cylinder with a radius $R_{d2\mu} < 3$ m (the axis being the muon track) is vetoed during 1.2 s. Note that the veto time is significantly larger than in the previous case to reject the cosmogenics (see muon-induced backgrounds in the previous section).
  - Muons that are tagged by the CD but that cannot be tracked, all the LS volume is vetoed during 1.2 s.

The IBD detection efficiency as well as the efficiency after applying the different selection cuts is shown in Table 2.1. It is based on simulation data. The expected rate of true IBD is 60 IBD.day^{-1}, with $\sim 7\%$ background contamination [76] that is dominated by the ^{9}Li/^{8}He component.

Sel. Crit.	IBD efficiency	IBD	Geo-ν	Accidental	^{9}Li/^{8}He	Fast n	(α,n)
None	100%	83	1.5	$\sim 10^4$	84	-	-
FV	91.8%	76	1.4	410	77	**0.1**	**0.05**
Energy	97.8%	73	1.3		71		
Time	99.1%						
Vertex	98.7%			1.1			
Muon veto	83%	**60**	**1.1**	**0.9**	**1.6**		
Combined	73%	60	3.75				

Table 2.1: *List of the IBD candidate selection criteria together with their efficiencies. The signal and background rates (day^{-1}) after applying each cut are also given. Those indicated in bold are the final ones after applying all the cuts. From [174].*

2.1.2 Neutrino Oscillation Parameter Measurements

JUNO will be able to measure four of the neutrino oscillation parameters. Indeed, with a baseline of 53 km, it will see the strong suppression and slow oscillations in the $\bar{\nu_e}$ spectrum which are driven by θ_{12} and Δm^2_{21} (Figure 2.2), respectively. Furthermore, as explained in the previous section, the excellent energy resolution of the detector allows to distinguish the small and fast oscillations guided by θ_{13} and Δm^2_{32} and thus to measure them.

Among these four parameters, the values of θ_{12}, Δm^2_{21} and $|\Delta m^2_{32}|$ will be measured at the per-mile level strongly constraining the PMNS matrix elements [38, 39]. The precision on θ_{13} won't be competitive with respect to the measurements from previous experiments [44, 46, 48]. The expected precisions are listed in Table 2.2.

Osc. Par.	PDG2020	JUNO 100 days	JUNO 6 years	JUNO 20 years
Δm^2_{21}	2.4%	1.0%	0.3%	0.2%
$\sin^2\theta_{12}$	4.2%	1.9%	0.5%	0.3%
Δm^2_{31}	1.3%	0.8%	0.2%	0.1%
$\sin^2\theta_{13}$	3.2%	47.9%	12.1%	7.3%

Table 2.2: *A summary of the expected precision levels for the oscillation parameters. The current best precisions taken from the Particle Data Group (PDG) 2020 review [5] are also indicated for comparison. From Ref. [175]*

It has to be pointed out that JUNO will be able to perform two semi-independent measurement of θ_{12} and Δm^2_{21}, with equivalent precisions. Indeed, the Central Detector of JUNO will be instrumented with two different Photomultiplier Tube (PMT) systems (see section 2.2). The detection, reconstruction and selection of the events occuring in JUNO can be done with each of these two systems, leading to two different measurements. These are called semi-independent measurements since the results obtained by each of the systems will share common systematics, related to the light production by the LS, the backgrounds etc.

2.1.3 Core-Collapse Supernova Burst Neutrinos

This section occupies a particular place in this manuscript since the different studies carried out during this thesis focused on Core-Collapse Supernova (CCSN) burst neutrinos. In addition, the subject of CCSN burst neutrinos and the implications of their detection has been extensively introduced in Chapter 1. This section is thus dedicated to the description of CCSN burst neutrinos detection *with JUNO*. The issues and figures that it contains are the one officially communicated by the collaboration and do not include the ones produced during this thesis.

The detection of a two dozen neutrinos by several neutrino experiments (Kamiokande [98], IMB [99], Baksan [100] and possibly LSD [176]) in 1987 confirmed that the neutrinos play a crucial role in all stages of the massive stars ($M > 8M_{\odot}$) collapse and explosion. It has corroborated many points of the delayed neutrino-driven explosion mechanism [125, 177], but way more statistics are required to fully constrain the models. JUNO is one of the future large neutrino detectors (with Deep Underground Neutrino Experiment (DUNE) [178], Cubic Kilometre Neutrino Telescope (KM3NeT) [151], Hyper-Kamiokande (HK) [136]) currently under development that will be able to detect several thousands of neutrinos from the next galactic CCSN, offering a unique opportunity to scrutinise the CCSN process in more details.

As shown in Fig.2.5, the most probable position of the next CCSN is close to the Galactic Center (∼10 kpc) since it is a more active star forming region. Given the time resolution of the detector, at this distance, $< 1\%$ of the events will pile-up (i.e. several events in the same trigger window). However, it is possible that a closer CCSN explodes[1], which would represent a real challenge for the readout electronics and DAQ with several hundreds of thousands of events to process and way more event pile-up (e.g. ∼10-15% for a 3 kpc away CCSN).

A CCSN is expected to produce a ∼10 seconds long neutrino burst in JUNO, with ∼60% of the events in the very first second. In comparison to the rates of events of the other neutrino sources and their corresponding energy range, the CCSN neutrinos detection can be considered as background free in a first approximation. The neutrinos will interact *via* six different channels in JUNO, they are listed in Table 2.3. The number of events is computed considering a visible energy threshold of 0.7 MeV (that is the one foreseen in JUNO for the reactor neutrino analysis).

Neutrinos interaction channels in JUNO

Interaction Chan.	Type	Num. evts (@10kpc)
$\overline{\nu}_e + p \rightarrow e^+ + n$	CC	∼5000
$\nu + p \rightarrow \nu + p$	NC	∼2000
$\nu + e^- \rightarrow \nu + e^-$	NC	∼300
$\nu + {}^{12}C \rightarrow \nu + {}^{12}C^*$	NC	∼300
$\nu_e + {}^{12}C \rightarrow e^- + {}^{12}N$	CC	∼100
$\overline{\nu}_e + {}^{12}C \rightarrow e^+ + {}^{12}B$	CC	∼100

Table 2.3: *Number of neutrino events in JUNO with their corresponding interaction channels for a typical CCSN at a distance of 10 kpc, where ν collectively stands for neutrinos and anti-neutrinos of all flavors.*

[1] As an example, Betelgeuse is located at ∼0.2 kpc from the Earth. Its explosion would produce several millions of neutrino interactions in JUNO.

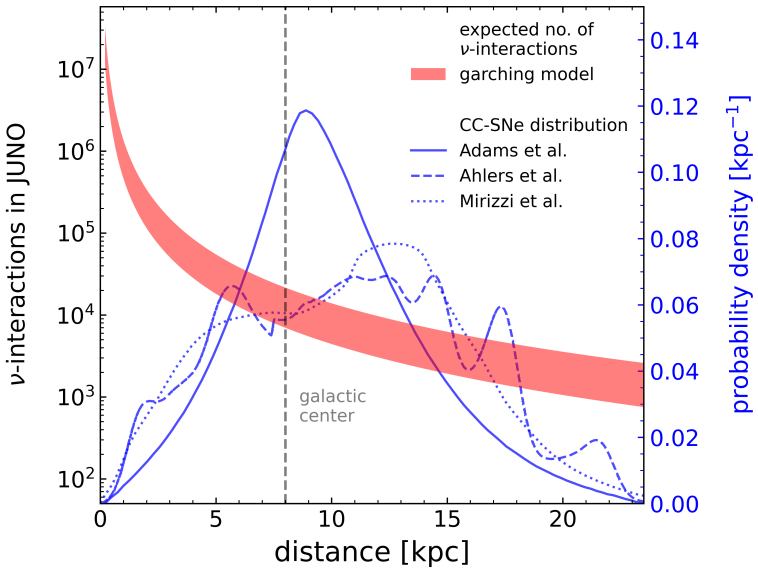

Figure 2.5: *The expected number of neutrino interactions events in JUNO as a function of the distance to the CCSN (red curve). The galactic CCSN probability as a function of the distance is also shown (blue curves).*

JUNO will benefit from high statistics in two interaction channels: the Inverse Beta Decay (IBD) and the Neutrino-Proton Elastic Scattering (νpES). The statistics of Neutrino-Electron Elastic Scattering (νeES) is also relatively significant. Various neutrino-Carbon *via* Neutral Current (NC) and Charged Current (CC) interactions are also expected but with only few statistics. A description of the channels is given below:

1. The IBD will be the dominant channel. It will represent a unique way to precisely determine the $\bar{\nu_e}$ energy spectra. The detection will be based on the powerful discriminating power provided by the temporal and spatial coincidence between two signals (see section 2.1.1.3). In addition, this channel gives a direct and model-independent access to the incident $\bar{\nu_e}$ energy.

2. The νpES channel will allow to partially extract the energy spectra of the other neutrino (and antineutrino) flavors generically denoted as ν_x (i.e. ν_μ, ν_τ, $\bar{\nu_\mu}$ and $\bar{\nu_\tau}$) [147, 179, 180]. Indeed, even though the total cross section is four time smaller than that of the IBD, all ν_x will contribute to this channel, hence the high statistics expected. According to the kinematics, the proton recoil energy T_p is such as $T_p \leq 2E_\nu/m_p$, where E_ν is the incident energy and m_p is the proton mass. The deposited energy is highly quenched in a LS detector. As a consequence, the visible energy will be very low (< 1 MeV for most of the events) in comparison to the incident neutrino energy. The cross section of this process has been calculated in Refs. [147, 181].

3. The νeES channel will be predominantly sensitive to the ν_e due to the larger cross-section [146]. In principle, the electron carries the directional information of the incident neutrino and this channel can be used to locate the CCSN. In practice, it is very challenging for a LS detector to retrieve the directionality from this channel. The Water Cherenkov detectors like Super-Kamiokande (SK) or Hyper-Kamiokande (HK) will be more sensitive to this channel.

4. The $\nu_e - {}^{12}C$ and $\bar{\nu_e} - {}^{12}C$ interaction channels provide a way to detect $\bar{\nu_e}$ and ν_e separately [182]. The energy threshold are 17.34 MeV and 14.39 MeV for the ν_e and

$\bar{\nu_e}$, respectively. The ^{12}B and ^{12}N nuclei created are β emitters and will decay with a 20.2 ms and 11.0 ms half-life, repectively. The cross sections of these processes have been calculated in Refs. [183–185]. As for the IBD, the spatial and temporal coincidence can be used to discriminate these events.

5. The neutrino-Carbon NC will produce a 15.11 MeV signal from the ^{12}C* de-excitation gamma. This channel is more sensitive to the ν_x, due to the cross section [183–185]. Thus, even though this channel does not give access to the neutrino energy, it can be used to constrain the flavor content of the CCSN neutrino flux.

The visible energy spectra for the different channels are shown in Fig.5.1. It ranges from 0.2 to 100 MeV with an average energy of ∼20 MeV for the IBD, <1 MeV for the νpES and ∼10 MeV for the νeES. The νpES and IBD channels dominante the ranges 0-2 MeV and 2-100 MeV, respectively, which is a great advantage when it comes to select the events using cuts on their visible energy.

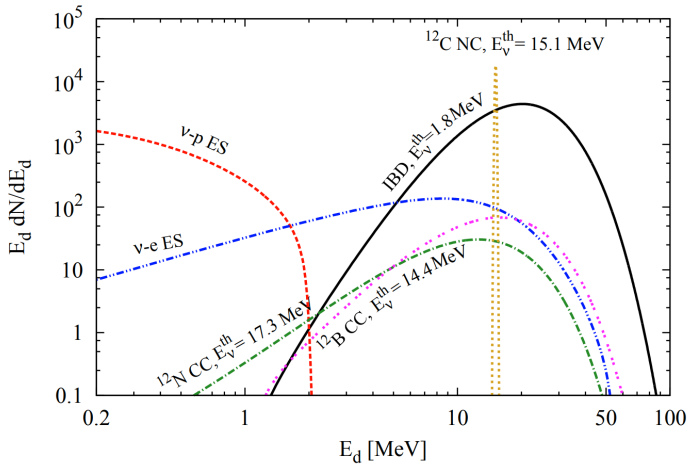

Figure 2.6: *The energy spectra of the different interaction channels in the JUNO detector for a typical CCSN at 10 kpc. Taken from [76].*

JUNO will also be sensitive to the pre-SN neutrinos (∼1 MeV) [109]. They are emitted up to several days before the CCSN explosion. The detection of them would trigger alerts to point the telescopes in the right direction to optimise the observations of the electromagnetic counterpart of the CCSN signal. Pre-SN neutrinos also represent an unique opportunity to probe the late-stage stellar evolution [108, 186]. With a sufficiently low energy detection threshold, Pre-SN neutrinos are detectable *via* the IBD and νeES channels. JUNO is expected to detect pre-SN neutrinos with a significance $> 3\sigma$ for distances < 1 kpc [109]. The pre-supernova neutrinos were not studied during this PhD thesis.

2.1.4 Diffuse Supernovae Neutrino Background

If the rate of CCSN is of the order of ∼1-2 per century in the Milky Way, the integrated rate in the observable universe is estimated to be considerably higher, at the level of ∼1 per second in average. It can also be expressed in units of Mpc^{-3}.year^{-1} and is estimated to be: $(1.25\pm0.25)\times10^{-4}$ Mpc^{-3}.year^{-1} [187]. Such a rate causes a constant background flux of neutrinos throughout the universe which is also called the Diffuse Supernovae Neutrino Background (DSNB). The flux of neutrinos from the DSNB is estimated to be ∼10 cm^{-2}s^{-1}. The measurement of the DSNB has strong astrophysical implications since

it bears information on the history of stellar birth and death, including their formation rate/death, the rate of failed CCSN, the fraction of black hole formation in the CCSN etc. [187]

In the last two decades, the SK experiment established the most stringent limits on the DSNB $\bar{\nu}_e$ flux [188–190]. The potentialities of this detector, if loaded with Gadolinium (improvement of the DSNB signal over background ratio), as well as those of the future HK detector are discussed in Ref. [191].

As a LS detector with an unprecedent detection volume, JUNO will probe the $\bar{\nu}_e$ component of the DSNB flux, with ∼2-4 IBD events expected per year – depending on the model – above 10 MeV. JUNO will also benefit from its high light yield that will allow to perform pulse-shape discrimination for background suppression purposes. The expected sensitivity of JUNO is shown in Figure 2.7 [192]. Works studying the potential combination of JUNO and SK are also ongoing [193]

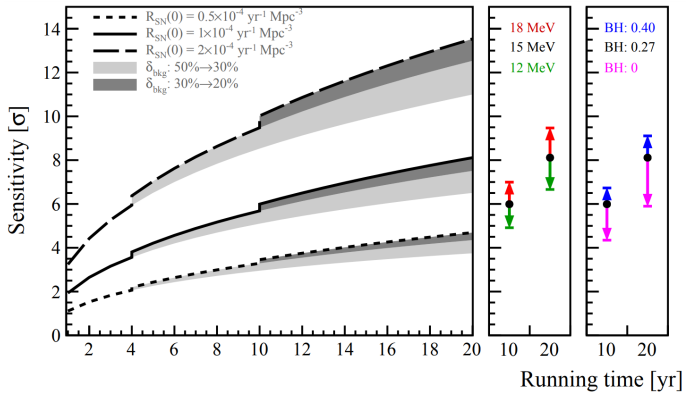

Figure 2.7: *The sensitivity of JUNO to the DSNB as a fuction of the time exposure. The DSNB signal models are represented with the black lines (full, short-dashed and long dashed) and black points (middle and right panels). The dark grey and grey regions represent different possible scenarii of systematic uncertainty from the background. The model variations for different neutrino spectra average energies (middle) and black hole fraction (right) are illustrated for 10 (middle) and 20 (right) years of exposure. From [192].*

2.1.5 Solar Neutrinos

The solar neutrinos are produced through thermonuclear reactions occuring into the Sun. These reactions can be separated into two different chains, both of which can be summarised as follows: $4p \longrightarrow {}^4_2\mathrm{He} + 2\mathrm{e}^+ + 2\nu_e$. These reactions are called the *pp-chain* and the *Carbon-Nitrogen-Oxygen (CNO)*-cycle [106] and are responsible for the production of ∼99% and ∼1% of the solar neutrinos, respectively.

The neutrinos that are emitted during these fusion processes represent valuable probes to investigate the deep interior of the Sun. More precisely, detect these neutrinos can help us improving our knowledge of the solar physics, notably about the mechanism ruling the Sun dynamics, the solar metallicity problem etc. The solar neutrinos have also been historically detected to study neutrino oscillation. Recently, the Borexino experiment reported a comprehensive measurement of the pp-chain [194] and the first experimental evidence of neutrinos produced in the CNO-cycle [195], representing a major step forward in the

study of solar neutrinos.

Thanks to its huge detection volume, excellent energy resolution and low energy threshold, JUNO is a promising detector for the detection of solar neutrinos. The potential new measurements of various components of the flux, especially from the ^{8}B and ^{7}Be β-decays [76, 196] (part of the pp-chain), could improve our understanding of the solar metallicity problem and matter effects in the neutrino oscillations [174]. However, the measurements of neutrinos from these two isotopes require very low levels of radio-impurities (10^{-15} g/g and 10^{-17} g/g, respectively) as well as an accurate determination of the cosmogenic backgrounds. Major efforts are currently being made in material selection and installation procedure to limit the nominal background level.

2.1.6 Atmospheric Neutrinos

Atmospheric neutrinos are produced through the decays of π and K particles themselves produced in the showers initiated when the cosmic rays interact with the Earth's atmosphere [197]. Atmospheric neutrinos occupy a special place in the neutrino oscillation history. Indeed, in 1998, the SK experiment reported a zenith angle dependent deficit of muon neutrinos with respect to the atmospheric neutrino flux models predictions [35]. It was the first evidence of neutrino oscillation. Since then, many different experiments like HK, ICAL [198], PINGU [199] and KM3NeT use or plan to detect atmospheric neutrinos to study neutrino oscillation (NMO, octant of θ_{23} and δ_{CP} value).

The detection of atmospheric neutrinos by JUNO is expected to enhance its sensitivity to the NMO by ∼0.9 σ in 10 years of data taking [174]. A combined sensitivity (reactor+atmospheric) will be estimated. Preliminary studies showed a great reconstruction potential in the low energy region (100 MeV - 10 GeV) [200]. The Figure 2.8 shows the expected energy spectrum for the ν_e and ν_μ (simulated and reconstructed separately) after 5 years of data taking. Strong efforts are ongoing within the collaboration in order to enhance these results. In addition, algorithms are currently being developed to discriminate between ν_e and ν_μ.

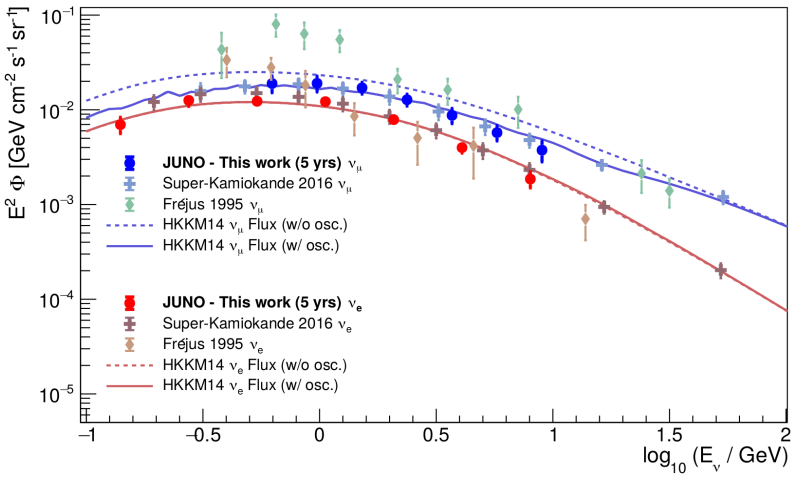

Figure 2.8: *Reconstructed atmospheric neutrinos energy spectra for ν_μ (blue) and ν_e (red). The results are compared to the HKKM14 model predictions [201] and the SK [202] and Fréjus [203] experiment results.*

2.1.7 Geo-Neutrinos

The so-called *geo-neutrinos* are $\bar{\nu_e}$ produced by the decay of Thorium, Uranium and Potassium isotopes present in the Earth's crust. These geo-neutrinos are excellent probes for determining the fraction of the Earth's heat flux that is attributable to radioactivity. This has strong implications on the Earth composition and the nature of the mantle convection. In the past, several experiments using LS as detection medium, like Borexino [204] and KamLand [205], detected geo-neutrinos and constrained the Earth heat flux models prediction.

Thanks to its large detection volume, JUNO will provide high statistics measurements of geo-neutrinos with approximately ∼400 geo-neutrinos per year. It means that in six months, JUNO will reach the largest sample of geo-neutrinos ever detected.

2.1.8 Nucleon Decays

The nucleon decay is not predicted by the particle physics Standard Model (SM) because it violates the baryon number conservation. However, some Grand Unified Theories (GTUs) (see Ref. [206] for example) – which unify the strong, weak and electromagnetic interactions into a single fundamental force – predict such processes *via* many different channels [207, 208]. Detecting a signature of nucleon decay would be a proof for Beyond Standard Model (BSM) physics.

The first experiment which probed the nucleon decay was the one lead by F. Reines and C.L. Cowan in 1954 [209]. The detector consisted in 300 l of liquid scintillator that aimed to detect neutrino interactions. At that time, they constrained the proton lifetime: $\tau > 10^{22}$ years [209]. Today, the best limit has been established by the Super-Kamiokande experiment and is of the order of $\tau > 10^{33}$-10^{34} years, depending on the channel [210].

JUNO is expected to be competitive on the nucleon decay search, especially through the following proton decay channel: $p \to \bar{\nu} + K^+$. In this detection channel, the K^+ produces a first signal and then decays ($\tau_K = 12$ ns) producing a μ^+ which itself decays producing a e^+ ($\tau_\mu = 2.2\mu$s). The expected signal is then a triple temporal coincidence with a specific shape, that is expected to be seen by JUNO, especially with the SPMT system (see section 2.2.2.3). the preliminary sensitivity of JUNO to this channel of the proton decay is $8.34{\cdot}10^{33}$ years (90% CL) [76]. In addition, JUNO should be able to give more stringent limits on other nucleon decay modes such as $n \to 3\nu$ or $p \to \mu^+ + \mu^+ + \mu^-$.

2.1.9 Other Physics

As described above, JUNO will be able to cover a broad range of topics in particle physics, nuclear physics, astrophysics and cosmology. Only those where the contribution will be significant were reviewed in this manuscript. Other subjects such as the search for sterile neutrinos, dark matter etc. can be studied with JUNO. They are discussed in Refs. [174] [76].

2.2 The JUNO detector

This part of the chapter aims to present the JUNO detector. The different elements as well as their purposes and main characteristics are listed. The foreseen calibration strategy is also briefly described. At first, a quick overview of the three sub-detectors that make-up JUNO is given. Then, the different sections enter more or less in detail in the different components of these sub-detectors, depending on whether they are relevant for this PhD thesis or not.

2.2.1 Detector Overview

The JUNO detector was designed with the aim of solving the NMO, requiring specific conditions, namely an energy resolution of 3% at 1 MeV, an energy accuracy $< 1\%$, the detection of a large number of $\bar{\nu}_e$ and a good control of the backgrounds. Thus, the JUNO detector is buried ∼700 m underground and includes:

- A 20 kton Liquid Scintillator (LS) detector, also called the **Central Detector (CD)** (section 2.2.2)
- A 35 kton cherenkov detector in which the CD is immersed. It is called the **Water Cherenkov Detector (WCD)** (section 2.2.3)
- A plastic scintillator detector, placed on top of the CD and WCD, also called the **Top Tracker (TT)**. These scintillation strips were originally used in the OPERA experiment as the "Target Tracker" [211] (section 2.2.3)

A schematic view of JUNO is shown in Figure 2.9.

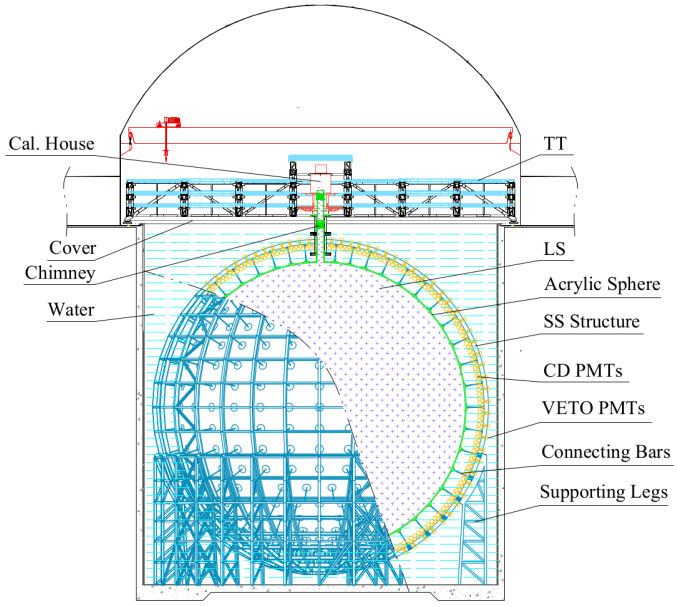

Figure 2.9: *Schematic view of the JUNO detector.*

The CD is the main part of the JUNO detector. The 20 ktons of liquid scintillator are the neutrino target and are contained in a 35.4 m acrylic sphere. The CD is instrumented with PMTs used to collect the light produced by the LS. In total, 17,612 20" PMTs (**Large Photomultiplier Tube (LPMT)**) [212] will be installed in the JUNO CD. They will allow to achieve a 75.2% photo-coverage in order to collect a great amount of light and

thus keep the stochastic term of the energy resolution $< 3\%$. In addition, 25,600 3" PMTs (**Small Photomultiplier Tube (SPMT)**) [213] will be placed in alternation with the LPMTs. The corresponding photo-coverage of the SPMT system is 2.7%. The SPMTs will work in photo-counting regime. It means that even for the most energetic reactor $\bar{\nu_e}$ ($\sim$10 MeV), a large majority of the SPMTs fired will see only one scintillation photon. Thus, they will ensure a better control of the energy resolution systematics term by mitigating the potential non-linearity in the LPMTs, thanks to the Dual Calorimetry Calibration (DCC) (see section 2.2.4). Furthemore, quasi-independent physics analyses will be performed using the two PMT systems independently. The SPMT system alone will be able to perform solar parameters measurements, core-collapse supernova neutrinos detection and proton decay search. It will also enhance the muon-tracking capability thanks to their low photo-coverage (no saturation) and good time resolution.

The WCD is a cylindrical vessel with a diameter of 43.5 m and a height of 44.0 m. It will consist in $\sim$35 kton of ultra pure water (< 0.2 Bq/m^3) instrumented with 2,400 20" PMTs (veto PMTs). This sub-detector will be used to tag the incoming cosmic muons and will constitute a shield against the surrounding rock radioactivity. The TT is made of three planes of plastic scintillator (47.0 m x 20.0 m each), it aims to precisely reconstruct the cosmic muons tracks. Indeed, the latter represent a non-negligible source of correlated background for the NMO analysis.

2.2.2 The Central Detector

The CD of JUNO includes an acrylic container for the LS as well as a support structure and finally the PMTs with their readout electronics. The acrylic container is a sphere with a diameter of 35.4 m and a thickness of 12 cm. It will be supported by a spherical stainless steel structure consisting of 590 connecting bars. This structure sits on another support made of 30 pairs of stainless steel pillars, as shown in Figure 2.10.

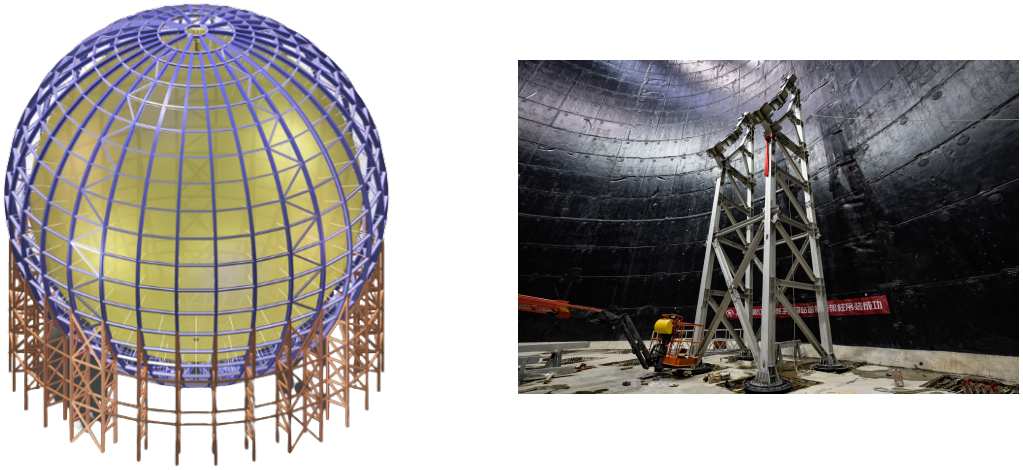

Figure 2.10: ***Left**: A scheme of the CD. The acrylic sphere is shown in yellow, its supporting stainless steel structure is shown in purple. The stainless steel legs are shown in orange (or brown, depending on your eyes).* ***Right**: A photograph of one of the first supporting structure legs installed in 2022.*

The JUNO PMTs together with their readout electronics will be installed on the supporting structure. The LPMTs and SPMTs will point toward the LS, while the veto

PMTs will view the water of the WCD. A very important point to mention here is that a 1.42 m water buffer will separate the PMTs and the acrylic sphere, in order to protect the LS from the PMTs radioactivity. The CD and the WCD will be optically separated. More info on these parts of the CD can be found in Ref. [76]. The following section focuses on the LS, the PMTs and the readout electronics.

2.2.2.1 Liquid Scintillator

The liquid scintillator technology has been used for several decades and by a large number of experiments to detect neutrinos. It is at the origin of several major steps forward in the neutrino physics (e.g. the first detection of the neutrinos [12, 13], the first measurement of solar neutrinos [17], precision measurements of θ_{12}, Δm^2_{21} [53] and θ_{13} [159–161]).

The production of light by a Liquid Scintillator is based on the excitation and ionisation of its molecules when a charged particle passes through. This light is then collected by the PMTs in order to retrieve the event characteristics, namely the energy, the vertex (or track) (see Chapter 4). The JUNO LS recipe is detailed below, together with the proportions and roles of each of its components:

1. The *Linear Alkyl Benzene (LAB)* is the solvent (i.e. a liquid substance in which other chemical compounds can be diluted without modifying their properties). The molecules of the LAB are excited by the passing charged particle. It represents ∼98% of the LS.
2. A fraction of the LAB molecules excitation energy is transferred (*via* a non-radiative process) to the second LS component, the *2,5-diphenyloxazole (PPO)* used as a first wavelength shifter. Indeed, the wavelengths of the photons emitted by the LAB have to be shifted at larger values in order to avoid re-absorptions during the propagation toward the PMTs. The PPO molecules de-excites by fluorescense and phosphorescence mechanisms and emit light with an average wavelength of ∼290 nm. The PPO concentration is 2.5 g/L, it represents ∼1.5% of the LS.
3. The last component is the *1,4-bis(2-methylstyryl)benzene (bis-MSB)*, it is used as a second wavelength shifter. In JUNO, the re-emitted photons have wavelengths with an average value of ∼430 nm. The bis-MSB concentration is 3 mg/L, it represents ∼0.5% of the LS.

A complete explanation of the LS scintillation processes is available in Ref. [214]. In order to meet the requirements in terms of energy resolution and background, various caracteristics of the JUNO LS have been studied and optimised. They're listed below:

1. The Light Yield (LY) has been optmised to be of the order of $\sim 10^4$ scintillation photons per MeV. By combining this with the LPMT system (see section 2.2.2.2), enough light is collected to achieve the required 3% energy resolution.
2. The transparency of the LS is also a key ingredient to maximise the number of photons that reach the PMT. For this reason, the attenuation length of the LS of JUNO has also been optimised. It is equal to 25.8 m [215, 216], which is comparable to the diameter of the JUNO detector.
3. The requirements in terms of Uranium/Thorium radiopurity is 10^{-15} g/g for the reactor neutrino programme, and 10^{-17} g/g for the solar neutrino programme. Before being mixed, the aformentioned three components will be filtered and purified in the JUNO surface area [217]. After the mixing, the freshly made LS will be sent to an

underground hall for two additional purification stages, namely the water extraction and stripping procedure [217]. At this point, it will be monitored by the Online Scintillator Internal Radioactivity Investigation System (OSIRIS) [218], a detector specifically design to evaluate the radiopurity levels and to see if they match the requirements before filling the CD. Finally, since the LS will constantly circulate in order to be purified during the data taking, OSIRIS will be continuously monitoring the radiopurity of the LS [76].

2.2.2.2 The Large Photomultiplier Tube system

The Large PMTs themselves

The use of PMTs makes it possible to convert the light produced by the LS into an electric current, detectable with conventional electronics. As shown in Figure 2.11, when a scintillation photon hits the photocathode of a PMT, it can be converted into a Photoelectron (PE) by photoelectric effect [219]. Then, this PE hits a dynode and multiple electrons (also called secondary electrons) are created and accelerated by the strong electric field (∼kV) generated into the PMT. This phenomenon repeats over several dynodes and an amplified electric signal is eventually created. It is then digitised by a readout electronics and the corresponding charge – in Coulomb [C] – and arrival time can be extracted. The *gain* of a PMT is then defined as the total charge that is obtained at the output of the PMT from the initial one. A detailed explanation on the PMT functioning is available in Ref. [220], for example.

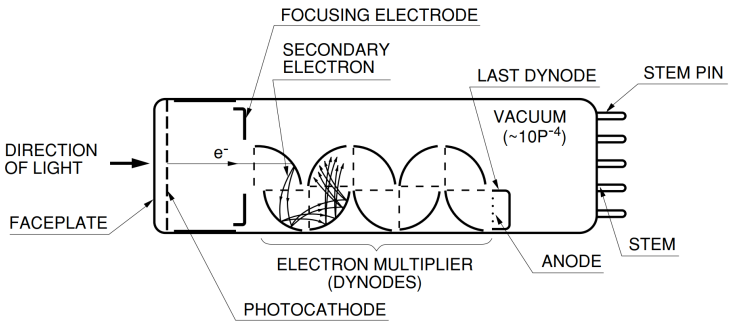

Figure 2.11: *A sketch showing the basic concept of a PMT. From [220].*

As for the LS, the LPMTs of JUNO were developed to meet the energy resolution requirement. The LPMT system includes ∼5,000 20" dynode-PMTs [221], produced by the the Hamamatsu© company and ∼15,000 20" Micro-Channel Plate (MCP) PMTs [222], produced by the NNVT© company (Figure 2.12). Among many different specification including the time resolution, charge resolution and Dark Count Rate (DCR), the most critical one was their Photo Detection Efficiency (PDE), on which the light collection strongly depends. The requested average value over all the PMTs was $\geq$ 27% and a minimum of 24% at the PMT level. The mass testing and characterisation of the produced PMTs confirmed that these requirements are satisfied [212]. Also, it has been showed that the PMTs Transit Time Spread (TTS) (i.e. the time resolution) are σ ∼2.6 ns and σ ∼8.4 ns for the dynode and MCP PMTs, respectively. Including the measured PDE in the simulations, ∼1345 PE/MeV are produced for an event at the detector center. With such statistics, the stochastic term of the energy resolution is maintained under 3% at 1 MeV.

Figure 2.12: *Pictures of the LPMTs of JUNO.* ***Left****: A prototype of MCP-PMT.* ***Right****: A Dynode-PMT.*

Electronics.

Before being exploitable, the output signal of the PMTs have to be amplified, digitised and packaged. This is the role of the readout electronics. As each component of the detector, it followed a dedicated R&D programme in order to fulfill the JUNO requirements [223]. As shown in Figure 2.13, the LPMT system electronics is divided into two parts: the *wet* electronics and the *dry* electronics. The "wet" electronics are stored in Under Water Boxes (UWB) that are immerged in the water, close to the PMTs. The "dry" electronics are located in dedicated rooms of the JUNO underground laboratory. Three LPMTs are connected to the same UWB that contains:

1. Three High Voltage (HV) units that provide the power supply to the LPMTs and split the power signal and the PMT output signal.
2. A Global Control Unit (GCU), the core of the readout electronics that is made of two main parts:
   - Six Analog-Digital Units (ADU) made of several sub-components. They receive the PMTs output signals, amplify and digitise them at a rate of 1 GSample/s with an effective resolution of 12 bits to produce *waveforms*.
   - A Field Programmable Gate Array (FPGA) that further processes the data from the ADU (local trigger generation, timestamp tagging, charge integration etc.). It also acts as a data buffer, and sends the data toward the DAQ when required by the trigger system (see later in this section).
3. An additional Dual Data Rate (DDR) memory in order to temporally store the data in case of a sudden increase of the input rate (in case of a nearby CCSN explosion for example).

The "dry" electronics notably aims to synchronise in time the signals from an UWB. It centralises the information from the 17,612 LPMTs of the CD. This is the role *Global Trigger* system. It aims to validate the sending of the data (waveforms) to the DAQ if the LPMT multiplicity condition (i.e. a number of PMT fired in a given time window) is fulfilled. If no request is sent by the Global Trigger system, the data are deleted and lost. Another scheme where all the readout electronics send the data to the DAQ, without requiering a request from the Global Trigger, is also foreseen. In this case, only the information on the time and charge (T,Q) are sent to the DAQ.

A Multi-Messenger (MM) trigger is also currently being developed within the JUNO collaboration. With an ultra-low detection threshold of $\mathcal{O}(10$ keV), it will enable JUNO

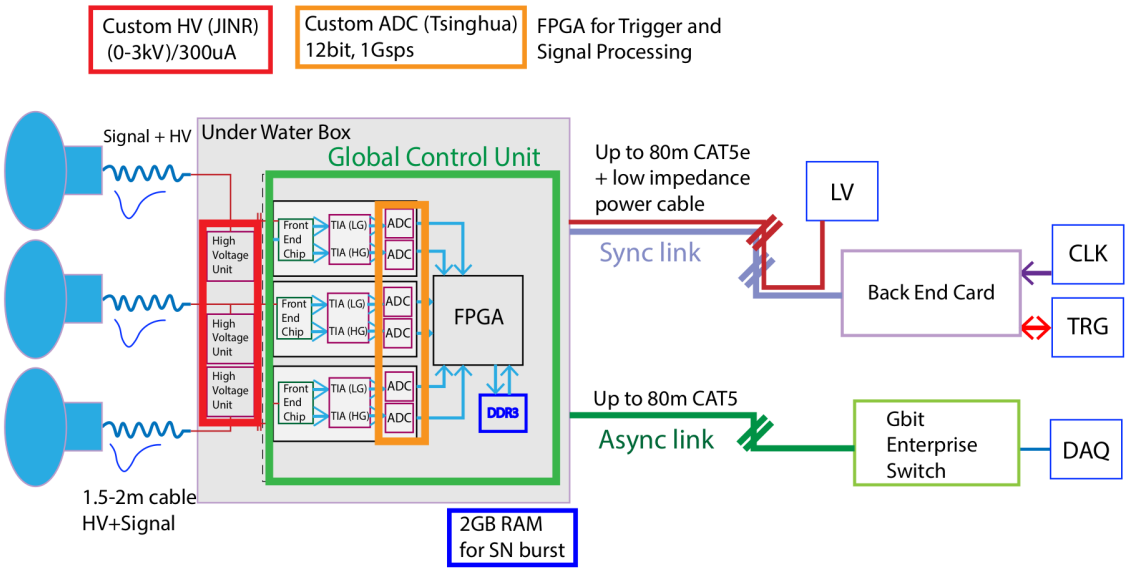

Figure 2.13: *A scheme presenting the LPMT system electronics, the grey squared symbolises the UWB containing the "wet" electronics, the rest represents the "dry" electronics. From [76].*

to act as a powerful monitor of the astrophysics neutrinos in the MeV energy range [76]. The MM trigger will also make JUNO a major player in the next-generation Supernova Early Warning System (SNEWS) [155].

2.2.2.3 The Small Photomultiplier Tube system

In this subsection, the main motivations for the the second PMT system of JUNO (the Small Photomultiplier Tube system) proposed in 2014 and fully approved in 2016 are described, including an overview of the PMTs and electronics of the system. More details about the readout electronics are given in Chapter 3, related to the work done during this PhD thesis.

As mentioned in the previous section, the PE yield (∼1345 PE/MeV) of JUNO allows to control the sotchastic term of the energy resolution (see equation 2.14) under the required 3% at 1 MeV. However, the energy resolution also comprises a non-stochastic term and can be expressed such as:

$$\frac{\sigma_E}{E} = \sqrt{\frac{\sigma^2_{stochastic}}{E} + \sigma^2_{non-stochastic}(E)} \tag{2.14}$$

where $\frac{\sigma_E}{E}$ is the energy resolution, $\sigma_{stochastic}$ is the stochastic term and $\sigma_{non-stochastic}$ the non-stochastic one. As shown in Figure 2.14, with the current PE yield, the non-stochastic term shall not exceed ∼1.5%. It is therefore necessary to be attentive to the slightest source of error that would increase the latter and then degrade JUNO's sensitivity to the NMO [224–226]. This represents a major challenge considering that the current best value of the non-stochastic term for a LS rector neutrino experiment is ∼2% [159, 227, 228]. Particularly, the large PE yield combined to the geometry of the detector implies that several photons will hit a single LPMT for events away from the center of the CD. In fact, the dynamic range of a single LPMT will be 1-100 PE in the reactor neutrino energy range. In case of multiple photon hits on a single LPMT, the corresponding waveform is more complex and non-linearity effects could be introduced during the waveform reconstruction.

The consequence could be an important Charge Non-Linearity (QNL) when performing the charge integration, which would eventually affect the estimation of the energy. Thanks to data tuned electronics simulation, the Daya Bay detectors QNL was narrowed down to ∼1% [229] but their dynamic range was ∼1-10 PE. It is then not guaranteed that the same performance can be achieved.

Furthermore, the potential QNL occurs at the readout electronics level. At the level of the particle energy deposition and light collection, other detector effects like the Liquid Scintillator Non-Linearity (LSNL) and detector Non-Uniformity (NU) can distort our energy estimate and degrade the energy resolution. At the readout electronics level, the QNL, LSNL and NU become hopelessly interwined, which has two consequences. First, it makes a fully independent calibration of the QNL impossible, which inevitably degrades the energy resolution. Second, the QNL can affect the modelling and calibration of the LSNL and NU. The LSNL and NU corrections applied to the estimated energy are then not fully independent from the QNL.

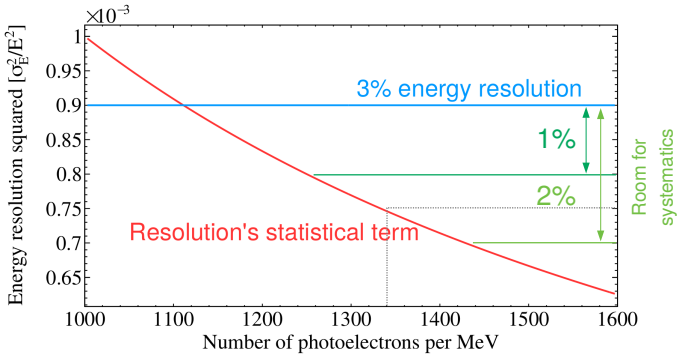

Figure 2.14: *A chematic view of the energy resolution contributions. The red curve shows the energy resolution stochastic term as a function of total number of photoelectrons (nPE). The green lines show the needed increase in the nPE to accomodate a systematic error of 1% or 2%.*

The use of the SPMT system will allow to independently measure the charge of the same events as the LPMTs, constituting the *Dual Calorimetry*. Due to their size (3"), ∼95% of the SPMTs will operate in photon-counting regime (1 PE per PMT fired), making the charge integration less complex and ensuring a robust linearity in the charge estimation. Thus, it will help to better control the systematic errors in the energy estimation through *an independent calibration* of the QNL of the LPMT system. The concept, development and performance of the DCC based on simulation data are presented in Ref. [230]. The SPMT system will also contribute to other physics analyses. It will perform a semi-independent measurement of the neutrino oscillation solar parameter (θ_{12}, Δm^2_{21}) with a very similar precision than the LPMT system [175], provide complementary measurement in the CCSN burst neutrinos detection. In addition, thanks to a much smaller pile-up and good time resolution, the SPMTs will better preserve the time structure of the high energy events (≥100 MeV), a valuable advantage for the proton decay search and muon tracking.

The Small PMTs themselves.

The SPMTs will be installed alternately with the LPMTs, as shown in Figure 2.15. The most important requirements for the SPMTs concerned their Single Photoelectron (SPE)

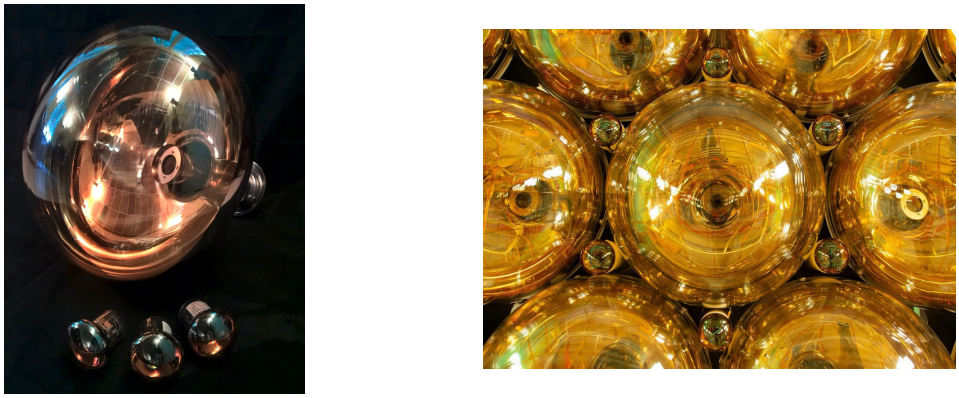

Figure 2.15: ***Left**: One LPMT and three SPMTs side-by-side.* ***Right**: Photograph showing a real size mock-up of the 3" PMTs placed in-between the 20" PMTs. These PMTs will look towards the center of the acrylic sphere.*

resolution, the Quantum Efficiency (QE), the Transit Time Spread (TTS) (i.e. the time resolution of the PMT) and the Dark Count Rate (DCR). The production of the 26,000 SPMTs of JUNO started in 2019 and finished in 2021. All the PMTs have been produced and tested by the HZC-Photonics© company. All along the production, 15 performance parameters of all SPMTs were monitored, including the aforementioned ones. As an example, the measured DCR of the SPMTs is ∼500Hz at 0.25 p.e (on average, over the full production sample) and the TTS is ∼1.6 ns (σ). The JUNO collaboration has performed complementary tests on random samples of the freshly produced PMTs. The list of the parameters, the requirements and the results of the tests operated by the HZC-Photonics© company and the JUNO collaboration are shown in Figure 5.22. More details on the different tests are fully reviewed in Ref. [213]. The deliverables fulfill the JUNO technical requirements and quality control level. All the SPMTs will be tested again before the commissioning of the detector, after cabling and potting, with a dedicated test-bench that includes the SPMT system electronics and that will be presented in Chapter 3 in connection with my PhD activities.

Electronics.

The SPMTs installed in the CD will have to operate under water for 20 years. During the installation, they will be grouped by 128. Each group will be connected to an UWB, a 40 cm in height and 30 cm in diameter passivated stainless steel box. As shown in Figure 2.16, it comprises two HV splitter boards (64 channels each, the same than for the LPMT system), an ASIC Battery Card (ABC) board and a GCU. The ABC board contains eight CATIROC [231] chips which will readout and digitise the charge and time of the 128 SPMTs signals (16 channels per CATIROC). The chip will be controlled by a Kintex-7 FPGA. The SPMTs will operate at a gain of $\sim 3{\cdot}10^6$. At such a gain, the CATIROC measures charges over a large dynamic range: 1/3 PE to several hundreds of PEs. It also provides a timing measurement with an accuracy of 200 ps (RMS) per channel. More details on CATIROC are given in Chapter 3. The ABC board will also contain a 1GB DDR memory to temporally store the data in case of a sudden increase of the input rate (e.g. nearby CCSN explosion). Finally, the GCU will handle the powering and controlling of the boards, transfer the data to the DAQ *via* Ethernet cables etc. In total, 200 UWB, 400 splitter boards, 200 ABCs and 200 GCUs will be produced for the SPMT system. All boards will be tested before shipping to the JUNO experimental site.

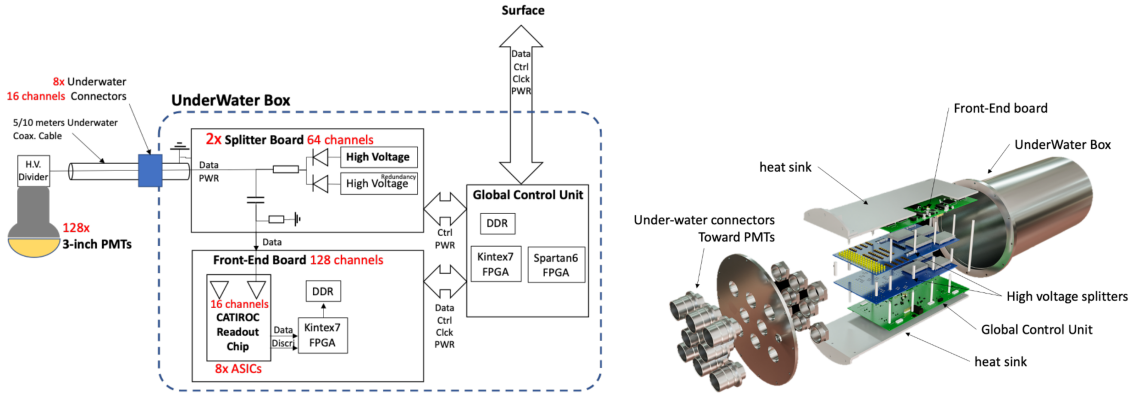

Figure 2.16: ***Left**: Overview of the SPMT system. **Right**: 3D modelisation of the main components of an UWB. Each UWB contains two HV splitter boards, an ABC and a GCU board. The two boards shown in green are connected to heat-sinks in order to dissipate the heat through the lid of the UWB. From [76]*

2.2.3 The Veto Detectors

The JUNO detector will be bathed in a constant background noise coming from the radioactivity of the detector environment, from its components [173] or form the cosmic muons. These background events can distort the results of the different physics analysis if they are not properly rejected. There exist many ways to reject them before or during the physics analyses. The CD being the neutrino target, it must be protected as much as possible from the radioactivity and cosmic muons. This section describes the two sub-detectors that aim to detect and identify them or simply to provide a passive shielding.

2.2.3.1 The Water Cherenkov Detector

The Water Cherenkov Detector (WCD) will consist in a 43.5 m in diameter and 44 m in height cylinder (Figure 2.17) filled with 35 ktons of ultrapure water. Such a large amount of water will provide a passive shielding against the gammas from the surrounding rocks natural radioactivity and thus will significantly reduce the backgrounds in the CD. The water itself contains radioactive isotopes, especially Radon 222 (^{222}Rn). A circulation and purification system will allow to keep the concentration in the water at the level of 0.2 Bq/m^3, as required for the reactor neutrino programme. However, studies showed that it can be narrowed-down to 50 mBq/m^3 [232, 233].

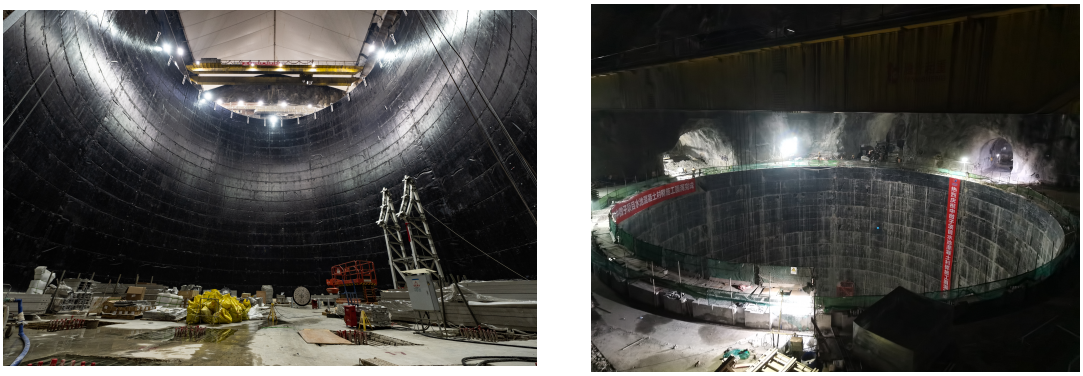

Figure 2.17: ***Left**: Photograph of the cylinder of the WCD from the inside (2022). **Right**: Photograph of the cylinder of the WCD from the top (2020).*

The WCD will also be used as a muon veto, the most important source of background for the NMO analysis (section 2.1.1.4). When passing in the water, the muons will produce light by Cherenkov effect [234]. This light will be collected by 2,400 MCP PMTs installed on the outer surface of the CD shell structure. In order to maximise the light collection, Tyvek reflective foils will cover the cylinder walls and CD support structure. The muon tagging is based on a PMT multiplicity condition. The PMTs are grouped into ten zones: Five in the top and five in the bottom hemisphere of the shell structure on which they are fixed. A local trigger is used to tag the passing muons. There are two different conditions – that can be fulfilled separately – for vetoing the detector:

1. The number of PMTs fired in one zone is above the threshold (∼19 PMTs)
2. The number of PMTs fired of two adjacent zones is simultaneously above a lower threshold (∼13 PMTs).

With such strategy, the muon detection efficiency reaches 99.5%. Finally, all the PMTs of JUNO may be affected by the Earth geomagnetic field, which would degrade their detection efficiency. In order to compensate it, a set of 32 circular coils surrounding the detector will be installed [235]. Simulations showed that the residual magnetic field matches the experimental requirements. More information on the WCD can be found in Ref. [76].

2.2.3.2 The Top Tracker

The Top Tracker (TT) consists of three horizontal layers of plastic scintillator with the following dimensions: 47.0 x 20.0 x 0.01 m. They will be vertically separated by gaps of 1.5 m. Given its dimensions, the TT will cover ∼58% of the WCD surface and ∼72% of the CD surface (taking the equator of the sphere to compute its largest surface). Each of the three layers will consist of 21 *walls* - as shown in Figure 2.18 - themselves made of plastic scintillator strips.

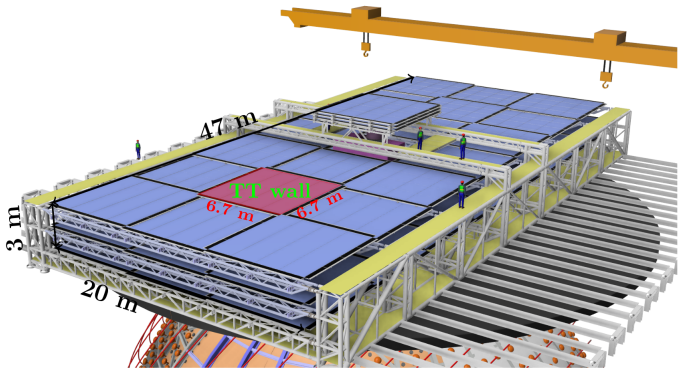

Figure 2.18: *The JUNO Top Tracker (TT) as it will be placed on top of the CD and WCD. The dimensions are indicated and a TT wall is highlighted in red.*

The detection principle of the TT is based on the production of light by the plastic scintillator when a charged particle passes through, similarly to the LS. In order to transport and collect the scintillation light, wavelength-shifting fibers are placed in each strip and are connected to 64-channel multi-anode photomultipliers. About 1/3 of the cosmic muons entering the CD will cross all the three layers of the TT, providing an unambiguous coincidence signal for vetoing the detector. The TT will also be able to precisely reconstruct the tracks of these muons, with an efficiency of 93%, with a purity of 99% – thanks to the coincidences between the sub-detectors – and with a median angular precision of

0.20°. As mentioned in section 2.1.1.4, the reconstruction of the muon tracks is a key component to determine the optimal muon veto cylinder (section 2.1.1.5) for cosmogenic background (^{8}He and ^{9}Li) rejection in the CD during the reactor neutrino analyses. For the rest of the muons that will cross the CD without being tagged by the TT, the veto strategy will only rely on the information from the WCD and CD, as explained in section 2.1.1.5. Other works on the muon events reconstruction in JUNO have already been conducted [236, 237]. More information on the TT can be found in Ref. [76, 238].

2.2.4 Calibration

The calibration of a detector consists in characterising its response, that is, being able to retrieve a physical quantity of interest from the observable provided by the detector. For most of its physics goals, the precise determination of the energy of the neutrino events occuring in JUNO is fundamental. The *energy scale* of the detector, that represents the conversion relationship between the number of PE and the corresponding true deposited energy, is a milestone in the calibration process. In a complex detector like JUNO, the energy scale suffers from non-linearity effects that are briefly mentioned in section 2.2.2.3 and in Chapter 4 and fully reviewed in Ref. [239]. Note that the calibration have other aspects and also includes the calibration of the readout electronics, synchronisation of the timing of the PMTs etc. The following focuses on the calibration of the energy and briefly describes how the aforementioned non-linearity effects will be addressed in order to reach the required 3% energy resolution and 1% energy precision.

In order to perform a comprehensive energy calibration of the detector, multiple calibration sources (Table 2.4) and dimensional scan systems (Figure 2.19) will be used. The large number of calibration sources covering a large energy range will be used to precisely determine the LSNL in the reactor IBD energy range. In addition, the ^{12}B cosmogenics (∼1000 events per day in JUNO) will provide a natural source of electrons and extend the energy range until ∼13.4 MeV [229].

Source	Radiation	Deposited Energy [MeV]
^{137}Cs	γ	0.662
^{54}Mn	γ	0.835
^{60}Co	γ	1.173 + 1.333
^{40}K	γ	1.461
^{68}Ge	e^+	annihilation 0.511 + 0.511
^{241}Am-Be	n,γ	neutron + 4.43 (^{12}C*)
^{241}Am-C	n,γ	neutron + 6.13 (^{16}O*)
(n,γ)p	γ	2.2
(n,γ)^{12}C	γ	6.94 or 3.36 + 1.26

Table 2.4: *List of the different calibration sources and radiation types, from [239].*

In order to address the detector position NU, four different systems will be used in order to place the calibration source at different points in the CD detector:

1. The Automated Calibration Unit (ACU) [240] will deploy the calibration sources along a vertical axis of the CD. The position of the source will be known to the centimeter. This system also supports the UV laser source.

2. The Cable Loop Sytem (CLS) [241] will deploy the source at many different positions in a 2D vertical plane thanks to two cables. The position of the source can be known to the centimeter thanks to an independent ultrasonic positioning system [242].

3. The Guide Tube (GT) [243] will deploy the sources along a longitudinal circle outside the CD acrylic vessel. Given the mean free path of the gammas, they will easily penetrate the acrylic sphere and deposit their energy in the LS. The GT is designed to calibrate the most external regions of the CD.

4. The Remotely Operable Vehicle (ROV) [244] is a complementary calibration system. It is capable to deploy the sources in any place of the LS. The ultrasonic positioning system can also be used for the ROV.

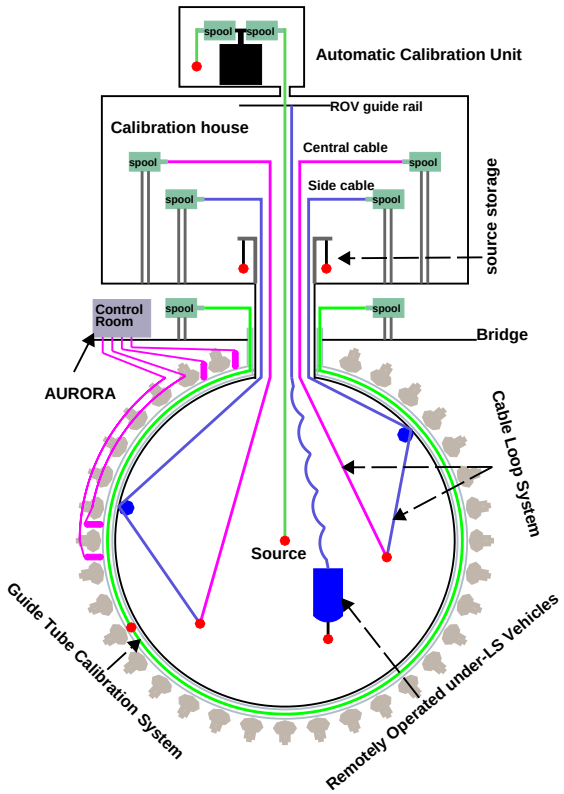

Figure 2.19: *Sketch of the different calibration systems of JUNO.*

Finally, a new concept of calibration is currently under development in JUNO: the DCC. It consists in an independent channel-wise calibration of the Charge Non-Linearity (QNL) using two independent PMT systems. Basically, the robust linearity of the charge reconstruction of the SPMT system will be used to correct for the potential QNL in the LPMTs. A tunable (keV to TeV) UV laser source (260 nm) [245] will notably be used.

2.2.5 Data Acquisition and Software

The Data Acquisition (DAQ) is responsible for the acquisition of the data from the different sub-detectors of JUNO (LPMT system, SPMT system, TT and WCD). It will have to build and process about 40 GBytes/s from the 20,012 LPMTs and 25,600 SPMTs with different algorithms (Online Event Classification (OEC), Software Trigger (ST) etc.) in order to reduce the data rate by ∼500. Then, the data will be transferred to the Institute of

High Energy Physics (IHEP) (Beijing, China) *via* Internet with a bandwidth of 1 GBits/s.

The Detector Control System (DCS) will permanently monitor the status of the experiment equipments (PMT high voltage, electronics, calibration system, water system etc.). It will also raise alarms if some of the monitored systems have a problem. The JUNO DCS is based on the Experimental Physics and Industrial Control System (EPICS) [246]. More information on the DCS can be found in Ref. [76].

For the processing and analysis of the data, JUNO will use Software for Non-collider Physics ExpeRiments (SNiPER) [247], a general-purpose software framework mainly based on C++ (for the functional modules) and Python (for the configuration scripts). SNiPER also contains an *offline software* that consists of a geometry managment system [248] that provides a complete description of the detector, event displayers [249, 250] and data analysis algorithms. The offline is used to perform a complete simulation chain of the detector [251], based on GEANT4. It has been widely used in this thesis. The simulation chain has four components:

1. The primary particle generator (Reactor IBD, solar neutrinos, Supernovae neutrinos etc.)
2. The detector simulation that consists in simulating the different JUNO sub-detectors geometries (CD, TT, WCD). In particular, that of the CD simulates the LS properties together with the scintillation photon propagation and part of the PMTs response, namely their geometry and Photo Detection Efficiency (PDE).
3. The electronics simulation, that consists in simulating the rest of the PMTs properties (time resolution, DCR etc.) as well as all the readout electronics of the different JUNO sub-detectors.
4. The trigger simulation that consists in building the events.

Various reconstruction algorithms (waveforms, vertices, energy and tracks) are also implemented in the offline. As it will be described in the next chapters, a significant part of my PhD work has been to use and to develop tools related to the SPMT system. Thus, more details on the CATIROC simulation code and on the event reconstruction algorithms will be given later on.

2.2.6 The Taishan Neutrino Observatory

This section describes a satallite experiment recently proposed by the JUNO collaboration named Taishan Neutrino Observatory (TAO) [252]. It consists in a ton level Gadolinium-doped LS detector placed at ∼30 m of one of the core of the Taishan nuclear power plant. This detector is designed for a high precision measurement of the reactor antineutrino spectrum that will serve as a reference spectrum for the determination of the NMO in JUNO. The TAO measurements will also represent benchmark measurements to test nuclear databases [169]. The required energy resolution of TAO is 3% at 1 MeV. However, thanks to an array of Silicon Photomultipliers (∼10 m^2) achieving a close-to-full geometrical coverage, about 4500 PE/MeV are expected. If the non-stochastic term of the energy resolution is well controled, the overall resolution could be maintained $< 2\%$ at 1 MeV [253]. The experiment is expected to start data-taking at a similar time than JUNO.

Chapter 3

SPMT readout electronics and their performance during a CCSN

Contents

At the beginning of this PhD thesis, the Subatech team was strongly involved in the development of the SPMT system, especially in the characterisation of the readout electronics (mainly CATIROC [231]) including the preparation of a test-bench for the SPMTs acceptance tests as well as in the development of a code that simulates the response of CATIROC. Thus, during the past three years, these tools have been extensively used to make different contributions. The first one concerned the charge calibration of CATIROC that is a milestone for the readout of the SPMTs, particularly in case of CCSN during which the system will be subject to an abrupt increase of the input rate. This contribution was a good preparation for the analysis that followed, which consisted in studying the performance of the SPMT system during a CCSN. First, the section 3.1 introduces the characteristics of CATIROC that are important for the understanding of this chapter. Then, the section 3.2 details my contribution to the charge calibration of CATIROC using the aforementioned test-bench. The two last sections present studies on the performance of the SPMT system during a CCSN neutrino burst in JUNO, notably by using the CATIROC response simulation code. More precisely, the section 3.3 focuses on its trigger performance. The resulting data flow is also computed and compared to the band-

width available to transfer to the DAQ. Moreover, the total amount of data is compared to the SPMT storage system. Finally, section 3.4 presents an *offline* event builder that has been developed and optimised for the SPMT system, by paying a particular attention to piled-up events (nearby CCSN).

3.1 The CATIROC features

In the hardware scheme of the SPMT system, the 25,600 SPMTs are grouped by 128. Each group is connected to a single board called ASIC Battery Card (ABC). As shown on Figure 4.23, eight CATIROC (OMEGA microelectronics laboratory [254]) and one Kintex-7 Field Programmable Gate Array (FPGA) (Xilinx, Inc. [255]) are embedded in an ABC. A single CATIROC ensures the readout of the signals from 16 different SPMTs through 16 channels with a common trigger threshold. It provides a measurement of the arrival time and integrated charge of the SPMTs signals. The range of charge measurable by CATIROC goes from 160 fC (1 PE at a gain of $3{\cdot}10^6$) to 70 pC (400 PEs). The charge and time information is then used for the event reconstruction (see Chapter 4). In this section, the way CATIROC measures the time and charge is introduced. Its dead-times are also presented.

When a signal is injected in the CATIROC inputs, it is first amplified by the pre-amplifiers of the channel fired. This can be done with two pre-amplifiers: the first one – namely the High Gain (HG) – is suitable for small signals while the second one – namely the Low Gain (LG) – is used when the input signal is larger than a user-configurable threshold (typically around 7 pC, i.e. 44 PEs for a SPMT gain of $3{\cdot}10^6$). Thus, for most of the signals from the SPMTs, only the HG is used. The acquisition of signals in LG mode is particularly interesting for high energy particles such as muons. The amplification ratio between the HG and LG is fixed and equal to 1/10 for all channels. Furthermore, the pre-amplifiers gain can be tuned for each channel (256 values), this feature can be used to compensate for the non-uniformity of the gain provided by the SPMTs (see section 2.2.2.2 in Chapter 2 for a quick reminder on the functioning of a PMT). After the pre-amplification phase, the signal enters two different circuits, one for the timing and trigger and one for the charge measurement. Their operation is described in a simplified way in the two sections below. The full description of CATIROC is given in Ref. [231].

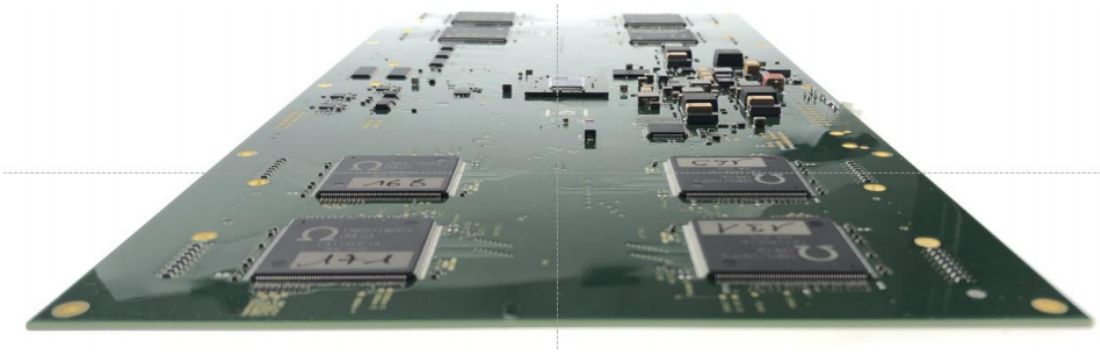

Figure 3.1: *Photograph of the ABC board. Four CATIROC are visible in the foreground and the four others are in the background. The grey component in the center of the ABC is the FPGA.*

3.1.1 Time measurement

The first channel (also called the *fast channel*) is responsible for the trigger and timing of the signal. The signal enters a discriminator that is responsible for the trigger formation and whose trigger threshold is common to the 16 channels of a CATIROC. The ABC, in which CATIROC is embedded, has three different trigger configurations that can be used for different purposes:

- Auto-trigger mode: If a signal passes the discriminator trigger threshold, it is processed. This mode is the standard one during the data taking.
- Force-trigger mode: The FPGA generates periodic pulses (1 kHz to 30 kHz) to force the CATIROC to process the incoming signals. This mode can be used to control the baseline noise of the ABC board that will not be triggered in auto-trigger mode but that has to be characterised in order to properly determine the charge of the physics signals. The baseline noise from the ABC is also referred to as *pedestal*.
- External-trigger mode: An external signal (i.e. from another device) forces CATIROC to take data.

The discriminator is followed by a circuit that measures the time and delays the trigger signal for the charge measurement (see section 3.1.2). The time measurement has two components:

$$T = \text{Coarse Time} \times 25 \text{ [ns]} - \text{Fine Time [ns]} \tag{3.1}$$

where the Coarse Time and Fine Time result from a Gray Counter and a Time to Analog Converter (TAC) that allow to measure the time of the trigger with a precision of $\mathcal{O}(200)$ ps (RMS) [231]. A first dead-time contribution arises from the formation of the trigger . As a consequence, if two consecutive signals hit the same channel, the circuit can trigger of the second signal depending on the time separation with the first one:

- Two consecutive signals separated by more than 90 ns are both triggered.
- If the time separation is between 60 ns and 90 ns, the probability to trigger the second pulse is less than a 100%. The trigger efficiency in such case is studied in Ref. [231].
- If the time separation is less than 60 ns, the second signal is not triggered but its charge sums up to the charge of the first one, depending on the time difference between the two hits (see section 3.1.2).

At this stage of the signal processing, it is possible to send the discriminator output directly to the FPGA, independently of the charge digitisation and read-out processes. This generates an independent data stream: the Discriminator Data Stream (DDS). In this case, the discriminator dead-time will be smaller than that described just above and the only limitation arises from the discriminator signal width (Figure 3.2, left). In addition, the FPGA can reconstruct the rise and fall times of the discriminator signal and extract the trigger width that can be used to retrieve the signal charge, but only up to an input charge of $\sim$1 pC for a SPMT gain of $3{\cdot}10^6$ (Figure 3.2, right). Such feature provides an additional information for the PE counting, notably to better handle the events that yield a high trigger rate (muons and CCSN).

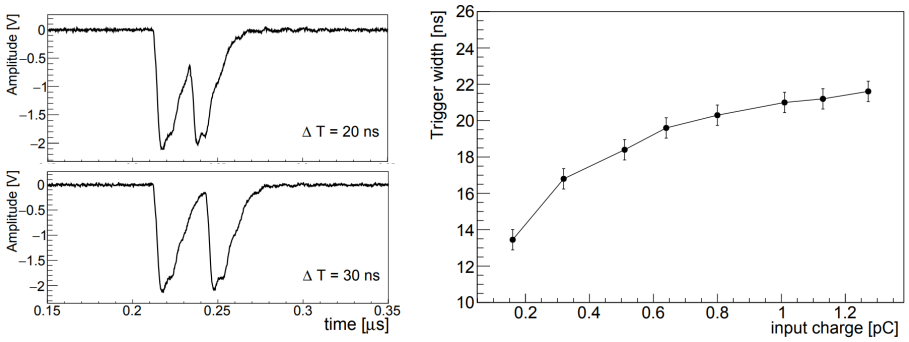

Figure 3.2: ***Left**: Example of a discriminator output signal as observed with an oscilloscope, two pulses were injected with a time difference of 20 ns (top) and 30 ns (bottom). **Right**: The width of each discriminator signal against the input charge up to 1 pC (∼2 PE at a gain of 3·10^6). From Ref. [231]*

3.1.2 Charge measurement

The second channel (also called the *slow channel*) is responsible for the charge measurement. In brief, a "slow shaper" (RCCR filter) modulates the incoming signal to form a bi-polar signal. The charge is then derived from the maximum amplitude of this bi-polar signal that is determined thanks to the trigger delay from the discriminator. As mentioned in the previous section, two signals hitting the same channel too close in time might not produce two independent triggers, in which case only the first one is recognised. Thus, when measuring the charge, only one slow shaper is produced with an output that is proportional to the sum of the two hits (see Figure 3.3). Part of the charge information is lost (charge acceptance).

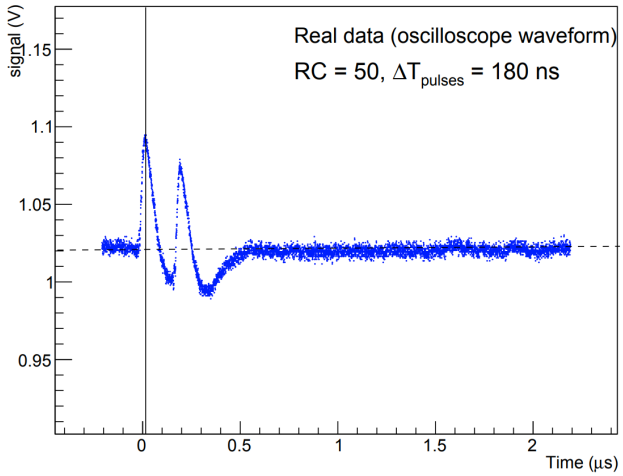

Figure 3.3: *Two signals entering a single channel close in time (ΔT = 180 ns). Their waveforms are measured at the oscilloscope. In such case, part of the charge information is lost. From Ref. [231]*

The charge measured at the peak of the slow shaper signal is then digitised by an Analog to Digital Converter (ADC). When the digitisation of a signal is ongoing, the digitisation of new signals in the same channel is not possible, bringing a second dead-time contribution. However, this problem is solved in CATIROC by the use of a Switch Capacitor Array (SCA) (one for each channel) so that the signals are temporally stored in two capacitors (called *PING* or in the *PONG*) before being digitised. Thus, a channel can digitise up to two different signals arriving in a time interval of 6.8 µs (9.3 µs) if one

channel (several channels) is fired. If a third signal arrives before the end of this time interval, it cannot be stored and is lost. The Figure 3.4 shows the linearity of the charge measurement by CATIROC for both HG and LG and for input signals ranging from 0 to 60 pC.

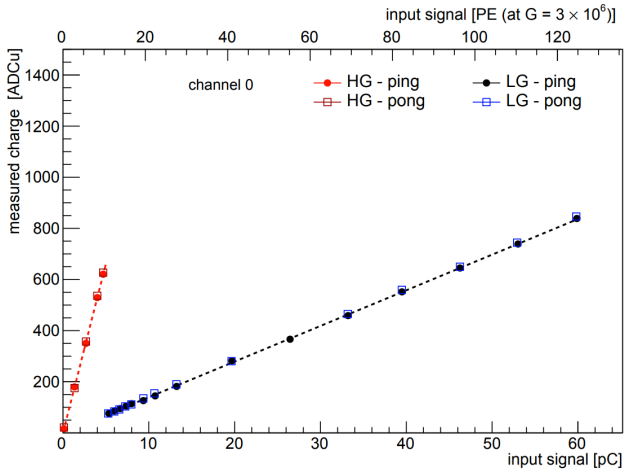

Figure 3.4: *The charge measured by CATIROC against the input charge for both HG mode (red) and LG mode (blue). The PING and PONG mode correspond to the filled and empty markers, respectively. From Ref. [231]*

Once the time and charge information is digitised, they are readout by CATIROC and sent to the FPGA to feed the main data stream of CATIROC: the Charge Data Stream (QDS). The impact of the aforementioned dead-time contributions in case of CCSN – during which the signal rate is expected to drastically increase – is investigated in section 3.3.

3.2 Procedure tests for the charge calibration of CATIROC

As explained in section 2.2.2.2 (Chapter 2), the PE generated by a scintillation photon is amplified by a sequence of dynodes in the PMT. The gain of a PMT is defined as the total charge that is obtained at the output of the PMT from the initial one. The higher the high voltage that powers the SPMT, the higher the gain. However, for a given high voltage, different PMTs can have slightly different gains. The latter is of the order of $3{\cdot}10^6$ for the SPMTs of JUNO but may vary by a factor 2 or 3 from one SPMT to another[1]. This means that for a single PE, the output signal total charge may vary among the SPMTs. The CATIROC provides the charge measurement of the signals from the SPMTs. As a consequence, to retrieve the number of PE – on which the energy reconstruction is based (see Chapter 4) – one has to convert the charge measured by CATIROC (ADCu) into Coulomb and then get back to the corresponding number of PE using the SPMT gain. Thus, in order to make the measurements from CATIROC exploitable, it is necessary to calibrate its charge response. Given the important number of channels of the SPMT system (25,600), the calibration will represent an important number of runs. It is worth mentioning that this calibration has to be done for both HG and LG modes, for several pre-amplifier gain values and for each of the 25,600 channel. In this section, a CATIROC charge calibration method is introduced and procedure tests for a faster calibration are presented.

[1]During the construction phase, the SPMTs have been grouped so that they have similar gains at a given High Voltage (HV)

3.2.1 The SPMT test-benches

All along the production, the HZC-Photonics© company has monitored various performance parameters of the SPMTs like for instance the Quantum Efficiency (QE), the Transit Time Spread (TTS), the Dark Count Rate (DCR)... After being potted and cabled, the 25,600 SPMTs must be tested again – *acceptance* tests – before being installed on the JUNO detector. These tests are done by means of two test-benches developed in collaboration between Subatech and the LP2I Bordeaux (ex-CENBG) and that are now installed at Guanxi university (China). They mainly consist of a Data Acquisition (DAQ) software, an HV splitter board, an ABC and connectors. The acceptance tests consist in the following sanity checks:

1. Verify the positive response.
2. Measure the PMT gain.
3. Measure the Single Photoelectron (SPE) resolution at nominal voltage.
4. Measure the Dark Noise (DN).

Before being installed on the detector, the response of the 200 ABC boards – including that of CATIROC – needs to be calibrated. Thus, before being shipped to China, the test-benches have been used to perform procedure tests for the charge calibration of CATIROC. This work is presented in the next sections.

3.2.2 Standard calibration procedure

The charge calibration of CATIROC is necessary to be able to convert any charge measured from ADCu to pC, in order to retrieve the corresponding number of PE. The calibration must be as precise as possible since the slightest uncertainty on the calibration directly translate into systematic errors in the measurements performed during the data taking. As shown in Figure 3.5, for a given injected charge (pC), the distribution of the readout charge (ADCu) varies for different channels within a CATIROC and among the CATIROCs of a single ABC board. As a consequence, each of the 25,600 channels of the SPMT system must be calibrated. Note that the PONG mode (not displayed here) leads to slightly different charge measurement – by a few ADCu at most – as already shown in Figure 3.4. Such discrepancy will also be calibrated. In the following, only the results for the PING mode are shown.

In the calibration startegy presented in the following, different values of charge are injected using a pulse generator whose amplitude, width and frequency can be adjusted. The input charge is varied from 1 to 50 pC and the pulses are injected at a frequency of 10 kHz. The acquisition time is set so that several thousands of pulses (i.e. signals) are digitised. Then, the mean and the standard deviation of the measured charge distribution for each injected charge are used to construct the calibration curve. The charge response of CATIROC is expected to be linear, the calibration points are then fitted with a one degree polynomial:

$$Q_{mes} = p_1 \times Q_{in} + p_0 \tag{3.2}$$

where Q_{mes} is the measured charge (in ADCu), p_1 is the slope (in $\frac{\text{ADCu}}{\text{pC}}$), Q_{in} is the injected charge (in pC) and p_0 is the intercept (in ADCu). The latter is expected to be equal to zero after the pedestal (baseline noise from the ABC) is subtracted for each charge distribution. It is important to mention that, since the pre-amplifier of each channel is tunable, the charge calibration must be known for both HG and LG and in principle for

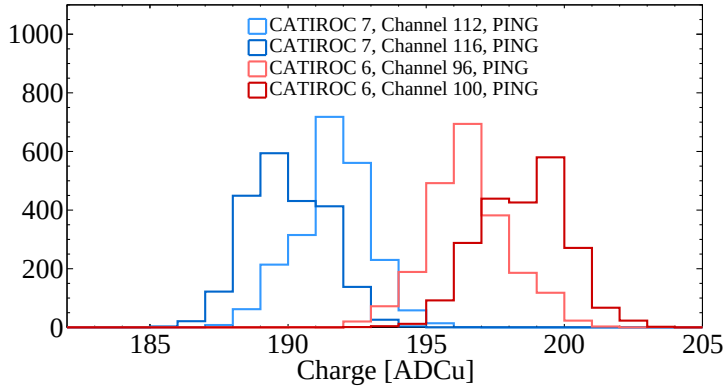

Figure 3.5: *The distribution of the readout charges for two CATIROCs and two channels of these CATIROCs in PING mode. The injected charge is 7 pC in the four cases. The measured charge of a single channel has a standard deviation of ∼1.5 ADCu.*

all the 256 pre-amplifier gain values. An example of the calibration curves for a given channel and for four gain values are shown in Figure 3.6. The results of the fit show that the intercepts are compatible with 0, within uncertainties for the HG but not for the LG. Since the objective of this work is to propose a faster calibration method and to compare it to the standard one, this point is not further investigated.

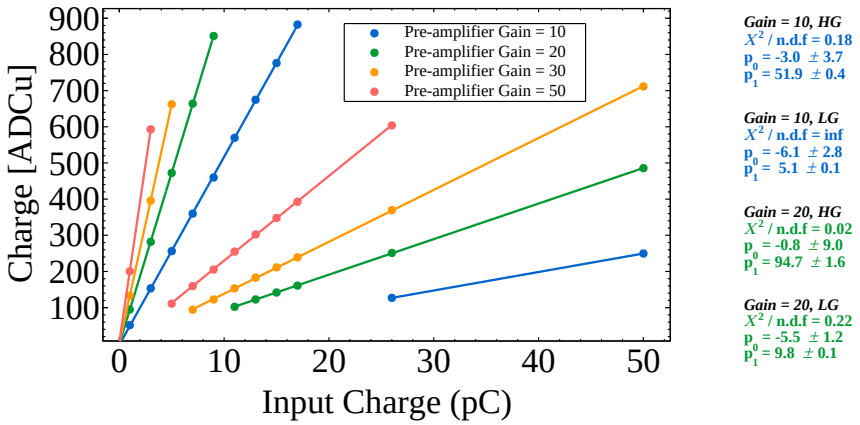

Figure 3.6: *An example of calibration curves for a channel of CATIROC obtained with 11 calibration points for four different values of pre-amplifier. The error bars are smaller than the size of the points. The four leftmost curves correspond to the HG while the rightmost ones correspond to the LG. The parameters of the fits for two of the curves are shown on the right, the $\tilde{\chi}^2$ is equal to "inf" when there are only two calibration points to fit, which is expected and implies that at least three points for both HG and LG should be taken during the calibration runs.*

Considering that at least 11 calibration points are necessary to get a proper calibration curve for each channel and that at least four pre-amplifier values must be tested to get a reasonnable extrapolation for the remaining 252 values, the charge calibration of the 25,600 channels of the SPMT system would require ∼1,500,000 calibration runs. The teams in charge of the SPMT system calibration plan to use a "Q-injector", a device that

allows to inject signals simultaneously in the 128 channels of an ABC. Still, other methods must be explored in order to further reduce the number of calibration runs required and automate the procedure. One such method is introduced in the following.

3.2.3 A fast calibration procedure

The principle of the procedure presented in this section is to construct the calibration curve of each channel for *a single* pre-amplifier gain value – called the "reference calibration curve" hereafter – and to use it together with a calibration of the pre-amplifier to extrapolate the calibration curves for all the other gain values. Thus, assuming that the reference calibration curve for a gain $G = 10$ is defined as:

$$Q_{ref} = p_1 \times Q_{in} + p_0 \tag{3.3}$$

where Q_{ref} is the measured charge (in ADCu), p_1 is the slope (in $\frac{ADCu}{pC}$), Q_{in} is the injected charge (in pC) and p_0 is the intercept (in ADCu). Then, the calibration curve at a given gain G can be extrapolated such as:

$$Q_G = A_G \times (p_1 \times Q_{in}) + p_0 \tag{3.4}$$

where A_G is a charge multiplicative factor that depends on the pre-amplifier gain value. Thus, determining A_G is the key point to extrapolate the calibration curve to all possible gains. Note that this work has been done by constructing the reference calibration curve with a gain $G = 10$, but it can also be done by taking a different gain value ($G = 20$ for example), as long as it is within the preferred gain range for the SPMT system ($G \in$ [10;40]) . The *pre-amplifier calibration* is done by injecting a charge (1 pC for the HG mode and 25 pC for the LG mode) in the channels and varying the pre-amplifier gain value. The curve obtained is normalised to the charge for a gain value of 10. An example of this calibration for the HG mode of four channels of a CATIROC is shown in Figure 3.7. It shows that the pre-amplifier is not linear, especially at high gain values. The four curves showed here have similar trends (with a relative difference within 3%). Furthermore, it has been shown in Ref. [231] that the additional variations observed among pre-amplifiers of different CATIROCs are very small. Thus, in the following, the calibration of the pre-amplifier of a single CATIROC channel is used for the extrapolation of the 16 channels of another CATIROC. This will further reduce the number of calibration runs required during the mass calibration of the ABCs.

In order to validate the results of the "fast calibration method", the results must be compared to the ones obtained with the standard procedure. Two approaches were adopted for the extrapolation:

1. The first one consists in multiplying each point of the reference calibration curve by the corresponding A_G from the pre-amplifier calibration and then to fit the distribution obtained to get the calibration curve.
2. The second method consists in directly multiplying the fit parameters of the reference calibration curve by A_G – as shown in equation 3.4 – to obtain the calibration function parameters for the other pre-amplifier gain values.

The left plot of Figure 3.8 compares the calibration curves obtained with the standard procedure to those obtained with the fast method. In order to assess the precision of the fast method, the relative difference between the slope of the extrapolated calibration curve ($p_{1,ext}$) and that obtained with the standard procedure ($p_{1,true}$) is computed such as:

$$\frac{p_{1,true} - p_{1,ext}}{p_{1,true}} \quad [\%] \tag{3.5}$$

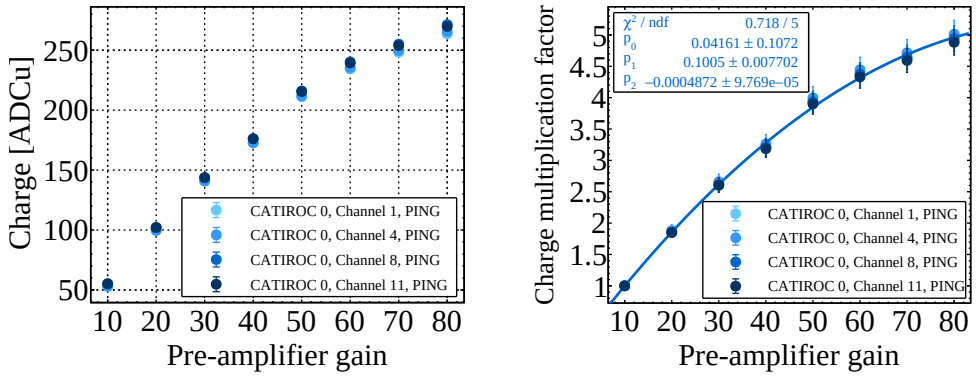

Figure 3.7: ***Left**: Example of a pre-amplifier calibration (HG) for four different channels of a single CATIROC. The injected charge is 1 pC and the gain is varied from 10 to 80 by steps of 10. **Right**: The ratio A_G (charge multiplication factor) between the measured charge at different gain values and that obtained for a gain of 10. The solid line represents a second degree polynomial function.*

The results (Figure 3.8, right) show that the relative difference increases with the pre-amplifier gain. The relative differences are below 2% in HG mode and below 3.5% for the LG mode.

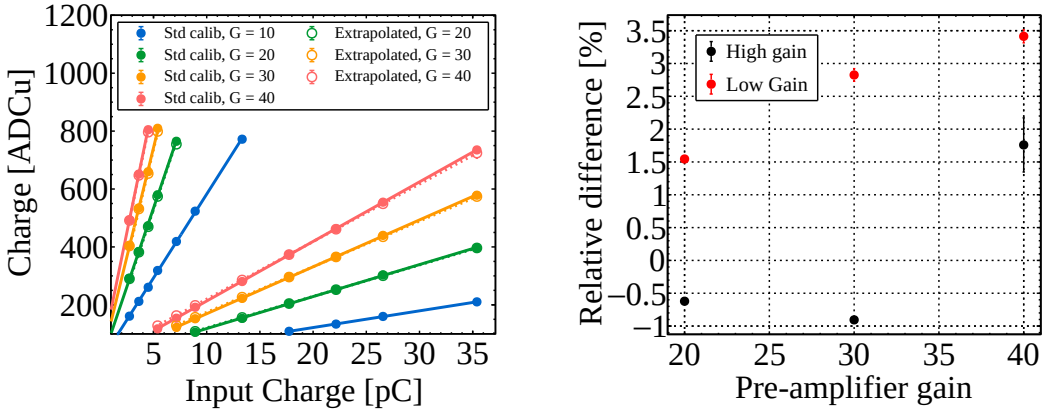

Figure 3.8: ***Left**: The calibration curves for four different values of pre-amplifier gain. The solid lines are obtained with the standard calibration procedure while the dotted lines are obtained by extrapolation. The reference calibration curve ($G = 10$) is shown in blue. **Right**: The relative difference between the slopes of the solid and dotted line calibration curves for the three different values of gain tested in both HG and LG mode.*

The same comparison is done for the 15 other channels of a CATIROC using the pre-amplifier calibration of a single channel. The results are shown on the left plot of Figure 3.9. The relative difference between the slopes is inferior to 3.5%. The comparison of the slopes of the curves obtained with the second method are shown on the right plot of Figure 3.9. The relative error is on average larger than with the first method, especially for the gains 20 and 30 where it can reach 5% for some channels. The better performance of the first method probably comes from the fact that the slope of the fit function ($p_{1,ext}$) is constrained by the extrapolated points while with the second method, it is not constrained since the slope is just obtained by multiplying $p_{1,true}$ by A_G.

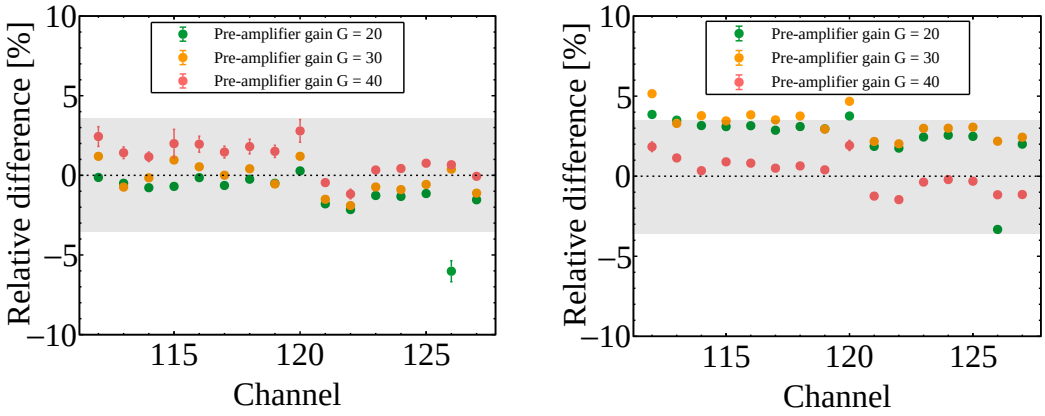

Figure 3.9: *Relative difference between the slopes (p_1) of the calibration curves obtained with the standard procedure and the first method (**Left**) and the second method (**Right**) for the three gain values tested in HG mode. The grey area shows the 3.5% relative error boundary.*

We have seen that when using the first method, as the pre-amplifier gain increases, the extrapolated curve's slope tends to be more and more different than that obtained with the standard procedure. The performance of the extrapolation at higher pre-amplifier gain values (G > 40) can be investigated in the future. However, for the JUNO purposes, a gain above 40 will be hardly used because of the loss of dynamic range for high energy events (e.g. muons). One of the major advantage of the calibration curve extrapolation is that it highly reduces the number of calibration runs required for the charge calibration by a factor ∼4 if the present method is applied for the mass calibration of the CATIROCs.

3.3 The SPMT system rate capability

For a typical 10 kpc away CCSN, JUNO will detect a burst of $\mathcal{O}(10^4)$ neutrino interactions with an average visible energy of ∼15 MeV. The length of the neutrino signal will be ∼10 seconds. As it will be shown in the next sections, ∼60% of the neutrino interactions occur during the first second of the burst, the rate could reach several kHz and even several MHz for a nearby CCSN (≥ 1 kpc). This represents a significant amount of data to deal with, within a very short timescale, especially if compared to the event rate expected in the other JUNO physics analyses (reactor, solar, DSNB etc.). First, the rate of signals that CATIROC will have to process will increase and the aforementioned dead-time contributions could cause a loss of information of the events and notably impact the quality of the event reconstruction and consequently the physics analysis and interpretations. Second, the data transfer bewteen the ABC and the DAQ has a limited throughput capability (∼0.5 Gigabit/s) resulting in possible data loss. In this section, the performance of the CATIROC in case of CCSN and more specifically the impact of its dead-times is studied. Then, the data rate expected from the SPMT system is computed and compared to the aforementioned throughput capability numbers. Finally, the resulting total amount of data is calculated and compared to the storage space available in the Under Water Boxes (UWB).

3.3.1 Simulation tools

The following subsection briefly describes the functioning of the simulation tools used for this study as well as their main characteristics, notably on the CCSN neutrino burst gen-

erator that is implemented in the JUNO simulation software as well as on the CATIROC simulation code. A brief introduction on the JUNO simulation software is given in Chapter 2.

3.3.1.1 CCSN neutrino burst generator in JUNO

The JUNO simulation software [248] includes a CCSN neutrino burst generator. This generator is based on existing CCSN neutrino emission models, see Chapter 2 and Refs. [127–129, 256, 257]. Starting from a CCSN progenitor, these models simulate the neutrino physics and signal formation during the core collapse and the explosion phase and are then able to predict the time and flavor-dependent neutrino luminosities (i.e. the energy released in neutrinos against the time) as well as the neutrino energy spectra. Currently, two models are implemented in the JUNO simulation software, the first one is referred to as the *Nakazato* model [128, 256] while the second is referred to as the *Garching* model [258–260]. Both provide simulations for progenitors with various characteristics. In the Nakazato model, the user can set three parameters:

- The progenitor mass: $13M_{\odot}$, $20M_{\odot}$, $30M_{\odot}$ or $50M_{\odot}$[2].
- The progenitor metallicity: Z = 0.02 and Z = 0.004, that corresponds to the fraction of nuclei that are not Hydrogen ${}^{1}_{1}$H or Helium ${}^{2}_{1}$He over the fraction of ${}^{1}_{1}$H + ${}^{2}_{1}$He.
- The revival time: 100 ms, 200 ms or 300 ms that corresponds to the time before the stalled shock is revived by the neutrino heating (see Chapter 1). The possibility to set the revival time is specific to the Nakazato model. Indeed, the neutrino signal calculations are split into two phases, the first one finishing when the shockwave stalls and the second one starting at the moment of the explosion.

In every simulation configuration the Nakazato model provides the neutrino signal from the onset of the collapse up to 20 seconds after the core bounce.

In the Garching model, the user can set three parameters:

- The progenitor mass: $11.2M_{\odot}$, $25M_{\odot}$, $27M_{\odot}$ or $40M_{\odot}$.
- The nuclear matter equation of state: Shen [261] or LS220 [262].
- The neutrino transport through the Proto-Neutron Star (PNS) and accreting matter can be impacted by the opacities arising from various effects (diffusion, convection of the nuclear matter, nucleon potential).

In this model, the duration of the neutrino signal varies from ∼2 seconds in some cases to ∼10 seconds in others. It is worth pointing out that the progenitor parameter combinations given here lead to the explosion of the CCSN, which is not always the case in CCSN simulations. The generator implemented in JUNO includes the neutrino oscillation equations to predict the flavor swapping during the propagation from the CCSN to JUNO and applies the neutrino-matter interaction cross-sections needed to calculate the number of neutrinos that interact with the JUNO LS (12% of protons and 88% of carbons). For each interaction, the corresponding channel is also given. Other parameters such as the distance to the CCSN and the NMO (Normal or Inverted) can be set. In the end, for a given set of input parameters, this generator gives a list of events for each neutrino that interacted with the LS of JUNO. Each entry of the list contains:

1. The energy of the corresponding incident neutrino.

[2] $M_{\odot}$ = solar mass

2. The time of interaction.
3. The number of produced particles. This number can be either 1, (for example in case of Neutrino-Proton Elastic Scattering (νpES) and Neutrino-Electron Elastic Scattering (νeES)) or 2 (as in the case of the Inverse Beta Decay (IBD)).
4. The PDGID [5] of the output particles.
5. The momentum (P_x, P_y and P_z) of the output particles.

To assess the performance of the SPMT system readout electronics in case of CCSN neutrino burst, only the configurations that predict the largest number of events and event rate in JUNO are considered. The parameter that has the largest influence is the distance R to the CCSN. Indeed, assuming the source is pointlike, the solid angle subtended by the detector depends on the distance to the source, hence the number of events decreases following the $\frac{1}{R^2}$ law (Figure 3.10, left). The second parameter that most influences the number of events is the mass of the progenitor star that can make the number of detected neutrinos by up to several tens of percent (Figure 3.10, right). Indeed, as explained in Chapter 1, the two main regions that produce neutrinos are the Proto-Neutron Star (PNS) and the mass accretion region. The density of the first one has strong impacts on the outward diffusion of the neutrinos while the mass accretion rate strongly influences the production of neutrinos. Also, the most massive stars can end-up their life in a black hole which abruptly decreases the neutrino emission. More details can be found in Ref. [119]. In addition, in most of the cases, the Nakazato model predicts more neutrino interactions in JUNO than the Garching model. For example, there is a factor 2 between the number of neutrino interaction predicted by the two models for the simulation configurations presented on the left plot of Figure 3.10.

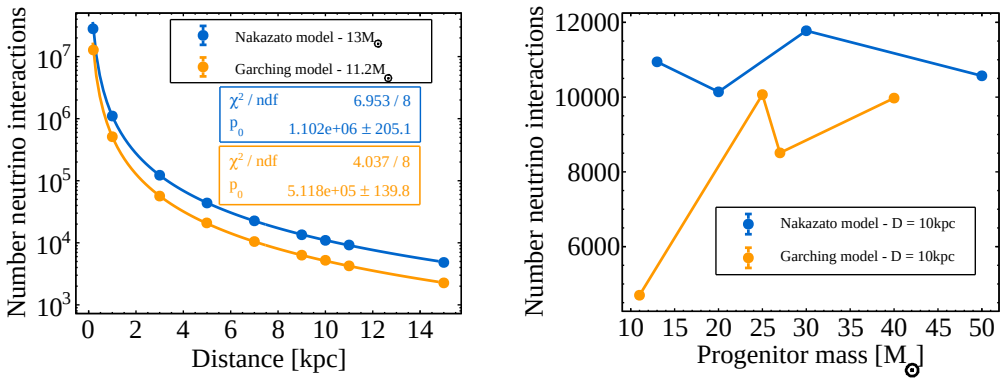

Figure 3.10: ***Left**: The number of neutrino interactions expected in JUNO as a function of the distance to the CCSN for the Nakazato (blue) and Garching (orange) models, the progenitor masses are 13 $M_\odot$ and 11.2 $M_\odot$, respectively. **Right**: The number of neutrino interactions expected in JUNO as a function of the mass of the progenitor for the Nakazato (blue) and Garching (orange) models. The distance is 10 kpc in both cases.*

The other parameters that can be configured (metallicity, equation of state, neutrino opacities) have a smaller influence on the number of events (variation of less than 10% from one configuration to the other). The event rate will also be determinant. Indeed, the timescale of a typical event in JUNO is of the order of a few hundreds of nanoseconds. Thus, it is not impossible that in case of a high rate some of them pile-up (i.e. overlap of their scintillation photon time distribution) making the event reconstruction challenging.

As shown in Figure 3.11, the event time distribution is not flat and, in both models, the first 500 ms have a larger rate than the rest of the burst. After the first second from the beginning of the signal, the number of neutrino interactions settles down at less than 50 interactions per 20 ms. In addition to predicting a higher number of neutrino interactions than the Garching model, the Nakazato model foresees that the time distribution of the neutrino interactions is highly peaked in the first 300 ms during which ∼40-45% of them occur. This proportion is rather of ∼20-25% for the Garching model. Is is important to highlight that since some neutrino interaction channels like the IBD produce two particles, the total number of events recorded by the JUNO detector will be even larger.

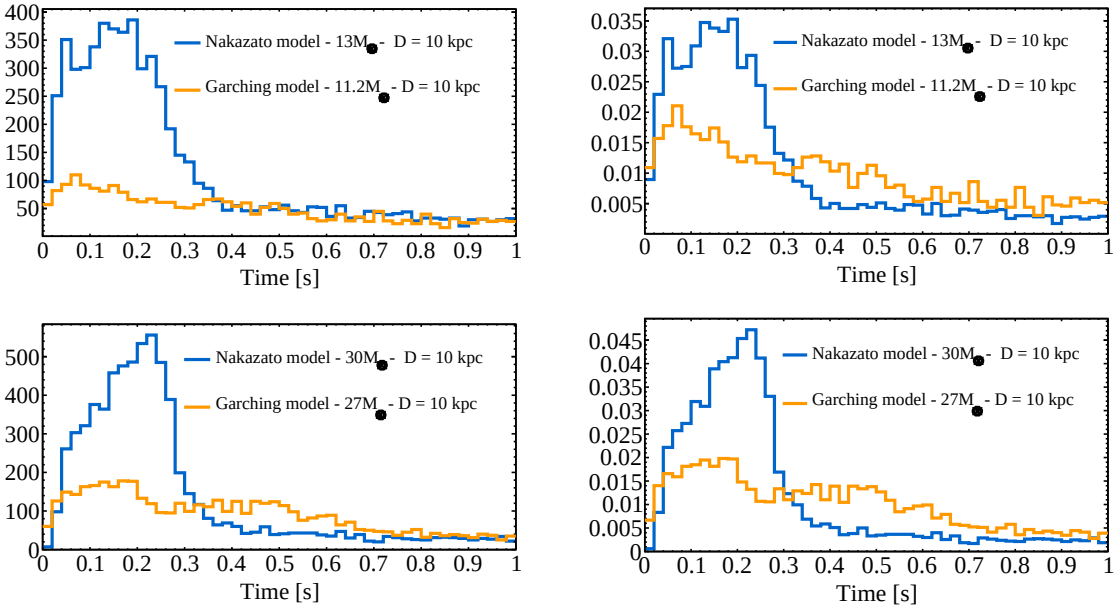

Figure 3.11: ***Top**: The time distribution of the neutrino interactions in the first second of the burst for Nakazato (blue) and Garching (orange) models. The progenitor masses are 13 $M_\odot$ and 11.2 $M_\odot$, respectively. The left plot shows the same distribution than the right one but normalised by the total number of neutrino interactions of the burst.* ***Bottom**: As in top but for progenitor masses of 30 $M_\odot$ and 27 $M_\odot$.*

Part of this PhD thesis was dedicated to the reconstruction of the CCSN neutrino energy spectra and the results of this work are detailed in Chapter 5. As previously mentioned, the CCSN generator provides the incident energy of the neutrinos that interacted in JUNO, but not their flavor. First of all, the models typically give the fluxes for the ν_e, $\bar{\nu_e}$ and ν_x (that collectively denote for ν_μ, ν_τ, $\bar{\nu_\mu}$ and $\bar{\nu_\tau}$) so that a complete flavor separation is not provided in input. In addition, the generator convolutes the fluxes with the interaction cross-sections to determine their interactions in JUNO. During this stage, the neutrinos are grouped by interaction channels and the information on the flavor is not preserved. In practice, tracking the neutrinos one-by-one and keeping the information on the flavor of each of them could be possible, but it would take more computational time. Since some interaction channels like the IBD or the $\bar{\nu_e} - {}^{12}C$ and $\nu_e - {}^{12}C$ are only possible for ν_e or $\bar{\nu_e}$, it is possible to partly recover the flavors, as shown in Figure 3.12. The energy spectra differ from one model to another and also within a single a model. Indeed, the Nakazato model tends to predict energy spectra with higher average energy and with faltter shapes than the Garching models. The mass also impacts the average energy and spectra shape. It is also the case for other parameters like the neutrino opacities in the

Garching model but to a lesser extent.

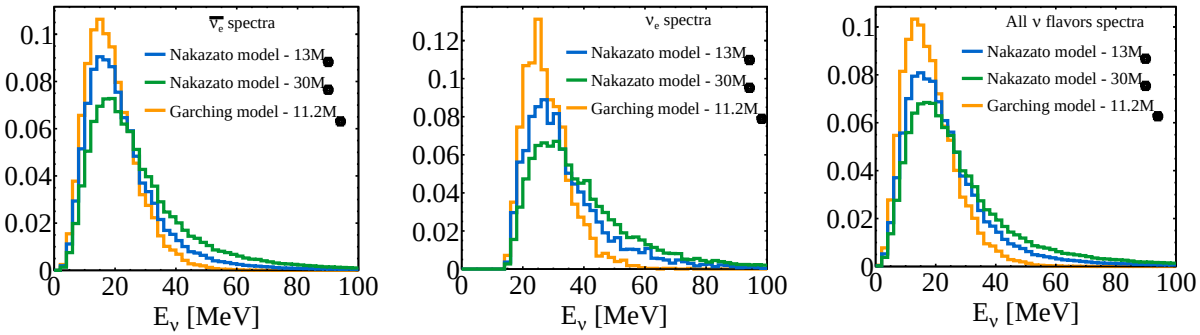

Figure 3.12: *Example of normalised energy spectra that can be constructed from the CCSN generator. The left plot only includes $\bar{\nu}_e$ from IBD and $\bar{\nu}_e$ $-^{12}C$ interaction channels. The middle plot only includes ν_e from the ν_e $-^{12}C$ interaction channel. The right plot include neutrinos of all flavors from the rest of the interaction channels.*

3.3.1.2 Detector and readout electronics simulation

After the generation of the CCSN neutrino interactions in JUNO, the detector simulation is ran using the GEANT4 simulation software implemented in SNiPER (detector geometry, secondary particles propagation, scintillation photon tracking until the PMTs etc.). This step of the simulation requires a lot of computing power and can take several weeks (considering the computing power to which I had access) for the closest CCSN. For this reason, the LPMT system was disabled during the simulation, which allowed to highly reduce the computing time. In addition, a stand-alone version of the SPMT system electronics code that is implemented in the JUNO simulation software has been used, allowing to reprocess simulations more easily for the studies conducted here. This code simulates the response of the SPMTs (Charge and Time resolution, Dark Noise etc.) as well as the response of CATIROC the readout electronics. It has been developed at Subatech after the comprehensive characterisation of the CATIROC [231].

3.3.2 The performance of CATIROC

As described in section 3.1, in case of high signal input rate, it is possible that CATIROC does not trigger on all of the signals because of its intrinsic dead-time. In this section, the trigger performance of CATIROC during a CCSN neutrino burst in JUNO is studied. For this purpose, the CCSN model that produces the highest event rate in the first second of the burst is selected. Compared to all the other available configurations, the Nakazato model with the following progenitor star parameters is chosen:

- Mass : 30M$_\odot$.
- Metallicity: Z = 0.02.
- Revival time: 300 ms.

Four different distances are studied: 10 kpc, 5 kpc, 3 kpc and 1 kpc. However, since the computing time was too large for the case at 1 kpc with this model, I took another one with the following configuration: Garching model, Shen equation of state, 25M$_\odot$, no neutrino-nuclear matter effects. Such configuration predicts ∼20% less events than

the aforementioned configuration of the Nakazato model at equivalent distance. The Table 3.1 summarises the number of neutrino interactions and the maximal event rate that is reached.

Distance	10 kpc	5 kpc	3 kpc	1 kpc
Number of neutrino interactions	14,539	57,877	160,882	$\sim 1.1 \cdot 10^6$
Maximal rate [kHz]	∼30	∼110	∼310	∼1250

Table 3.1: *The number of neutrino interactions and the maximum interaction rate (20 ms^{-1}) for a simulation using the Nakazato model with the configuration stated at the beginning of this sub-section.*

Before describing the analysis and its results, the typical number of hits per SPMT expected at the detector level – *before* the CATIROC simulation – is shown in Figure 3.13 for a 10 kpc away CCSN, assuming no event pile-up. It is typically in the cases where the number of hits exceeds 1 that CATIROC may suffer from dead-time. The left plot shows that ∼94% of the SPMTs have only 1 hit, ∼5% have 2 and the remaining ∼1% have 3 hits or more. This regime is close to that expected in the reactor neutrino energy range (0-10 MeV) [230] in which the dead times of CATIROC have a negligible impact on its ability to trigger on the incoming signals. The event rate and the probability of event pile-up – for which the total number of scintillation photon produced within a single event time scale – both increases. Thus, it is expected that the dead-time of CATIROC has more and more impact as the distance to the CCSN decreases. The right plot of Figure 3.13 shows that the number of hits per SPMT is more likely to be larger than 1 when the events are close to the CD edges. Finally, the bottom plot of Figure 3.13 shows the time separation between two consecutive hits on the SPMTs that have several hits during an event. It is important to mention that ∼60% of the distribution is contained between 0 and 10 ns. The *SPMT integration window* is ∼10 ns. Consecutive hits on a single SPMT with a time separation inferior to it are not separated and will enter CATIROC as a single signal.

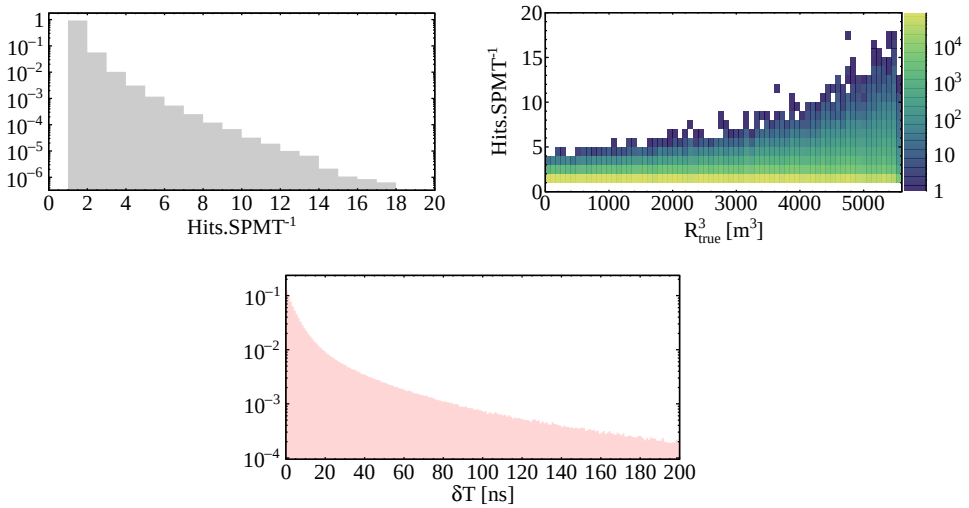

Figure 3.13: ***Top left**: The normalised distribution of the number of hits per SPMT during a CCSN neutrino burst (10 kpc). **Top right**: The distribution of the number of hits per SPMT during a CCSN neutrino burst (10 kpc) as a function of the cubic radius of the event R^3_{true} (the "radius" of the event is its distance to the center of the acrylic sphere). For example, 1000 m^3 corresponds to a radius of 10 m, 3000 m^3 corresponds to a radius of ∼14.4 m and 5000 m^3 corresponds to a radius of ∼17.1 m. **Bottom**: The time separation between consecutive hits on the SPMTs that have multiple hits.*

In order to reproduce as accurately as possible the conditions of a real CCSN neutrino burst, the events are sorted on a timeline, the possible pile-up between them is carefully simulated and the dark counts from the SPMTs, that constitute additional input signals to CATIROC, are also simulated all along the burst duration. The only missing element is the events from the JUNO detector intrinsic radioactivity whose rate is expected to be $\mathcal{O}(100$ Hz) [173]. It is considered negligible compared to the event rate reached during a CCSN. The trigger threshold of CATIROC is set at 1/3 PE assuming a SPMT gain of $3{\cdot}10^6$. Given the shape of the neutrino signal, whose peak occurs within the first 0.5 second and that suddenly settles down after that (Figure 3.11), only the first ∼5 seconds of the burst are analysed over the 20 seconds of data available in the simulation files. First, this allows to limit the computing time, especially for close CCSN. Second, a duration of 5 seconds is sufficient to comprehensively analyse the performance of CATIROC. After the detector and electronics simulations, the true number of hits on the SPMTs are compared to the number of triggers in the two output data streams (QDS and DDS). The results for the QDS are presented in Figure 3.14 for the first 600 miliseconds of the burst: the number of hits on a SPMT – averaged over the 25,600 SPMTs – is compared to the average number of triggers in the QDS. The fraction of non-triggered hits increases as the distance to the CCSN decreases. For the cases at 10 kpc and 5 kpc, the fraction of hits lost is always $< 5\%$ while it can reach ∼6.5% at 3 kpc and ∼8% at 1 kpc. It also shows that at 10 kpc, 5 kpc and 3 kpc, when the signal rate settles down after the first ∼0.5 second, the fraction of non-triggered hits stabilises at 2% or less until the end of the burst. The shape of the signal is different for the Garching model, it stabilises ∼1 second after the beginning of the burst. The fraction of non-triggered hits over the five seconds of the burst simulated is 0.5%, 1.3%, 2.8% and 3.9% for CCSN at 10 kpc, 5 kpc, 3 kpc and 1 kpc, respectively.

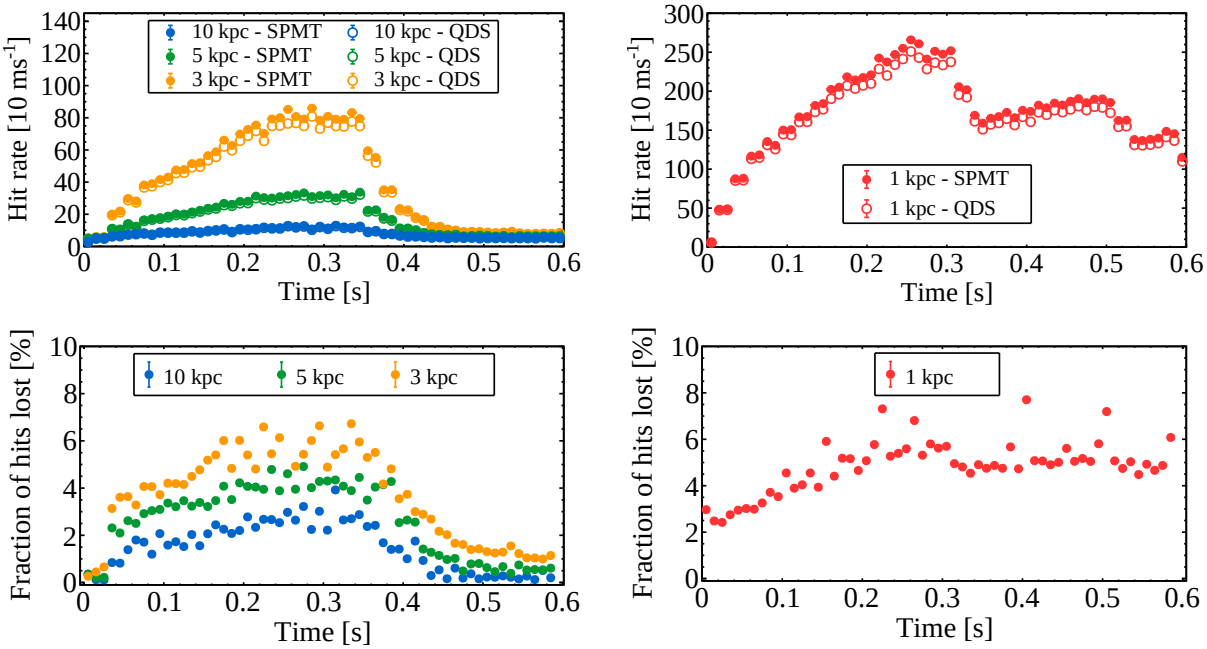

Figure 3.14: ***Top**: The SPMT hit rate (full dots) and trigger rate (empty dots) in the QDS for a single SPMT during the first 0.6 second of a CCSN neutrino burst for three different distances (left) and for 1 kpc (right) averaging over 25,600 SPMTs.* ***Bottom**: The ratio between the full and empty dots of the top plots, showing the fraction of non-triggered hits (i.e the hits that are lost) as a function of time.*

The charge information of the signals that are not triggered by CATIROC is not systematically lost thanks to the "charge acceptance" (see section 3.1). Thus, it is also necessary to compare the total number of PEs before and after the simulation of CATIROC. This notably allows to evaluate the possible impact on the energy reconstruction of the events. The results show that the fraction of PE lost over the five seconds of the burst simulated is 0.5%, 1.2%, 2.3% and 3.5% for CCSN at 10 kpc, 5 kpc, 3 kpc and 1 kpc, respectively. These numbers are very similar to the number of triggers lost that is expected since we have seen that ∼95% of the SPMTs have only 1 hit per event. As explained in section 3.1, CATIROC provides a second data stream, the Discriminator Data Stream (DDS), that has a smaller dead-time. The capability of the discriminator to distinguish two consecutive signals is not perfectly constant and depends on many parameters, including the discriminator threshold and the ABC firmware. It has been measured as being $<$ 30 ns. As a conservative hypothesis, an equivalent dead-time of ∼30 nanoseconds is set for this study. More information on the functioning of the CATIROC discriminator can be found in Ref. [231]. As for the QDS, the number of hits on a SPMT is compared to the number of triggers in the data stream. The results are shown in Figure 3.15. As expected, the fraction of non-triggered signal is smaller in the DDS. As previously explained, the triggers does not contain the charge information of the signals although the width of the discriminator output can be used as an estimator of the charge (see section 3.1.1). However, since the SPMTs work in photo counting regime, most of the signals will correspond to 1 PE.

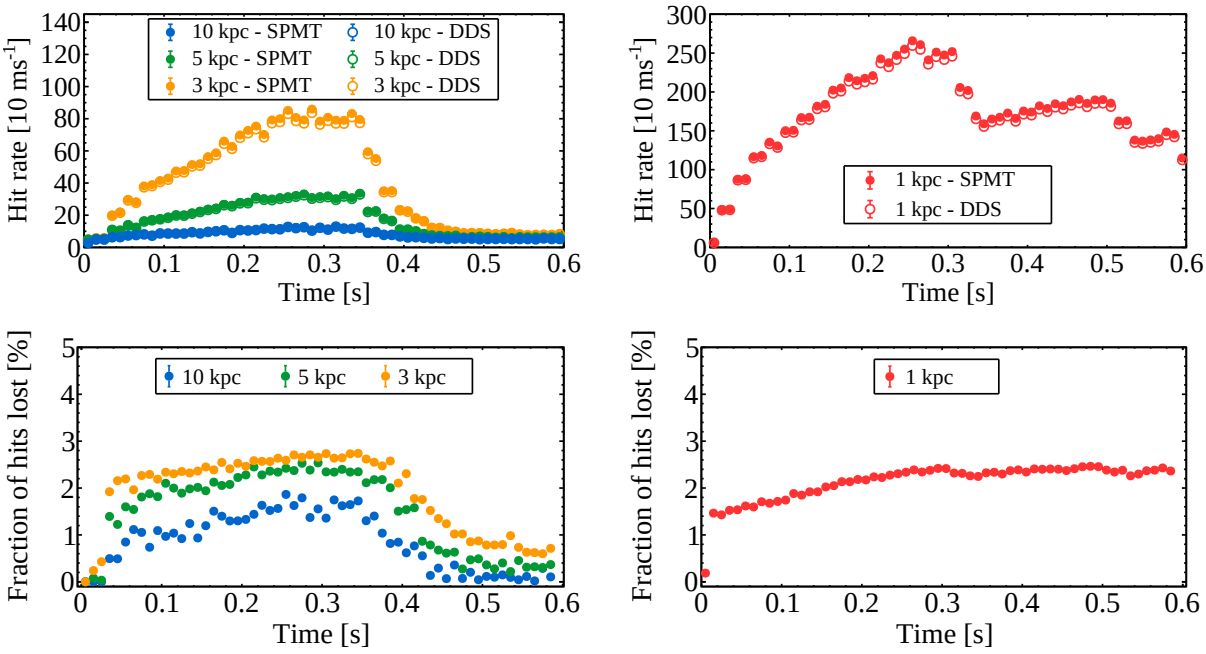

Figure 3.15: ***Top**: The SPMT hit rate (full dots) and trigger rate (empty dots) in the DDS for a single SPMT during the first 0.6 second of a CCSN neutrino burst for four different distances. The average rate is obtained over 25,600 SPMTs.* ***Bottom**: The ratio between the full and empty dots of the top plots, showing the fraction of non-triggered hits as a function of time.*

3.3.3 The data rate

During the regular data taking (no CCSN), the two PMT systems will continuously transfer the charge and time information (T,Q) to the DAQ while the LPMTs waveforms will only be transfered upon a request from the Global Trigger. The equivalent data throughput has been estimated to be ∼40 Gigabits/s [263]. In case of CCSN, the sudden rise of the event rate will cause a sharp increase of data and it is not guaranteed that the bandwidth between the GCUs and the DAQ will be large enough to keep tranferring them in real time. If not, the transfer could result in a substantial loss of data or in data corruption. In order to avoid such a problem, the front-end electronics of the two PMT systems contain DDR memory spaces where the data can be stored temporarily. Each of the 200 ABC boards of the SPMT system is equipped with 1 Gigabyte (GB)[3] Dual Data Rate (DDR) memory space and each GCU provides an additional 2 GB. Then, in case of CCSN, the data shall be transferred to the DAQ at an acceptable rate, preventing any loss. A study of the total amount of data has been performed, initially with the aim of dimensioning the DDR during the ABC design. This study is reported with the latest version of the SPMT data format[4] to confirm that the storage space available is enough. Then, in the continuity of the results presented in the previous section, the data rate produced by the SPMT system during a CCSN neutrino burst is estimated. Then, the total amount of data is calculated and compared to the space available.

The FPGA embedded in the ABC board handles the packing and transferring of the data to the DAQ. The different elements of the data format as well as the information that each of them contain are arranged as the sketch in Figure 3.16. The 128 channels are split into 16 blocks. Each block contains 8 channels so that there are two blocks per CATIROC. Each time that a signal is triggered, a time window of 37 nanoseconds is opened and the information about all the triggers are packed. Each data block has three main parts:

1. A Block Header (BH) of 8 Bytes that contains the block ID, the event type (QDS or DDS), the number of channels hit, the number of coarse time cycle etc.
2. An Event Channel Data (ECD) or DDS Channel Data (DCD) (according to the trigger type) of 8 Bytes that contains the information by channels, e.g. the channel number, the time and charge information, the pre-amplifier gain mode and its value etc. For any event in the QDS packed in the ECD, the corresponding event in the DDS is packed in the DCD.
3. A Block Trailer (BT) of 8 Bytes used to ensure that all the information is transfered. It will also include debug information.

If one of the channels of the block triggers two signals within the 37 nanoseconds, the current BH is closed, a new 37 nanoseconds time window is opened with new BH, BT and ECD. It is worth mentioning that an additional header will be added by the GCU each time that data will be transferred to the DAQ. This header will include, among others, the absolute time stamp as well as the GCU ID. It has not been taken into account in this work.

Given the dead-time of CATIROC, it is impossible that the QDS of a channel contains two consecutive hits separated by less than 60 nanoseconds. Thus, in order to simplify the computation of the data rate, the 5 seconds of CCSN neutrino signal are divided into windows of 37 nanoseconds for each of the 16 blocks and the amount of data within each of them is computed. Even though the dead-time of the discriminator is inferior to 37 ns

[3] 1 Byte = 8 bits

[4] May 2022

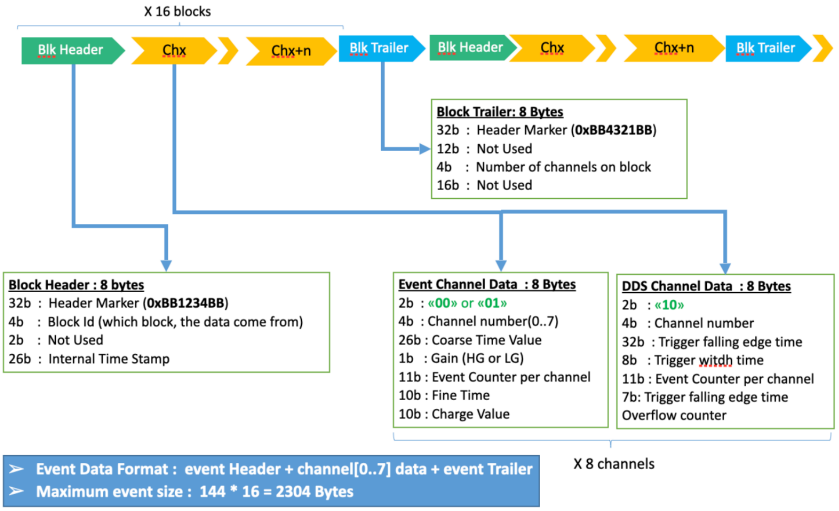

Figure 3.16: *Sketch of the data format of the ABC [264]*

(set at 30 ns for this analysis), the data from the DDS are counted in the same way. Given the weak probability that two consecutive hits are separated by less than 37 nanoseconds, it is assumed that such approximation has a negligible impact on the calculation of the amount of data. The data thoughput from a single ABC as a function of time – for the first 0.6 second of the burst – is shown on the top plots of Figure 3.17. As the hit rate on the SPMTs presented in the previous section, the data rate increases sharply during the first hundreds of miliseconds of the burst and then stabilises. It reaches 0.65 Megabyte (MB)/50 ms (13 MB/s) at 10 kpc, 2.3 MB/50 ms (46 MB/s) at 5 kpc, 6.9 MB/50 ms (138 MB/s) at 3 kpc and 20.8 MB/50 ms (416 MB/s) at 1 kpc. These data flow are of the order of the maximum data transferring throughput between a single ABC and the DAQ that is of ∼0.5 Gigabit/s (65.2 MB/s). A first important conclusion that can be made here is that it would certainly be preferable to store the data in the DDR memory space available on the ABC (1 GB) and on the GCU (2 GB) before tranferring it to the DAQ. The bottom plots of Figure 3.17 shows the cumulated data – also for a single ABC – along the burst duration. After 5 seconds, the total amount of data produced by 1 ABC reaches ∼292 MB at 1 kpc, far below the aforementioned storage space available in each UWB.

3.4 Event builder

At the level of the DAQ, the SPMT and LPMT data that are correlated to the same Global Trigger are packed into a single event (based on their timestamp) by the DAQ event builder and are sent to the IHEP servers (ethernet, 1 Gigabits/s). At the time of this PhD thesis, the strategy is to temporally stored all the data – for 15 days – in the DAQ storage disks (∼100 TBytes available). The DAQ storage disks have two advantages. First, since it is not guaranteed that the bandwidth between the DAQ and the IHEP servers will be sufficient for a real-time tranfer of the data during a CCSN event, storage of the data at the DAQ level prevents from any data corruption or loss in case of overflow. Second, in the current event building strategy when an event is triggered, 1 µs of signal is captured and packed [263]. This is called the *readout window* in the following. It has been established according to the typical event signal length in JUNO as well as the event rate that is expected to be $\mathcal{O}$(100 Hz). However, depending on the distance to the CCSN, the event rate could increase up to the MHz. In such case, it is likely that

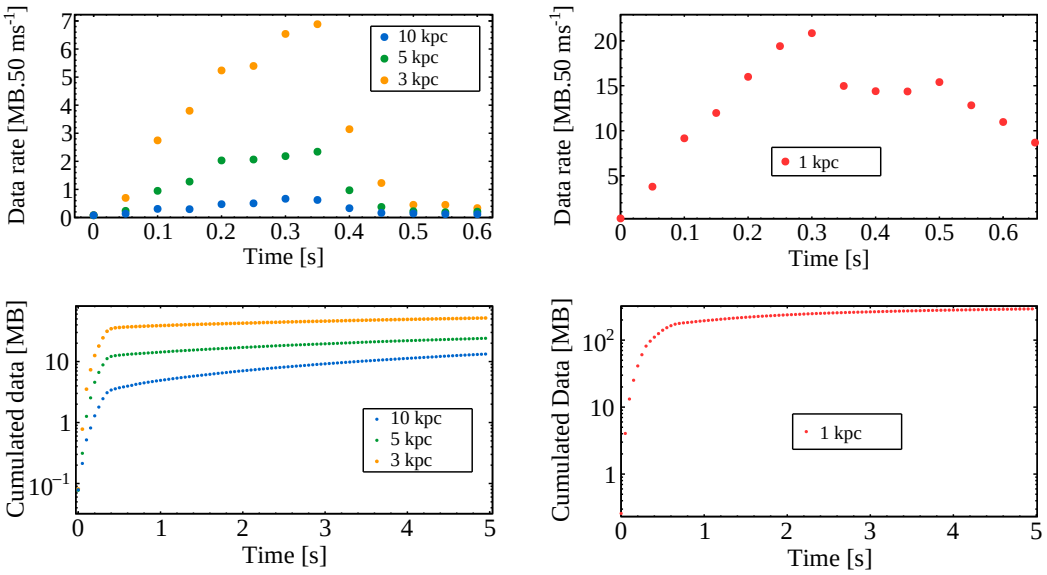

Figure 3.17: ***Top**: Example of the data throughput of a single ABC as a function of the time for the first 0.6 second of the burst. **Bottom**: The cumulated data of a single ABC against the time for the 5 first seconds of the burst.*

several events occur within 1 µs, meaning that the current event building strategy would pack several events in the same readout window. In such case, several events would be reconstructed as one, degrading the reconstruction quality. Thus, the storage of the data in the DAQ disks provides the opportunity to build the events *offline*, once the CCSN event is established. In this context, the event pile-up for CCSN at different distances has been studied, a preliminary offline event builder for the SPMT system has been developed and its performance has been evaluated. This work has been done by analysing the same simulation files than in the previous section (Nakazato model, mass = 30 $M_{\odot}$, revival time = 300 ms, metallicity = 0.02) since they represent the most extreme cases in terms of event rate.

3.4.1 Event pile-up

In this manuscript, the event pile-up is defined as the overlap of the scintillation photons time distribution of two (or more) consecutive events. To evaluate if consecutive events are piled-up, the events are sorted in time according to their first hit time. Then, the last hit time of each of the events is compared to the first hit time of the event that comes right after it. This is done at the detector simulation level, before the electronics and event building. A cluster of two or more events that are piled-up is called a *pile-up event* in the following. The simulation showed that the fraction of the events that are part of pile-up events is ∼2.5% at 10 kpc, ∼7.9% at 5 kpc, ∼17.6% at 3 kpc and ∼45.3% at 1 kpc. The distribution of the number of events per pile-up event for the different distances is shown in Figure 3.18.

As the distance to the CCSN decreases, the average number of events per pile-up event increases. To summarise, for CCSN farther than or equal to 3 kpc, more than 80% of the pile-up events include only two events. When the distance is 1 kpc, this number reduces to ∼55% and ∼40% of the pile-up events have three or more events interwinded with each other.

The current event building strategy – described in introduction of this section – con-

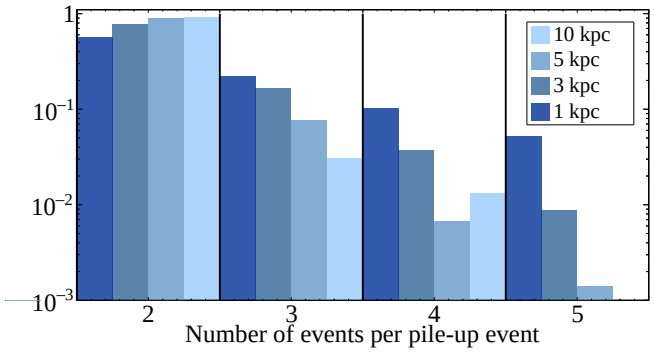

Figure 3.18: *The number of events per pile-up event for four different distances to the CCSN. The histogram are normalised to their number of entries.*

structs the events using the time information, the readout window is 1 µs. The Figure 3.19 shows the distribution of the time seperation (δT) between the first hit time of consecutive events that are piled-up. For the four distances studied, ∼95% of the δT are inferior to 1 µs, meaning that very few events involved in pile-up would be built separately with the current event building strategy. It is also important to note that the Figure 3.19 shows that a small fraction of the events that are piled-up have a time separation δT of several microseconds. This happens for events for which the scintillation photons time distribution has a very long tail and that superimpose with the events that comes after it. In such cases, the 1 µs window is sufficient to build the events separately.

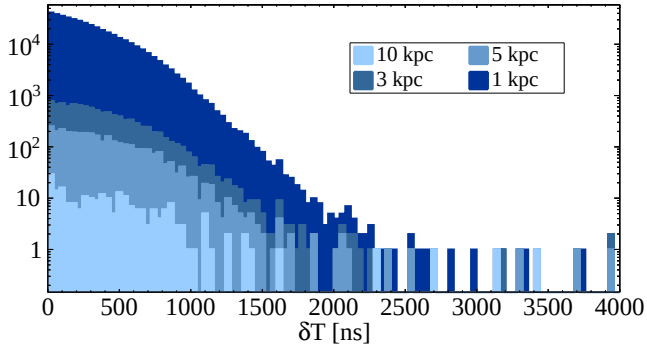

Figure 3.19: *The distriubtion of the δT for four different distances to the CCSN.*

The Table 3.2 summarises the information about the event pile-up presented in this subsection. It also provides the number of IBD separately. Indeed, a very small fraction (∼0.1%) of them have a neutron capture time that is inferior to the prompt signal duration. As a consequence, the prompt and the delayed signals are piled-up. These IBDs contribute to the total number of pile-up events given in the table. The value of δT at 1σ of the distribution is also given.

3.4.2 High-level trigger optimisation

Before being built, the events must be identified in a continuous stream of data. The event builder presented here identifies the events in the QDS from the signals of the 25,600 SPMT channels. For an event to be built, the number of triggers in a time interval must exceed a certain threshold, typically the expected value from background (Dark Noise (DN)). The search for events in the data stream is based on a sliding window method whose principle

Distance	10 kpc	5 kpc	3 kpc	1 kpc
Num. evts (doubles are split)	∼18,500	∼73,200	∼204,200	$\sim 1.5 \cdot 10^6$
Fraction of piled up events	∼2.5%	∼7.9%	∼17.6%	∼45.3%
Num. IBD w short n capt. time	11	73	216	792
$\delta T_{1\sigma}$	∼540 ns	∼460 ns	∼420 ns	∼340 ns

Table 3.2: *Information on event pile-up for different CCSN distances. The first row gives the total number of events considering that the IBD, $\bar{\nu}_e - {}^{12}C$ and $\nu_e - {}^{12}C$ interactions include two signals. The number of IBD with a neutrino signal arriving before the end of the prompt one is given in the third row.*

is shown in Figure 3.20. The number of triggers within a time window is counted. If it exceeds the threshold, the event is constructed. Otherwise, the sliding window is shifted to the next trigger in the QDS and the number of triggers in the time window is counted again etc.

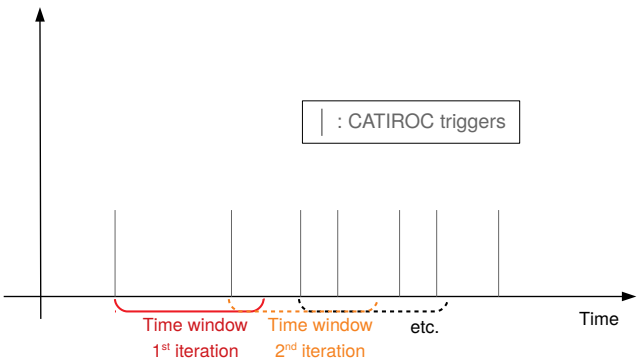

Figure 3.20: *A sketch of the sliding window method that is used to identify an event in the continuous stream of data.*

This event builder is designed to trigger on the neutrino interactions – referred to as the *signal* in the following – without triggering on the dark counts – hereafter *background* – that constitute the baseline noise of the data stream. For this reason, the optimal combination between the threshold and the time window length must be determined. The signal events are taken from a typical simulation file presented in section 3.3.1. The background events consist in 2 µs long clusters of dark counts from the 25,600 SPMTs. The DN rate of each SPMT is randomly picked up from a distribution based on experimental measurements [213]. For each configuration the trigger efficiency is computed as the ratio between the number of events triggered over the total number of simulated events. The time window varies from 5 to 1200 nanoseconds in steps of 5 while the threshold ranges from 1 to 40 triggers in steps of 1. The results are shown in Figure 3.21.

The average visible energy of the CCSN events is ∼10 MeV but the νpES event channel populates the low energy range (< MeV). The average number of PE for this channel, that corresponds to the number of triggers as a first approximation, is about 9 with a median of 5 (dark counts excluded), explaining that a lot of configuration – except those with a very low threshold – does not allow to trigger 100% of the signal events. Since the dark counts are uniformly distributed over time, the threshold that allows not to trigger on the background events increases linearly with the time window length. The next step is to

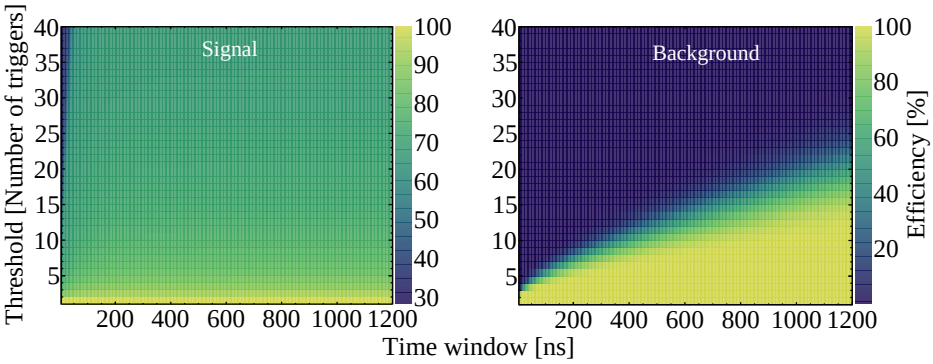

Figure 3.21: ***Left**: Map of the trigger efficiency using the sliding window method on the signal events for different conbinations of threshold and time windows. **Right**: The same plot than the left one but for DN events.*

find the combination that maximises the signal over background:

$$R = \frac{S}{S+B} \tag{3.6}$$

where S is the trigger efficiency for the signal and B is that for the background. This ratio is computed for all the configurations and the one with the highest R is considered the optimal (Figure 3.22). The combination that maximises R is the one with a threshold of 11 triggers and a time window length of 115 ns. In such case, $R = 99.93\%$. The same study is done by counting the number of SPMTs fired instead of the number of CATIROC triggers. The same optimal configuration is found (11 SPMTs fired within 115 nanoseconds), which is expected since we have seen that most of the SPMTs have one hit per event.

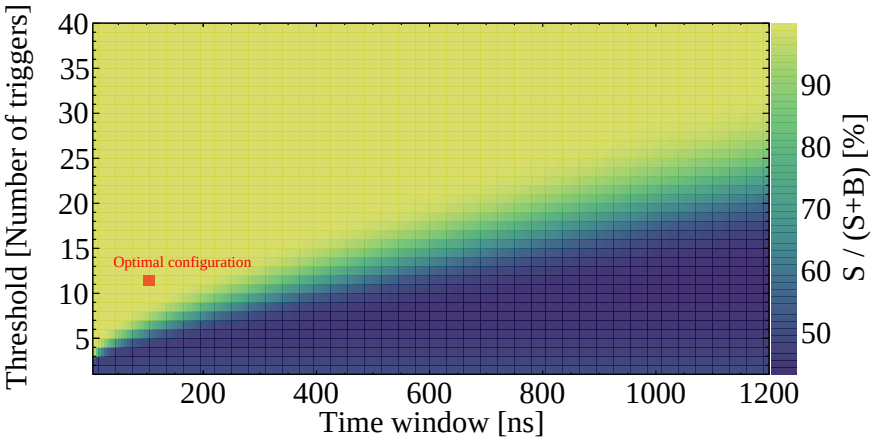

Figure 3.22: *Map of the R for the different combinations of threshold and time window. The one that maximises R is indicated by the red square: 11 triggers within 115 ns.*

The trigger efficiency of the event builder is then explored for the different interaction channels. A particular attention is brought to the IBD that is the golden channel for JUNO. Each event is tracked from the CCSN event generator to the event builder level. This work is realised for a 10 kpc away CCSN and results are presented in Table 3.3. The first column gives the number of events for each channel at the CCSN generator level. For some channels, especially the IBD delayed signal and νpES, the number of events decreases after the detector simulation. It corresponds to events with a very small visible

energy so that eventually, no hits are registered on the SPMTs (finite acceptance). The right most column shows the efficiency of the event builder, after the electronics simulation and the event builder are ran. The dark noise is simulated for each event. As mentioned previously, the trigger efficiency for the νpES channel is very low, hence $\sim$23% of the events are triggered. The efficiency for the other channels is $> 96\%$. A few delayed signals are not triggered because the visible energy is very low and only few hits are registered by the SPMT system. The loss of events that are involved in pile-up is not considered in this table and is studied later on.

ν-channel	Generator	Detector	Electronics + Event Builder [No pileup]
IBD Prompt	5125	5125	5125 (100%)
IBD Delayed	5125	5103	5062 (98.7%)
pES	8220	6741	1964 (23.9%)
eES	350	350	339 (96.8%)
γ (from $^{12}C^{*}$)	505	505	497 (98.4%)
$\overline{\nu}_e + ^{12}C$ Prompt	143	143	143 (100%)
$\overline{\nu}_e + ^{12}C$ Delayed	143	143	142 (99.3%)
$\nu_e + ^{12}C$ Prompt	196	196	196 (100%)
$\nu_e + ^{12}C$ Delayed	196	196	196 (100%)

Table 3.3: *The number of events at the different simulation levels for the different interaction channels. The possible event pile-up is not taken into account here.*

This event builder can be used beyond the CCSN scope, i.e. for any physical event. For this purpose its trigger efficiency against the visible energy (E_{vis}) has also been studied, especially in the low energy range ($\sim$MeV) that is widely dominated by the νpES channel. The results are shown in Figure 3.23. The trigger efficiency is $\sim$50% at 0.4 MeV and reaches 100% at $\sim$0.8 MeV. For the sake of comparison, the current configuration of the Global Trigger – that also uses a LPMT multiplicity within a time window – has a trigger efficiency of 100% at 0.7 MeV and studies are ongoing to narrow it down at 0.5 MeV. The Multi-Messenger (MM) trigger is expected to lower the threshold at a few tens of keV (for astrophysics purposes) using more advanced techniques.

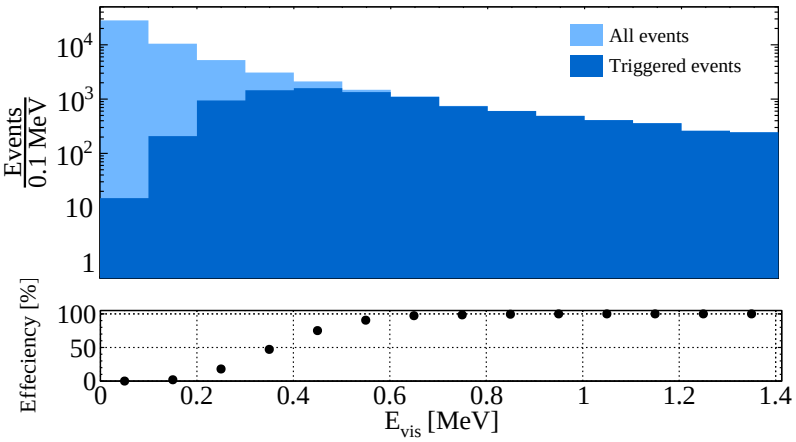

Figure 3.23: *The trigger efficiency of the event builder in the low energy range (0 - 1.4 MeV). The efficiency reaches 50% at 0.4 MeV and 100% at 0.8 MeV.*

3.4.3 Readout window optimisation

As mentioned previously, setting a readout window of 1 µs for building the triggered events implies that several events could occupy the same readout window in case of high event rate. A first solution to avoid this is to shorten the readout window. However, the readout window can only be shortened up to a certain point. Indeed, if the readout window length is too short, a fraction of the scintillation photon signal is lost, having negative impacts on the event reconstruction. For this reason, the quality of the event reconstruction against the readout window length has been studied. Part of this PhD thesis was dedicated to the development of vertex and energy reconstruction algorithms (see Chapter 4). The optimisation of the readout window shown here has been done using them. The start of the readout window is taken as the first trigger of each event. The quality of the vertex reconstruction at a given energy is evaluated by reconstructing several groups of ∼5000 positrons events with fixed visible energies (1.022 MeV, 4.022 MeV and 9.022 MeV) uniformly distributed in the detector. The difference between the reconstructed radius and the true one ($R_{rec} - R_{true}$) is plotted and a gaussian fit of this distribution gives the radial resolution (standard deviation) and the bias (mean). The $\tilde{\chi}^2$ of the fit is also shown. The Figure 3.24 shows the evolution of these three parameters (top to bottom) as a function of the readout window, for three visible energies (left to right).

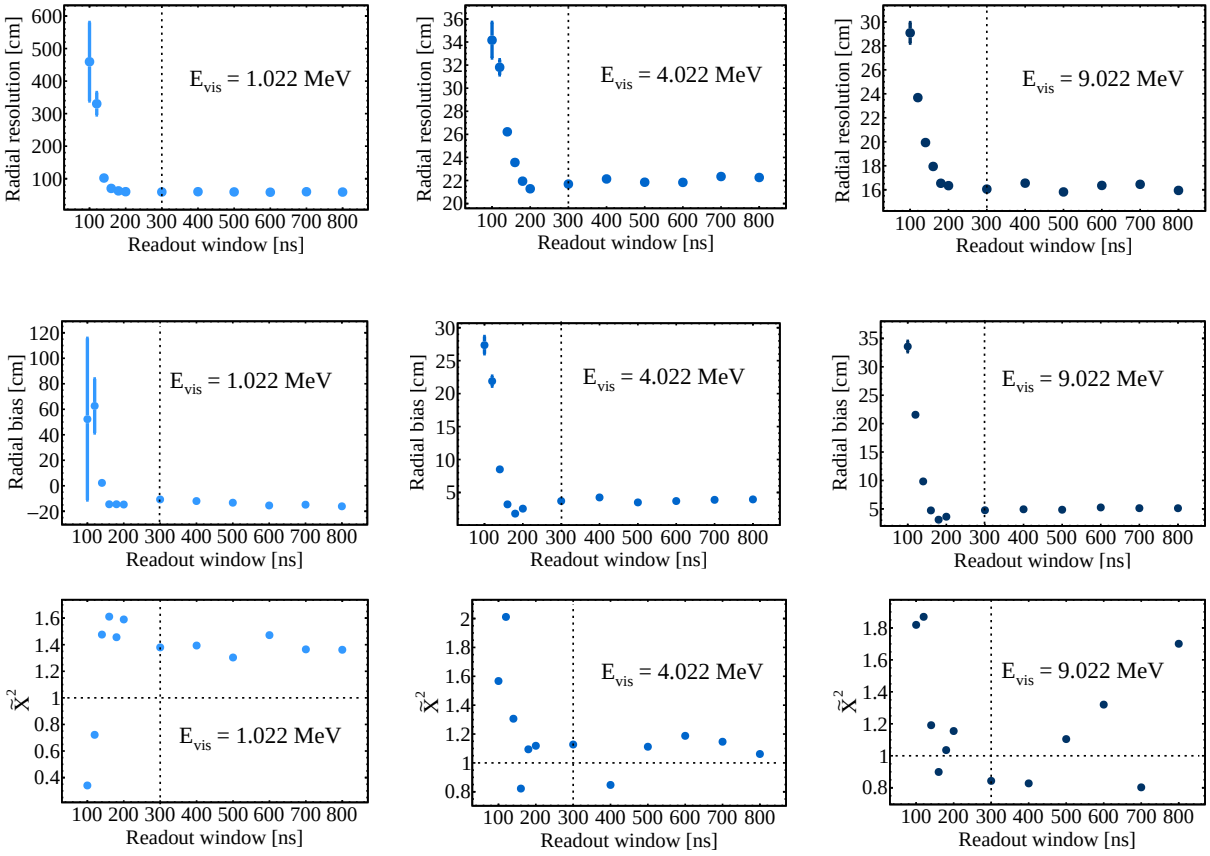

Figure 3.24: *The radial resolution (**top**), radial bias (**middle**) and gaussian fit reduced chi-square of the R_{rec} - R_{true} distribution (**bottom**) of the vertex reconstruction as a function of the readout window for three different energies.*

The results show that a readout window inferior to 200-300 ns degrades the radial resolution and bias as well as the quality of the fit. The fact that the $\tilde{\chi}^2$ tends to worsen as the readout window increases in the case E_{vis} = 1.022 MeV can be explained by the

low number of PE that makes the reconstruction quite unstable at such energy. More information and explanation can be found in Chapter 4. For readout windows superior to 300 ns, these quantities remain roughly constant. This study is also done for the energy reconstruction. The same quantities, that are determined by looking at the distribution of the difference between the reconstructed and true visible energy ($E_{rec} - E_{true}$), are evaluated. The results are shown in Figure 3.25. As for the vertex reconstruction, a readout window inferior to 200-300 ns degrades the reconstruction quality and the three quantities presented here remain roughly constant for readout windows superior to 300 ns.

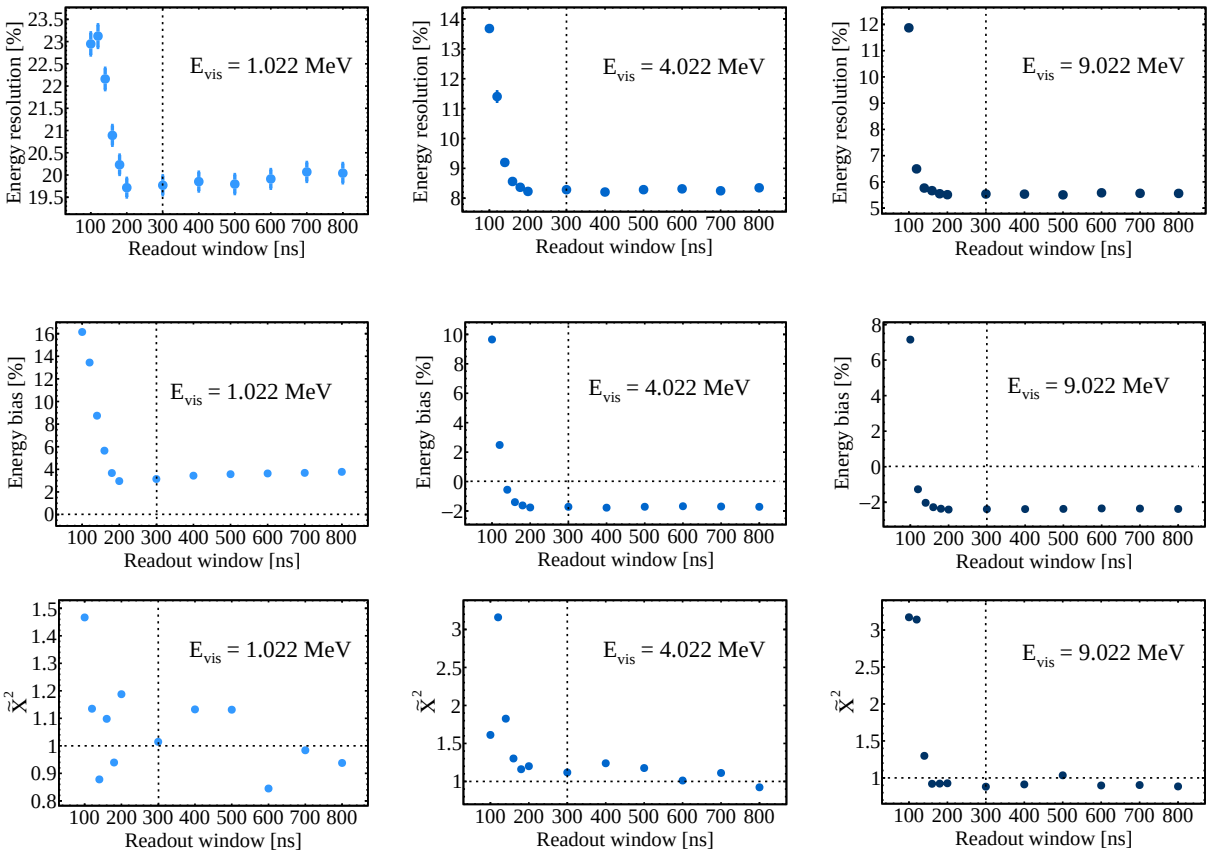

Figure 3.25: *The energy resolution (**top**), energy bias (**middle**) and gaussian fit reduced chi-square of the E_{rec} - E_{true} distribution (**bottom**) of the vertex reconstruction as a function of the readout window for three different energies.*

In the following, a 300 ns long readout window is taken as a conservative hypothesis in order to be sure that the reconstruction of some particularly short events would not be degraded. The performance of the event builder with such readout window is investigated in the next section.

3.4.4 Performances on piled-up event

In this section, the ability of the event builder to retrieve the events involved in pile-up is studied for CCSN at 10 kpc, 5 kpc, 3 kpc and 1 kpc. The performance is evaluated by means of confusion matrices that compare the true number of events to the number of events that are actually built. The left plot of Figure 3.26 shows the results for a 10 kpc away CCSN, the columns with a true number of events > 1 correspond to pile-up events.

In an ideal case, the true number of events and the number of events built should be the same so that such matrix should be diagonal. The pile-up being almost negligible at 10 kpc, only a small fraction of events are piling up. The right plot of Figure 3.26 shows the same confusion matrix but the content of each bin is the percentage of the total number of events in the column it belongs to. For example, over the total number of pile up events containing two events:

1. in 19.7% of the cases, the event builder reconstructs one event instead of two.
2. in 50.0% of the cases, the event builder reconstructs the two events.
3. in 27.8% of the cases, the event builder reconstructs three events instead of two.

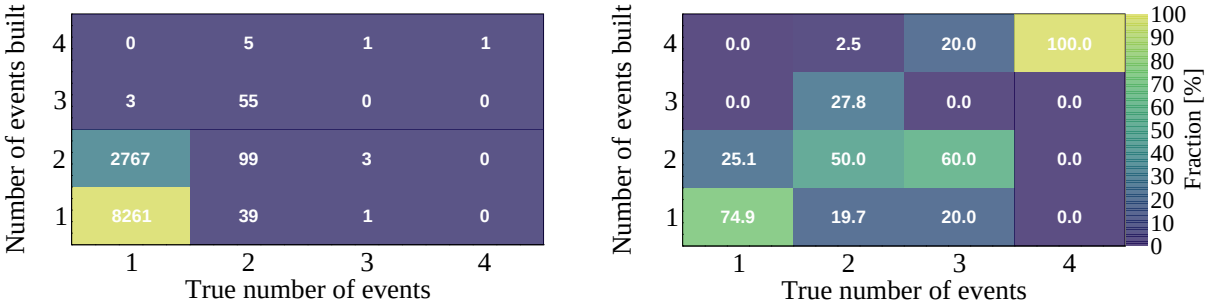

Figure 3.26: ***Left**: Confusion matrix between the number of events per pile-up event and the number of events actually built for a 10 kpc away CCSN. **Right**: As left figure but in percentage of the total number of events in the column.*

After the event builder indentifies an event and builds it, the search resumes right after the end of the freshly built event in the data stream. As mentioned previously, some events may have long signal tails. In such cases, it can happen that the event builder triggers again. This situation is illustrated on the left plot of Figure 3.27 and is called a *false trigger* in the following. The combination of threshold and time window that is used to obtained these results (11 trigger within 115 ns and 300 ns readout window) causes a significant number of false triggers. For example, in 2767 of the 11031 single events triggered, the event builder identifies a second event because of the long tail. The right plot of Figure 3.27 shows the distribution of the number of PE of the false trigger events, the mean is ∼28.5 PEs and the median is ∼12 PEs which is relatively low in comparison to the typical number of PE for the CCSN events. Thus, these events can then be rejected later in the analysis by applying a cut on the number of PEs. The consequences of such cut on the higher level analyses are investigated in Chapter 5. If needed, the number of false triggers can be reduced by increasing the trigger threshold of the event builder. The drawback would be a smaller trigger efficiency for the physics events with low visible energy. Finally, the fraction of events involved in pile-up that are actually retrieved can be determined by summing the three upmost bins of the second column (Figure 3.26, right). In the case at 10 kpc, ∼80% of the events involved in pile-up are retrieved.

The same analysis is done for the case at 5 kpc, 3 kpc and 1 kpc and the results are presented in Figure 3.28. Due to lack of statistics in the other columns, we only focus on the two first ones (single events and pile-up events containing two events). The tendency observed at 10 kpc is confirmed for 5 kpc and 3 kpc. That is, the proportion of false triggers remains roughly constant and ∼75% of the events involved in pile-up events (true number of events > 1) are retrieved. For the case at 1 kpc, where enough statistics is available in all columns, the performance start to degrade. For example when the true number of events is 2 (second column), both events are retrieved in only ∼65% of the

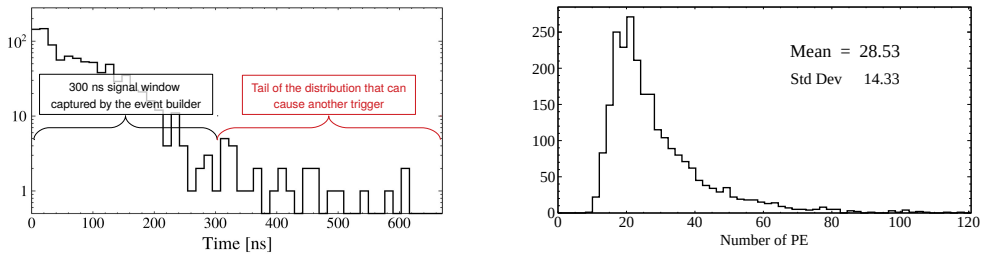

Figure 3.27: ***Left**: Example of an event for which the first 300 ns of the signal are recorded by the event builder. A second event is recorded (false trigger) because the number of triggers of the signal tail (signal + dark counts) exceeds the threshold.* ***Right**: The distribution of the number of PE for the false triggers. The mean is ∼28.5 PEs and the median is ∼12 PEs.*

case. Moreover, the results show that the ability of the event builder to retrieve the correct number of events gets worse as the multiplicity increases. This is expected since the higher is the multiplicity in a pile-up event, the shorter the time seperation between them.

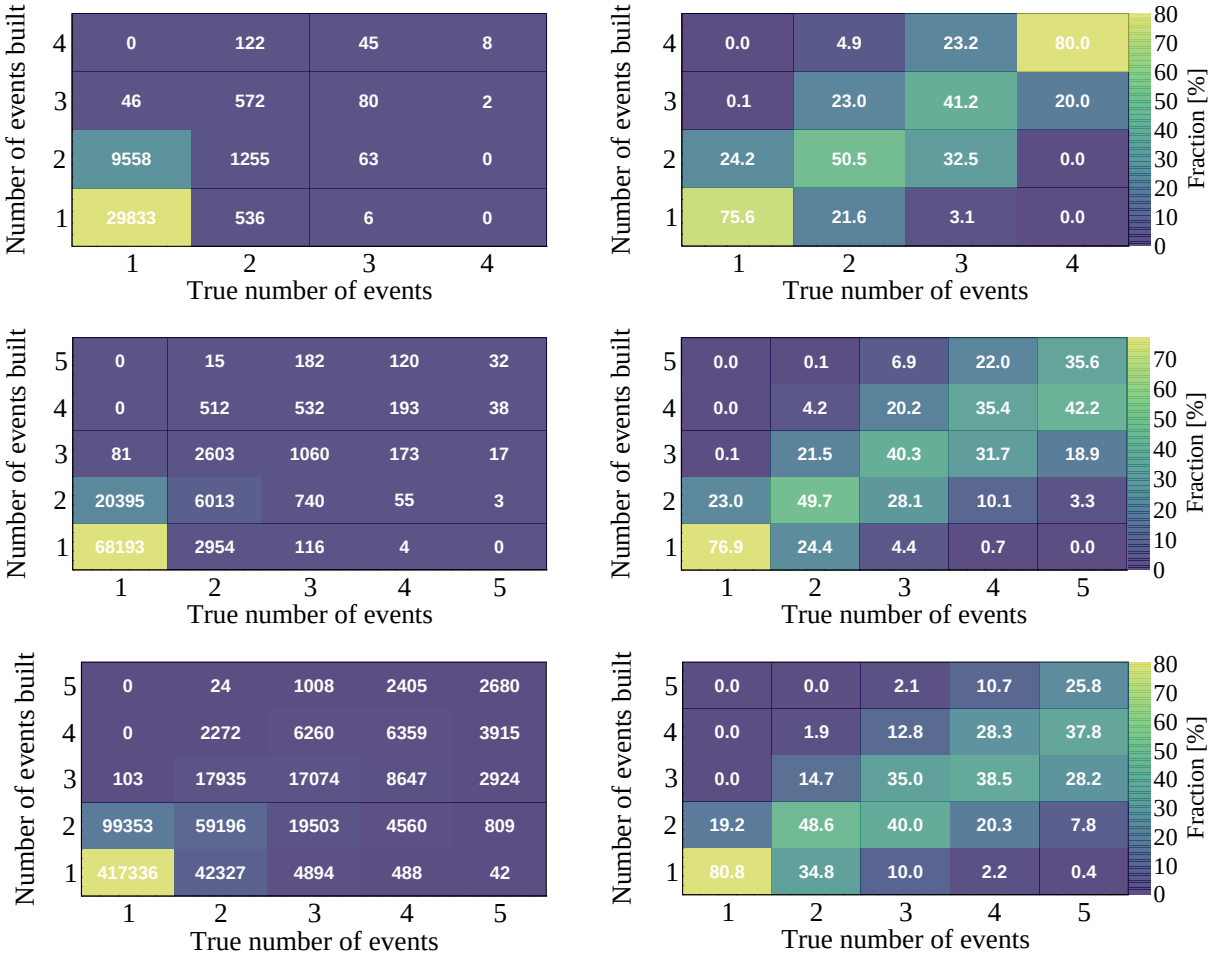

Figure 3.28: *The same confusion matrices as in Figure 3.26 for the case at 5 kpc (**Top**), 3 kpc (**Middle**) and 1 kpc (**Bottom**).*

As demonstrated above, the event builder presented here does not allow to build all

the piled-up events separately, particularly if they are too interwined. The first limitation comes from the intrinsic event time scale of a liquid scintillator detector of the size of JUNO, which is $\mathcal{O}(100$ ns). The simulation shows that many events that are piled-up are separated by a few tens of nanoseconds and it is then impossible to build them independently by using only the time information. The Figure 3.29 shows the distribution of the 3D spatial distances between events that are piled-up. For all the distances, the distributions show that there is no strong spatial correlation between them. The position of the fired PMTs of each event could represent an additional information to properly build the events occuring very close in time but distant in space.

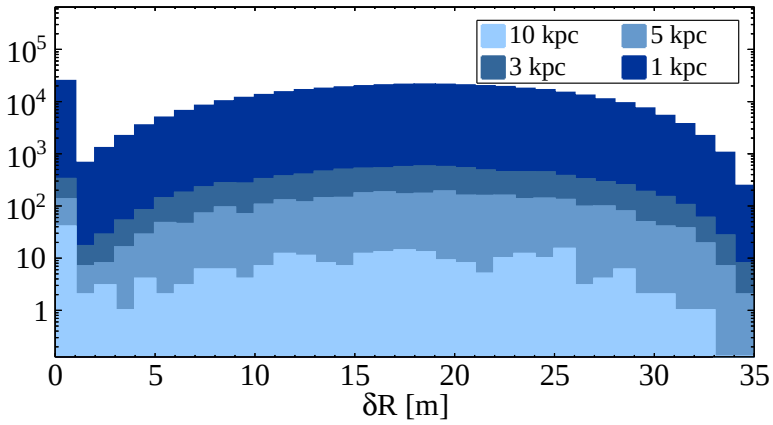

Figure 3.29: *The 3D spatial distance between consecutive events that are piled-up.*

Summary

This chapter presented different contributions made at different levels of the SPMT system. First, a faster charge calibration of CATIROC has been proposed and validated for the ABC mass test production. Its major advantage is a reduction of the number of calibration runs required by a factor four without degrading the precision of the calibration compared to the standard method. The second part of the chapter focused on the SPMT system rate capabilities (based on simulation data) during a CCSN neutrino burst. Particular attention was brought to the impact of the dead-time of CATIROC on its trigger capability. The study showed that up to 8% of the signal can be lost within 10 ms for a nearby CCSN (1 kpc), when the event rate reaches its maximum. However, the number of non-trigger hits and charge lost during the burst both are $< 5\%$, whatever the distance is. The resulting data rate has been computed using the latest version of the ABC data format. The results showed that in case of CCSN, it would be preferable to automatically store the data in the DDR memory available on each board whose storage space is more than sufficient event for a CCSN at 1 kpc. At this point, a first conclusion that can be made is that the readout electronics of the SPMT system and its data format should allow it to completely handle a CCSN explosion at a distance beyond or equal to 1 kpc. This chapter also introduced an event builder designed for the reconstruction of events ($E_{vis} > 1$ MeV) with the SPMT system. It searches for clusters of trigger from CATIROC to identify the events in the continuous stream of data. Its performance is studied, paying a particular attention to its capability to build separately the events that are piled-up. For distances ≤ 3 kpc, it retrieves ~70-80% of the events, but the performance degrades for a 1 kpc away CCSN for which this number goes down to ~55%. The events that are too much interwined cannot be built separately by using only the time information, more avanced techniques would

be required. The impact of CATIROC and of the event builder on the CCSN neutrino events detection are further studied in Chapter 5 that focuses on the event selection and neutrino energy spectrum unfolding.

Chapter 4

Event Reconstruction with the SPMT system

Contents

In a detector such as JUNO, any prompt emission of light due to the interaction of a charged particle with the LS molecules is called "event" (Figure 4.1). The *reconstruction* consists in using the information provided by the detector in order to determine some physical observables about this event. This task is the preliminary step to any physics analysis. In JUNO, four different types of reconstruction are needed:

1. The *waveform reconstruction* that consists in retrieving the time and charge information from the PMTs output signals.
2. The *vertex reconstruction* that consists in determining the position of a point-like event in the detector.
3. It happens that particularly heavy and energetic particles, such as muons, interact in the detector and produce light along a several meters-long track. For such events, the *track reconstruction* consists in determining the direction of the track.
4. The *energy reconstruction* that consists in determining the energy deposited during an event (point-like or track-like).

The present chapter focuses on the reconstruction of the vertex and the energy of point-like events using only the information provided by the SPMT system[1]. Indeed, as mentioned earlier, part of the physics goals of JUNO can be achieved by using both PMT systems independently of each other. It is therefore essential to develop reconstruction algorithms that use one or the other system. Furthermore, at the beginning of this PhD thesis, no reconstruction algorithms dedicated to the SPMT system existed. Part of the work realised consisted in the development and testing of such algorithms that are necessary to perform analyses on the CCSN neutrino signal. Since the detector is under construction, the development has been realised using data from the official JUNO simulation software. This chapter is divided into two main parts. The first one focuses on the vertex reconstruction algorithm (section 4.1). Its structure is described together with its performance in both reactor and CCSN neutrino energy ranges. The second part focuses on the energy reconstruction (section 4.2). The strategy adopted is detailed and the performance is studied for both reactor and CCSN neutrino energy ranges are presented.

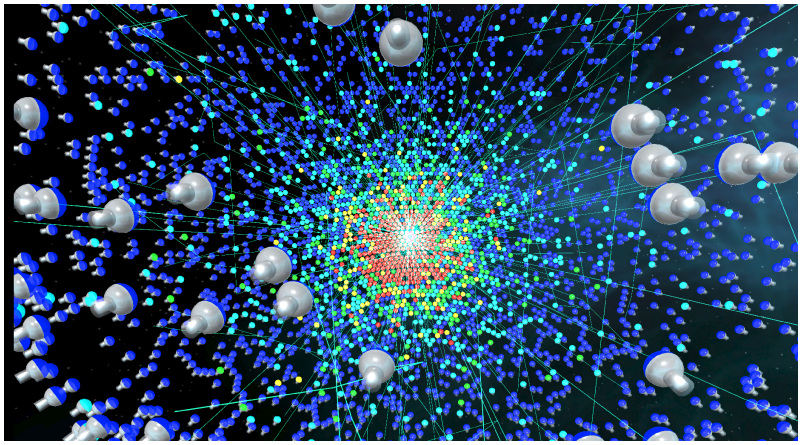

Figure 4.1: *A positron event displayed in the JUNO Central Detector. The white spot is the event vertex and the thin lines represent the trajectory of the scintillation photons. The color scale from blue to red symbolises the number of Photoelectron (PE) of each PMT.*

4.1 Vertex Reconstruction

The determination of the neutrino oscillation solar parameters (θ_{12}, Δm^2_{21}) and the study of the CCSN neutrino signal will be based on the reconstruction of the neutrino energy spectra. In a detector as large as JUNO, the amount of light collected - on which the energy estimation is based - strongly depends on the position of the emission point (detector Non-Uniformity (NU), see section 4.2.3.2). If this dependence is not properly taken into account, errors are made on the estimation of the energy and the energy spectra are eventually distorted. The determination of the position of the events is then critical in order to correct for the detector NU in the energy reconstruction process. In addition, both of the aforementioned physics analyses will require a rigorous IBD candidate selection, based on a spatial and temporal coincidence between two signals within specific energy ranges (section 2.1.1.3). The vertex reconstruction is then crucial to fully exploit the IBD events topology during the event selection. Knowing the position of the events is also useful for optimising the Fiducial Volume (FV), among many other use-cases. This section

[1]This work led to the drafting of two internal notes that were shared with the entire JUNO collaboration.

is divided into seven subsections. The first three introduce the experimental context as well as the concept of *time of flight*, necessary for the time-based reconstruction. The three following parts describe the three different reconstruction methods that have been tested together with their performance. The final part briefly present the performance of the algorithm for IBDs in a energy range up to ∼80 MeV which includes both reactor and CCSN $\bar{\nu_e}$.

4.1.1 Experimental context

Due to the small size of the SPMTs bulb (3") and the large size of the CD, the SPMT system produce ∼40 Photoelectron (PE)/MeV and works in the photo-counting regime. For instance, for 10 MeV positron events, ∼95% of the SPMTs fired produces only 1 PE. The SPMT system benefits from a good time resolution. In fact, the time resolution of the SPMTs - referred to as the Transit Time Spread (TTS)[2] - is of ∼1.6 ns (1σ) [213]. Such a value is small before the time scale of the events in JUNO (several hundreds of nanoseconds), hence the SPMTs provide an accurate information on the timing of the scintillation photons. Then, the time measurement of the SPMTs output signals is operated by the CATIROC readout chip [231] with a precision of a few hundreds of picoseconds (see Chapter 3). This measurement is smeared by the intrinsic "time walk" of the chip that can be modeled as a gaussian with a standard deviation that goes up to ∼0.6 ns and that decreases with the amplitude of the input signal. Nevertheless, the accuracy remains satisfactory. To summarise, the SPMTs charge information will be poor – in the MeV and tens of MeV energy range – and the vertex reconstruction will mainly rely on the precise timing of the scintillation photons.

4.1.2 Time of flight

The use of the time information for vertex reconstruction requires the calculation of a *residual time*. The residual time is computed from the time of flight of the scintillation photons between the vertex and the PMTs and their hit time on the PMTs, assuming that the energy deposition is *point-like*. Such calculation is necessary to make the reconstruction independent of the event location. The residual time can be generally expressed such as:

$$t_{res} = t_i - tof - t_0 \tag{4.1}$$

where t_{res} symbolises the residual time, t_i is the scintillation photon hit time on the PMT, tof is the time of flight and t_0 is the time of interaction of the particle (i.e the time at which the scintillation photons are emitted). The estimation of t_i is not trivial because of the fluctuations induced by the instrumentation (PMTs, readout electronics etc.). Thus, t_i can be expressed as follows:

$$t_i = t_{RO} - t_{tt} - t_{elec} \tag{4.2}$$

where t_{RO} is the time at which the signal was digitised by the readout electronics, t_{tt} is the PMT transit time (i.e the time it takes to the PE pulse to go from the cathode to the output of the PMT) and t_{elec} the readout electronics time processing. Then, equation 4.1 can be rewritten as:

$$t_{res} = t_{RO} - t_{tt} - t_{elec} - tof - t_0 \tag{4.3}$$

[2]The TTS is defined as the temporal fluctuations of the PE to go from the photocathode to the output of the PMT (see section 2.2.2.2)

The values of t_{tt} and t_{elec} are not known with absolute precision. The value of t_{tt} is $\sim$10 ns in the simulation and its fluctuations are of 1.6 ns (σ) [213] while the value of t_{elec} is dominated by the time walk of CATIROC and is estimated to be $\sim$5 ns with fluctuations up to 0.6 ns (σ) [231, 265], as mentioned in section 4.1.1. These spreads eventually degrade the estimation of t_i and consequently the accuracy of the vertex reconstruction. More information about the computation of the t_0 are given in section 4.1.5. The computation of the tof is also non trivial. Indeed, during their travel, the scintillation photons undergo different physical processes. The three main ones being:

- The absorptions and re-emissions by the bis-MSB molecules contained in the LS. The location of re-emission can be slightly different from the absorbtion one. It is at most of the order of the size of a few molecules ($\sim \mu m$) which is negligible before the size of the detector.
- The Rayleigh scatterings off bound electrons of the LS molecules as well as the Mie scatterings from dirt and dust particles in the LS.
- The reflections and refractions of the scintillation photons at the interfaces between the different detector parts with specific refraction indices (LS, acrylic sphere, water buffer, PMTs bulbs...)

These different processes contribute to make the path of the scintillation photons chaotic and induce fluctuations in the time of flight. A previous work within JUNO [266] showed that it is still reasonable to assume that the scintillation photons path follows a straight line. Thus, their time of flight can be determined such as:

$$tof = \sum_n d_n / c_n \tag{4.4}$$

where the sum runs over media with different refractive indices, d_n is the distance traveled and c_n is the speed of light. In this work, two different media are considered for the computation of the time of flight: the LS contained in the acrylic sphere (refractive index $\sim$1.5 [267]) and the water that separates the acrylic sphere and the PMTs (refractive index $\sim$1.3 [268]). One can determine the distance traveled in each of them by using the geometrical model showed in Figure 4.2 [266]. To do this, the angle δ between the vertex and the center of the CD is determined using the generalised Pythagore theorem [269]:

$$\delta = \arccos\left(\frac{d^2 + R_{PMT}^2 - ||\vec{r_0}||^2}{2 \times d \times R_{PMT}}\right) \tag{4.5}$$

where d symbolises the distance from the vertex to the PMT (equivalent to $d_{LS} + d_{water}$ in Figure 4.2), R_{PMT} is the position (radius) of a PMT and $\vec{r}_0$ is the position of the vertex in cartesian coordinates (X, Y and Z. see Figure 5.23 (Appendix) for the coordinates convention used in this manuscript).

The part of the path travelled in the LS and water can be derived using the value of δ and by solving trigonometric equations. The thickness of the acrylic sphere ($\sim$12 cm) and of the PMTs bulbs are neglected in this computation since they are small compared to the size of the CD (35.4 meters) and water buffer (1.4 meter). In addition, the refractive indices of the LS and acrylic are similar [270] hence the reflections and refractions at the interface are considered negligible before that at the acrylic and water interface. Finally, the time of flight is computed such as:

$$tof = \sum_n d_n / c_n = d_{LS} \times \frac{n_{LS}}{c_{vac}} + d_{water} \times \frac{n_{water}}{c_{vac}} \tag{4.6}$$

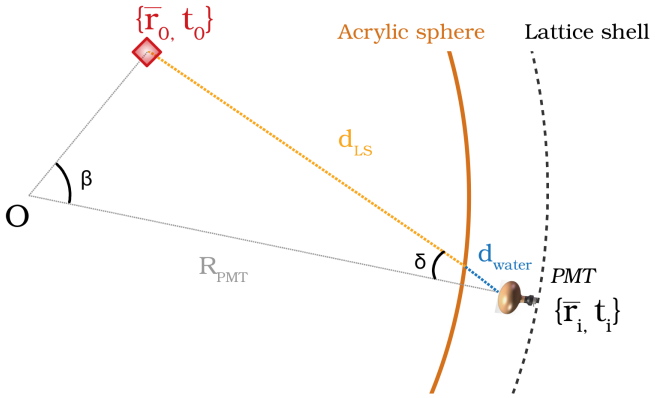

Figure 4.2: *Geometrical model used to determine the time of flight of the scintillation photons from the vertex to the PMTs. The red diamond represents an event vertex at a time t_0 and a position $\vec{r}_0$ in the CD, β and δ are angles, R_{PMT} is the position (radius) of the PMTs, $\vec{r}_i$ and t_i are the coordinates and the photon hit time on the i^{th} PMT, respectively. Finally, d_{LS} and d_{water} are the path lengths of the photon in the LS and water, respectively.*

where c_{vac} is the speed of light in vacuum (299.792 mm/ns), n_{LS} and n_{water} are the refractive indices of the LS and water, respectively. As investigated in Ref. [267], the speed of the scintillation photons slightly depends on their wavelength. This is taken into account in the computation by introducing *effective* refractive indices. The indices used for the results presented in this chapter are: $n_{LS} = 1.538$ and $n_{water} = 1.373$ [266].

4.1.3 The Total Reflection area

This section briefly introduces the aforementioned reflections and refractions that the scintillation photons can undergo at the interface between the acrylic sphere and the water buffer. Let's consider the problem with the Snell-Descartes law [271], that desribes the relationship between the incidence and refraction angles of light when it passes through the boundary of two different isotropic media. As an example, let's consider two media: the acrylic sphere with an index of $n_{AS} \sim 1.5$ and the water with an index of $n_{water} \sim 1.3$, as illustrated in Figure 4.3.

The Snell-Descartes law can be written such as:

$$n_{AS} \times \sin\theta_{AS} = n_{water} \times \sin\theta_{water} \tag{4.7}$$

where θ_{AS} and θ_{water} are the incident angle and refraction angle, respectively. Then, θ_{water} can be expressed such as:

$$\theta_{water} = \arcsin\left(\frac{n_{AS} \times \sin\theta_{AS}}{n_{water}}\right) \tag{4.8}$$

The behavior of this function is represented in Figure 4.4. It shows that for a scintillation photon with an incident angle $\theta_{AS} \lesssim 0.9$ rad ($\sim 50°$), the refraction angle is $\theta_{water} < 0.25$ rad ($\sim 15°$). The deviation becomes larger and the function is asymptotic when $\theta_{AS} \to 1.03$ rad ($\sim 59°$). Thus, for any incidence angle $\theta_{AS} \geqslant 59°$, the scintillation photon is reflected and remains in the acrylic sphere or in the LS.

Such reflections have two main consequences. First, the hypothesis of straight line trajectory for the scintillation photons is no more valid for such events, which has an impact

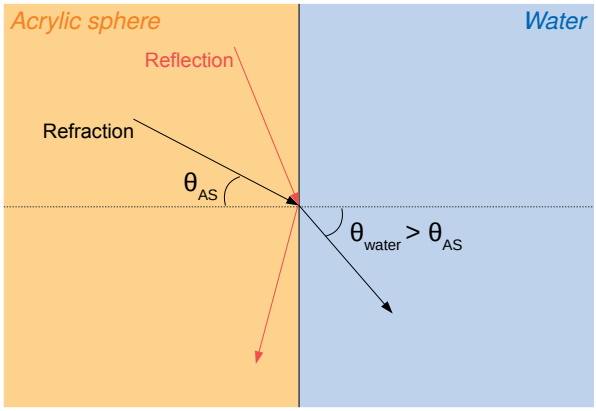

Figure 4.3: *Sketch of the refraction/reflection occuring at the interface between acrylic sphere and water. The black and red arrows represent examples of the scintillation photons refracted and reflected trajectories, respectively.*

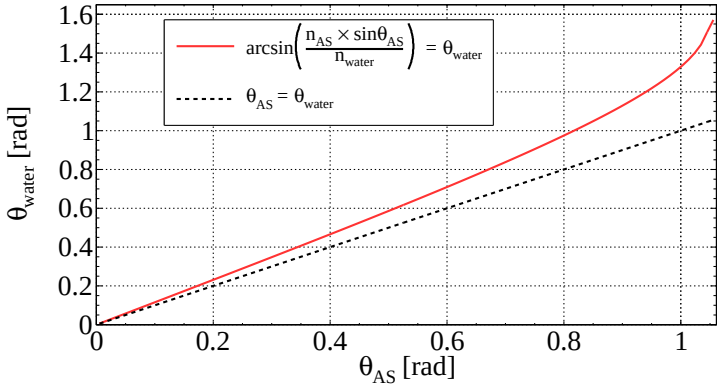

Figure 4.4: *The function describing the refraction angle of the scintillation photons as a function of their incidence angle at the boundary between the acrylic sphere and water.*

on the vertex reconstruction of the events as demonstrated in the following sections. Second, part of the scintillation photons will undergo reflections each time they will reach the acrylic sphere/water interface and will eventually be definitely absorbed before reaching the PMT, with an impact on the estimation of the energy. In a spherical detector such as JUNO, the reflection of the scintillation photons takes place only for the events occuring at a distance from center R superior to $R_{AS}.n_{AS}/n_{water} \simeq 15.9$ m [272].

4.1.4 Center of charge as a first estimation of the vertex

The two reconstruction methods that use the temporal information provided by the SPMTs (see section 4.1.5 and section 4.1.6) start from an hypothetical vertex and then converge to a solution. Rather than starting with a position that would be randomly picked into the CD, a first rough estimation is done using the so-called Center of Charge (COC) method that uses the charge information. In this method, the X, Y, and Z cartesian coordinates of the vertex are estimated by computing the barycenter of the number of PEs – also referred to as *nPE* in the following – recorded by each SPMT. It uses, the

number of PEs recorded by each SPMT channel as well as their positions:

$$\vec{R}_{coc} = A \times \frac{\sum\limits_{PMTs} q_i \vec{r_i}}{\sum\limits_{PMTs} q_i} \tag{4.9}$$

where $\vec{R}_{coc}$ corresponds to the reconstructed coordinates, q_i is the number of PEs recorded by the i_{th} SPMT and $\vec{r_i}$ is its position. A is a multiplicative factor that corrects the intrinsic bias of the barycenter computation in a sphere. This factor can be tuned thanks to calibration data. In this study it has been set to 1.3 [266]. As an example, the performance of this method on the reconstruction of the radius[3] of electron events uniformly distributed in the CD are shown in Fig. 4.5. In the LS, electrons with a kinetic energy in the MeV energy range deposit it all over a very short distance (of the order of a few millimeters), constituting a point-like source compared to the size of the detector. First of all, one can notice that as the visible energy increases the reconstruction is more precise. Indeed, the number of SPMTs fired increases together with the number of those that have several PEs, hence the better effectiveness of the center of charge. Nevertheless, the strong negative bias that appears for events in the Total Reflection (TR) area ($R^3_{true} > 4000$ m^3, $R_{true} > 15.9$ m) remains, even when the visible energy increases. The linear fit shows that between 0 and 4000 m^3 (0 and 15.9 m), the recontructed radius has a positive bias of several tens of centimeters.

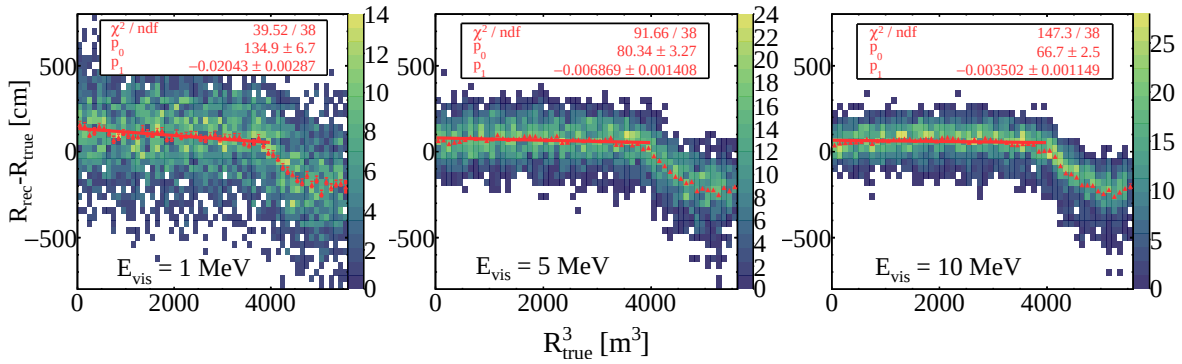

Figure 4.5: *Difference between the reconstructed and the true radius for a batch of electron events uniformly distributed in the CD using the center of charge method. The red points represent the profile of the 2D distribution that is fit with a one degree polynomial function. Three different visible energies (E_{vis}) are investigated. The SPMT system is not simulated. Similar precisions are observed for the X, Y and Z coordinates separately.*

The Figure 4.6 shows the impact of the SPMT system response[4]. The DCR is expected to have an impact only at low energy. In 1 µs, all the scintillation PE are collected by the SPMT. In this time interval, ∼14 ± 3.7 PE are generated because of their intrinsic Dark Count Rate (DCR), which represents ∼25% of the total signal for a 1 MeV event. Since the dark counts are uniformly distributed, they will tend to bias the reconstructed

[3]In this chapter, the expressions *radius*, *reconstructed radius* or *true radius* refer to the distance to the center of the acrylic sphere. The radius is computed such as $R = \sqrt{X^2 + Y^2 + Z^2}$

[4]The SPMT system response includes: the SPMTs charge resolution, time resolution (TT and TTS), Dark Count Rate (DCR) as well as the CATIROC features for the time and charge measurements (see Chapter 3). The Quantum Efficiency (QE) is not considered as part of the SPMTs response since it is already implemented at the level of GEANT4.

radius towards the center of the CD, hence the smaller bias with respect to Figure 4.5. As the visible energy increases, the dark counts become negligible and their impact weaker. At low energy, the length of the signal window can be optimise (i.e shorten) in order to eliminate the dark counts while retaining most of the signal from the energy deposition. This has not been investigated in this work. The fit range is the same than in Figure 4.5. At low energy (1 MeV) the bias is negative and the slope is even more negative than in Figure 4.5 which can be explain by the significant fraction of dark counts that are uniformly distributed and then tend to bias the reconstructed radius towards the center of the detector. At higher energy, the biases are slightly reduced compared to Figure 4.5 which can also be explained by the dark counts.

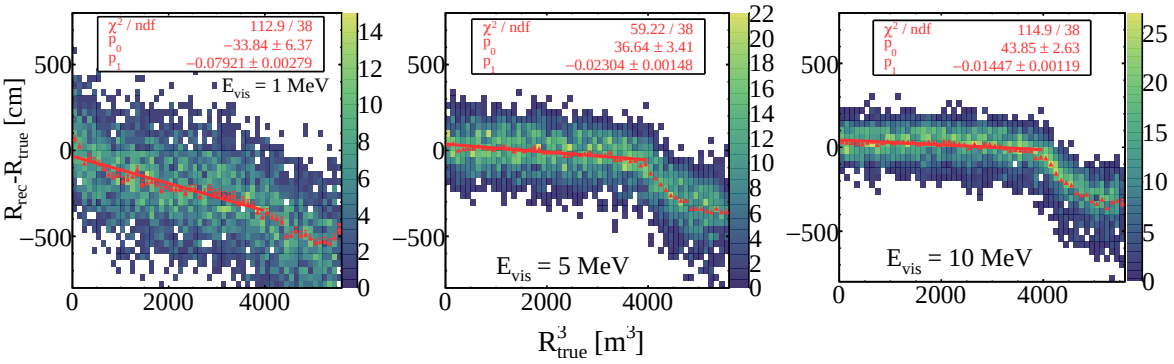

Figure 4.6: *Difference between the reconstructed and the true radius for a batch of electron events uniformly distributed in the CD using the center of charge method. Three different visible energies (E_{vis}) are investigated, 1 MeV, 5 MeV and 10 MeV from left to right. The SPMT system response is simulated. Similar precisions and behaviors are observed for the X, Y and Z coordinates.*

The precision that the center of charge method allows to obtain does not satisfy the JUNO requirement. Indeed, as mentioned in section 2.1.1.3, the distance between the prompt and the delayed signal of the IBD is of the order of several tens of centimeters while the present resolutions are of the order of the meter or more, with strong biases. Moreover, such a resolution would not allow to properly correct for the detector NU in the energy reconstruction process. A more precise vertex reconstruction method is required. Nevertheless, even if this method is unsatisfactory, it gives a reasonable first estimate of the vertex that is used as an input for the reconstruction methods that use the time information.

4.1.5 Peak time fitter as a second estimation of the vertex

The Peak Time Fitter (PTF) method computes a correction vector that is applied to the vertex estimated with the center of charge method. The newly computed vertex is corrected iteratively until the condition for stopping the process - see later in this section - is met. The peak time fitter uses the first hit time of each SPMT fired as well as their position. Taking the first hit times allows to mitigate the biases that secondary scintillation photons can induce. Indeed, the latters are more likely to have experienced reflections and refractions during their travel and the hypothesis of straight trajectory is then no more valid. Furthermore, due to the geometry of the JUNO detector, the first hit time of the SPMTs that have more than one PE is biased toward earlier hit times. This can be corrected for in order to enhance the precision of the algorithm (more details on the importance of the scintillation photons timing for the event reconstruction can be found

in Ref. [273]). However, the majority of the SPMTs having only one PE, such correction is not applied. Thus, from the vertex estimated with the center of charge method, the residual time is calculated for each first hit time using equation 4.1 and the geometrical model presented in section 4.1.2. Once the residual time of each first hit time has been calculated, the correction vector $\vec{\delta}[\vec{r}(n)]$ is computed with the following formula :

$$\vec{\delta}[\vec{r}(n)] = \frac{1}{N(n)} \cdot \left(\sum_{i=0}^{PMTs} \frac{t_{res,i}(n) - t_{res}^{peak}(n)}{tof_i} \times (\vec{r}(n) - \vec{r}_i) \right) \tag{4.10}$$

where the sum runs over the fired SPMTs; N is the number of fired SPMTs, $t_{res,i}$ is the residual time, t_{res}^{peak} is the time corresponding to the maximum of the residual time, n is the iteration number, $\vec{r}(n)$ and $\vec{r}_i$ are the current vertex position and the SPMT position, respectively. At each new iteration, a new correction vector is calculated using this new vertex position, the corresponding new tof, $t_{res,i}$ and t_{res}^{peak}. The algorithm stops when the correction vector becomes inferior to 0.1 mm, far below the spatial resolution that a LS detector can achieve [273].

The peak time fitter method also allows to determine the time of interaction (t_0). In principle, it corresponds to the value of the residual time when its distribution is maximal (t_{res}^{peak}). However, we checked and the precision that the SPMT system can reach is of the order of the tens of nanosecond or more which is not satisfactory. In addition, as demonstrated in Ref. [266], the LPMT is expected to provide a precision of the order of a few nanoseconds using this method. Such result could be used by the SPMT system, if needed. In what follows, the t_0 provided by GEANT4 is used. As for the center of charge method, the performance on the reconstruction of the radius of electron events uniformly distributed in the CD is shown in Fig. 4.7.

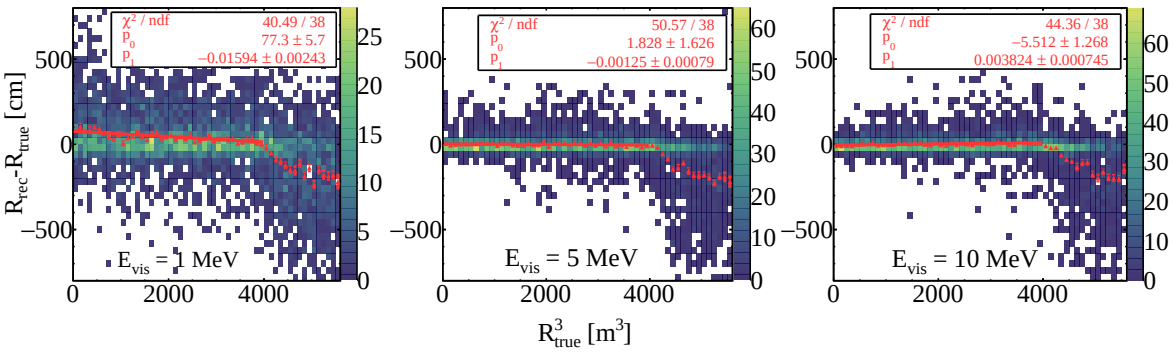

Figure 4.7: *As in Figure 4.5 for the peak time fitter method. Similar precisions and behaviors are observed for the X, Y and Z coordinates.*

As expected, a method that uses the time information is more precise than the center of charge, the spread is smaller. In addition, the parameters of the fit show a smaller bias that remains more constant when the radius increases, especially at higher energies where it is < 10 cm. Furthermore, while all the events occuring in the TR area were reconstructed at lower radii with the center of charge method, some of them are actually well reconstructed when using the peak time fitter method. The poorly reconstructed events are still biased toward lower radii. Indeed, the reflections make the time of flight of the scintillation photons longer which results in an under estimation of the radius. The Figure 4.8 shows the performance of the peak time fitter when the SPMT system response is enabled. Since the peak time fitter uses the time information, the charge resolution is

expected to have no impact contrary to the PMTs TTS, Dark Noise and readout electronics time resolution. As expected, the SPMT system time resolution degrades the precision of the peak time fitter by a few centimeters. The DN biases the reconstruction toward smaller value, especially at low energy, in the same way than when using the center of charge method. In conclusion, the peak time fitter enhances the precision on the vertex reconstruction and allows to achieve precisions of the order of a few tens of centimeters. However, both center of charge and peak time fitter are not fully reliable in the TR area (we show later a way to provide a selection of the misreconstruced events). A better precision must be reached especially for the reconstruction of the IBD delayed signal whose visible energy is $\sim$ 2.2 MeV.

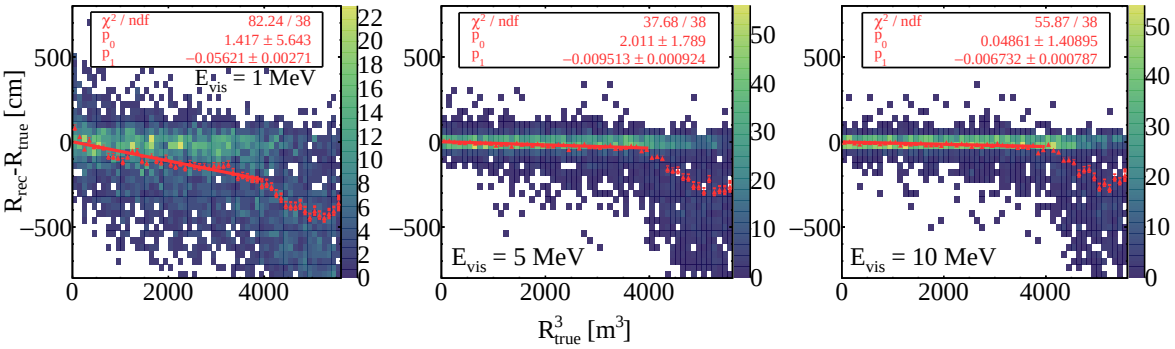

Figure 4.8: *As in Figure 4.6 for the peak time fitter method. Similar precisions and behaviors are observed for the X, Y and Z coordinates.*

4.1.6 Vertex reconstruction with the Likelihood method

4.1.6.1 Definition of the likelihood function

The last vertex estimate is done with a *maximum likelihood method* [274]. It is a statistical method that aims to estimate model parameters from a data set. Generally, a likelihood function can be expressed such as:

$$\mathcal{L}(a) = \prod_j f(x_j|a) \tag{4.11}$$

where j corresponds to the elements of the data set and $f(x_j|a)$ is the probability to measure x_j under the assumption of the parameter a. Thus, from a measured data set, the principle is to compute $\mathcal{L}$ for different values of a. The value of a that maximises $\mathcal{L}$ is the most likely to be the true one. In the present work, the parameters to estimate are the vertex coordinates while the data set consists of the residual times. As for the peak time fitter, it is estimated from the first hit time on the SPMTs together with the geometrical model introduced in section 4.1.2. Thus, the likelihood function has the following form:

$$\mathcal{L}(\vec{r}) = \prod_j f(t_{res,j}|\vec{r}) \tag{4.12}$$

where the product runs over the SPMTs fired and $\vec{r}$ contains three coordinates: x, y and z. First, the function $f(t_{res})$ is determined. This function depends on the detector response

(LS, PMTs, readout electronics etc.). It is expected to have the following form:

$$f(t_{res}) = \underbrace{\frac{1}{\sigma\sqrt{2\pi}} e^{-\frac{(t_{res}-\mu)}{2\sigma^2}}}_{PMT+RO+photon\,path} * \underbrace{\sum_{i=1}^{n} \frac{n_i}{\tau_i} e^{-\frac{t_{res}}{\tau_i}}}_{LS\,response} \tag{4.13}$$

where μ and σ depends on the detector response, and n_i and τ_i are the intensity and time constant of the i^{ih} component of the LS de-excitation time profile, respectively. After being normalised, this distribution is a Probability Density Function (PDF) of the residual times. The construction of the residual time PDF using the Monte Carlo (MC) simulation of JUNO has shown that it is in reality much more complex than that described in equation 4.13, especially because of the geometrical effects that take place in such a large detector. In addition, since the intensity and time constants of the LS depends on the energy deposition processes, different particles will lead to different PDF shapes. For these reasons, MC-generated PDFs were used in this work. As for the two previous reconstruction methods, the performance of the maximum likelihood method has been tested in different detector configurations. It has also been tested on two different types of particles (electrons and positrons). On the one hand, the electron provides a point-like energy deposition which is the starting hypothesis of this reconstruction algorithm. On the other hand, the reactor neutrinos and part of the CCSN neutrinos will be detected *via* the IBD channel, whose prompt signal comes from a positron. Indeed, particular attention should be paid to the effect of annihilation gammas on the reconstruction, whose energy deposition is made over a larger distance than for electrons and positrons, making it less point-like. The center and left panels of the Figure 4.9 show examples of PDF with different simulation configurations. The PDF generated with positrons is less sharp than that generated with electrons, because of the less point-like energy deposition pattern due to the annihilation gammas. In addition, the TTS and the CATIROC time walk fluctuations that smear the time measurement also contribute to flatten the PDF. Finally, as mentioned in section 4.1.5, the first hit time of the SPMTs that have more than one PE is biased toward earlier hit times. As shown on the right panel of Figure 4.9, the PDF shape changes according to the number of PE/PMT. This change gets negligible when a PMT has more than 5 PEs.

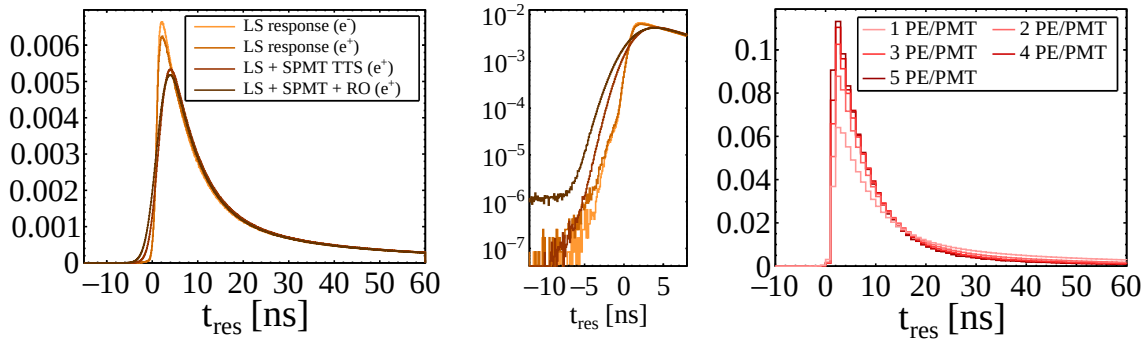

Figure 4.9: ***Left**: The residual time PDF for different detector simulation configurations and different particles. **Center**: Zoom on the peaks of the left panel distributions, shown in log scale. The simulation of the PMTs Dark Noise is implemented at the level of the readout (RO) electronics simulation, hence the flat distribution appearing at low t_{res} in the dark brown distribution. **Right**: Example of the residual time PDF for different number of PE/PMT.*

For practical reasons, the $-log$ of the likelihood function is taken for the estimation of parameters. Indeed, the logarithm function preserves the monotony of $\mathcal{L}$ and transforms the product into a sum. Also, with the sign "-", it is a minimisation and not a maximisation that is done, which is more practical in terms of calculation. Thus, the likelihood function used in the algorithm is:

$$\mathcal{L} = -\sum_{j} log(f(t_{res,i}|\vec{r})) \tag{4.14}$$

The minimization is performed using the MIGRAD algorithm of the TMinuit package [275] provided by ROOT [276].

4.1.6.2 Likelihood function value and event selection

The performance of the maximum likelihood method on the reconstruction of electron events uniformly distributed in the CD is shown in Figure 4.10. The range of the Y axis is willingly set at the same value than for the two previous methods to make the plots comparable with each other. The performance is discussed more in details later.

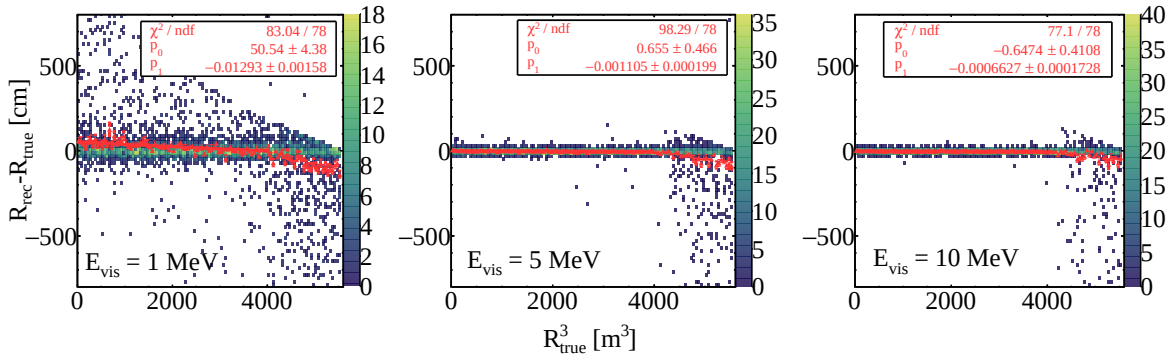

Figure 4.10: *As in Figure 4.5 for the likelihood method. Similar precisions and behaviors are observed for the X, Y and Z coordinates.*

The likelihood method allows to obtain a better precision with respect to the center of charge and the peak time fitter, with a smaller bias that remains constant over about 16.0 m. At low energy (E_{vis} = 1 MeV), many events are still poorly reconstructed. When the energy increases, the only events that are reconstructed far from the true vertex are those occuring in the TR area, and their number decreases as the visible energy is larger. Indeed, it seems that the increase of scintillation light generated at higher energy compensates the error made because of the reflections of the scintillation photons which is expected since a larger proportion of light travels to the PMTs in straight light. An indication of this effect can be observed with the LPMT system. In fact, for 1 MeV deposited, which corresponds to ≥1345 PE, all the events are well reconstructed, the reflections and refractions only degrade the resolution by a few milimeters [266].

The performance was also tested when the SPMT system response is simulated, they are presented in Figure 4.11. In that case, the PDF built with the full SPMT system response is chosen. As expected, the radial resolution is degraded, the spread is larger. As in the previous case, the bias remains constant over 16 m. As already observed, for a visible energy of 1 MeV, the overall bias is weaker than when the SPMT system response is not simulated, which is due to the PEs from the PMTs DN as explained before. The

bias slightly increases with the energy, but remains of the order of a few centimeters.

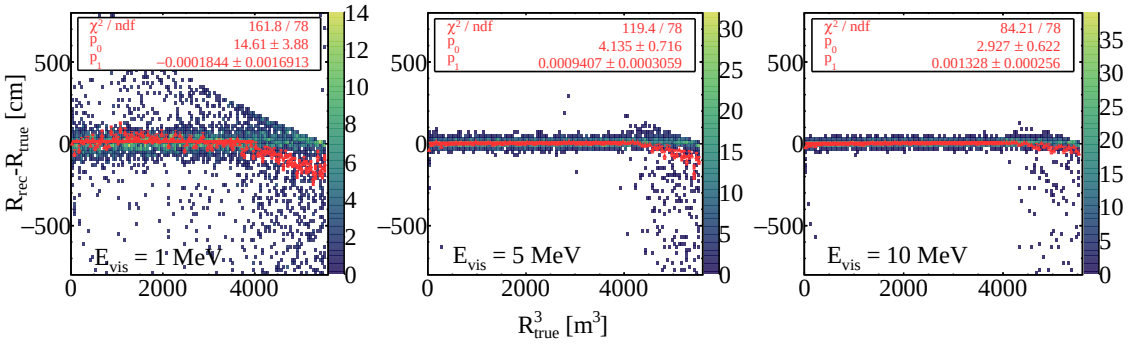

Figure 4.11: *As in Figure 4.6 for the likelihood method. Similar precisions and behaviors are observed for the X, Y and Z coordinates.*

The poor reconstruction of the some events' vertices has two main impacts. First, the aforementioned detector Non-Uniformity (NU) correction (energy reconstruction) is wrong, which eventually degrade the energy resolution. Second, the selection of the IBD candidates based on the spatial coincidence (section 2.1.1.3) is not reliable. Thus, it is of crucial importance to identify the poorly reconstructed events, at least for rejecting them in the analyses, or even to reconstruct them with more efficient techniques (Machine Learning (ML) for example [277]). The identification of these events can be done using the value of the likelihood function after the minimizer has converged. Indeed, this value is significantly larger for the poorly reconstructed events than for the correctly reconstructed ones as shown in Figure 4.12[5]. This arise from the way the likelihood function is minimised. Indeed, for a given vertex that is tested by the algorithm, the value of the PDF for residual times (t_{res}) that are out of the range (i.e < -20 ns and > 300 ns) is equal to zero, so that nothing is subtracted to $\mathcal{L}$ (see equation 4.14). Thus, when the algorithm does not manage to converge and only tests vertices that are far away from the true vertex, very few residual times feed the likelihood function so that when the algorithm stops the final value is on average larger than when it converges close to the true vertex. As a consequence, the poorly and correctly reconstructed events can be separated by means of a cut on the minimised likelihood function value, referred to as the *likelihood quality cut* in the following.

Furthermore, the distribution of the minimised likelihood function value shows a low dependence on energy, as shown on the left plot of Figure 4.13. For instance, ∼25% (∼2%) of the events are rejected when setting a cut at 7.5 for 0 MeV (8 MeV) positrons. In the following, the same cut is used for all the reconstructed events at any energy. One can also observe that some of the correctly reconstructed events have a minimised likelihood function value that is the same than that of the poorly reconstructed ones, which implies that they are also rejected by the likelihood quality cut. This concerns ∼0.7% of all the reconstructed events and ∼15.0% of the rejected events. The right plot of Figure 4.13 shows the radial resolution after the likelihood quality cut is applied. A batch of 140,000 positron events with a flat visible energy distribution ranging from 1 to 10 MeV were simulated, with the full detector and readout electronics simulation. The likelihood quality cut shown on the left plot of the same figure is applied to each reconstructed event. In

[5]In Figure 4.12 the 3D spatial difference between the true and the reconstructed position is computed such as $\delta R = \sqrt{(X_{rec} - X_{true})^2 + (Y_{rec} - Y_{true})^2 + (Z_{rec} - Z_{true})^2}$.

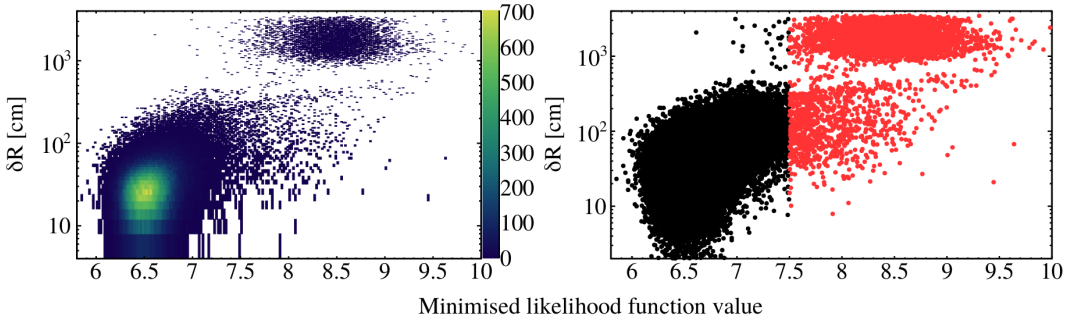

Figure 4.12: ***Left**: Correlation between the vertex reconstruction performance – δR is the 3D spatial distance between the true and the reconstructed vertex – and the minimised likelihood value for positron events with a visible energy between 1.022 and 10.022 MeV (flat distribution).* ***Right** Scatter plot of the correlation shown on the left panel. Setting a cut at 7.5 allows to reject all the poorly reconstructed events and a small sample of well reconstructed ones.*

total, over the 140,000 events simulated, ∼133,000 (∼95%) of them pass the cut.

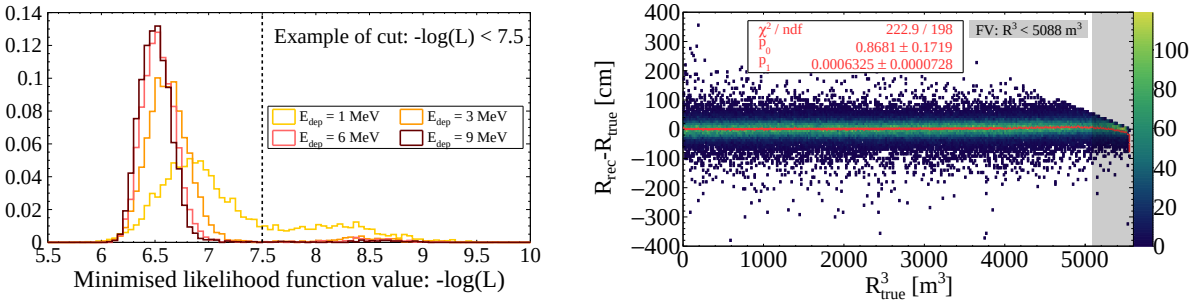

Figure 4.13: ***Left**: The minimised likelihood function distribution for batch of events with different visible energies. The distributions show a slight energy-dependence.* ***Right**: The difference between the reconstructed and true radius for a batch of positron events uniformly distributed in the CD using the likelihood method. The visible energy distribution is flat and ranges between 1.022 and 10.022 MeV. The likelihood quality cut is applied to select the events. The SPMTs charge resolution, the readout electronics response and the PMTs dark counts are simulated.*

As expected, over the three different methods explored here, the maximum likelihood method provides the best precision and stability over all the detector and is the only one that allow to identify and reject the poorly reconstructed events. The radial resolution performance shown here is of a few tens of centimeters, i.e of the order of the distance between the prompt and the delayed signal of the IBD, which is satisfactory. Such resolution is two orders of magnitude below that of the size of the detector, which will allow a precise detector NU correction in the energy reconstruction.

4.1.6.3 Bias and Resolution in the reactor energy range

In this section, the performance of the maximum likelihood method is investigated more in detail. The resolution in the cartesian (X, Y, Z) and spherical (R, θ, ϕ) coordinates are shown (see Figure 5.23 (Appendix) for the coordinates convention used in this manuscript). Moreover, a particular attention is paid to the bias and resolution of the reconstruction

at different energies. The full detector and electronics response were simulated to obtain the results presented below - unless mentioned otherwise in the plot - and the likelihood quality cut is systematically used.

The Figure 4.14 shows the resolution along the X, Y and Z coordinates for 1 MeV (kinetic energy) positrons uniformly distributed in the CD. The distributions can be fit with a gaussian function and the corresponding reduced chi-squared is $\tilde{\chi}^2 \leqslant 1.7$. The modelling of the distributions with a gaussian function allows to estimate the bias and statistical error on the reconstruction and to associate a confidence interval [274]. The statistical error is referred to as the "resolution" here. For example, according to the fit of the left plot in Figure 4.14, the resolution along the X coordinate is 35.4 cm and the bias is of 0.8 cm, with a confidence level of 1σ (68% of the distribution). The same results are observed for Y and Z, within ∼1 cm. This method is used to evaluate the biases and resolutions presented in the following.

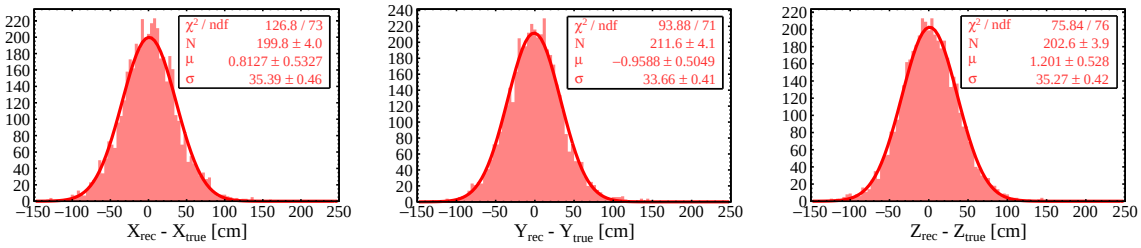

Figure 4.14: *The resolutions of the vertex reconstruction against the X, Y and Z coordinates for positron events (E_{vis} = 2.022 MeV).*

The reconstruction of positron events with kinetic energies < 1 MeV cannot be perfectly modelled by a gaussian fit, notably because of non-gaussian tails in the distributions. At such energies, the $\tilde{\chi}^2$ is ∼3. This means that some systematic effects come into play. There are at least two reasons for this:

1. The lack of scintillation photon statistics. Indeed, too little information provided on the timing of the events in such a large detector can make the performance of the reconstruction less stable.

2. This reconstruction is based on the principle that the scintillation photons have a straight trajectory and that their source is pointlike. For low energy positrons, the energy deposition is dominated by the annihilation gammas (1.022 MeV), for which the light source cannot be considered as point-like. As shown in the previous section, in cases where the starting assumptions are not valid, the algorithms are less efficient.

As it will be described more in detail in section 4.2, the detector NU is mostly radial and zenithal (θ) dependent. The performance along these coordinates must also be carefully studied. They are shown for 1 MeV kinetic energy positrons in Figure 4.15, together with that along ϕ.

As mentioned earlier, the performance along the R coordinates is similar to that along X, Y and Z. The bias is of 0.8 cm and the resolution is of 33.5 cm for 1 MeV positrons. The resolution along the ϕ and θ angles are of 2.0° and 1.6°, respectively. Such values are satisfactory and will allow a precise detector NU correction in the energy reconstruction.

Finally, the Figure 4.16 shows the radial bias and resolution (1σ) as a function of the visible energy, ranging from 1 to 10 MeV. The performance for both electron and positron

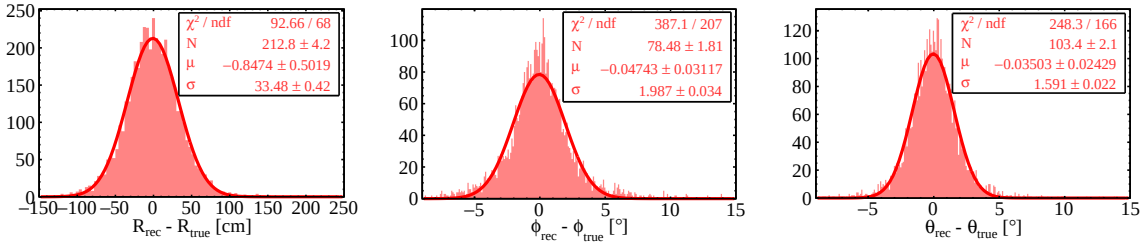

Figure 4.15: *The resolutions of the vertex reconstruction against the R, θ and φ coordinates for positron events (E_{vis} = 2.022 MeV).*

events is detailed. In the low energy range ($E_{vis} < 3$ MeV), the performance for electrons is better than for positrons, being 40 cm and 60 cm at 1 MeV, respectively, when the SPMT system response is simulated. This arises from the energy deposition pattern that is point-like for electrons while for the positrons, the annihilation gammas lay down their energy over a few tens of centimeters. However, when the visible energy increases – i.e when the kinetic energy of the electrons/positrons increases – the resolutions are similar for both particles. Indeed, the energy deposition of the positron events – that includes the kinetic energy of the positron and the annihilation gammas – becomes more and more point-like as the kinetic energy of the positron becomes dominant, hence the performance becomes similar for positrons and electrons when the visible energy (E_{vis}) exceeds 3 MeV.

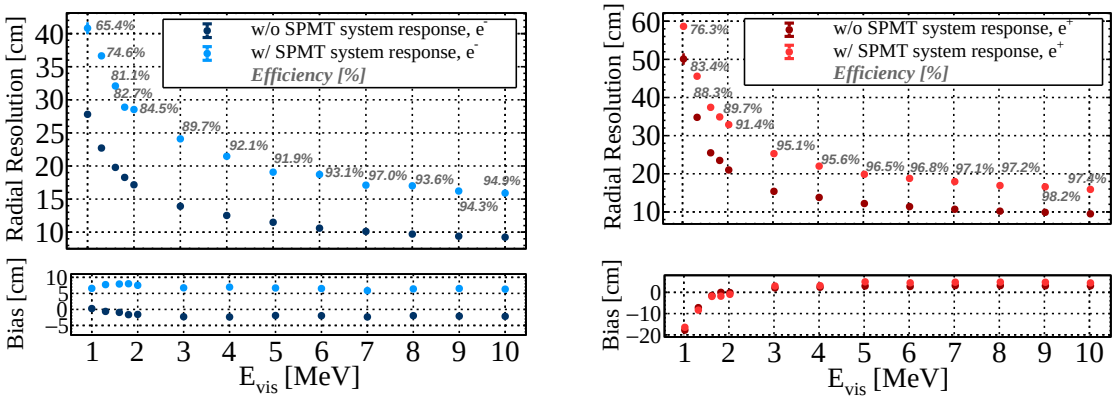

Figure 4.16: ***Left**: Radial bias and resolution of the vertex reconstruction for electron events. The SPMT system response is simulated for the light blue points. **Right**: Same plot but for positrons. The SPMT system response is simulated for the light red points. In both panels, the efficiency (in grey) corresponds to the fraction of events that were not rejected by the likelihood quality cut in the case the SPMT system response is simulated.*

The SPMTs and readout electronics time response degrade the resolution over all the energy range. In the low energy range, the resolution is degraded by ∼45% for electrons and by ∼17% for positrons. As the energy increases, the deterioration of the resolution is of 45% in both cases. This confirms that the energy deposition pattern plays an important role in the performance of the algorithm. For both particle types, the bias of the reconstruction is within 10 cm, except in the very low energy range ($E_{vis} \sim 1$ MeV) where it can reach ∼20 cm for positrons which remains two order of magnitudes smaller than the size of the detector. The selection efficiency after the likelihood quality cut is displayed

in grey. The efficiency for electrons is ∼5% smaller than that for positrons in almost all the energy range. Indeed, the same likelihood quality cut (optimised for positrons) has been used to obtain the electrons and positrons results presented here. However, we have seen that different PDF have been used (one for the electrons and one for the positrons) leading to slight different distributions of the minimised likelihood function values in each case, hence the cut for positron does not perfectly suit to the electrons. A finer tuning of the likelihood quality cut would allow to fix this problem. The efficiencies remain however around ∼90-95%. Thus, since this algorithm originally aims to be used for the reconstruction of CCSN neutrino events whose average visible energy is > 10 MeV, this discrepency was not investigated further.

4.1.7 Application to IBDs from CCSN neutrino events

In JUNO, the reactor $\bar{\nu_e}$ as well as ∼50% of the CCSN neutrinos will interact via the Inverse Beta Decay (IBD) which will produce two temporally and spatially correlated signals (see section 2.1.1.3 for more details). The neutron produced during the IBD will be captured by an hydrogen nucleus ($^1_1$H) - in more than 99% of the cases - or by a Carbon-12 nucleus. The neutron capture by an hydrogen nucleus will induce the emission of a single 2.2 MeV gamma while several gammas with a total energy of 4.95 MeV will be produced as it is captured by a Carbon-12 nucleus. In the previous section, we have seen that the efficiency of the vertex reconstruction algorithm is not 100% when using the maximum likelihood method, especially at low energy. This is important for the reconstruction of the delayed IBD delayed signal consists of a 2.2 MeV gamma. Furthermore, such a gamma deposits its energy over several tens of centimeters, making the assumption of point-like source of scintillation photons less strong. As a consequence, the resolution along the R, X, Y and Z coordinates are of the order of ∼37 cm against ∼30 cm for the positrons and ∼27 cm for the electrons with the same visible energy. The efficiency is of the order of ∼90%. In the case of CCSN, the IBD prompt energy spectrum ranges from 0 to 100 MeV with an average energy of ∼15 MeV. The resolution is of the order of ∼10 cm and the efficiency reaches ∼98%.

The prompt and delayed signals of the IBD being temporally and spatially correlated, the selection of the IBD events partly relies on the vertex reconstruction of them. The Figure 4.17 shows the distance between prompt and delayed signals for the true (dark red) and the reconstructed (light red) vertices of a set of IBDs from CCSN $\bar{\nu_e}$ events. In order to assess which of the center of charge method or the peak time fitter method is the best to recover the events rejected by the likelihood quality cut, two configurations of the algorithm were tested. On the left plot, when a reconstructed event does not pass the likelihood quality cut, the vertex is reconstructed using the peak time fitter while in the right one, it is reconstructed using the center of charge.

According to the Monte Carlo (MC) truth, δR is typically below 5 meters while it goes up to 35 meters when using the reconstructed vertices. The distributions from the reconstruction clearly shows three structures. The leftmost one - peaked within few meters - corresponds to the IBDs whose both prompt and delayed signals are well reconstructed by the likelihood method (∼90% of the events). The peak is less sharp compared to the MC truth because of the finite resolution of the reconstruction. The second structure, between 5 and 10 meters, corresponds to IBDs whose delayed signal was rejected by the likelihood quality cut and then reconstructed with a less effective method (∼8.1% of the events). Finally, the rightmost structure - the flat one, above ten meters - corresponds to IBDs whose gamma of the delayed signal escaped from the detector before depositing all its energy, making the reconstruction very difficult (∼1.5% of the events). Their numbers

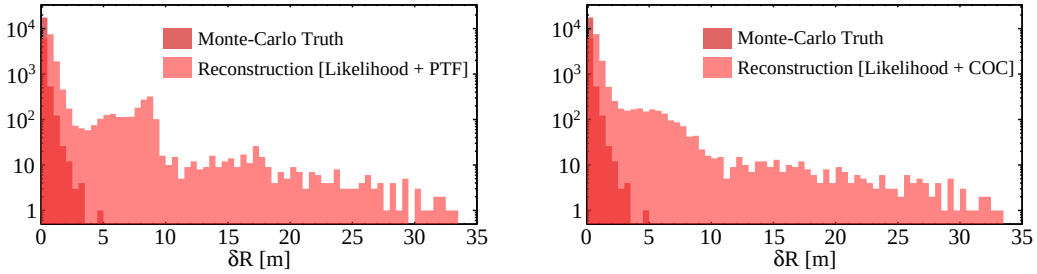

Figure 4.17: ***Left**: The 3D spatial distance between IBDs prompt and delayed signals from CCSN $\bar{\nu}_e$ events. The peak time fitter method is used to reconstruct the events that did not pass the likelihood quality cut.* ***Right**: Same plot but the center of charge method is used to reconstruct events that did not pass the likelihood quality cut.*

is negligible with respect to the rest of the distribution. The structures resulting from the reconstruction using the center of charge method (right plot of Figure 4.17, between 4 and 35 meters) are smoother and show higher stability. As a consequence, when an event is rejected by the likelihood quality cut, the reconstructed vertex from the center of charge method is used for the analysis. The impact of the reconstruction on the CCSN neutrino event selection are investigated Chapter 5.

4.2 Energy Reconstruction

As previously mentioned, the reconstruction of the events is of paramount importance for most of the physics goals of JUNO. In a LS detector, the reconstruction of the energy of the events is based on the number of PEs. Previous experiments using cylindrical and spherical LS detector have shown that the observed nPE is not linear with the energy deposited, this effect is referred to as the *Liquid Scintillator Non-Linearity (LSNL)* and is well reproduced by the GEANT4 simulation of the JUNO detector. The nPE also depends on the event location due to geometrical effects which is referred to as the detector *Non-Uniformity (NU)*. If they are not properly taken into account in the energy reconstruction, these effects have a non-negligible impact on the energy resolution. As a consequence, the energy reconstruction must be carefully studied and optimised. This section presents an energy reconstruction method that have been developed for the SPMT system and that is based on the nPE (section 4.2.1). The aforementioned detector effects are corrected for in the reconstruction process, the LSNL is addressed with calibration data from the DayaBay experiment [229] while the NU is addressed using the vertex reconstruction algorithm presented above (section 4.2.3). The performance of the algorithm in terms of energy resolution and bias is tested on events in the MeV energy range. Particular attention is paid to the evolution of the energy resolution with the deposited energy and the consistency with the so-called *abc model* is checked (section 4.2.5). Finally, the performance is tested on prompt and delayed signals of IBD events from CCSN $\bar{\nu_e}$ (section 4.2.6).

4.2.1 Energy estimator

The LS of JUNO has been designed and optimised to produce ∼13,000 scintillation photons for 1 MeV of energy deposited. Thus, counting the number of scintillation photons produced by a particle that interacted in the LS provides a direct measurement of the energy it deposited. The JUNO detector is designed to collect a sample of the scintillation photons, by means of PMTs. Indeed, when they hit the photocathode of the latter, the scintillation photons have a probability to be converted into PE by photoelectric effect (see section 2.2.2.2). As explained in section 2.2.2.3, the reconstruction of the time and charge of the SPMTs output signal is ensured by CATIROC [231], a readout chip embedded in the SPMT system front-end electronics. Thus, for each event, the SPMT system provides a number of PEs that is used as an estimator for the energy deposited. The SPMT system is expected to have ∼40 PE/MeV for an event occuring at the center of the CD. This number will be referred to as the *energy scale* in the following. This number depends on the characteristics of the LS and the SPMTs with the main contributions listed below for the typical case of a 1 MeV electron at the center of the detector:

- Light Yield : ∼**13000**
- Attenuation factor from quenching effects : ∼**0.99**
- Attenuation factor from absorptions and re-emissions by the bis-MSB [278] : ∼**0.92**
- Attenuation length of the LS [215] ∼25.8m → attenuation factor : ∼**0.47** (19.3 m)
- SPMTs Quantum Efficiency (QE) [213] : ∼**0.27**
- SPMT system photo-coverage [76] : ∼**0.027**

By multiplying these numbers, one can get a rough estimation of the SPMT system energy scale. Of course, a precise determination of the energy scale is needed, as described in section 4.2.2.

With a photo-coverage of ∼2.7%, the SPMT system works in the photo-counting regime. Thus, for a typical reactor neutrino energy spectrum, more than 95% of the SPMTs fired have 1 PE and ∼ 4.8% have ∼2-5 PEs. In comparison, in the same energy range, ∼42% of the LPMTs have 1 PE and the rest of them have > 2 PEs. Thus, interestingly, the reconstruction of the energy with the SPMTs can also be based on the total number of CATIROC triggers[6] registered by the SPMT system, disregarding the number of PEs. Indeed, the SPE resolution of the SPMTs and the possible electronics non-linearity smear the number of PEs and consequently degrade the energy resolution. Counting the number of CATIROC triggers also give an estimation of the energy, without suffering from the SPE and readout electronics finite charge resolution. However, as explained in section 3.3.2, because of the SPMTs functioning, if two scintillation photons hit the same SPMT in a time interval inferior to 10 ns, a single signal (with double charge) is produced and sent to CATIROC. In such a case, the use of the number of CATIROC triggers would not properly measure the PEs since it would count one PE instead of two. The energy would then be underestimated. As a consequence, in the following, the charge reconstructed by CATIROC is used as input for the energy reconstruction. The CATIROC trigger counting method is only explored at the end of this section.

4.2.2 Energy scale determination

The energy scale of the JUNO detector is determined using several radioactive sources [239] as well as a UV laser for the Dual Calorimetry [230]. The calibration strategy of the JUNO experiment notably involves the use of an AmC (Americium-Carbon) source, which will serve two different purposes. The first one is the determination of the LSNL in the higher energy range of the reactor antineutrino spectrum thanks to the 6.13 MeV gamma emitted by the excited Oxygen ($^{16}_{8}O^{*}$) (Eq. 4.15). The second one is the determination of the energy scale, by measuring the 2.2 MeV gamma emitted during the neutron capture (Eq. 4.16).

$$^{241}_{95}Am \longrightarrow ^{237}_{93}Np + ^{4}_{2}\alpha + \gamma(49.5keV)$$
$$^{4}_{2}\alpha + ^{13}_{6}C \longrightarrow ^{16}_{8}O^{*} + n \quad (4.15)$$
$$n + ^{1}_{1}H \longrightarrow ^{2}_{1}d + \gamma(2.2MeV) \quad (4.16)$$

In principle, by applying a 2μs cut on the PMTs hit times, the 2.2 MeV gamma signal can be isolated from the Oxygen de-excitation gamma one. In this work, for simplicity and in order to save computational time, solely 2.2 MeV gamma events were simulated instead of all the AmC source decay chain. The Figure 4.18 compares the total number of PEs obtained for small data sets of 2.2 MeV gammas emitted in the center of the CD and the encapsulated AmC source also positioned at the center of the detector. The nPE differs by 1.4%, which is considered as negligible for this study.

By dividing the average number of PEs found in Figure 4.18 by 2.2 MeV, the energy scale found for the SPMT system is 40.01 PE/MeV. This number is defined as Y_0 in the following. In real conditions, the energy scale could slightly change with time (SPMT system dead channels, opacification of the LS...). For this reason, it will be weekly monitored, as described in Ref. [239]. At this stage, the estimation of the energy can be done such as:

$$E_{rec} = \frac{nPE}{Y_0} \quad (4.17)$$

[6] As a reminder, the CATIROC readout chip directly integrates the SPMTs output signals and compute the corresponding time and charge (i.e PE) information (see section 2.2.2.3).

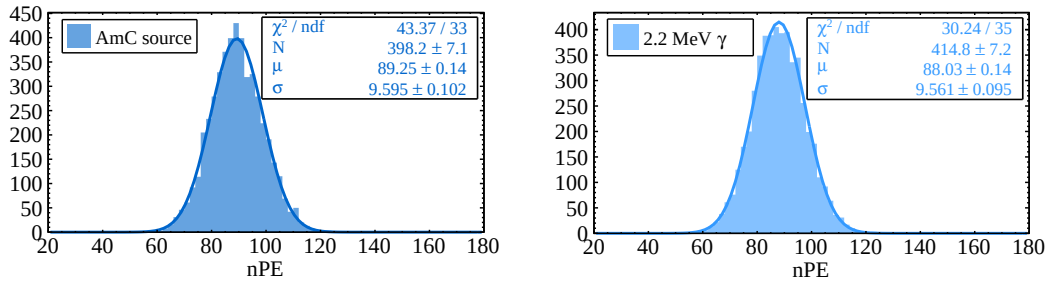

Figure 4.18: ***Left**: The total number of PEs from 2.2 MeV gammas from the neutron capture of an AmC source, by setting a 2 μs cut to isolate it from the rest of the AmC decay chain. **Right**: The total number of PEs from solely 2.2 MeV gammas. In both cases, the events are simulated at the center of the detector.*

where nPE is the number of PEs for a given event and Y_0 is the energy scale. However, this formula does not take into account the LSNL and NU. The corrections that are needed as well as the way they are determined are detailed in the following section.

4.2.3 Visible energy correction

In this section, the LSNL and NU are introduced and the way they are addressed in this energy reconstruction method is described.

4.2.3.1 Liquid scintillator non-linearity

When charged and neutral particles interact with the LS molecules, scintillation photons are emitted [279]. Basically, the molecules are excited by the energy deposition and then de-excite *via* phosphorescence and fluorescence. However, there is always a part of the deposited energy that is irreversibly absorbed and lost. These effects are referred to as *quenching effects* [280]. The proportion of energy which is quenched varies with the deposited energy and also depends on the particle mass.

The energy deposition processes in the LS also include a Cherenkov light contribution [234]. The Cherenkov light is emitted when the speed of a particle propagating in a given medium is larger than the speed of light in this medium. As for the scintillation light, the Cherenkov light emission depends on the energy and on the mass of the particle, making the overall quantity of light produced even more non-linear. When it is emitted, part of the Cherenkov light is absorbed and re-emitted by the wavelength shifters of the LS. The re-emitted photons are in the same wavelength range than the scintillation photons, making them hardly distinguishable of each other.

The left plot of Figure 4.19 – from Ref. [281] – sums up the contribution of both quenching and Cherenkov effects to the LSNL for electrons depositing their energy in the LS of JUNO. It has been obtained with simulation data. The plot shows that the ratio between the visible energy (E_{vis}) and the deposited one (E_{kin}) is not constant and increases with the kinetic energy of the particle. The quenching effects make the visible energy smaller than the deposited one while the add of the Cherenkov effect in the simulation makes the ratio larger than unity as the kinetic energy of the particle increases. Since this work is focused on the reconstruction of positron events, the corresponding LSNL must be used. Even if the mass of the electron and positron are the same, the gammas from the positron annihilation will make the shape of the curve different. The one used for this

work is shown in the right plot of Figure 4.19. It has been determined from measurements at Daya Bay [229, 278], which has a similar liquid scintillator recipe than JUNO. An extrapolation in the low energy range (< 1 MeV) is derived for this work. Note that the value of E_{vis} / E_{dep} is referred to as f_{LSNL} in the following.

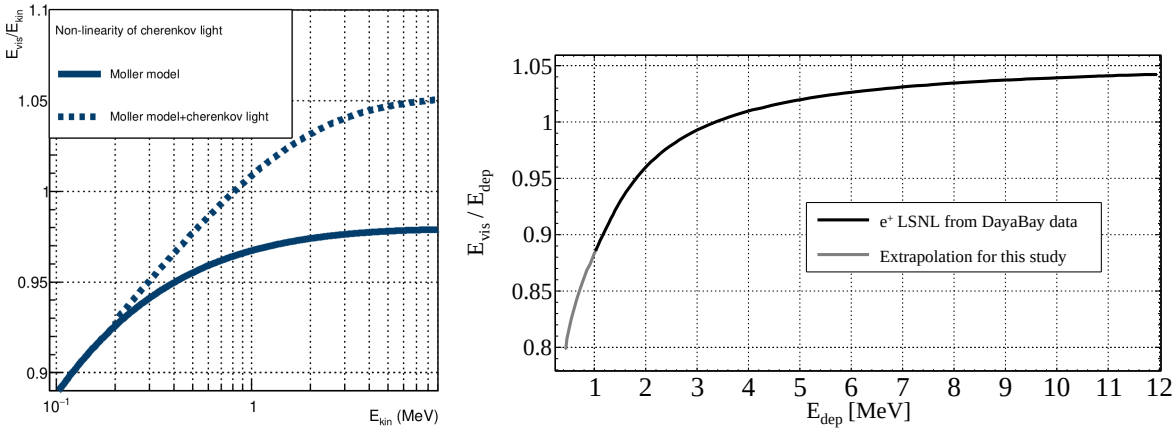

Figure 4.19: ***Left**: An example of a LSNL curve for electrons - from [281]. This plot is only intended to show the contributions of the scintillation light (full line) and the Cherenkov light (dashed line) to the LSNL. **Right**: The LSNL curve for positrons down to 1 MeV from the Daya Bay data. This curve is used for the neutrino oscillation parameters and NMO sensitivity studies. At lower energy, the curve is extrapolated.*

It is important to mention that, as explained in section 2.2.2.3, the LSNL cannot be determined absolutely. Since its measurement is based on the ratio between the true and the reconstructed energy – using known radioactive sources – it means that it is in fact interwined with the instrumental non-linearity (from the PMTs and electronics). The Dual Calorimetry Calibration (DCC) [230] (see Chapter 2) is expected to allow a more precise calibration of the instrumental non-linearity and by extension enhance the LSNL calibration.

4.2.3.2 Non-uniformity correction

The detector response NU mainly arises from the non-perfect transparency of the LS as well as the fact that the PMTs are not perfectly uniformly distributed around the acrylic sphere. Indeed, the number of scintillation photons that will hit the PMTs depends on the distance they travel in the LS, because of the different physical processes they will undergo (see section 4.1.2). The closer to the PMTs is the emission point, the more likely the scintillation photons will hit them. The TR area (see section 4.1.3) also contributes to decrease the number of scintillation photons that reach the PMTs. As a consequence, the energy reconstruction is position dependent. Since the SPMTs and LPMTs are part of two different systems, a NU correction specific to each of them must be determined.

The spherical shape of the JUNO central detector (CD) makes the number of PEs mostly radial dependent. However, the layout of the PMTs on its internal surface lead to a non-negligible dependence along the zenithal angle, referred to as θ in the following. The dependence along the longitudinal angle (Φ) is considered negligible in this study. The dependence of the total number of PEs on these three variables is shown in Figure 4.20. It shows that along the radial component, the number of PEs increases by ∼10% between events at the center of the CD and events occuring at a radius $R^3 \sim 3000$ m^3. Moreover, it drops by ∼10-15% when the events occur at the very edge of the acrylic sphere with

respect to events occuring at the center. Along the θ coordinate, the difference between the maximum and the minimum number of PEs is of ∼14%. These variations are not negligible.

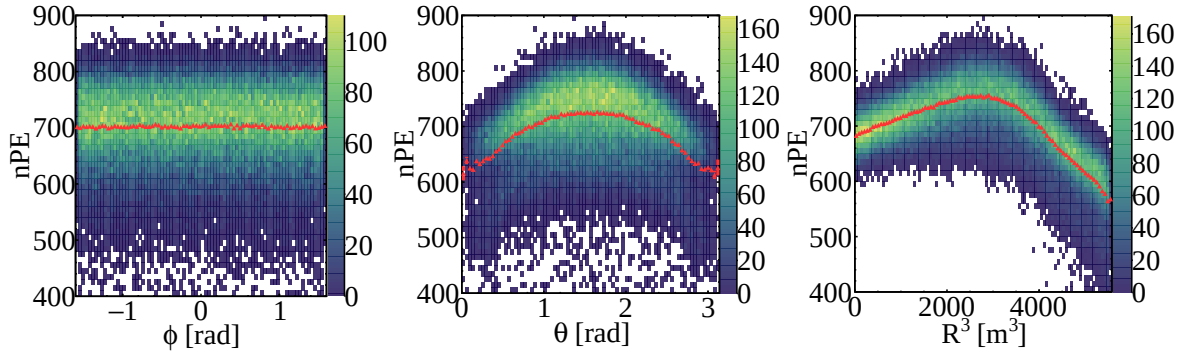

Figure 4.20: *The evolution of the nPE as a function of ϕ, θ and R for a batch of 15 MeV (E_{kin}) positron events uniformly distributed in the CD.*

As a consequence, the number of PEs must be corrected according to the position of the event, hence the need for a precise reconstruction of the events' position. The correction of the number of PEs following the event position is done with a correction factor that is determined by simulating 2.2 MeV gammas at different calibration points, that have been preliminary determined [239]. In real conditions, an AmC source will be deployed, but as explained previously, using solely 2.2 MeV gamma leads to a difference that is considered as negligible in this study. The calibration source is deployed in ∼245 points distributed on a vertical plane (X,Z), as shown in Figure 5.24 (Appendix). The calibration units that will be used to place the source at the different points allow to know the position of the source with a precision better than 3 cm (Chapter 2). In this study, we consider that the position of the calibration source is perfectly known. For each of these points, a batch of 10,000 events is simulated and a gaussian fit is performed in order to retrieve the average number of PEs, in the same way than in Figure 4.18. The possible tails that can appear in the spectrum - because of leakage effects like particles escaping the detector - are not fitted. If one wants to fit the tails, appropriate fit functions can be found in Ref. [282]. The correction factor is then calculated such as:

$$f_{corr} = \frac{nPE(R_{calib},\theta_{calib})}{Y_0} \tag{4.18}$$

where $nPE(R_{calib},\theta_{calib})$ is the average number of PEs at the calibration point and Y_0 is the energy scale. In order to determine the value of f_{corr} at any point in the detector, a Delaunay interpolation is performed with the ROOT [276] software. The map obtained after the interpolation is shown in Figure 4.21.

The correction factor is applied on the numer of PE using the reconstructed radius and zenithal angle (R_{rec} and θ_{rec}). The reconstructed vertices of the events that are rejected by the likelihood quality cut (see section 4.1.6) will not be used to correct for the detector NU. Since these vertices are reconstructed sometimes several meters away from the true vertex and the number of PEs varying a lot with the position, the estimation of the energy of these events would be completely skewed. In practice we could ignore these events but it means that many of them would be lost, especially in the low energy range, where the vertex reconstruction efficiency is of ∼70%. Here an alternative is tested.

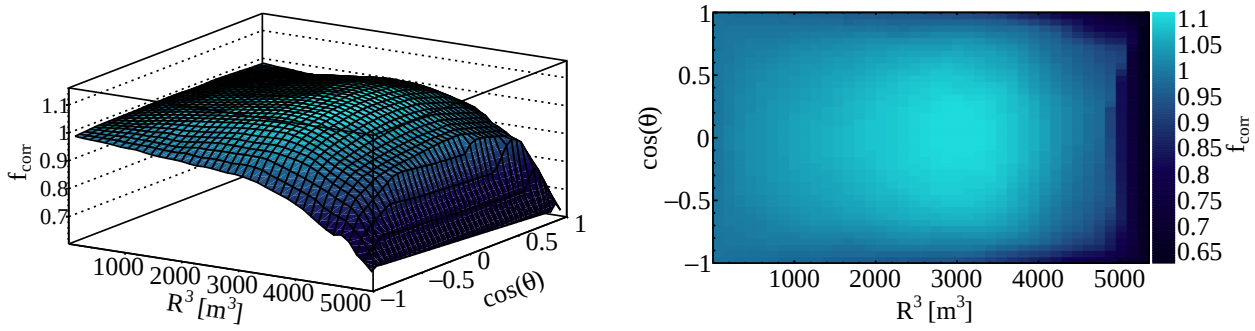

Figure 4.21: *Map of the non-uniformity correction factor following the R and θ coordinates. The* ***Left*** *plot is a 3D representation while the* ***Right*** *one is a 2D representation.*

When an event is identified as poorly reconstructed, the detector NU is corrected following a coarser correction factor - as shown in Figure 4.22 - which replaces the f_{corr} determined in Figure 4.21. This new correction factor was determined by comparing the total number of PEs for the poorly and correctly reconstructed events. To be fully consistent, the parametrisation should be done by comparing the total number of PEs of the poorly and correctly reconstructed events only for the ones that occured in the TR area, where the efficiency of the maximum likelihood method drops. Indeed, using all the events as it is done here adds the detector NU systematics effect that we don't want in this parametrisation specifically. However, at the time of this work, not enough simulation data were available. This parametrisation is fully reproductible with the calibration sources that are forseen to be used in JUNO. From Figure 4.22, an average correction factor $f_{corr} = 0.923$ – that is energy independent – is determined and is applied to any event with a poor reconstruction of the vertex.

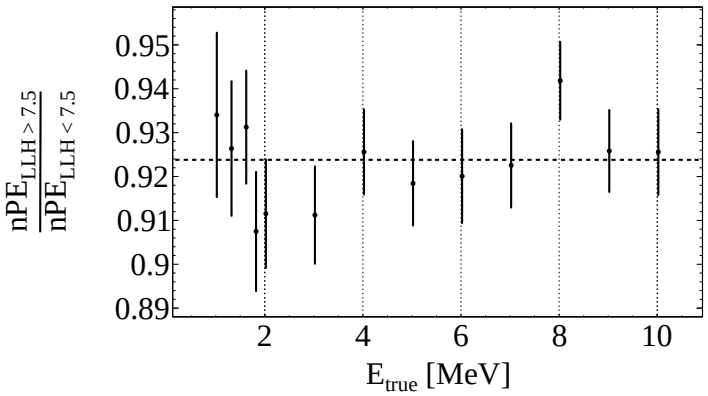

Figure 4.22: *The ratio between the total number of PEs for the poorly and well reconstructed events as a function of the energy. From this plot, an average correction factor* $f_{corr} = 0.923$ *is determined.*

4.2.4 Visible energy computation

This section details how the energy is determined and the applied corrections. Based on what has been detailed in the previous sections, we first reconstruct the energy using the energy scale and correct the value with the correction factor corresponding to the

reconstructed vertex: $f_{corr}(R_{rec},\theta_{rec})$. The result obtained is defined as E_{rec} :

$$E_{rec} = \frac{nPE(R_{rec},\theta_{rec}) - N_{DC}}{Y_0 \times f_{corr}(R_{rec},\theta_{rec})} \tag{4.19}$$

where $nPE(R_{rec},\theta_{rec})$ is the number of PEs reconstructed, Y_0 is the energy scale, $f_{corr}(R_{rec},\theta_{rec})$ is the NU correction factor corresponding to the reconstructed vertex and N_{DC} is the average number of dark counts expected from the SPMT system within the time window length for an event triggered by the JUNO global trigger system. In this study, we consider that $N_{DC} = \sim$13 PE/MeV.

Then, E_{rec} is corrected from the LSNL using f_{LSNL} (Figure 4.19, right plot) and the final reconstructed energy is defined as E_{vis}:

$$E_{vis} = \frac{E_{rec}}{f_{LSNL}} \tag{4.20}$$

If an event has a reconstructed energy higher than 12 MeV – which will happen for CCSN neutrino events – the LSNL correction value is set at 1.05, according to the trend of the right plot curve in Figure 4.19. Note that, in principle, the LSNL correction for reconstructed energies higher than 12 MeV could also be determined from the JUNO simulation in order to obtain more accurate correction values. When reconstructing a batch of events at a given energy, the energy resolution is derived from the distribution of E_{vis} and is computed as:

$$E_{res} = \frac{\sigma_{E_{vis}}}{E_{true}} \tag{4.21}$$

where $\sigma_{E_{vis}}$ is the standard deviation of the fit of the distribution – assuming that it follows a Gauss function – and E_{true} is the deposited energy (from the MC truth). The relative bias is defined as :

$$Bias = 100 \times \frac{E_{true} - E_{vis}}{E_{true}} \ [\%] \tag{4.22}$$

where E_{vis} is the mean of the fit of the distribution.

4.2.5 Energy resolution model

As the deposited energy increases, the evolution of the energy resolution is expected to follow a specific model. The modelling of the energy resolution is of crucial importance when it comes to estimate the uncertainties on a reconstructed energy spectra, for example. In a LS detector, the energy resolution as a function of the visible energy can be expressed such as:

$$\frac{\sigma_E}{E} = \sqrt{\frac{\sigma^2_{stochastic}}{E} + \sigma^2_{non-stochastic}(E)} \tag{4.23}$$

$\sigma_{stochastic}$ is the stochastic term and $\sigma_{non-stochastic}$ the non-stochastic one. In JUNO, the resolution is also expressed using the so-called *abc model*:

$$\frac{\sigma_E}{E} = \sqrt{\left(\frac{a}{\sqrt{E}}\right)^2 + b^2 + \left(\frac{c}{E}\right)^2} \tag{4.24}$$

where a corresponds to the stochastic term while b and c corresponds to the non-stochastic ones. The a term is mostly driven by the fluctuations of the nPE that follow a Poissonian statistics. In such case, the uncertainty on the number of PEs is computed such as $\sqrt{\text{nPE}}$

and the energy resolution is then proportional to $1/\sqrt{\text{nPE}}$. The latter shows that the energy resolution is expected to get better when the visible energy increases. Typically, with ∼40 PE/MeV, statistical term of the energy resolution is expected to be ∼15.8%. Several studies within the JUNO collaboration that consisted in simulating electron and positron events at the center of the detector considering only the LS and PMTs responses demonstrated that the "b" term vanishes when the Cherenkov light and quenching effects are disabled while it is of the order of 1% when these effects are enabled [283]. It was notably demonstrated that even if the Cherenkov light contribution to the nPE is corrected (see section 4.2.3.1), the corresponding statistical fluctuations add a constant noise to the nPE that eventually feed the "b" term [239, 284]. The "b" term is also driven by the capability to address the detector response non-unformity using the event vertex reconstruction. Finally, the "c" term is mostly driven by the PMTs Dark Noise. Indeed, the dark counts constitute additional PEs that do not come from the energy deposition in the detector. Since the number of dark counts is constant in a given time window, the "c" term linearily decreases with the visible energy. It is also important to mention that the aforementioned study of the energy resolution in JUNO [283] showed that the annihilation gammas from the positrons also contribute to the "c" term. The Figure 4.23 shows the contribution of the three terms to the model, assuming values that are close to that expected combining the two PMT systems of JUNO. It shows that the energy resolution is largely dominated by the PE stochastic fluctuations.

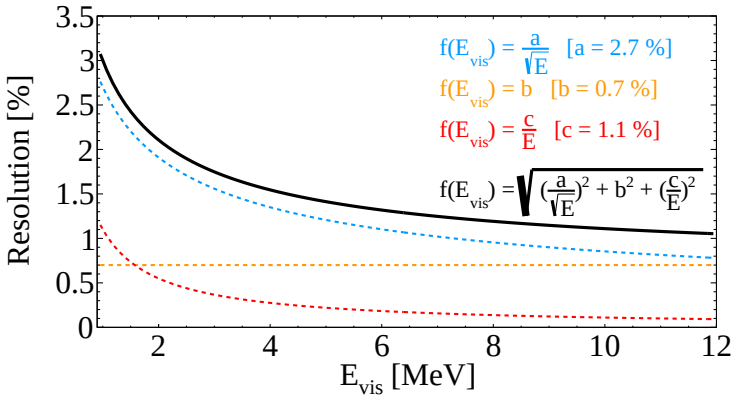

Figure 4.23: *Example of the energy resolution model used in this work (equation 4.24) for values of a, b and c that are close to that expected in JUNO (using all the PMTs).*

In order to better understand the impact of the different components of the detector response on the energy resolution and bias, the performance of the energy reconstruction presented here has been tested under different detector response configurations. More precisely, the distribution of the events in the CD is varied (center, uniform) and the SPMT system response[7] as well as the spatial reconstruction are enabled or disabled. The following configurations are tested:

- Events at the center of the CD, no SPMT system response, no spatial reconstruction [ideal case]
- Events at the center of the CD, SPMT system response, no spatial reconstruction [study of the impact of the SPMT system response]

[7]The SPMT system response includes: the SPMTs charge resolution, time resolution (TT and TTS), Dark Count Rate (DCR) as well as the CATIROC features for the time and charge measurements (see Chapter 3). The Quantum Efficiency (QE) is not considered as part of the SPMTs response since it is already implemented at the level of GEANT4.

- Events uniformly distributed in the CD, no SPMT system response, no spatial reconstruction [study of the impact of the non-uniformity correction]
- Events uniformly distributed in the CD, no SPMT system response, spatial reconstruction [study of the impact of the spatial resolution on the non-uniformity correction]
- Events uniformly distributed in the CD, SPMT system response, spatial reconstruction [more realistic case]

For each configuration, the consistency of the energy resolution with the abc model is verified by fitting the energy resolution against the energy with equation 4.24. This study also allows to identify ways to optimise the energy resolution of the SPMTs system.

4.2.5.1 Events at the center of the CD

First, the events are generated at the center of the detector, the true vertex is considered and the SPMT system response is not simulated. The reconstructed energy (E_{vis}) distribution is fitted with a Gauss function, the standard deviation σ and the mean μ are extracted and used to compute the energy resolution and bias using equation 4.21 and equation 4.22. The results for positrons with $E_{kin} = 0$ MeV are shown in Figure 4.24. The expected total visible energy is 1.022 MeV.

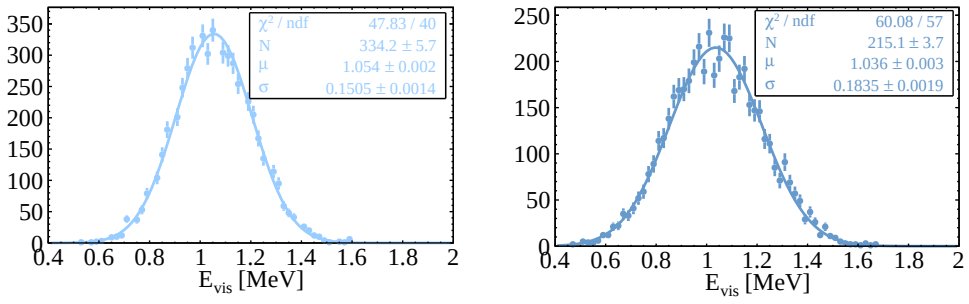

Figure 4.24: ***Left**: Distribution of the reconstructed energy for $E_{kin} = 0$ MeV positron events at the center of the CD, the SPMT system response is disabled. **Right**: Same plot as the one on the left, the SPMT system response is enabled.*

The resolution is of 14.7% when the SPMT system response is disable, which is below the bottom limit of 15.8% expected because of the stochastic term in case of a number of PEs of 40 per MeV. This inconsistency comes from the LSNL correction used in this study that does not exactly corresponds to that of the JUNO LS simulation (see section 4.2.3.1). The resolution at 1 MeV goes from 14.7% to 17.9% when the SPMT system response is simulated. This mostly arises from the SPMTs DN. Indeed, the number of dark counts in an event follows a Poissonian statistics with a standard deviation of $\sqrt{N_{DC}}$ where N_{DC} is the number of dark counts in a given time window. Although N_{DC} can be subtracted from the nPE - as in Eqn. 4.19 - the uncertainty on the latter and thus on the reconstructed energy increases correspondingly. As already mentioned in section 4.1.4, the signal time window – i.e the signal captured by the global trigger of JUNO – that is used for the reconstruction could be optimised in order to reject as many dark counts as possible without losing the LS signal. The impact of the offline event builder readout window (Chapter 3) on the energy resolution has not been studied. The resolution of the Single Photoelectron (SPE) – ∼30% on average for the SPMTs – also degrades the energy resolution but to a

lesser extent. It increases the PE uncertainty at the channel level. Finally, the readout electronics charge integration uncertainty is expected to have a negligible impact on the reconstruction of the number of PEs. In both case, the bias of the reconstructed energy is within 4%.

The Figure 4.25 shows the evolution of the energy resolution as a function of the energy, fitted with the model in equation 4.24. For this plot and all the following ones, the errors are computed and displayed but they can't be seen because they're smaller than the size of the points.

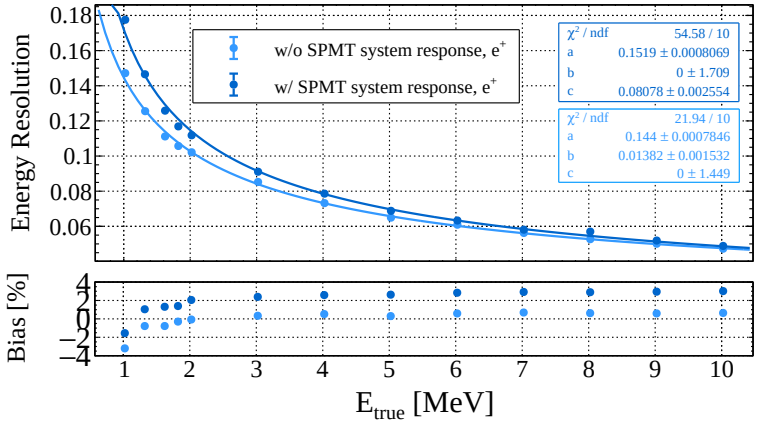

Figure 4.25: ***Top**: Energy resolution as a function of the visible energy for positrons for two different cases. In light blue, the SPMT system response is disabled while it is enabled for the dark blue curve. **Bottom**: Relative bias on the reconstructed energy.*

When the SPMT system response is disabled, the "a" term is 14.4%. The "b" term is 1.4% which can be explained by the cherenkov light and LS quenching effects. Finally, the "c" term is vanishing but with a large uncertainty so that no conclusion can be made on this value. The overall energy resolution being widely dominated by the statistical fluctuations of the nPE, it is likely that the systematic fluctuations that are expected to feed the "b" and "c" term are too tiny and are then not identified when fitting with the abc model.

When the SPMT system response is taken into account, "a" increases (15.2%) mainly because of the SPE resolution and the DN. Indeed, the PE amplification process that occurs in the PMTs follows a Poissonian distribution, adding stochastic fluctuations to the nPE. The "c" term is now 8.0%, mainly because of the DN as explained earlier. The "b" is now compatible with 0% but with a large uncertainty so that no conclusion can be done here. Finally, the bias is within ∼4% all along the energy range, in both cases. Also, the $\tilde{\chi}$ is 5.5 while it is 2.2 when the SPMT system response is disabled.

4.2.5.2 Events uniformly distributed in the CD

In this section, we consider events uniformly distributed in the CD in order to study the influence of the detector response NU as well as that of the vertex reconstruction on the energy resolution. In fact, in one case, the NU correction (section 4.2.3.2) is done by using the true event position and in the other case, the reconstructed position is used. The SPMT system response is disabled in this configuration. The events being uniformly distributed in the CD, the nPE is on average larger than the case of center-simulated

events leading to smaller statistical fluctuations (decrease of "a"). The results are shown in Figure 4.26.

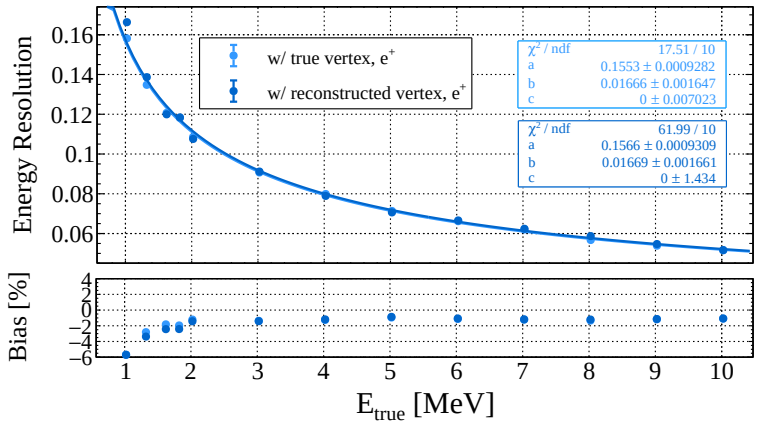

Figure 4.26: ***Top**: Energy resolution as a function of the visible energy of positrons using the true (light blue) and reconstructed (dark blue) vertex for the non-uniformity correction. The SPMT system response is disabled. **Bottom**: Bias on the reconstructed energy.*

First of all, comparing the value of a, b and c of the present cases with those of the previous one (events simulated at the center of the detector, no SPMT system response), in both cases the "a" term has actually increased from 14.4% (Figure 4.25) to 15.5% and 15.6% (Figure 4.26). This anomaly has not been investigated in this manuscript but cross-contaminations between the different terms (a, b and c) could explain this inconsistency. Concerning the "b" term it has also increased in both cases (by 0.3%) meaning that a residual NU remains even after the correction. The reason is that the NU correction map is generated with finite calibration points, it is not absolutely precise, hence the NU cannot be perfectly corrected. As in the previous case for which the SPMT system response is disabled, the "c" term vanishes. The $\tilde{\chi}$ of the light blue curve is of 1.7 and it increases to 6.2 when using the reconstructed vertex (dark blue), which mostly come from the points at low energy.

One can also notice that, whether using the true or the reconstructed vertex, the "b" term is the same – within uncertainties – meaning that the vertex reconstruction performance allows to keep the energy resolution at a level very close to the one using the true vertex. This is not totally correct at low energy (< 1.5 MeV). Indeed, we have seen (section 4.1.6) that the precision on the vertex reconstruction is of the order of $\sim$50 cm, with a non-negligible proportion of events that are rejected by the likelihood quality cut and for which the NU correction factor is less accurate (Figure 4.22). Hence the degradation of the energy resolution. In the contrary, when the visible energy increases, the precision of the spatial reconstruction gets totally negligible before the size of the detector and the efficiency increases. The NU correction is then more accurate.

Finally, concerning the bias, it is a bit larger than for events simulated at the center of the detector. This is explained by the events occuring at the edge of the acrylic sphere. Such events do not deposit all their energy in the LS - especially because of the annihilation the gammas that cover larger distances ($\sim$20 cm) - or a large fraction of the scintillation photons never reach the PMTs because of the reflections. The non-linearity correction is then also potentially false, hence the bias. This also contribute to degrade the resolution.

At higher energy, the fraction of energy deposited in the LS - mostly by the positrons - is larger, hence the smaller bias. A study focused on applying a fiducial volume cut could be done in order to reject the events occuring at the edges of the acrylic sphere. A quick test using the true vertex and a FV cut of 17.2 m showed that this enhances the energy resolution by 1% for E_{vis} = 1 MeV and by 0.3% for E_{vis} = 10 MeV.

In the configuration considered in the following, the events are uniformly distributed, the reconstructed vertex is used for the NU correction and the SPMT system response is abled. The results are shown in Figure 4.27. In the first case (light blue), the readout charge from CATIROC is used. The "b" term vanishes with a non-negligible uncertainty. The "c" term is non-zero since the DN is simulated. The resolution is E_{res} = 19.5% at 1 MeV. In the second case (dark blue), the number of CATIROC triggers is used instead of the nPE in order to mitigate the SPMT charge resolution, as explained in section 4.2.1. A smaller value of the "a" term is expected since the stochastic fluctuations of the SPMTs charge amplification process does not impact the reconstruction. The "b" and "c" term both increase by ∼3%. Comparing the two approaches, according to the points, the one using the CATIROC triggers allows to significantly enhance the energy resolution for energies between 1 MeV and 5 MeV, beyond, the resolutions of the two approaches get similar. However, according to the fit functions which $\tilde{\chi}$ are relatively bad (8.4 and 4.4) the use of the CATIROC triggers only allows to narrow the energy resolution down to 19.2% at 1 MeV. Also, as the visible energy increases, the probability to have several PEs in the 10 nanoseconds long integration window of the SPMTs is larger so that the relative bias of the reconstructed energy increases.

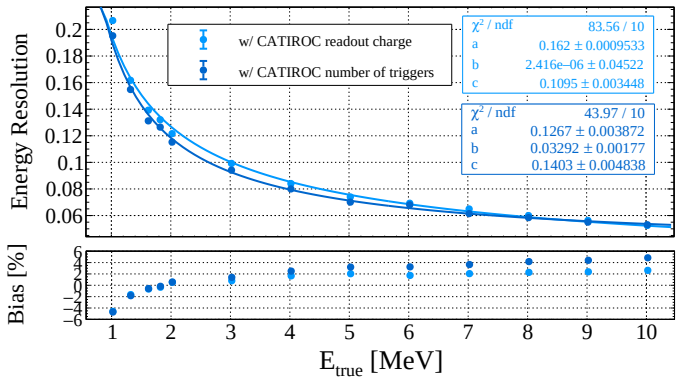

Figure 4.27: ***Top**: Energy resolution as a function of the visible energy for positrons uniformly distributed in the CD. In light blue, the energy is reconstructed using the readout charge of CATIROC to estimate the nPE, while in dark blue the number of CATIROC triggers is used.* ***Bottom**: Bias of the reconstructed energy.*

All the results presented in this section were obtained with a simulation of the JUNO detector. The effects that will have the strongest impact on the event reconstruction are already included in the software. However, the aging of the detector [239], that could lead to a decrease of the light yield, the LS opacification or to the loss of some SPMT system channels, is not taken into account here. This would represent new uncertainty sources on the energy reconstruction, which can be patially corrected by periodic calibration campaigns.

4.2.6 Application to the CCSN IBD neutrino events

The development of this energy reconstruction algorithm was primarily intended for use in the studies of CCSN neutrino bursts in JUNO. The information about the energy of the events is used in the selection of the IBD candidates, for example for the identification of the delayed signal (2.2 MeV). In addition, as explained in Chapter 1, the reconstruction of the CCSN neutrinos energy spectra is an important observable that will help constraining the explosion models. This section briefly presents the performance on a sample of prompt and delayed signals of IBDs from CCSN $\bar{\nu}_e$. The full detector and readout electronics simulation have been included. The plots comparing the true and the reconstructed energy spectra of both prompt and delayed signals are shown in Figure 4.28.

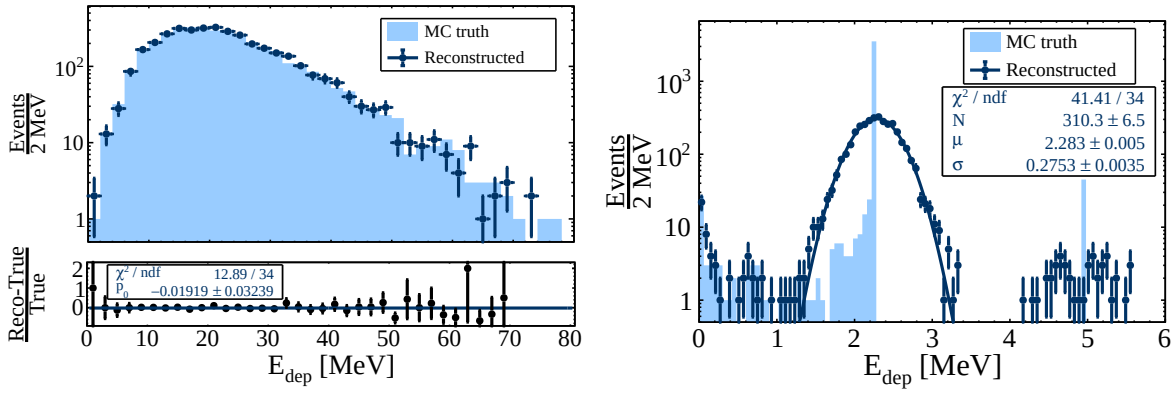

Figure 4.28: ***Left**: Comparison between the true prompt signal energy spectrum (blue histogram) and the reconstructed one (dark blue dots). The relative bias for each bin is shown on the bottom panel. **Right**: Comparison between the true delayed signal energy spectrum and the reconstructed one. The three structures are well identified but the resolution of the SPMT system in this energy range strongly smears them out.*

The bias of the prompt signal reconstructed energy spectrum with respect to the true one is <2% on average over the full energy range, as shown in the bottom panel of the left plot of Figure 4.28. Regarding the delayed signal spectrum, two different pics are expected, the first one around 2.2 MeV and the second one around 4.95 MeV. A third structure is observed on the left part of the plot. It comes from gammas that escaped the detector and did not deposit all their energy. The reconstructed spectrum does show these three structures, but the energy resolution of the SPMT system in this energy region is > 10%, hence the smeared shape. A gaussian fit of the Hydrogen peak shows that the energy resolution is about 12.05%. It is worst than the results presented in the previous section. The first reason arises from the vertex reconstruction, that is less precise for 2.2 MeV gamma (large energy deposition area, the event is less point-like) so the non-uniformity correction is skewed. The second one arises from the energy non-linearity correction used in the reconstruction. It is the one for positron while here we are reconstructing gammas. However, as it will be demonstrated in the next chapter, these precisions are satisfactory for the selection of the IBD events for CCSN neutrinos studies.

Summary

Some physics analyses like the measurement of the neutrino oscillation solar parameters or the reconstruction of the CCSN burst neutrinos signal can be done using the SPMT system only. They will notably include the reconstruction of the neutrinos energy spectra as well as a rigorous event selection. It is then mandatory to test the performance of the SPMTs as a standalone system for the energy and vertex reconstruction.

As a first step, a vertex reconstruction algorithm was developed. Indeed, the reconstruction of the position of the events is necessary to fully exploit the IBD events topology during the event selection. It is also essential to correct the error made on the energy estimate due to the non-uniformity of the detector. The algorithm consists of three different reconstruction steps. The first one uses the charge information to fastly get a preliminary estimation of the vertex. It serves as a starting point for a second approach that uses the time information and that enhances the resolution of the preliminary estimation by $\sim$70%. Finally, the position estimated by this second method is used as the starting point of a maximum likelihood method. The latter improves the resolution by $\sim$25%. The algorithm has been tested with different detector simulation configurations in order to understand the influence of the detector response on the reconstruction precision. In addition, electron and positron events were reconstructed in order to probe the impact of the energy deposition pattern on the reconstruction quality. The first point that this work highlighted is that using the time information to reconstruct the position of the events allows to get better resolutions. However, a fraction of the events, especially those with a small visible energy (< 3 MeV) or occuring in the TR area, are reconstructed far from the true vertex (several meters away). They can be identified and rejected thanks to the minimised likelihood function value. With the cut applied on the latter, for positrons at rest (1.022 visible energy from annihilation gammas), the resolution is 60 cm with a $\sim$70% efficiency while it is 15 cm with a 97% efficiency for 9 MeV ones. These resolutions are almost 2 orders of magnitude under the size of the detector which will allow a precise correction of the detector NU in the energy reconstruction process. The aforementioned partial efficiency has an impact on the IBD event selection, which is investigated in Chapter 5. Machine Learning (ML) techniques are under investigation beyond the scope of this thesis in order to retrieve the events that are poorly reconstructed by the method presented in this chapter.

In JUNO, the estimation of the energy deposited during an event is based on the number of PEs combined to the energy scale (nPE/MeV). The latter must be precisely determined by means of calibration sources. It is then possible to determine the energy of any event from the number of PEs recorded by the PMTs. However, the intrinsic non-linearity of the LS (LSNL) as well as the huge size of the detector make the energy scale not sufficient to precisely determine the energy. The calibration strategy of the JUNO experiment [239] includes a precise determination of the detector LSNL and NU using calibration sources. While waiting for JUNO data, in this work, the LSNL determined at Daya Bay - that is used for the preparation of the NMO analysis in JUNO - is taken, and the NU is determined using simulation data. The performance of the method is assessed by determining the resolution and the bias at different energies in the reactor neutrino energy range. As for the vertex recosntruction, different simulation configurations are set in order to understand the influence of the detector response on the quality of the reconstruction. The evolution of the resolution with the visible energy consistency with the "abc" model is systematically checked. It has been demonstrated that the energy resolution is dominated by the statistical fluctuations of the nPE due to the small energy

scale of the SPMT system. In addition, the DN from the PMTs as well as their charge resolution - to a lesser extent - seems to have the largest impact on the energy resolution and the performance. The impact of the DN could be reduced by optimising the event readout window (rejection of the dark counts) while the latter can be mitigated by using the number of CATIROC triggers rather than on the corresponding readout charge for the reconstruction of the energy. The performance of the vertex reconstruction algorithm allows a good correction of the detector response NU and the related systematic term is at the level of $\sim$2%. This number could be constrained even more thanks to a better efficiency of the reconstruction and to the application of a fiducial volume cut to the data. After the full simulation of the detector geometry and electronics, the resolutions given by the best fit are $\sim$19.2% at 1 MeV and $\sim$5.4% at 10 MeV with $\chi^2/d.o.f = 4.4$. In the CCSN energy range, the algorithm allows to obtain satisfactory results with an average relative difference between the true and the reconstructed spectra $< 2\%$. It is satisfactory to work on the reconstruction of the CCSN energy spectra with the SPMTs.

Chapter 5

CCSN neutrino energy spectra reconstruction with the SPMT system

Contents

The study of CCSN burst neutrinos with the SPMT system is motivated by two main aspects. The first one is that performing such analysis with two different PMT systems (LPMT and SPMT) – although they are only semi-independent – will allow to maximise JUNO's potential to extract the CCSN physics from the neutrino signal. The second one is that the small size of the SPMTs notably provides a fast response and smaller saturation effects which will surely constitute assets, especially for nearby CCSN[1]. The analysis presented in this chapter is a continuation of the tools presented in the two previous chapters. Indeed, as already mentioned, the rate capability of the SPMT system – see readout electronics performance and event builder (Chapter 3) – has a direct impact on the event vertex and energy reconstruction performance (Chapter 4) whereas the latter is of paramount importance for the physics analysis that are foreseen to be done with the SPMT system, including the CCSN analysis. As a reminder, the two main observables that will allow to probe the CCSN mechanisms and to retrieve its parameters are the

[1]It is worth pointing out that at the beginning of this PhD thesis, the SPMT was the only PMT system of JUNO that planned to operate in *trigger-less mode* (i.e all the data are sent continuously to the DAQ). Such feature constitutes an asset, especially when the event rate drastically increases (CCSN), it notably gives the opportunity to adapt the event builder strategy afterwards and to be sure not to loose data. However, recently, the LPMT system teams also developed a trigger-less mode (continuous transfer of the T, Q pairs – not the full waveforms – toward the DAQ.

flavor-wise neutrino luminosities and energy spectra (Chapter 1). As indicated in the title of this chapter, the work presented in the following focuses on the latter subject, using the SPMT system. In section 5.1, an event selection strategy that aims to perform a preliminary classification of the interaction channels – and thus of the incident neutrino flavors – is presented. Then, section 5.2 presents preliminary results on the energy spectra unfolding. The unfolding procedure applied here mitigates the detector response effects in the energy reconstruction of the IBD and Neutrino-Electron Elastic Scattering (νeES) selected samples. Such work is necessary before comparing the energy spectra to the ones predicted by models or to compare the energy spectra from different experiments.

5.1 Event selection

In Chapter 2, we have seen that the CCSN neutrinos can interact with the JUNO LS *via* six channels, they are recalled in Table 2.3. This table shows that some of the channels are exclusive to an (anti)neutrino flavor while (anti)neutrinos of all flavors can interact *via* some of the others. Thus, the determination of the flavor-wise neutrino luminosities and energy spectra primarily depends on the ability to distinguish the interaction channels of each other.

Neutrinos interaction channels in JUNO

Interaction Chan.	Type	Num. evts (@10kpc)
$\bar{\nu}_e + p \rightarrow e^+ + n$	CC	∼5000
$\nu + p \rightarrow \nu + p$	NC	∼2000
$\nu + e^- \rightarrow \nu + e^-$	NC	∼300
$\nu + {}^{12}C \rightarrow \nu + {}^{12}C^*$	NC	∼300
$\nu_e + {}^{12}C \rightarrow e^- + {}^{12}N$	CC	∼100
$\bar{\nu}_e + {}^{12}C \rightarrow e^+ + {}^{12}B$	CC	∼100

Table 2.3: *Number of neutrino events in JUNO with their corresponding interaction channels for a typical CCSN at a distance of 10 kpc, where ν collectively stands for neutrinos and anti-neutrinos of all flavors.*

Some of these interaction channels (IBD and CC interactions on ^{12}C) produce a coincidence between two signals while the others (νpES, νeES and NC interaction on ^{12}C) result in a single one. Moreover, each of these signals lie in specific visible energy range, as show in Figure 5.1.

Thus, before describing in detail the selection strategy and its performance, the spatial and temporal *topology* of the events with two signals as well as the typical visible energy of each signal type are introduced. They will constitute the main *selection criteria* in this analysis. In Chapter 3, we have seen that the distance to the CCSN is the parameter that has the biggest impact on the number of neutrino interactions (and rate) in JUNO. In addition, at a fixed distance, the two CCSN explosion models available in the JUNO simulation software (Garching and Nakazato) also lead to differences in the total number of events, event rate as well as in the neutrino energy spectra etc. Thus, the optimal selection cuts – that would allow to properly select the different channels limiting the contaminations between them – vary according to these parameters. Since 10 kpc is the most probable distance to the next galactic CCSN, the study presented in the following is done with CCSN progenitors at such distance. Also, the simulation files used for the analysis presented in the following were produced using the Garching model with the following configuration:

- Shen et. al equation of state

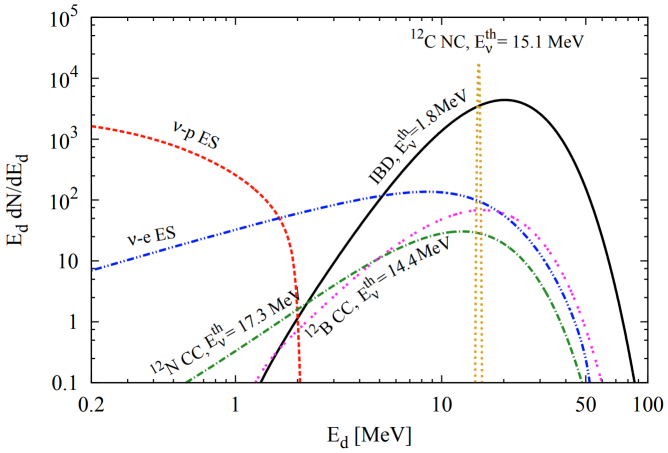

Figure 5.1: *The energy spectra of the different interaction channels in the JUNO detector for a typical CCSN at 10 kpc. Taken from [76].*

- 25 M$\odot$
- No neutrino opacities

Such configuration was chosen because the number of neutrino interactions and the event rate are in the average of all the configurations available for the two models.

5.1.1 Event topology and visible energy

The event topology and visible energy are studied after having simulated large samples of each of them using the model presented above. The detector and readout electronics simulations are included, and the events are reconstructed following the process described in Chapter 4. Each events are reconstructed independently of the others. For each channel, the reconstructed and true energy spectra are compared. The spatial and temporal coincidences of the double signal events obtained from the reconstruction are also compared to those from the MC truth.

Inverse Beta Decay (IBD)

The performance of the vertex and energy reconstruction of IBD events from CCSN $\bar{\nu}_e$ was already presented and discussed in Chapter 4, respectively in section 4.1.7 and section 4.2.6. The plots are shown again in this paragraph for convenience, the reader can refer to the aforementioned sections for details about them. The temporal coincidence that, in the analysis, is computed by subtracting the first hit time of the prompt signal to that of the delayed one is also shown. It is compared to the subtraction between the time of creation of the positron and the neutron capture time (Figure 5.2). The distributions are the same, which is expected since the possible difference induced by the scintillation photons travel time are of the order of the tens of nanoseconds, well below the average temporal difference between the positron creation time and the neutron capture time that is of $\sim$220 µs. The impact of the reconstruction performance on the event selection is presented later in this chapter.

νeES and νpES

Figure 5.3 compares the true and reconstructed spectrum for νeES (left) and νpES (right) events. The νeES spectrum ranges from 0 to 50 MeV. It is worth pointing out that whereas the energy spectra for the other interaction channels compare the true and reconstructed

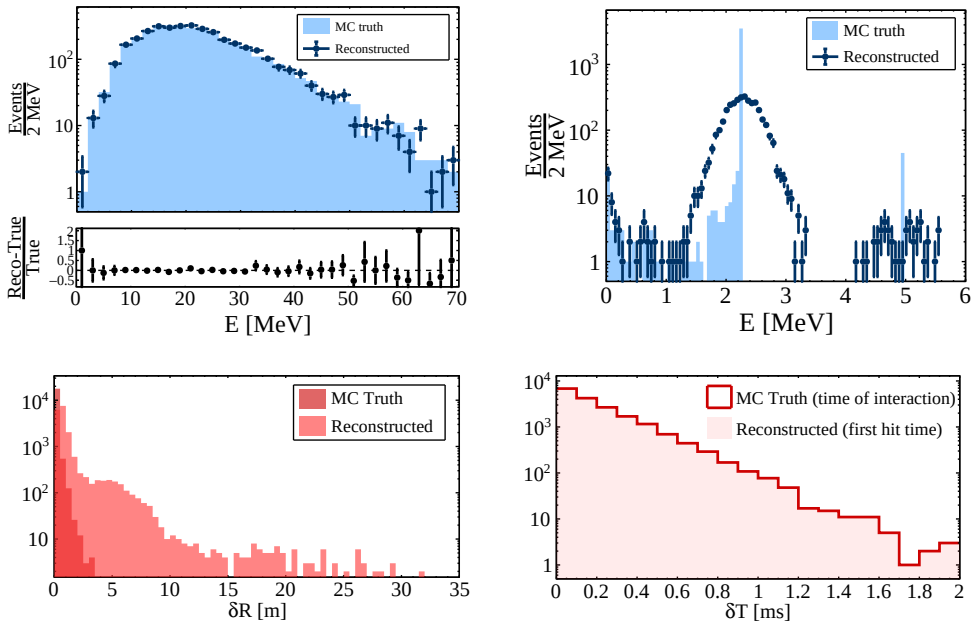

Figure 5.2: ***Top left**: Comparison of the true (blue histogram) and reconstructed (dark blue dots) IBD prompt signal energy spectrum. The relative bias for each bin of the histogram is shown on the bottom panel. **Top right**: Comparison of the true and reconstructed IBD delayed signal energy spectrum. **Bottom left**: 3D spatial distance between the IBD prompt and delayed signals. The results from the MC truth are shown in dark red while those from the reconstruction are shown in pink. **Bottom right**: Temporal difference between the IBD prompt and delayed signals.*

deposited energy – i.e after correction of the Liquid Scintillator Non-Linearity (LSNL) – the νpES one compares the true *visible* energy – i.e before the correction of the LSNL – to the reconstructed one. Indeed, as detailed in Ref. [285], the scintillation light is highly quenched for proton energy depositions in liquid scintillators so that the number of scintillation photons produced is way smaller than for gammas, electrons and positrons at equal deposited energies. Yet, the event selection energy cuts optimisation and the subsequent event selection on a "blind" data file presented later in this chapter have been done with events whose energy was systematically corrected from the LSNL (following the energy reconstruction procedure presented in Chapter 4). To be fully consistent, in the future, the optmisation of the selection cuts and the selection itself should be repeated with events whose reconstructed energy is not corrected from the LSNL. In fact, such correction must be done after the event selection, once the particle type have been identified (when it is possible). Concerning this work, since the LSNL of positrons, electrons and gammas are relatively close to each other (within a few percent at most), especially in the CCSN energy range where they all tend to saturate (see Ref. [229] for gammas and positrons LSNL at Daya Bay and Ref. [239] for those implemented in the JUNO simulation software) it is assumed that the energy reconstruction procedure adopted is reasonable and that it has no significant impact on the results. The visible energy spectra of the νpES shown here ranges from 0 to 3 MeV and the large energy resolution of the SPMT system in this energy range tends to distort the energy spectrum.

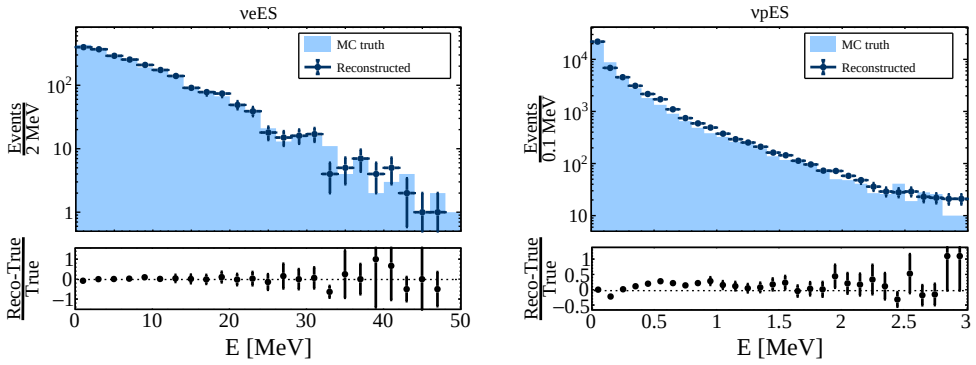

Figure 5.3: ***Left**: Comparison of the true (blue histogram) and reconstructed (dark blue dots) νeES energy spectrum. The relative bias for each bin of the histogram is shown on the bottom panel. **Right**: Comparison of the true and reconstructed νpES energy spectrum. The relative bias for each bin of the histogram is shown on the bottom panel.*

CC and NC on ^{12}C

The upper plots of Figure 5.4 compare the true and reconstructed spectra for the prompt (left) and delayed (right) signals of the $\bar{\nu}_e + ^{12}C \rightarrow e^+ + ^{12}B$ reaction. The prompt signal ranges from 0 to 60 MeV while the delayed one ranges from 0 to 13 MeV. The lower plots show the equivalent distributions for the $\nu_e + ^{12}C \rightarrow e^- + ^{12}N$ reaction. Here, the prompt signal also ranges from 0 to 60 MeV while the delayed one ranges from 1 to 17 MeV.

The spatial and temporal coincidence between the two signals is shown in Figure 5.5. The upper plots show the distributions for the $\bar{\nu}_e + ^{12}C \rightarrow e^+ + ^{12}B$ reaction. Even if the temporal coincidence is of the order of the tens of miliseconds, the 3D spatial difference[2] is of the order of a few tens of centimeters, representing a strong asset for the selection since the probability to have several events in such a small space is weak in a detector as large as JUNO. The lower plots show the same distributions but for the $\nu_e + ^{12}C \rightarrow e^- + ^{12}N$ reaction. The temporal coincidence is similar to the previous case and here also, the selection can certainly benefit from the strong spatial correlation between the signals. All in all, the topologies of the two CC interactions on ^{12}C are very similar and it will be difficult to distinguish them from each other.

Finally, the Figure 5.6 compares the true and reconstructed energy spectra of the 15.11 MeV gamma from the $^{12}C^*$ de-excitation. The finite energy resolution of the SPMT system smears the reconstructed spectrum but it is well centered around 15.11 MeV. Also, the plot shows that a small fraction of the events deposit less energy. These events correspond to gammas that can escape from the acrylic sphere before having deposited all their energy. A FV cut can be applied to reject these events during the selection.

5.1.2 Event selection strategy

The major step forward anticipated from the detection of neutrinos from the next galactic CCSN compared to the SN1987A is the number of interactions expected in the neutrino detectors. Indeed, thanks to the present (SK) and future (JUNO, HK, DUNE...) large scale neutrino detectors, the statistics should be increased by one to two order(s) of magnitude at an equivalent distance (∼50 kpc), allowing to precisely constrain the CCSN explosion models. The most probable distance has been evaluated to be ∼10 kpc and in such case, JUNO is expected to be able to reconstruct the luminosities and energy spectra of the three neutrino flavors thanks to the IBD and νpES detection channels. We have

[2]The 3D spatial difference between two signals position is computed such as $\delta R = \sqrt{(X_1 - X_2)^2 + (Y_1 - Y_2)^2 + (Z_1 - Z_2)^2}$.

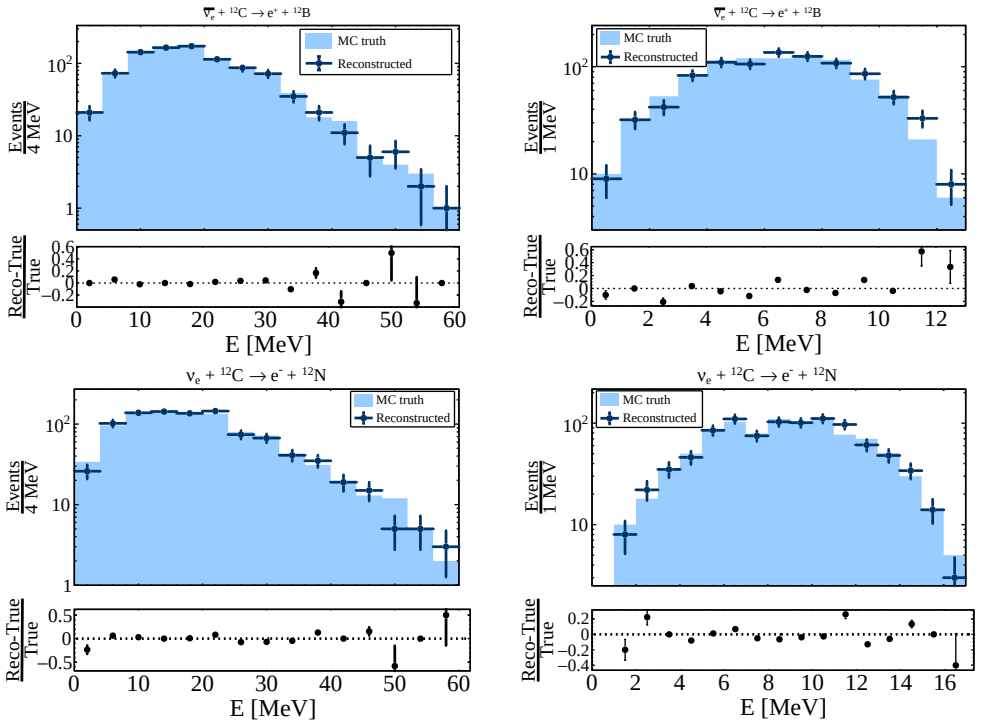

Figure 5.4: ***Top left**: Comparison of the true (blue histogram) and reconstructed (dark blue dots) prompt signal energy spectrum of the $\bar{\nu}_e$ + ^{12}C reaction. As for the other plots of this Figure, the relative bias for each bin of the histogram is shown on the bottom panel. **Top right**: Comparison of the true and reconstructed delayed signal energy spectrum of the $\bar{\nu}_e$ + ^{12}C reaction. **Bottom left**: Comparison of the true and reconstructed prompt signal energy spectrum of the ν_e + ^{12}C reaction. **Bottom tight**: Comparison of the true and reconstructed delayed signal energy spectrum of the ν_e + ^{12}C reaction.*

seen that four additional interaction channels, from which $\mathcal{O}(100)$ events are expected, are also relevant for JUNO. The challenges for the selection of the six channels are quickly described below and further investigated later in this section:

- **Inverse Beta Decay (IBD)** The coincidence between two signals and the fixed energy of the delayed one constitute a powerfull discrimination tool that makes the IBD the golden detection channel for JUNO. This channel is only sensitive to $\bar{\nu}_e$.
- **Neutrino-Proton Elastic Scattering (νpES)** The νpES consist in single signals that widely dominates in the lower energy range (0 to 3 MeV). In this work, the selection of the νpES can only rely on the visible energy criteria. Given the low energy resolution of the SPMT system in such range, the selection presented in the following does not focus on this channel. This channel is sensitive to the three (anti)neutrino flavor.
- **Neutrino-Electron Elastic Scattering (νeES)** The νeES also consists in single signals whose visible energy ranges between 0 and 50 MeV. The selection of these events can only rely on the energy selection criteria. It is important to point out that the energy spectrum is superimposed with almost all the spectra of the other channels (Figure 5.1), making the selection of them challenging. This channel is sensitive to the three (anti)neutrino flavors even if it favors ν_e [146].
- **NC interaction on ^{12}C** This channel results in a gamma with a fixed energy of 15.11 MeV. The selection of it can also only rely on the energy criteria. Moreover,

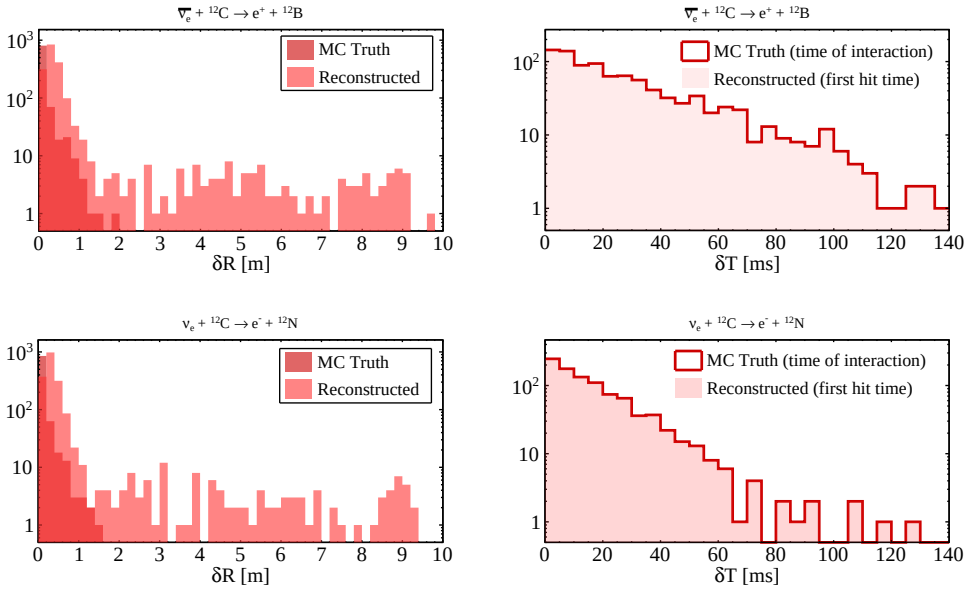

Figure 5.5: ***Top left**: The 3D spatial distance between the prompt and delayed signals from the $\bar{\nu}_e$ + ^{12}C reaction. The results from the MC truth are shown in dark red while those from the reconstruction are shown in pink. **Top right**: The temporal difference between the prompt and delayed signals from the $\bar{\nu}_e$ + ^{12}C reaction. **Top left**: The 3D spatial distance between the prompt and delayed signals from the ν_e + ^{12}C reaction. **Top right**: The temporal difference between the prompt and delayed signals from the ν_e + ^{12}C reaction.*

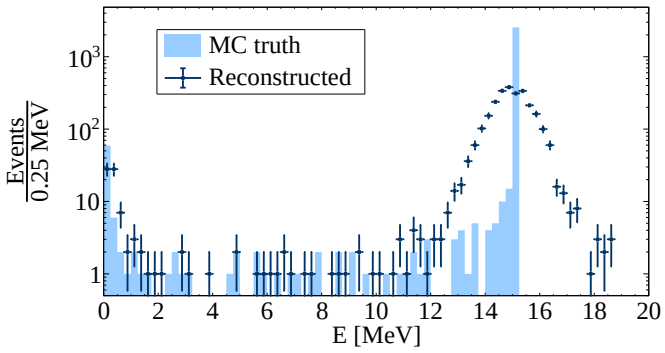

Figure 5.6: *The comparison between the true (blue histogram) and the reconstructed (dark blue dots) energy spectrum of 15.11 MeV gamma events from $^{12}C^*$ de-excitation.*

this channel only gives an information on the (anti)neutrino luminosities (all flavors), not on the energy spectra, making this channel irrelevant regarding the objective of this work.

- **CC interactions on ^{12}C** These channels also consist in a coincidence between two signals, constituting a powerfull dscrimination power. However, the large temporal separation between the two signals makes the selection of them more difficult than that of the IBDs. Note that for one of the channels, the prompt signal is an electron and the delayed signal is a positron while it is the inverse for the other one. Thus, distinguishing between these two channels is challenging and would require to be able to distinguish between electrons and positrons. Such a possibility was not explored in this PhD thesis. These channels are sensitive to $\bar{\nu}_e$ and ν_e.

In the end, the two most relevant channels *for the SPMT system* are the IBD – whose high statistics and topology makes it the perfect channel to detect $\bar{\nu_e}$ – and the νeES that is the only channel that offers the opportunity to probe the heavier lepton flavors (ν_μ, ν_τ, $\bar{\nu_\mu}$ and $\bar{\nu_\tau}$). As a consequence, the selection strategy has been organised as follows. It is designed for the selection of the IBDs and νeES by making the most of the interaction channel topologies:

1. Selection of the IBDs using the spatial and temporal correlation between the prompt and delayed signals. The $\bar{\nu_e}$ spectrum can be extract from this channel.
2. Selection of the CC interactions on ^{12}C. Since their visible energy spectra overlap with that of the νeES, they must be removed from the data before selecting the latter. They are selected using the spatial and temporal correlation between the prompt and delayed signals.
3. Selection of the NC interactions on ^{12}C. The signal consists in a gamma ray with a fixed energy of 15.11 MeV that also overlaps with the νeES spectrum.
4. At this stage of the selection, all the events populating the higher visible energy range (1-100 MeV) are expected to be selected except the νeES events. Then, they can be identified according to their visible energy only.

5.1.3 Simulation for event selection

Before starting the analysis, the events are generated using the CCSN generator implemented in the JUNO simulation software using the model indicated in introduction of section 5.1, the distance is 10 kpc, the detector as well as the electronics simulation are processed. The events are ordered on a time line as a function of their first hit time on the SPMTs and the event builder presented in Chapter 3 (section 3.4) is applied. Note that the potential false trigger events of the event builder are reconstructed and taken into account in the analysis. As a reminder, in such configuration, ∼1-2% of the events are piled-up and the event builder allows to separate ∼75% of them. In addition, the number of events expected per 2 milliseconds (maximum temporal difference between the prompt and delayed signal of the IBD) is ∼0.75 when the event rate reaches its maximum (∼200 ms after the start of the burst). The diameter of the acrylic sphere is ∼35.4 meters. Thus, the probability that two consecutive neutrino interactions occur in a "virtual" sphere of 4 meters of diamater (maximum spatial difference between the prompt and delayed signal of the IBD) is ∼1% according to the ratio between the two corresponding volumes. The event rate from the detector intrinsic radioactivity is expected to be 60 Hz without Fiducial Volume (FV) cut and ∼7 Hz with FV cut of 17.2 meters (radius), considering an energy threshold of 0.7 MeV [173]. Given that the energy threshold of the event builder is ∼0.8 MeV and that $\sim 10^4$ neutrino interactions are expected within a few seconds, the intrinsic background of the detector is considered as negligible and is consequently not simulated. A FV cut of 17.2 meters is applied during the event selection. Note that this cut is only applied on the events that are identified as well reconstructed by the likelihood quality cut of the vertex reconstruction algorithm (see Chapter 4). Those that does not pass the likelihood quality cut are not rejected from the data file and are analysed anyway.

In order to evaluate the impact of the event reconstruction on the selection, the latter is performed twice. Once using the MC truth information (true vertex, true energy, true timing) – i.e assuming that the detector is perfect – and once after having run the simulation chain described in the previous paragraph. The selection cuts are optimised on a set of data files and then the selection is applied on other data files which data are "blinded" in order not to bias the estimate of the selection performance. It is important

to mention that the selection using the MC truth information also allows to estimate the limits of the selection strategy and technique presented here. In order to estimate the effectiveness of the selection, three quantities are defined:

$$\epsilon = \frac{N_{sel,i}}{N_i} \quad \text{and} \quad \phi = \frac{N_{sel,i}}{N} \quad \text{and} \quad \theta = \frac{N_{unsel,i}}{N_i} = 1 - \epsilon \tag{5.1}$$

where ϵ, ϕ and θ indicate the efficiency, the purity and the loss, respectively. Also, $N_{sel,i}$ is the number of events of the i-th signal type – e.g. IBD prompt signal, IBD delayed signal, νeES, νpES etc. – in the selected sample, N_i is the total number of events for the i-th signal type in the data file, N is the number of events in the selected sample and $N_{unsel,i}$ is the number of events of the i-th signal type that were not selected. Requirements on the efficiency, purity and loss of the selected samples are used to determine the optimal selection cuts. It mainly consists in a trade-off between preserving the purity of the sample – notably to conserve the shape of the energy spectrum – and keep a significant number of events in the selected sample – to have a reasonable statistical uncertainty. The number of interactions expected in the different channels going from a hundred to several thousands, the preferred purity and loss criteria are not always the same. Typically, concerning the IBD, for which several thousands of events are expected, strong purity constraints can be imposed. Indeed, even if some events are lost, in the end the statistics of the selected sample will remain large enough. In the contrary, for the νeES for which the number of events expected varies between 100 and 300, the margin on the loss is smaller. In the following sub-sections, they are systematically stated, for each channel. Also, the results and discussions are always those obtained with the full simulation chain (detector, electronics, reconstruction etc.) and the results obtained with the MC truth information are indicated at the end of each sub-section for comparison.

5.1.4 Selection of the IBDs

In section 5.1.1, we have seen that the prompt and delayed signals of the IBD lie in specific energy ranges and that they are temporally and spatially correlated. These information are used to tagg so-called *IBD candidates* among all the events present in the data. The strategy to identify them is the following:

1. Identify a prompt signal candidate based on a specific visible energy criteria.
2. Open a time window with a specific length.
3. Identify a delayed signal candidate in this time window, based on a specific visible energy criteria.
4. Calculate the spatial distance between the prompt and the delayed candidates.
5. The delayed candidate found must be the only existing candidate in the time window. This is referred to as the *unicity* condition in the following.

The cuts applied on the selection criteria (time, vertex and energy) must be optimised in order to select as many IBDs as possible (high efficiency) without selecting signals from other interaction channels (high purity). First, the optimal energy windows are determined and then the temporal and spatial cuts are optimised.

5.1.4.1 Prompt and delayed energy window

As seen previously, the IBD prompt signals occupy the entire energy range of the events. The Figure 5.7 shows that defining the prompt signal energy cut such as $\mathbf{E_{vis} > 3.0\ MeV}$ allows to select $> 99.5\%$ of them and to reject $\sim 98\%$ of the νpES and IBD delayed signals.

Furthermore, such a cut would also allow to reject 100% of the events from the JUNO detector intrinsic radioactivity. No improvements are identified with a different energy cut when using the MC truth information, therefore the same cut is used.

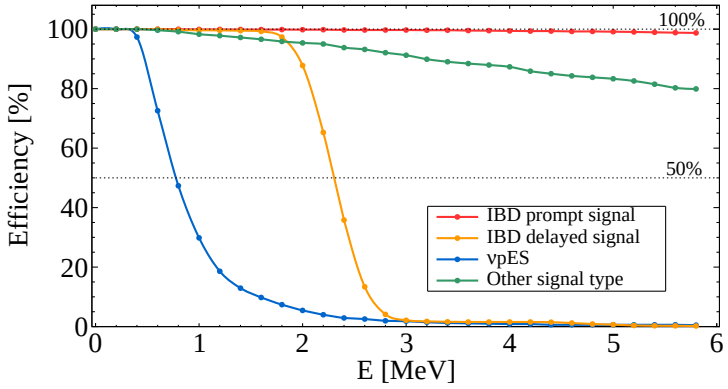

Figure 5.7: *The selection efficiency (ϵ) as a function of the inferior visible energy cut for different signal types. The green line – labelled as "other" – include all the signal types that are not represented by the other colored line.*

The delayed signal energy window is defined as $\mathbf{E_{vis} \in [1.6; 6.0]\ MeV}$. The lower limit of 1.6 MeV aims to reject as many νpES event as possible. Indeed, given the low reliability of the vertex reconstruction in the low energy range, the objective is to reject as much signal as psossible before the spatial coincidence cut. The upper limit of 6.0 MeV allows to tag the events from the neutron capture on ^{12}C and to reject the signals from the other channels that have higher visible energies. With such energy window, $>$ 99% of the delayed signals are selected and $\sim$90% of the νpES signals are rejected. The optimal energy cut when using the MC truth information is $E_{vis} \in [1.6; 5.0]$ MeV. The upper cut is lower since the delayed signal $^{12}_{6}$C peak is not smeared by the energy resolution.

5.1.4.2 Prompt and delayed coincidence

The temporal and spatial cuts are optimised by running the IBD candidate selection with different $\delta T/\delta R$ pairs (where δT is the upper limit of the time window and δR is the upper limit for the 3D spatial difference between the two signals). The energy cuts defined above are used and the aforementioned unicity condition is applied. For each pair, the purity (ϕ) of the selected sample as well as the loss (θ) are computed. To check if a pair selected is an actual IBD, it has to meet the three following conditions:

- The prompt candidate is a positron from and IBD (and not from another channel).
- The delayed candidate is indeed a 2.2 MeV gamma from an IBD.
- Both candidates originate from the same $\bar{\nu_e}$

Given the size of the detector ($\sim$35 meters), the typical spatial distance between a prompt and a delayed signal ($\sim$1 meter), the fraction of IBDs expected in the total number of neutrino interactions ($\sim$40%) and the maximum neutrino interaction rate for the model used ($\sim 10 \cdot \mathrm{ms}^{-1}$) it is quite unlikely that prompt and delayed signals from several IBD are mixed after applying the spatial cut. The purity and loss against different $\delta T/\delta R$ pairs are shown in Figure 5.8.

The pair that maximises the ratio ϕ/θ is retained, provided that $\phi > 99\%$. Indeed, the powerful selection criteria of the IBD and the large statistics expected allow to impose such requirement on the purity. The operation is repeated on five different files from the

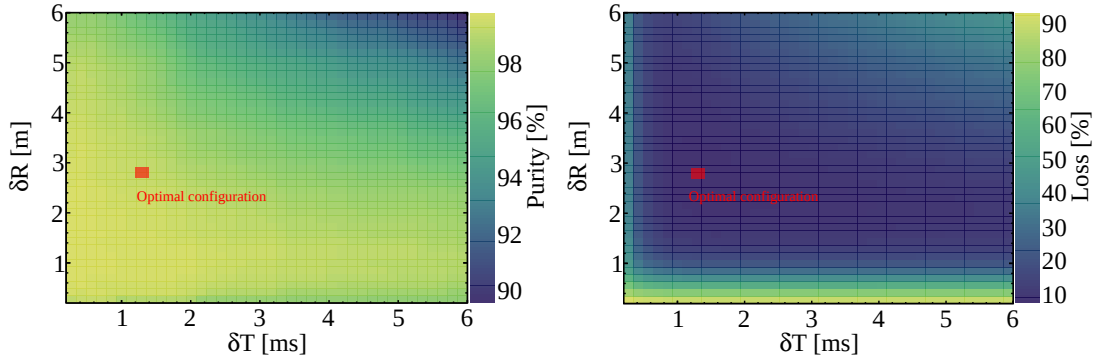

Figure 5.8: ***Left**: Example of the evolution of the purity of a selected sample for different $\delta T/\delta R$ pairs. **Right**: Example of the IBD loss for different $\delta T/\delta R$ pairs. On both plots, the optimal configuration (calculated with the ratio x/y) is indicated.*

same model but generated with different seeds. The optimal δT and δR are obtained by averaging the five results. The best cuts are $\boldsymbol{\delta T < 1.20\ ms}$ and $\boldsymbol{\delta R < 2.76\ m}$. The corresponding purity and loss are ∼99.4% and ∼7.1%, respectively. The main reason for such a large fraction of IBDs lost is mainly the poor reconstruction of the delayed signals. Indeed, we have seen that they can be reconstructed several meters away from the true vertex so that they do not pass the spatial coincidence cut. The bottom left plot of Figure 5.2 that shows the distribution of the reconstructed prompt-delayed δR, one can see a bump between 3 and 10 meters. As a consequence, after the selected IBD candidates have been removed from the data, a second attempt is performed to try to retrieve the unselected IBDs by relaxing the δR cut. The latter needs to be optimised again, together with the temporal coincidence cut. The pair that maximises the ratio ϕ/θ is selected, the requirement on the purity is such as $\phi > 95\%$. The analysis showed that if the purity required is too high, the number of IBDs that are retrieved is too small. The best cuts are $\boldsymbol{\delta T < 0.60\ ms}$ and $\boldsymbol{\delta R < 5.16\ m}$. As expected, the relaxed spatial cut must be combined with a tighter temporal cut in order to conserve a high purity of the selected sample. The corresponding purity and loss are in average ∼95.8% and ∼70.0%, respectively. Such a configuration allows to retrieve ∼30% of the untagged IBDs without degrading too much the purity of the selected sample. In the end, the purity and the loss of the IBD selected sample – after the two selections – are the following:

$$\phi = 99.3\% \quad \text{and} \quad \theta = 4.8\% \tag{5.2}$$

Most of the remaining untagged IBDs have a prompt-delayed signal distance that is larger than the cut because of delayed signals that are poorly reconstructed. The Figure 5.9 compares the normalised IBD prompt signal true energy spectrum, the one of the selected IBD prompt signal sample and the one of the unselected IBD prompt signals. It shows no significant energy bias in the selected sample, except in the low energy range (< 3 MeV) which is explain by the prompt signal energy selection window that indeed starts at 3 MeV.

A new vertex reconstruction algorithm based on Machine Learning (ML) techniques is currently under development at Subatech. The first results showed that, in contrary to the algorithm presented in this manuscript, no event is reconstructed far – i.e several meters away – from the true vertex, even those occuring in the Total Reflection (TR) area. Such performance should allow to get an equivalent efficiency/purity with only one selection. The optimal cuts from the MC truth information are $\delta T = 1.64$ ms and $\delta R = 1.52$ m. The resulting purity and loss are $\phi = 99.8\%$ and $\theta = 1.2\%$, respectively. The loss is due

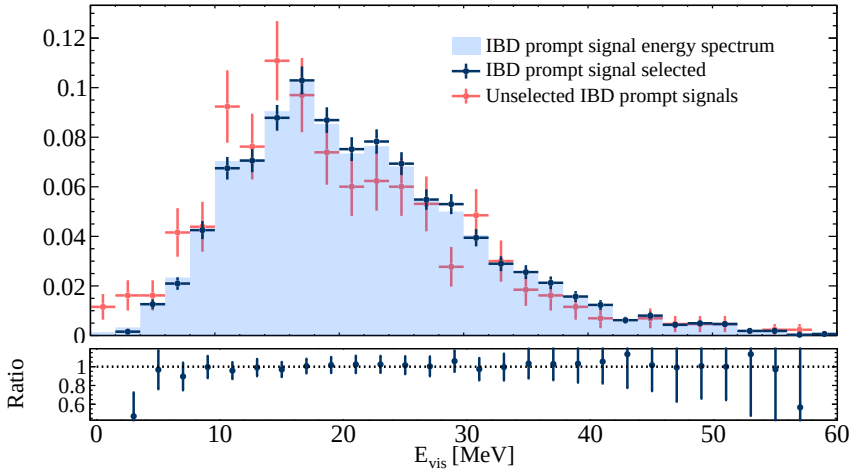

Figure 5.9: ***Top**: Comparison of the IBD prompt signal true energy spectrum, the one of the selected IBD prompt signal sample and the one of the unselected IBD prompt signals. **Bottom**: Ratio plot between the true energy spectrum and the selected one.*

to the unicity condition.

5.1.5 Selection of CC interactions on ^{12}C

The CC interactions on ^{12}C selection strategy is the same than that for the IBDs, it relies on the prompt-delayed signal coincidence as described at the beginning of section 5.1.4. The effectiveness of the selection is also evaluated.

5.1.5.1 Prompt and delayed energy window

The Figure 5.10 shows that the selection efficiency of the prompt signals remains 100% if a lower selection cut on the visible energy is set at 1.6 MeV. As for the IBDs, such a cut allows to eliminate part of the νpES and other low energy signals that could contaminate the prompt signal selected sample. We have seen in section 5.1.1 that the visible energy of the prompt signals of both CC interaction on ^{12}C does not exceed 60 MeV. Since the IBD selection strategy presented in the previous section does not allow to obtain a 100% efficiency, some prompt signal – whose energy varies from 0 to 100 MeV – remain in the data. Thus, in order to limit the CC interaction on ^{12}C prompt signal contamination by the remaining IBD prompt signals, the energy window is defined as $\mathbf{E_{vis} \in [1.6; 60.0]\ MeV}$. It is also used in the selection using the MC truth information.

The energy range of the delayed signal is smaller than that of the prompt signal. Given the energy spectrum of the ^{12}B decay, a relatively low limit of the energy window is required to have a 100% selection efficiency, as shown in Figure 5.10. However, given the non-perfect IBD selection efficiency, some IBD delayed signals (2.2 MeV) remain in the data after the IBD candidate selection and then a too low energy selection cut leads to a heavy contamination of the selected sample. For this reason, the delayed signal energy window is defined as $\mathbf{E_{vis} \in [3.0; 17.0]\ MeV}$ so that a large fraction of the remaining IBD delayed signals are rejected. The drawback is that a significant fraction ($\sim$15%) of signals from the ^{12}B decay are not selected. In the previous sub-section, we have seen that the fraction of IBDs that are not selected is of $\sim$1.2% when using the MC truth information. Thus, the number of IBD delayed signals remaining in the file being smaller, the inferior cut of the delayed signal energy window can be lowered so that the selection window in the MC truth analysis is: $E_{vis} \in [1.0; 17.0]$ MeV.

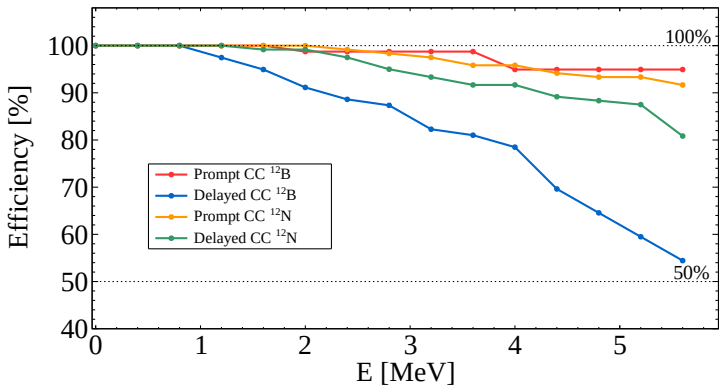

Figure 5.10: *The selection efficiency (ϵ) as a function of the visible energy window lower limit for the different signals from CC interaction on ^{12}C.*

5.1.5.2 Prompt and delayed coincidence

As for the IBD selection, the temporal and spatial cuts are optimised together and the $\delta T/\delta R$ pair that maximises the ratio ϕ/θ is retained. As a reminder, the sole purpose of selecting these interaction channels is to "clean up" the data file in anticipation of the selection of νeES events that comes afterwards and that will only be made according to the visible energy. The search of the optimal ϕ/θ following various purity and loss requirements showed that the best trade-off – for this work – is to require a purity $>$ 90%. Indeed, a higher requirement leads to a number of non-selected signals that is too important ($>$ 50%), which would result in a prohibitive contamination of the νeES. The purity and loss against different $\delta T/\delta R$ pairs are shown in Figure 5.11. The cuts that are retained for the selection are $\boldsymbol{\delta T < 102\ ms}$ and $\boldsymbol{\delta R < 0.72\ m}$. The corresponding average purity and loss are the following:

$$\phi = 96.5\% \quad \text{and} \quad \theta = 17.9\% \tag{5.3}$$

A large part of the signals that are not selected arise from the delayed signal energy window that starts at 3 MeV. The rest is not selected either because of the temporal and spatial cuts – especially the latter – that are necessarily tight because of the requirement of the selected sample's purity, either because the prompt or the delayed signal of a given pair was already selected during the IBD selection. One could expect that the large δT cut ($\sim$100 ms) would mean that the unicity condition would often not be met, but the analysis showed that it does not. This is explained by the large size of the detector that makes very unlikely to have several signals in a small area. However, since many more neutrino events are expected for closer CCSN, this case could occur more often. The optimal cuts from the MC truth information are $\delta T = 101.6$ ms and $\delta R = 0.7$ m, they are very similar to those determined with the full chain simulation which is expected since the reconstruction quality is very good for events at such energies. The resulting purity and loss are $\phi = 90.6\%$ and $\theta = 9.1\%$, respectively. The purity drops by 5% because of the relaxed delayed signal energy window. Finally, the loss is mainly due to the tight spatial cut.

5.1.6 Selection of the NC interactions on ^{12}C

The signals that remain in the data file after the IBD and CC interaction on ^{12}C events are the "single" signals: the νpES, the νeES and the 15.11 MeV gammas from $^{12}C^*$ de-excitation. In this analysis, the selection of them only relies on the visible energy and

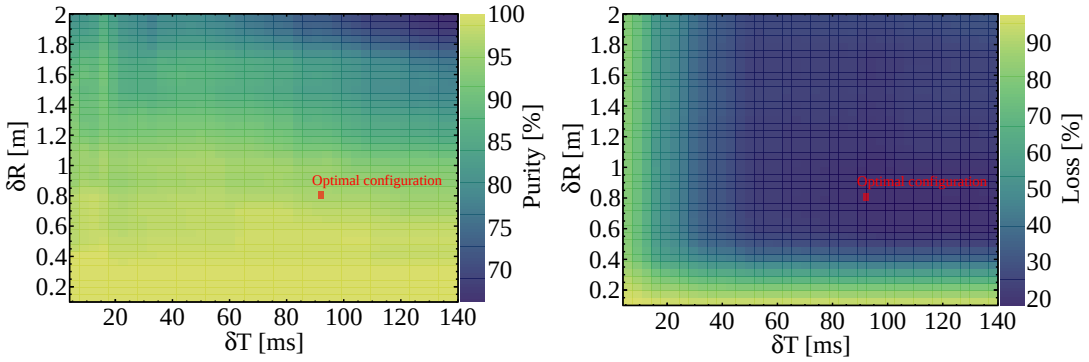

Figure 5.11: ***Left**: Example of the evolution of the purity of a selected sample for different $\delta T/\delta R$ pairs. **Right**: Example of the CC on ^{12}C events loss for different $\delta T/\delta R$ pairs. On both plots, the optimal configuration is indicated.*

we have seen that the energy spectra of the νeES and gammas overlap. The Figure 5.12 shows the reconstructed energy spectra of a large data set of both of them (no selection applied). The selection strategy being designed to retrieve the neutrino energy spectra from the νeES events, the 15.11 MeV gamma events are selected first so that they do not distort the energy spectrum. In order to select as few νeES events as possible, the energy window must be optimised.

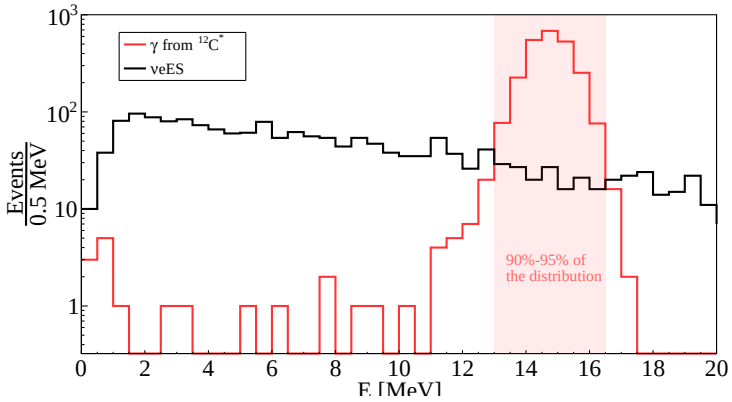

Figure 5.12: *Example of the reconstructed energy spectra of νeES and 15.11 MeV gamma events. The red box shows that ∼90-95% of the gamma events have a reconstructed energy that is between 13.0 MeV and 16.5 MeV.*

The fiducial volume cut does not allow to reject all the events that leaked out of the detector before depositing all their energy. Moreover, the small reconstructed energy of some events can also be due to the TR area, hence the reconstructed spectrum of the gamma events is distributed between 0 and 18 MeV. About 90-95% of the distribution ranges between 13.0 and 16.5 MeV. It is in this interval that the distribution of the gamma events is higher than that of the νeES and would distort the most the νeES energy spectrum. As a consequence, the gamma events selection energy window is defined as $\mathbf{E_{vis} \in [13.0; 16.5]\ MeV}$. The average purity and loss of the selected sample are the following:

$$\phi = 86.2\% \quad \text{and} \quad \theta = 6.4\% \tag{5.4}$$

Such "poor" purity mainly arises from the SPMT system energy resolution. Indeed, the

smearing of the 15.11 MeV gamma energy peak imposes a relatively wide selection energy window that inevitably also contains νeES events. Thus, about 30% of the contamination consists of νeES, another 30% consists of unselected IBD prompt signals and the rest mainly consists of unselected signals from CC interactions on ^{12}C. In the analysis with the MC truth information, the selection energy window can be drastically reduced: $E_{vis} \in [15.0; 15.2]$ MeV. In such case, the purity of the selected sample is $\phi = 99.4\%$ and the fraction of gamma events lost is $\theta = 3.2\%$.

5.1.7 Selection of the νeES

At this stage of the selection, ∼85% of the events (false triggers excluded) that occured within the FV have been selected. Among the remaining ones, ∼60% are νpES, ∼20% are prompt or delayed signals from IBDs, ∼15% are νeES and ∼5% are events from CC/NC interaction on ^{12}C. In view of these numbers and given the visible energy spectra of the different channels (Figure 5.1), it is clear that the selection of the νeES based on a selection energy window only will result in a contamination of the selected sample by the remaining prompt IBD signals as well as by the CC/NC interactions on ^{12}C events. In addition, as already mentioned, the number of νeES expected in JUNO varies between 100 and 300 depending on the CCSN model. Such small statistics impose strong constraints on the loss. Indeed, the more the event loss the more information lost for studying CCSN physics. First of all, the contamination by the other channels can be limited by optimising the selection energy window. Thus, the lower limit is fixed at 3 MeV. This allows to reject >98% of the νpES as well as the remainig IBD delayed signals (see Figure 5.7). About 95% of the νeES visible energy spectrum being contained between 0 and 30 MeV, the selection energy window is defined as $\mathbf{E_{vis} \in [3.0; 30.0]\ MeV}$. Even if ∼5% of the νeES is lost, the upper limit allows to reduce the contamination by part of the remaining IBD prompt signal. However, the latter remain numerous in the selection energy window just defined. For this reason, an additional requirement is formulated. The 2 miliseconds that follow a νeES candidate must not contain a signal with a visible energy such as $\mathbf{E_{vis} \in [0.5; 3.0]\ MeV}$. Such a requirement allows to attenuate the contamination by IBD prompt signals by a factor ∼6 but inevitably results in the rejection of some νeES signals. Since the vertex of most of the remaining IBD delayed signals are poorly reconstructed, no spatial coincidence cut is used. After applying this selection, the average purity and loss for the νeES are the following:

$$\phi = 63.7\% \quad \text{and} \quad \theta = 60.8\% \tag{5.5}$$

About ∼10% of the νeES events are lost because they were selected with the γ events and another ∼20% is lost because of the selection energy window. The rest is rejected because of the temporal cut that aims to reject IBDs. The Figure 5.13 compares the normalised νeES true energy spectrum, the one of the selected νeES sample and the one of the unselected νeES. Given the important number of events in the first bin (0-2 MeV) of the true energy spectrum and the selection energy window that starts at 3 MeV, the spectrum of the selected events looks strongly distorted compared to the true spectrum, their shape are relatively similar. This is further investigated in section 5.2 where the comparison of the true and selected spectra focuses on the energy range of the selected one.

In the analysis using the MC truth information, the events that remain in the data file at this stage of the selection are mostly νpES (∼75%) and νeES (∼20%), the fraction of IBD prompt signals is < 1%. Thus, the νeES energy window selection is relaxed: $E_{vis} \in [3.0; 50.0]$ MeV. The same temporal and energy cuts are used to reject the contamination from the few remaining IBDs. The purity of the selected sample is then $\phi =$

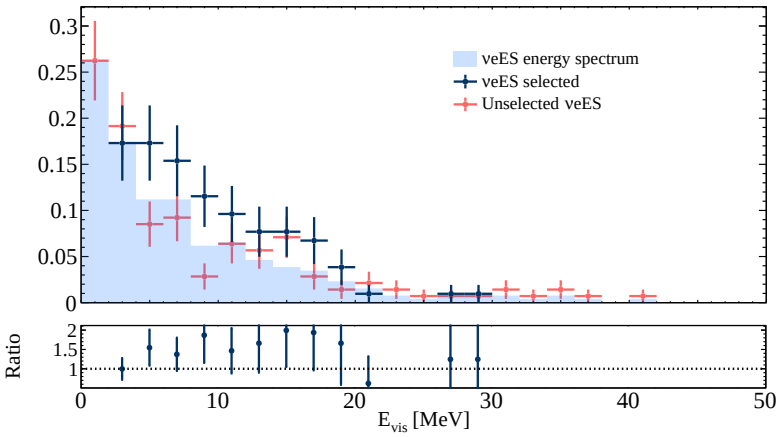

Figure 5.13: ***Top**: Comparison of the νeES true energy spectrum, the one of the selected νeES sample and the one of the unselected νeES signals. **Bottom**: Ratio plot between the true energy spectrum and the selected one.*

77.5% and the fraction of νeES events lost is $\theta = 46.6\%$, the majority of the latter coming from the lower boundary of the selection energy window that reject many νeES events, actually more than in the analysis using the informtion from the reconstruction. Indeed, the SPMT system energy resolution smears the spectrum at low energy and the straight lower cut (3 MeV) has really different consequences depending on whether the MC truth or the reconstruction information is used.

Any remaining signal with an energy that is such as $\mathbf{E_{vis}} \in [\mathbf{0.7}; \mathbf{2.2}]$ **MeV** is considered as a νpES. The results show that the selected samples is highly contaminated by false trigger events from the event builder (see Chapter 3, section 3.4.4). The average purity and loss are the following:

$$\phi = 25.2\% \quad \text{and} \quad \theta = 89.3\% \tag{5.6}$$

As mentioned previously, the selection of the νpES events was not the objective of this work, it is therefore not investigated further. In the next section, the performance of the selection for each of the channels is summarised and the results are further discussed.

5.1.8 Summary and discussions

The cuts and the performance of the IBD, CC/NC interactions on ^{12}C and νeES selections using the information after full chain simulation and the MC truth information is summarised in Table 5.1 and Table 5.2.

The selection strategy presented in the previous section is optimised for the IBDs and νeES events. Despite the poor reconstruction of ∼10% of the IBD delayed signals – that makes the spatial coincidence cut not usable for the selection of them – the purity and loss of the prompt signal selected sample are $> 99\%$ and $< 5\%$, respectively. Such results guarantee the preservation of the $\bar{\nu}_e$ energy spectrum shape as well as a good reconstruction of their time-dependent luminosity. The poor reconstruction of the IBD delayed signals is in fact more problematic for the rest of the selection. Indeed, the ∼5% of unselected IBDs, which represent ∼150 prompt and ∼150 delayed signals, populate the entire energy range: the remaining delayed signals around 2.2 MeV and the prompt signals between 0 and 80 MeV. The Figure 5.14 is a contamination matrix that summarises the performance of the selection of each channel. It shows that the selection of the CC interactions on

	MC	FC
Prt. E_{vis} [MeV]	> 3.0	> 3.0
Dld. E_{vis} [MeV]	[1.6;5.0]	[1.6;6.0]
δT [ms]	1.64	1.20
δR [m]	1.52	2.76
ϕ [%]	99.8	99.3
θ [%]	1.2	4.8

(a) Summary of the IBD selection.

	MC	FC
Prt. E_{vis} [MeV]	[1.6;60.0]	[1.6;60.0]
Dld. E_{vis} [MeV]	[1.0;17.0]	[3.0;17.0]
δT [m]	101.6	102.0
δR [ms]	0.70	0.72
ϕ [%]	90.6	96.5
θ [%]	9.1	17.9

(b) Summary of the CC on ^{12}C selection.

Table 5.1: *Summary of the double signal event selection. The left table is for IBDs and the right one is for CC on ^{12}C. The column "MC" is for the analysis using the MC truth information while the column "FC" is for the analysis with the full chain simulation.*

	MC	FC
E_{vis} [MeV]	[15.0;15.2]	[13.0;16.5]
ϕ [%]	99.4	86.2
θ [%]	3.2	6.4

(a) Summary of the 15.11 MeV γ selection.

	MC	FC
e^- E_{vis} [MeV]	[3.0;50.0]	[3.0;30.0]
Dld. E_{vis} [MeV]	[0.5;3.0]	[0.5;3.0]
δT [ms]	2.0	2.0
ϕ [%]	77.5	63.7
θ [%]	46.6	60.8

(b) Summary of the νeES selection.

Table 5.2: *Summary of the single signal events selection. The left table is for γ and the right one is forνeES. The column "MC" is for the analysis using the MC truth informtion while the column "FC" is for the analysis with the full chain simulation.*

^{12}C events is not contaminated by these remaining IBDs which is due to the spatial and temporal coincidence that is a powerful way to reject the IBDs. In contrast, given that the selection of the single signals (νeES and γ) only relies on the reconstructed energy, strong constraints on the selection energy windows must be imposed in order to limit the contamination. The analysis showed that such constraints are not sufficient – the purity of the selected sample would be $< 30\%$ – and that an additional selection criteria allows to mitigate further more the contamination (see section 5.1.7). The analysis showed that actually very few νeES events are rejected because of this condition. In the end, $\sim$10% of the νeES events selected are actually IBD prompt or delayed signals.

The selection strategy also allows to obtain relatively good purity and loss of the $^{12}C^*$ de-excitation gamma selection: $\sim$88% and $\sim$6%, respectively. Even though this channel is not relevant for the neutrino energy spectra reconstruction, it allows to probe the global neutrino flux. In Chapter 1, we have seen that the combined luminosities of the ν_e and $\bar{\nu_e}$ can be used to constrain the Proto-Neutron Star (PNS) properties (Chapter 1). Thus, even if this work does not allow to distinguish between the two CC interactions on ^{12}C, these channels, that are identified with a relatively good purity ($\sim$95%), also constitute candidates to study the CCSN.

5.2 Energy spectra unfolding

In Chapter 1, we have seen that the neutrino flavor-wise luminosities and energy spectra are the two main observables that can be used to retrieve various parameters of the CCSN (PNS mass, size, mass accretion rate, progenitor compactness etc.). The analysis presented in the previous section consisted in making an initial selection of the neutrino events in order to classify them, that is, identify the interaction channel. Such work is necessary

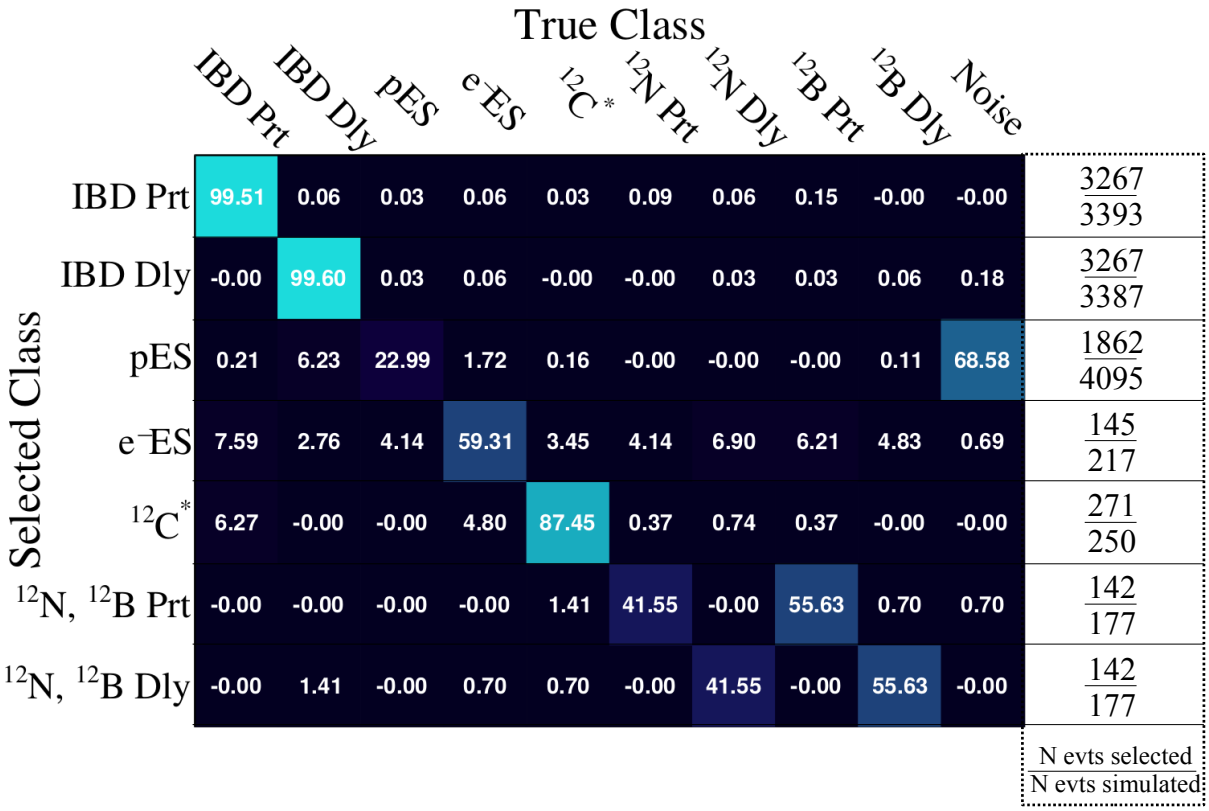

Figure 5.14: *Example of a contamination matrix obtained with the selection strategy applied on a CCSN neutrino burst (10 kpc) after full processing of the events (detector and electronics simulations, event builder, vertex and energy reconstruction). The results are slightly different than those presented in the previous section because they are obtained from a single file while those of the previous section are averaged on several files. The sum of the cases of each line is equal to 100%. The "true class" includes the different types of signals of the different channels as well as the false trigger events (referred to as "noise"). The "selected class" includes the label of the events as identified in the selection strategy. In the rightmost column, the numerator indicates the number of events selected in the sample (even those that are not selected as the right class) and the denominator indicates the number of events that were simulated in the FV.*

to derive the incident neutrino flavor. The results showed that it is very challenging to separate the interaction channels from each other so that cross-contaminations between them occur throughout the selection. Furthermore, even if the selection would have allowed to achieve a perfect classification, information about the events would still be missing:

- The flavor content of the selected sample is incomplete since the three elastic scattering channels derive from the three neutrino flavors.
- The energy deposited through elastic scatterings is only a fraction of the total energy of the incident neutrino. Thus, the energy spectrum of the latter still needs to be extracted from the reconstructed one.
- The measured energy of the events is actually distorted by the finite resolution of the detector.
- The neutrino luminosities remain undetermined. Indeed, the total number of neutrinos that in fact crossed the detector can be extracted from the number of neutrino interaction registered. Then, the neutrino luminosities at the level of the CCSN can be extrapolated.

The determination of these observables from the data constitutes a significant part of the CCSN neutrino analysis. The present section focuses on the third item of the above list, the energy spectra of the IBD prompt signals and νeES selected samples are studied. First of all, unfolding methods are used in order to retrieve the underlying true energy distribution by correcting the reconstructed energy spectra from the detector response.

5.2.1 Unfolding methods

Unfolding methods are widely used in particle physics to solve inverse problems, for example to determine cross-sections using events counted by a detector or to extract true distributions from experimentally measured ones. Indeed, any experimental measurement is inevitably *folded* with the response of the detector that is used to make it. Thus, the unfolding procedure consists in using the detector response (resolution, acceptance etc.) – that is preliminary determined thanks to calibration data and MC data – to correct for the measured distribution from the distortions caused by detector effects. For example, let's consider a binned energy distribution. Basically, because of the detector energy resolution, some events feed the i^{th} bin while according to its true energy it should be in the $\mathrm{i}^{th}+1$ bin (see *migration effects* in the following). Typically, in such case, the unfolding procedure aims to rebin the distribution by taking into account how the energy resolution distorts it.
Unfolding methods will also play a central role in the context of the future galactic CCSN neutrino burst. Indeed, the burst will be seen by several detectors with different responses ((Chapter 1, section 1.2.3). As already mentioned, the pooling of data will maximise the information about the CCSN that can be extracted from the signal. To make these data comparable with each other, it will be of paramount importance to unfold them from the detector responses. In the following, the two unfolding methods that have been used for the energy spectra unfolding are briefly introduced.

5.2.1.1 TUnfold unfolding algorithm

The *TUnfold* algorithm [286, 287] is a tool implemented in the ROOT software that aims to correct for migration and background effects in distributions, which is particularly relevant for the present use-case. Before going any further, it is worth pointing out that, even though the "backgrounds" could here refer to the contamination of the selected samples (IBD and νeES) by events from other interaction channels, the present work only focuses on the migration effects. Thus, the inverse problem can here be written such as:

$$\tilde{y}_i = \sum_{j=1}^{m} A_{ij}\,\tilde{x}_j,\ 1 \leq i \leq n \tag{5.7}$$

where m is the number of bins of the true distrubution $\tilde{x}_j$, $\tilde{y}_i$ is the distribution of the average expected counts at the detector level and A_{ij} is the matrix of probability that describes the migrations from the j^{th} bin of the true distribution to any of the n bins of $\tilde{y}_i$. Note that, as other unfolding algorithms [288, 289], TUnfold requires that the measured distribution has a finner binning than that extracted through the unfolding process. The matrix A_{ij} is also referred to as the *detector response matrix* in the following. Equation 5.7 can be shematised as in Figure 5.15.

Inverse problems are often solved using a least square regression. However, it can happen that for a given matrix A, there exists several x that satisfy the equation (ill posed problem) so that such method is not suitable anymore. Then, one has to choose a unique solution, that can be prefered compared to the others for reasons that depend on the problem itself (for example, solutions with negative energies would not be relevant in the

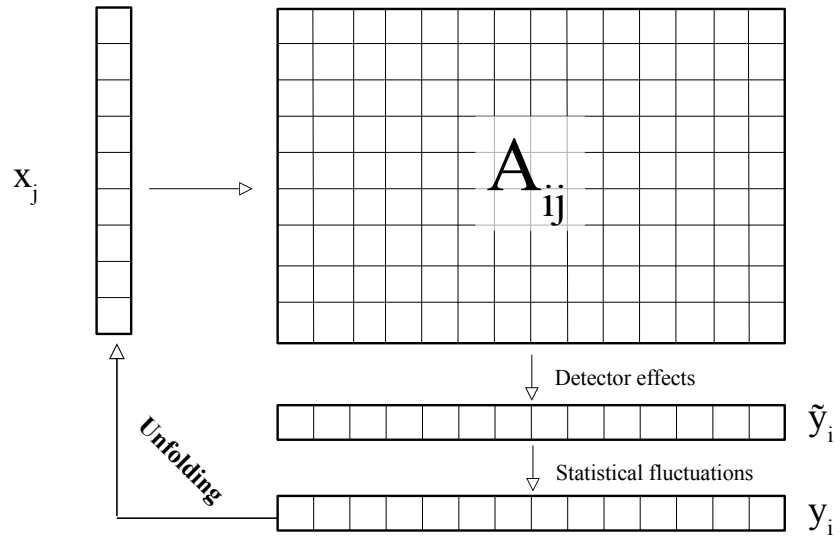

Figure 5.15: *Schematic view of the migration effects and statistical fluctuations between a true (x) and measured (y) distribution. Each case represents a bin. The matrix A contains the probability of migration from one bin to another.*

present case). A way to optimise the choice of the solution is to introduce a *regularisation term* to the inverse problem, so that equation 5.7 can be rewritten such as:

$$\tilde{y_i} = \sum_{j=1}^{m} A_{ij}\,\tilde{x}_j + \Gamma\tilde{x}_j \tag{5.8}$$

where Γ is referred to as the regularisation matrix. This method, on which the TUnfold algorithm is based, is also known as the *Tikhonov regularisation* [290]. There are several ways to find the optimal regularisation term (Γ), the TUnfold algorithm uses an *L-curve* scan [291]. It consists in a plot that shows the evolution of the regularised solution of the inverse problem against the corresponding residuals. The best Γ is the one for which the curvature is maximal. An example of L-curve scan is shown in Figure 5.25 (Appendix). A complete description of the TUnfold algorithm is available in Ref. [286].

5.2.1.2 SVD unfolding algorithm

In mathematics, the *Singular Value Decomposition (SVD)* consists in the factorisation of a matrix. It is in fact applicable to unfolding problems in particle physics in which the detector response matrix can be decomposed [292]. The ROOT software implements a SVD approach [293]. The principle is to decompose the detector response matrix in a product of matrices such as:

$$A = U \times S \times V^T \tag{5.9}$$

where U and V are square and orthogonal matrices and S is a diagonal matrix with non-negative diagonal elements. The SVD highlights many information on the detector response matrix that can be used for the unfolding. Note that the algorithm requires that the detector response matrix is a square matrix and that the dimensions of the input and

output spectra are equal. As the TUnfold algorithm, the approach consists in regularising the inverse problem which is simplified thanks to the SVD. A full description of the SVD approach is available in Ref. [292].

5.2.2 Detector response matrix

The detector response matrix occupies a central part in the unfolding procedure. It is important to mention that since the JUNO detector is still under construction, the detector response matrix used in this analysis is based on MC data only. In the future, when the data will come, the simulation software of JUNO will be tuned with real data in order to match the detector response simulation with the actual detector response. A detector response matrix for each interaction channel (IBD and νeES) is generated using large sample of events that followed the full processing (detector and electronics simulation, event builder, reconstruction) except the event selection. The one for the IBD prompt signals is shown in Figure 5.16. On the left, it is displayed with a fine binning in order to see in detail how the reconstructed and true energy are correlated. The profile of the matrix is also drawn and compared with a one degree polynomial function whose slope and intercept are equal to 1 and 0, respectively. The comparison shows that the profile deviates from the function. Indeed, the event builder used preliminarily to the event reconstruction (see Chapter 3) has been designed to capture 300 nanoseconds of signal when it triggers. Such length was optimised on events with energies between 0 and 9 MeV, it allows to capture at least 95% of the signal without bringing any additional bias to the vertex and energy reconstruction and to retrieve a large fraction ($> 75\%$) of the events piled-up for CCSN at a distance farther or equal to 3 kpc. However, in a LS detector, the average signal length of the events increases with the deposited energy. Thus, a larger and larger fraction of signal is lost for an increasing deposited energy when fixing the event builder signal window capture at 300 ns, which explains the difference between the reconstructed and true enegy observed. This raises an important point concerning the event builder strategy of JUNO for CCSN burst neutrino event reconstruction, particularly for nearby progenitors. Indeed, the setting of the event builder will have to be optimised to retrieve as much piled-up events as possible (shortest possible window) without biasing the energy reconstruction of the high energy (> 30 MeV) events. Such setting will mainly consist in a trade-off between event separation and precise energy reconstruction. In the present case, the deviation observed in Figure 5.16 typically causes migration effects in the reconstructed energy spectrum (i.e events reconstructed with a smaller energy than the real one will feed the wrong bins). Typically here, the unfolding procedure is expected to correct for these migrations. On the right side of Figure 5.16, the detector response matrix is displayed with a coarser binning, it is used in such configuration in the unfolding procedure. Note that the TUnfold requires a second response matrix – generated with another data set – that is used to derive systematic errors due to MC parameters uncertainties. This possibility was not explored in this work.

As already mentioned in Chapter 4, the LSNL is particle-dependent. The top left plot of Figure 5.17 shows the detector response matrix of νeES events which reconstructed energy is corrected with the electron LSNL implemented in the JUNO simulation software [239] while the top right plot shows the same response matrix with the reconstructed energy of the νeES events corrected with the positron LSNL as used in the reconstruction procedure (Chapter 4). The profile of both matrices is also displayed and fitted with a one degree polynomial function (full red line) whose parameters are shown in red. These fits show that using the electron LSNL correction allows to slightly decrease the intercept of the profile fit, from 0.13 to 0.04 MeV, and to enhance the $\tilde{\chi}^2$ from 2.5 to 1.5. Thus, before the unfolding procedure, the energy of the events selected as νeES is corrected using the electron LSNL correction. A second one degree polynomial function (dashed red line)

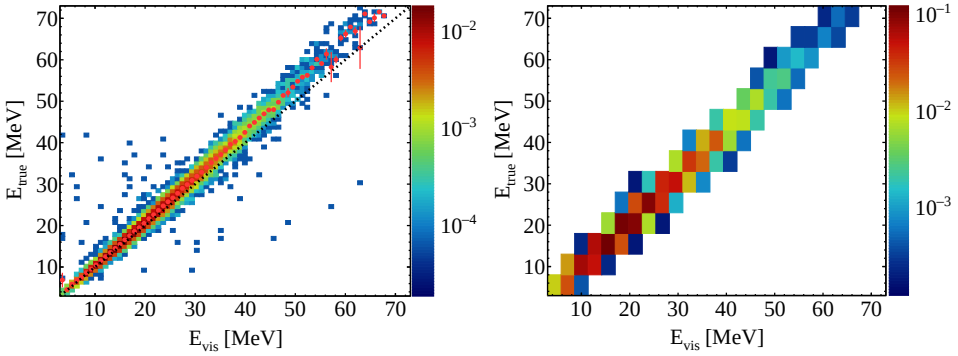

Figure 5.16: ***Left**: Detector response matrix showing the correlation between the reconstructed (E_{vis}) and true (E_{true}) energy of the IBD prompt signals. The profile of the matrix (red points) is also shown. A one degree polynomial function (black dashed line) whose slope and intercept are equal to 1 and 0, respectively, is shown for comparison. **Right**: Same response matrix but with a coarser binning, it is used for the unfolding procedure.*

whose slope and intercept are equal to 1 and 0, respectively, is also shown on each matrix for comparison. The reconstructed and true energy display the same discrepancy than for the IBD prompt signals – it arises from the event builder strategy – but in a lesser extent since the average energy is smaller for these events. The matrix used in the unfolding procedure is shown in the bottom plot of Figure 5.17, its coarse binning is explained in the next section.

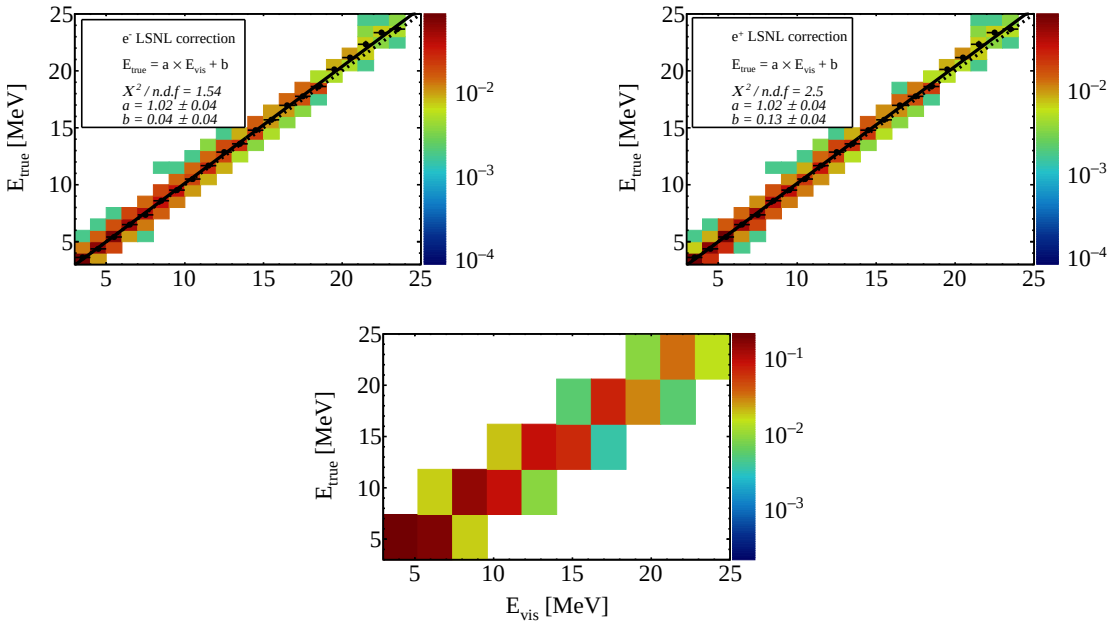

Figure 5.17: ***Top left**: Detector response matrix showing the correlation between the reconstructed (E_{vis}) and true (E_{true}) energy of the νeES events after having corrected the energy with the electron LSNL. The profile of the matrix (red points) is also shown and fitted (full red line). A one degree polynomial function (red dashed line) whose slope and intercept are equal to 1 and 0, respectively, is shown for comparison. **Top right**: Same response matrix, the reconstructed energy is corrected with the e^+ LSNL. **Bottom**: Same response matrix with a coarser binning, it is used for the unfolding procedure.*

5.2.3 Unfolded energy spectra

As mentioned previously, the rate distortion – i.e the fluctuations in the number of events expected per bin – due to possible contamination by background events is not studied. Thus, since the unfolding analysis only intends to correct for migration effects that could distort the spectrum shape, the input and output spectra are normalised. The Figure 5.18 shows the true IBD prompt signal spectrum, the one obtained after the selection and the unfolded one (TUnfold). Only the statistical uncertainties are propagated to the unfolded spectrum. A plot of the ratio between the two reconstructed spectra (after selection and after unfolding) and the true one is also displayed to make the comparison more convenient. First of all, the comparison of the true spectrum with the one before the unfolding shows that there shapes are very similar, there is only a little room for improvement. Indeed, we have seen that the selected sample is very pure ($\sim$99%) and that the correction of the migration effects is especially expected in the higher energy range ($>$ 30 MeV), where the energy reconstruction is the most biased (Figure 5.16). However, the statistics are low in this range and the statistical error is important so that the improvement from the unfolding is not easy to see, if it exists. The comparison of the true spectrum with the unfolded one shows that for some bins, the spectrum is well corrected while for others, it is worsen. A fit of the ratio plots in the [0;30] MeV energy range with a zero degree polynomial function shows that the unfolding makes the shape of the unfolded spectrum slightly closer to that of the true spectrum: the parameter of the fit changes from 0.94 to 0.95. However, both fits are compatible within uncertainties. A more global examination of the spectra shows that the unfolding smoothens the spectrum. Indeed, the spectrum as it is prior to the unfolding has stronger differences between consecutive bins (for example between the second and the third one) with respect to the unfolded one.

Figure 5.19 shows the true νeES spectrum, the one obtained after the selection and the unfolded one (TUnfold). Only the statistical uncertainties are propagated to the unfolded spectrum. A ratio plot is also displayed to make the comparison more convenient. The unfolding performance is limited by the poor event statistics of the selected sample. Indeed, any empty bin in the distrubtion makes it crash. As explained in section 5.1.6, the selection of the 15.11 MeV gammas also implies the selection of all the νeES events in the selection energy window. As a consequence, the selected νeES energy spectrum has a "hole" in it and a coarse binning (10 bins here) is required to have no empty bins. Furthermore, the binning of the extracted distribution (see section 5.2.1.1) is even coarser (5 bins here). In such case, no important migration effects correction can be expected since the flexibility is very small, which is confirmed by the fits of the ratio plots whose parameter p_0 are both equal to 0.83.

The results of the unfolding using the SVD approach are shown in Figure 5.20 (IBD) and Figure 5.21 (νeES). In both cases, the unfolding allows to smooth the spectrum and the bin-to-bin comparison shows an improvement, especially for the νeES spectrum where the parameter of the fit of the ratio plots change from 0.83 to 0.96. The better performance of the SVD approach can be partly explained by the larger dimension of the detector response matrix that gives it more flexibility. However, it is important to point out that the error on the fit parameter for ratio plot of the the unfolded spectrum is larger (0.15). Indeed, the algorithm used includes stochastic *and* systematic fluctuations from the unfolding procedure. These errors are propagated to the ratio plot and thus to the fit parameter which, although close to one, is still compatible with the fit parameter of the spectrum before the unfolding.

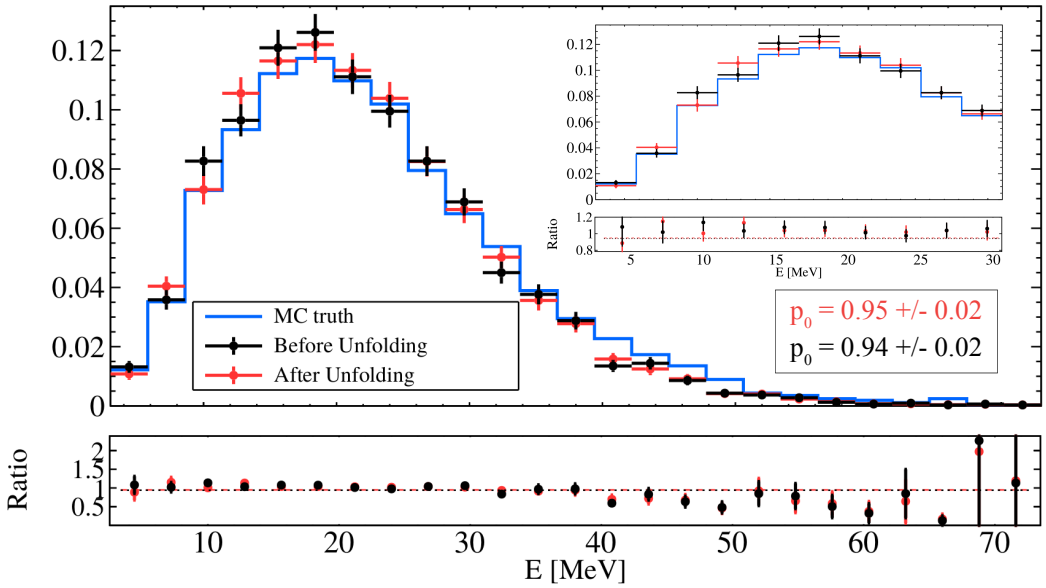

Figure 5.18: ***Top**: Normalised true IBD prompt signal energy spectrum (full blue line), the one obtained after the event selection (black dots) and the unfolded one (red dots, TUnfold) for a 25$M_\odot$ CCSN progenitor (Garching model 82500). The small panel focuses on the [0;30] MeV energy range. **Bottom**: The ratio to the true spectrum for both spectra from selection (black dots) and unfolding (red dots), they are fitted with a zero degree polynomial function whose parameter (p_0) is shown on the top panel with the corresponding color.*

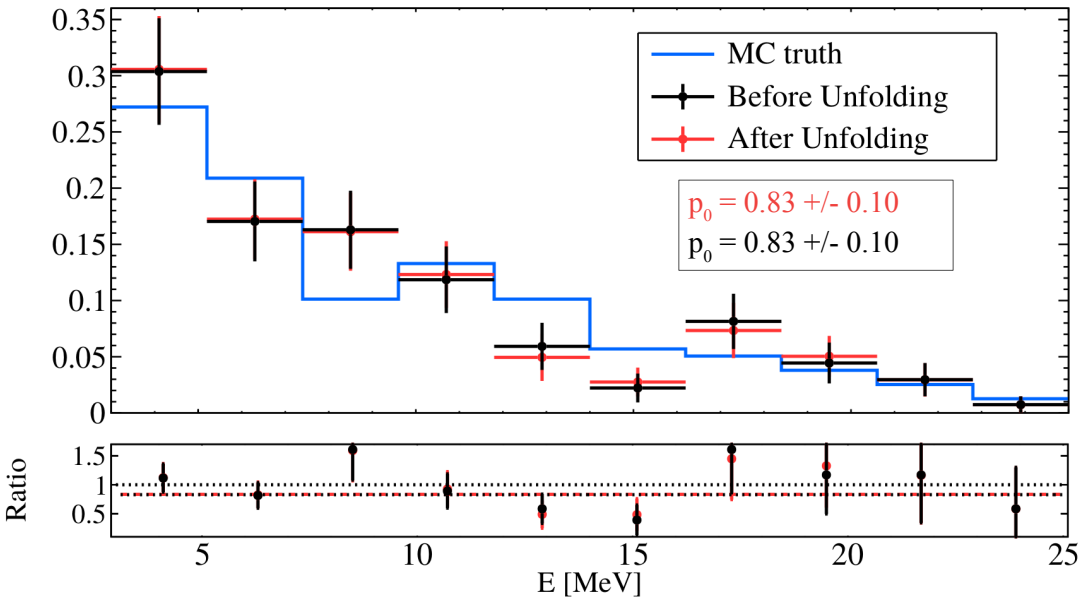

Figure 5.19: ***Top**: Normalised true νeES energy spectrum (full blue line), the one obtained after the event selection (black dots) and the unfolded one (red dots, TUnfold) for a 25$M_\odot$ CCSN progenitor (Garching model 82500). **Bottom**: The ratio to the true spectrum for both spectra from selection (black dots) and unfolding (red dots). They are fitted with a zero degree polynomial function whose parameter (p_0) is shown on the top panel with the corresponding color.*

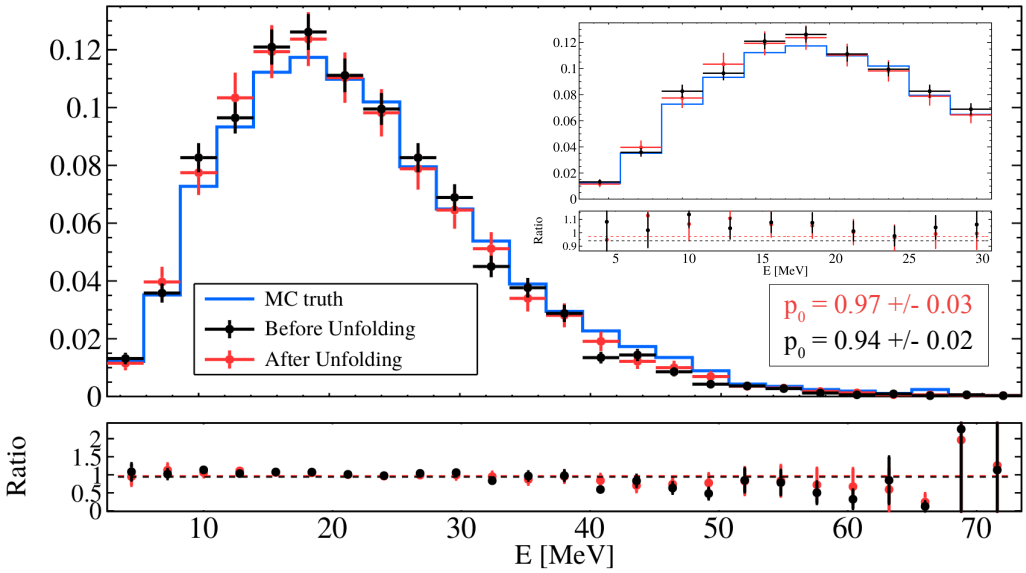

Figure 5.20: ***Top**: Normalised true IBD prompt signal energy spectrum (full blue line), the one obtained after the event selection (black dots) and the unfolded one (red dots, SVD) for a 25$M_\odot$ CCSN progenitor (Garching model 82500). The small panel focuses on the [0;30] MeV energy range. **Bottom**: The ratio to the true spectrum for both spectra from selection (black dots) and unfolding (red dots), they are fitted with a zero degree polynomial function whose parameter (p_0) is shown on the top panel with the corresponding color.*

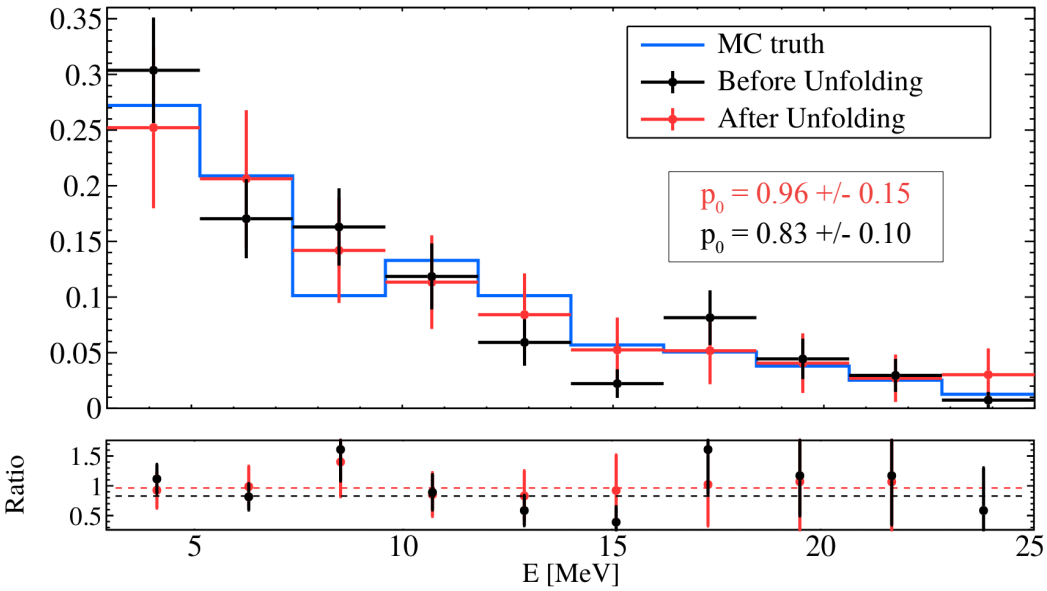

Figure 5.21: ***Top**: Normalised true νeES energy spectrum (full blue line), the one obtained after the event selection (black dots) and the unfolded one (red dots, SVD) for a 25$M_\odot$ CCSN progenitor (Garching model 82500). **Bottom**: The ratio to the true spectrum for both spectra from selection (black dots) and unfolding (red dots). They are fitted with a zero degree polynomial function whose parameter (p_0) is shown on the top panel with the corresponding color.*

Summary

In this chapter, a CCSN neutrino event selection strategy was presented and applied to a CCSN neutrino burst simulated in the JUNO detector. This analysis was in continuity with the study of the SPMT system rate capability and event reconstruction and allowed to have a first estimate of the performance of the SPMT system for CCSN neutrino energy spectra reconstruction. The primary objective is to get a(n) (in)direct access to the incident neutrino flavor, whose respective luminosities and energy spectra will be used to probe the collapse and subsequent explosion mechanisms of the CCSN. Before starting the analysis, the events were fully processed, from the detector simulation to the reconstruction. The event selection strategy focused on the IBDs whose selection benefits from the powerful discrimination power provided by the temporal and spatial coincidence of the prompt and delayed signal. This channel is particularly relevant for the study of the $\bar{\nu_e}$. Although it is more sensitive to the ν_e, the νeES interaction channel derives from neutrinos of all flavors and the visible energy of such events is relatively high ($\sim$10 MeV on average) representing a good candidate for the event selection with the SPMT system. The purity and loss of the IBD selected sample are $> 99\%$ and $< 5\%$, respectively, while those of the νeES are $\sim$63% and $\sim$60%, respectively. Indeed, the νeES selection only relies on the energy selection criteria which makes it difficult to separate from the rest of the events. The event selection is in fact the very first step towards the extraction of the luminosities and energy spectra. Indeed, we have seen that the complete flavor content determination also requires the use of interaction cross-sections for some channels (νpES, νeES, NC on ^{12}C). Furthermore, the computation of the luminosities and energy spectra requires unfolding techniques. Thus, this chapter also includes a preliminary unfolding analysis for the IBD prompt signal and νeES energy spectra. Two different unfolding approaches (Tikhonov regularisation and SVD + regularisation) were used to correct for the migration effects in the energy spectra that are notably due to the finite resolution of the SPMT system and to the event builder strategy. The spectrum of the IBD selected sample had only little room for improvement. When comparing the spectra before and after the unfolding to the true one, it appears that the unfolding does not allow significant corrections of the migration effects, especially at higher energy. This is explained by the low statistics per bin in this energy range. However, the unfolding procedure allowed to smooth the shape of the spectrum. No significant improvement is observed for the νeES sample neither although the low purity of the νeES selected sample leaves more margin for imporovement. In this case also, the spectrum shape is smoothed by the unfolding procedure, especially when using the SVD method. Given the high contamination of the spectrum, it is more distorted and taking it into account in the unfolding procedure – which would actually be equivalent to consider background effects – could improve the results. Better energy spectrum reconstruction will also require better event selection performance.

Conclusion

Thirty-five years ago, the Kamiokande, IMB and Baksan detectors measured a burst of two dozens of neutrinos from a Core-Collapse Supernova (CCSN) located 50 kpc away from the Earth, this event is nowadays referred to as *SN1987A*. Such experimental achievement opened a new era in the study of CCSN. Indeed, in contrary to the electromagnetic radiations emitted throughout the collapse and subsequent explosion and that only allow to probe the surface layers of the dying star, the neutrinos are emitted from the deep interior of it and therefore offer the unique opportunity to scrutinise in more details the CCSN mechanism. JUNO is a future large-scale liquid scintillator neutrino detector of 20 ktons currently under construction in China to be completed by the end of 2023. JUNO has for primary objectives to resolve the Neutrino Mass Ordering (NMO) – 3σ in 6 years of data taking – and to measure at the sub-percent level three neutrino oscillation parameters. However, its huge detection volume also makes it a good candidate for the detection of the next galactic CCSN neutrino burst, foreseen to be at an average distance of $\sim$10 kpc. More precisely, the detection of a few hundreds to a few thousands of neutrinos will allow a precise flavor-wise reconstruction of the neutrino luminosities and energy spectra. In addition to strongly constrain the multiple CCSN models that have been developed during the last decades, such observables are expected to give a direct access to various parameters of the Proto-Neutron Star (PNS), neutrinosphere and even on the progenitor star, having direct implications for nuclear physics and particle physics. The JUNO detector is composed of two complementary Photomultiplier Tube (PMT) systems, the LPMTs ($\sim$18,000) and the SPMTs ($\sim$26,000). In addition to provide a better control of the energy resolution systematic errors, the SPMT system will also allow to perform semi-independent physics analyses. In particular, their fast time response and smaller saturation effects are expected to be assets in case of CCSN, especially for a very nearby one. Indeed, the neutrino burst is expected to last $\sim$10 seconds so that, according to the distance to the explosion, the neutrino interaction rate in JUNO is expected to range between the kHz and the MHz, representing an unprecedent challenge for a liquid scintillator detector. The work realised and presented in this manuscript focuses at different levels of the SPMT system detection chain.

During the first year of this PhD thesis, the Subatech laboratory was strongly involved in the development of the SPMT system, especially in the characterisation of the readout electronics (mainly CATIROC), including the preparation of a test-bench for the SPMTs acceptance tests as well as in the development of a code that simulates the response of CATIROC. Thus, first of all, a fast charge calibration method for CATIROC has been tested and validated. It will allow to significantly reduce the number of calibration runs which is a critical point given the number of channels of the SPMT system. Then, the CATIROC simulation code has been used to test the SPMT system performance during a CCSN neutrino burst. The main result from this analysis is that for a neutrino burst from CCSN at a distance equal or farther than 1 kpc, the performance of CATIROC will allow to trigger on $> 96\%$ of the input signals from the SPMTs and to measure $> 96\%$ of the total charge. The majority of the information loss will occur during the first

hundreds of miliseconds of the burst. The main conclusion raised from this analysis is that the impact of CATIROC on the CCSN neutrino events reconstruction is expected to be negligible. The SPMT output data rate resulting from a CCSN neutrino burst is also of critical importance due to potential data loss during the transfer to the DAQ in case of data overflow. It has been computed together with the resulting total data amount. The latter reaches ∼300 MB per 128 SPMTs for a 1 kpc away CCSN. The DDR storage memory that will be embedded in the front-end electronics (1 GB per ABC + 2 GB per GCU) of the SPMT system is more than enough to temporary store all the data produced. The ∼10 seconds of data from the burst will then be tranferred and stored at the DAQ level. Given the risk of event pile-up due to the potential high neutrino interaction rate, it provides the opportunity to optimise the event building strategy, notably to retrieve the events piled-up. Thus, an *offline* event builder has been developed and optimised for the SPMT system. If capturing 300 ns of data each time an event is triggered by the event builder, which allows to conserve the reconstruction quality of the events in the reactor energy range, ∼75% of the events that are piled-up (for distances equal or farther than 3 kpc) are retrieved. This number drops at ∼55% for a 1 kpc away.
The events vertex and energy reconstruction constitute milestones in most of the physics analyses of JUNO. The vertex reconstruction is of particular relevance for detector Non-Uniformity (NU) corrections in the energy reconstruction and to fully exploit the IBD event topology during the event selection, which is the main detection channels for both reactor and CCSN analyses. The reconstruction algorithms developed only use the information from the SPMT system. The vertex reconstruction mainly uses the time information and is based on a maximum likelihood method, its performance was tested in both reactor and CCSN energy range (1-100 MeV). The simulation revealed the existence of a so-called Total Reflection (TR) area (see Chapter 4). Part of the events occuring in this region of the detector are reconstructed far from the true vertex. These events can be identified by means of a likelihood quality cut and rejected in the analysis if necessary. Thus, the efficiency of the algorithm is ∼70-75% at 1 MeV and reaches ∼98% at 10 MeV, the resolutions are ∼60 cm and ∼20 cm, respectively, for positron events with the full detector and electronics simulation. Such resolution are about two orders of magnitude below the size of the JUNO detector. Machine Learning (ML) techniques are currently being developed by the Subatech team and the preliminary results showed that it can achieve similar resolutions but also retrieve the poorly reconstructed events (in the TR area). The energy reconstruction is based on the number of PE registered by the SPMT system. The Liquid Scintillator Non-Linearity (LSNL) and detector NU are corrected for in the energy reconstruction process. A study of the energy resolution model of JUNO – the so-called *abc model* – is done and applied to the results obtained for positron events in the reactor energy range. Given the low energy scale of the SPMT system (∼40 PE/MeV), the energy resolution is largely dominated by the stochastic term. With the full detector simulation, according to the best fit ($\chi^2/d.o.f = 4.4$), the resolution is ∼19.2% at 1 MeV and ∼5.4% at 10 MeV. Ways to improve these results were also identified and described in Chapter 4. The performance in the higher energy range allows a precise reconstruction of most of the events from CCSN neutrinos, νpES excluded (low energy processes).
In continuity to the SPMT system readout electronics performance study and event reconstruction development, a selection strategy has been developed for the CCSN neutrinos. Such work constitute the first step towards the reconstruction of the aforementioned flavor-wise luminosities and energy spectra. The strategy is primary designed for the selection of the IBD and νeES events, but also allow to classify the events from the other channels. The purity and loss of the IBD selected sample are $> 99\%$ and $< 5\%$, respectively. Those of the νeES selected sample are ∼60% and ∼60%. A preliminary unfolding procedure to correct for the migration effects – that are due to the detector response – in the energy

spectra of the selected samples has also been tested using two different unfolding algorithms (TUnfold and another one implementing a SVD). Even though the comparison of the unfolded energy spectra with the true ones show no significant improvement, they are in good agreement. More work would be required to identify ways of improvement and retrieve the luminosities as well as the true energy spectra of the incident neutrinos from νeES events.

Several aspects of the CCSN neutrino detection with the SPMT system have been explored throughout this thesis and useful tools have been developed for the SPMT system. The different studies realised allowed to obtain a relatively accurate picture of the performance of the system in both reactor and CCSN energy range. In addition, ways of improvement at each level were identified, particularly in the event reconstruction and CCSN neutrino analysis. More broadly, the JUNO detector will enable the testing of a new instrumental calibration system for neutrino detectors: The Dual Calorimetry. The SPMT system is the centrepiece of this technique. Furthermore, JUNO will be one of the spearhead detectors for neutrino astronomy, not only through the detection of the next CCSN neutrino burst but also by becoming a powerful machine to monitor the transient sky thanks to the development of a Multi-Messenger (MM) trigger and by joining the Supernova Early Warning System (SNEWS).

Appendix

Parameters	Class	Requirement		Test fraction		Tolerance	Results
		(limit)	(mean)	HZC	JUNO	of diff.	(mean)
Φ (glass bulb)	A	(78, 82) mm	-	100%	10%	-	OK
QE@420 nm	A	>22%	>24%	100%	10%	<5%	24.9%
High Voltage	A	(900,1300) V	-	100%	10%	<3%	1113 V
SPE resolution	A	<45%	<35%	100%	10%	<15%	33.2%
PV ratio	A	>2	>3	100%	10%	-	3.2
DCR@0.25 PE	A	<1.8 kHz	<1.0 kHz	100%	10%	-	512 Hz
DCR@3.0 PE	A	<30 Hz	-	100%	10%	-	7.2 Hz
TTS (σ)	B	<2.1 ns	-	-	3%	-	1.6 ns
Pre-pulse	B	<5%	<4.5%	-	3%	-	0.5%
After-pulse	B	<15%	<10%	-	3%	-	3.9%
QE non-uniformity	B	<11%	-	-	3%	-	5%
Φ (eff. cathode)	B	>74 mm	-	-	3%	-	77.2 mm
QE@320 nm	C	>5%	-	-	1%	-	10.2%
QE@550 nm	C	>5%	-	-	1%	-	8.6%
Aging	D	>200 nA·years	-	-	3 PMTs	-	OK

Figure 5.22: *Summary of the SPMTs acceptance criteria and test results for different parameters.*

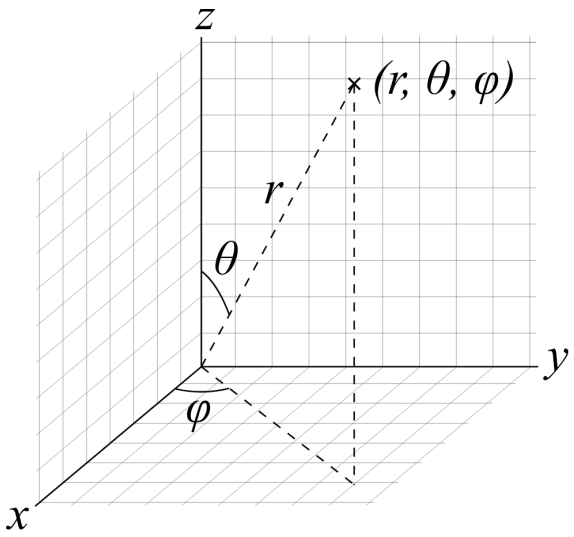

Figure 5.23: *Cartesian and spherical coordinates convention used in this manuscript.*

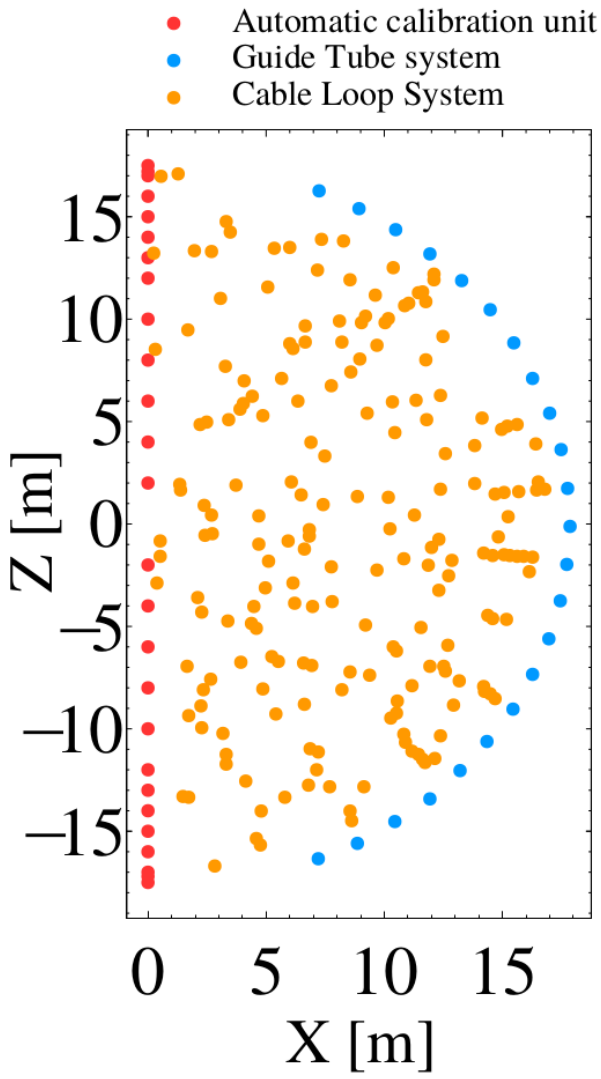

Figure 5.24: *Positions of the calibration points that will be used during the calibration campaigns of the JUNO detector. They are distributed on a vertical plane.*

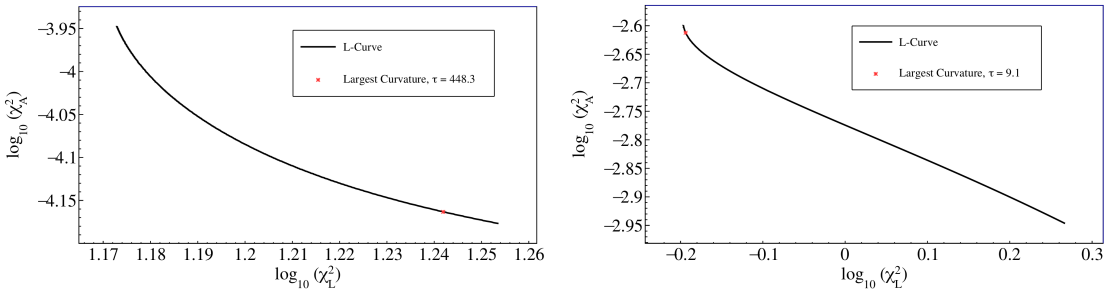

Figure 5.25: ***Left**: The L-curve scan of the IBD prompt signal selected sample spectrum unfolding. **Right**: The L-curve scan of the νeES selected sample spectrum unfolding. In both plots, The red star indicates the τ used for the regularisation.*

List of Figures

List of Tables

Acronyms

νeES Neutrino-Electron Elastic Scattering. 5, 17, 34, 35, 46, 47, 48, 75, 129, 130, 131, 132, 134, 135, 136, 137, 141, 142, 143, 144, 146, 147, 149, 150, 151, 154, 155, 159, 161, 168, 169, 170, 171

νpES Neutrino-Proton Elastic Scattering. 34, 36, 46, 47, 48, 75, 86, 87, 88, 130, 131, 132, 133, 134, 137, 138, 140, 141, 143, 144, 154, 155, 168

$0\nu\beta\beta$ Neutrinoless Double Beta Decay. 24, 26

ABC ASIC Battery Card. 59, 66, 67, 70, 71, 72, 74, 80, 81, 82, 83, 93, 155, 163, 165

ACU Automated Calibration Unit. 62

ADC Analog to Digital Converter. 68, 69, 70, 72, 163

ADU Analog-Digital Units. 56

ANTARES Astronomy with a Neutrino Telescope and Abyss Environmental Research. 23

BH Block Header. 82

BSM Beyond Standard Model. 51

BT Block Trailer. 82

CC Charged Current. 5, 17, 33, 36, 41, 46, 129, 130, 132, 133, 135, 136, 140, 141, 142, 143, 144, 145, 161, 169, 171

CCSN Core-Collapse Supernova. 3, 11, 12, 11, 12, 15, 26, 27, 28, 29, 31, 32, 33, 34, 35, 36, 46, 47, 48, 56, 58, 59, 65, 67, 69, 74, 75, 76, 77, 78, 79, 80, 81, 82, 83, 84, 85, 86, 87, 88, 90, 91, 93, 95, 96, 105, 110, 111, 113, 119, 124, 125, 126, 129, 130, 131, 133, 136, 141, 143, 145, 146, 147, 149, 151, 154, 155, 157, 162, 164, 165, 167, 168, 169, 170, 171

CCSN Core-Collapse Supernovae. 27

CD Central Detector. 44, 45, 52, 53, 54, 56, 57, 59, 60, 61, 62, 63, 64, 79, 96, 97, 98, 100, 101, 102, 103, 106, 107, 109, 113, 114, 116, 117, 120, 121, 124, 162, 163, 165, 166, 167, 168

CEνNS Coherent Elastic Neutrino-Nuclei Scatterings. 36

CENBG Centre d'Etudes Nucléaires de Bordeaux-Gradignan. 70

CL Confidence Level. 22, 23, 24, 51, 161

CLS Cable Loop Sytem. 62

COC Center of Charge. 100

CP Charge-Parity. 11, 21, 26, 27

DAQ Data Acquisition. 12, 46, 56, 59, 63, 65, 70, 74, 81, 82, 83, 129, 155

DARWIN DARk matter WImp search with liquid xenoN. 36

DCC Dual Calorimetry Calibration. 52, 58, 63, 116

DCD DDS Channel Data. 82

DCR Dark Count Rate. 55, 58, 64, 70, 101, 120

DCS Detector Control System. 64

DDR Dual Data Rate. 56, 59, 81, 82, 93, 155

DDS Discriminator Data Stream. 67, 79, 80, 81, 82, 165

DN Dark Noise. 70, 85, 86, 103, 105, 106, 119, 121, 122, 124, 126, 165, 166

DSNB Diffuse Supernovae Neutrino Background. 11, 48, 49, 74

DUNE Deep Underground Neutrino Experiment. 26, 27, 34, 36, 46, 133

ECD Event Channel Data. 82

ENSDF Evaluated Nuclear Structure Data File. 41

FPGA Field Programmable Gate Array. 56, 59, 66, 67, 69, 82, 163

FV Fiducial Volume. 43, 44, 45, 96, 123, 133, 136, 143, 145, 169

GB Gigabyte. 81, 82

GCU Global Control Unit. 56, 59, 81, 82, 155, 163

GEANT4 GEometry ANd Tracking. 101, 103, 113, 120

GT Guide Tube. 63

GTUs Grand Unified Theories. 51

HG High Gain. 66, 68, 69, 70, 71, 72, 73, 163, 164

HK Hyper-Kamiokande. 26, 27, 34, 35, 46, 47, 49, 50, 133

HV High Voltage. 56, 59, 69, 70, 163

IBD Inverse Beta Decay. 5, 11, 17, 18, 28, 34, 35, 36, 41, 42, 43, 44, 46, 47, 48, 49, 62, 64, 75, 76, 77, 78, 85, 87, 96, 102, 105, 107, 108, 111, 113, 124, 125, 126, 129, 130, 131, 133, 134, 135, 136, 137, 138, 139, 140, 141, 142, 143, 144, 146, 147, 149, 151, 154, 155, 159, 161, 162, 164, 167, 168, 169, 170, 171

IHEP Institute of High Energy Physics. 63, 83

ILL Institut Laue-Langevin. 40

IO Inverted Ordering. 21, 24, 26, 39, 161

JUNO Jiangmen Underground Neutrino Observatory. 11, 26, 27, 34, 36

K2K KEK-to-Kamioka. 23

KATRIN Karlsruhe Tritium Neutrino experiment. 24

KM3NeT Cubic Kilometre Neutrino Telescope. 34, 35, 46, 50

LAB Linear Alkyl Benzene. 54

LArTPC Liquid Argon Time Projection Chamber. 36

LBνB Long-Baseline Neutrino Beam. 23, 26

LG Low Gain. 66, 68, 69, 70, 71, 72, 73, 163, 164

LP2I Laboratoire de Physique des Deux Infinis. 70

LPMT Large Photomultiplier Tube. 11, 52, 53, 54, 55, 56, 57, 58, 59, 63, 78, 81, 83, 88, 103, 106, 113, 116, 129, 155, 163

LS Liquid Scintillator. 11, 36, 41, 43, 44, 45, 47, 49, 50, 52, 53, 54, 55, 57, 61, 63, 64, 75, 95, 98, 99, 101, 103, 104, 105, 113, 115, 116, 119, 121, 122, 123, 126, 130, 149, 165

LSNL Liquid Scintillator Non-Linearity. 58, 62, 113, 114, 115, 116, 119, 121, 126, 131, 149, 150, 155, 167, 169

LXeTPC Liquid Xenon Time Projection Chamber. 36

LY Light Yield. 54

MB Megabyte. 82

MC Monte Carlo. 105, 111, 119, 131, 133, 136, 137, 138, 139, 140, 141, 142, 143, 144, 147, 149, 168, 171

MCP Micro-Channel Plate. 55, 60

MINOS Main Injector Neutrino Oscillation Search. 23, 24, 161

ML Machine Learning. 107, 126, 139, 155

MM Multi-Messenger. 56, 88, 157

NC Neutral Current. 5, 17, 46, 48, 129, 130, 132, 134, 136, 141, 143, 144, 154, 161

NMO Neutrino Mass Ordering. 11, 21, 23, 26, 37, 38, 39, 43, 50, 52, 53, 57, 60, 64, 75, 116, 126, 155, 161, 167

NO Normal Ordering. 21, 22, 23, 24, 26, 39, 161

NPP Nuclear Power Plant. 37, 40

NU Non-Uniformity. 58, 62, 96, 102, 107, 108, 109, 113, 114, 115, 116, 117, 119, 122, 123, 124, 126, 155

OEC Online Event Classification. 63

ORCA Oscillation Research with Cosmics in the Abyss.. 26

OSIRIS Online Scintillator Internal Radioactivity Investigation System. 54

PDE Photo Detection Efficiency. 55, 64

PDF Probability Density Function. 105, 106, 107, 110, 166

PDG Particle Data Group. 45, 171

PE Photoelectron. 55, 57, 58, 59, 62, 64, 66, 67, 69, 70, 79, 80, 86, 89, 91, 96, 97, 100, 101, 102, 105, 106, 113, 114, 113, 114, 116, 117, 118, 119, 121, 122, 124, 126, 155, 163, 165, 166, 167

PMT Photomultiplier Tube. 11, 18, 44, 45, 52, 53, 54, 55, 56, 57, 58, 60, 61, 62, 63, 64, 66, 69, 70, 81, 92, 95, 96, 97, 98, 99, 103, 104, 105, 106, 107, 113, 114, 116, 119, 120, 122, 123, 126, 129, 155, 163, 165, 166, 167

PNS Proto-Neutron Star. 30, 31, 32, 33, 34, 75, 76, 145, 155, 162

PTF Peak Time Fitter. 102

QDS Charge Data Stream. 69, 79, 80, 82, 85, 164

QE Quantum Efficiency. 58, 70, 101, 113, 120

QNL Charge Non-Linearity. 57, 58, 63

ROV Remotely Operable Vehicle. 63

SASI Standing Accretion Shock Instabilities. 31

SCA Switch Capacitor Array. 68

SK Super-Kamiokande. 19, 22, 23, 24, 35, 36, 47, 49, 50, 133, 161, 162

SM Standard Model. 11, 15, 16, 24, 51, 161

SN Supernovae. 27

SN Supernova. 27, 29, 34, 48, 133, 162

SNEWS Supernova Early Warning System. 36, 56, 157

SNiPER Software for Non-collider Physics ExpeRiments. 64, 78

SNO Subdury Neutrino Observatory. 19

SPE Single Photoelectron. 58, 70, 113, 121, 122

SPMT Small Photomultiplier Tube. 4, 5, 11, 12, 51, 52, 53, 57, 58, 59, 63, 64, 65, 66, 67, 69, 70, 71, 72, 74, 76, 78, 79, 80, 81, 82, 83, 85, 86, 87, 93, 95, 97, 100, 101, 102, 103, 104, 105, 106, 107, 109, 110, 113, 114, 113, 116, 120, 121, 122, 123, 124, 125, 126, 129, 130, 129, 132, 131, 133, 134, 136, 135, 136, 138, 140, 142, 144, 143, 146, 148, 150, 152, 154, 155, 157, 163, 164, 165, 166, 167, 168

ST Software Trigger. 63

SVD Singular Value Decomposition. 148, 151, 154, 155, 170

T2K Tokai-to-Kamioka. 22, 23, 24, 26, 161

TAC Time to Analog Converter. 67

TAO Taishan Neutrino Observatory. 41, 64

TR Total Reflection. 101, 103, 106, 116, 126, 139, 142, 155

TT Top Tracker. 44, 52, 53, 61, 63, 64, 101, 120, 163

TTS Transit Time Spread. 55, 58, 70, 97, 101, 103, 105, 120

UWB Under Water Boxes. 55, 56, 59, 74, 82, 163

WCD Water Cherenkov Detector. 44, 52, 53, 60, 61, 63, 64, 163

Bibliography

[1] Frank Close, Michael Marten, and Christine Sutton. *The particle odyssey : a journey to the heart of the matter*. Oxford University Press, 2004.

[2] Donald H. Perkins. *Introduction to High Energy Physics*. Cambridge University Press, 4 edition, 2000.

[3] R. P. Feynman. The theory of positrons. *Phys. Rev.*, 76:749–759, Sep 1949.

[4] L Alvarez-Ruso, Y Hayato, and J Nieves. Progress and open questions in the physics of neutrino cross sections at intermediate energies. *New Journal of Physics*, 16(7):075015, jul 2014.

[5] P. A. Zyla et al. Review of Particle Physics. *PTEP*, 2020(8):083C01, 2020.

[6] H. Becquerel. Sur les radiations invisibles émises par les sels d'uranium, 1896.

[7] M. Curie. Rayons émis par les composés de l'uranium et du thorium, 1898.

[8] J. Chadwick. Intensitatsverteilung im magnetischen spektrum der beta-strahlen von radium b+c, 1914. Verhandlungen der deutschen Physikalischen Gesellschaft 16 (1914) 383.

[9] C.D. Ellis and W.A. Wooster. The average energy of disintegration of radium e. *Proc. R. Soc. Lond. A117*, page 109–123, 1927.

[10] Marie-Christine de La Souchère. La saga des neutrinos.

[11] J. Chadwick. The existence of neutron. *Proc. R. Soc. Lond. A136*, pages 692–708, 1932.

[12] F. Reines and C. L. Cowan. The neutrino. *Nature*, 178:446–449, September 1956.

[13] C. L. Cowan, F. Reines, F. B. Harrison, H. W. Kruse, and A. D. McGuire. Detection of the free neutrino: A Confirmation. *Science*, 124:103–104, 1956.

[14] E. Fermi. Tentativo di una teoria dei raggi β. *Il Nuovo Cimento*, 11, 1934.

[15] F. Suiekane. *Neutrino Oscillations - A practical guide to Basics and Applications*. Springer, 2015.

[16] G. et al. Danby. Observation of High-Energy Neutrino Reactions and the Existence of Two Kinds of Neutrinos. *Phys. Rev. Lett.*, 9:36–44, 1962.

[17] Raymond Davis. A review of the homestake solar neutrino experiment. *Progress in Particle and Nuclear Physics*, 32:13–32, 1994.

[18] B. T. et al. Cleveland. Measurement of the solar electron neutrino flux with the Homestake chlorine detector. *Astrophys. J.*, 496:505–526, 1998.

[19] W. Hampel et al. Gallex solar neutrino observations: results for gallex iv. *Physics Letters B*, 447(1-2):127–133, 1999.

[20] M. Altmann et al. Gno solar neutrino observations: results for gno i. *Physics Letters B*, 490(1):16–26, 2000.

[21] J.N. Abdurashitov et al. Results from sage (the russian-american gallium solar neutrino experiment). *Physics Letters B*, 328(1):234–248, 1994.

[22] Y. et al. Fukuda. Solar neutrino data covering solar cycle 22. *Phys. Rev. Lett.*, 77:1683–1686, Aug 1996.

[23] Y. et al. Fukuda. Measurements of the solar neutrino flux from super-kamiokande's first 300 days. *Phys. Rev. Lett.*, 81:1158–1162, Aug 1998.

[24] B. Pontecorvo. Mesonium and anti-mesonium. *Sov. Phys. JETP*, 6:429, 1957.

[25] B. Pontecorvo. Inverse beta processes and nonconservation of lepton charge. *Zh. Eksp. Teor. Fiz.*, 34:247, 1957.

[26] Ziro Maki, Masami Nakagawa, and Shoichi Sakata. Remarks on the unified model of elementary particles. *Prog. Theor. Phys.*, 28:870–880, 1962.

[27] G. J. Feldman et al. Inclusive Anomalous Muon Production in e+ e- Annihilation. *Phys. Rev. Lett.*, 38:117, 1977. [Erratum: Phys.Rev.Lett. 38, 576 (1977)].

[28] K. Kodama et al. Observation of tau neutrino interactions. *Phys. Lett. B*, 504:218–224, 2001.

[29] K Kodama et al. Detection and analysis of tau–neutrino interactions in donut emulsion target. *Nuclear Instruments and Methods in Physics Research Section A: Accelerators, Spectrometers, Detectors and Associated Equipment*, 493(1):45–66, 2002.

[30] K. S. Hirata et al. Experimental Study of the Atmospheric Neutrino Flux. *Phys. Lett. B*, 205:416, 1988.

[31] K. S. Hirata et al. Observation of a small atmospheric muon-neutrino / electron-neutrino ratio in Kamiokande. *Phys. Lett. B*, 280:146–152, 1992.

[32] D. et al. Casper. Measurement of atmospheric neutrino composition with the imb-3 detector. *Phys. Rev. Lett.*, 66:2561–2564, May 1991.

[33] R. et al. Becker-Szendy. Electron- and muon-neutrino content of the atmospheric flux. *Phys. Rev. D*, 46:3720–3724, Nov 1992.

[34] Maury C. Goodman. The Atmospheric neutrino anomaly in Soudan-2. *Nucl. Phys. B Proc. Suppl.*, 38:337–342, 1995.

[35] Y. et al. Fukuda. Evidence for oscillation of atmospheric neutrinos. *Phys. Rev. Lett.*, 81:1562–1567, Aug 1998.

[36] Y. et al. Ashie. Evidence for an oscillatory signature in atmospheric neutrino oscillations. *Phys. Rev. Lett.*, 93:101801, Sep 2004.

[37] P. A. M. Dirac. A new notation for quantum mechanics. *Mathematical Proceedings of the Cambridge Philosophical Society*, 35(3):416–418, 1939.

[38] Stephen Parke and Mark Ross-Lonergan. Unitarity and the three flavor neutrino mixing matrix. *Phys. Rev. D*, 93:113009, Jun 2016.

[39] Sheng Fong, Hisakazu Minakata, and Hiroshi Nunokawa. A framework for testing leptonic unitarity by neutrino oscillation experiments. *Journal of High Energy Physics*, 2017, 09 2016.

[40] E. Schrödinger. An Undulatory Theory of the Mechanics of Atoms and Molecules. *Physical Review*, 28(6):1049–1070, December 1926.

[41] D.J. Griffiths. *Introduction to Quantum Mechanics: Pearson New International Edition*. Always learning. Pearson Education Limited, 2013.

[42] L. Wolfenstein. Neutrino oscillations in matter. *Phys. Rev. D*, 17:2369–2374, May 1978.

[43] D. Motta. The Double Chooz experiment. *Acta Phys. Polon. B*, 37:2027–2037, 2006.

[44] The Double Chooz Collaboration. First Double Chooz θ_{13} Measurement via Total Neutron Capture Detection. *Nat. Phys.*, 16(5):558–564, May 2020. arXiv: 1901.09445.

[45] Eun-Ju Jeon. Status of reno experiment. *Nuclear Physics B - Proceedings Supplements*, 217(1):137–139, 2011. Proceedings of the Neutrino Oscillation Workshop (NOW 2010).

[46] G. et al. Bak. Measurement of reactor antineutrino oscillation amplitude and frequency at reno. *Phys. Rev. Lett.*, 121:201801, Nov 2018.

[47] Jun Cao and Kam-Biu Luk. An overview of the daya bay reactor neutrino experiment. *Nuclear Physics B*, 908:62–73, 2016. Neutrino Oscillations: Celebrating the Nobel Prize in Physics 2015.

[48] Daya Bay Collaboration. New measurement of θ_{13} via neutron capture on hydrogen at Daya Bay. *Phys. Rev. D*, 93(7):072011, 2016. Publisher: American Physical Society.

[49] K. et al. Abe. Measurement of neutrino and antineutrino oscillations by the t2k experiment including a new additional sample of ν_e interactions at the far detector. *Phys. Rev. D*, 96:092006, Nov 2017.

[50] I. Esteban et. al. Nufit.

[51] I. Esteban et al. The fate of hints: updated global analysis of three-flavor neutrino oscillations. *J. High Energ. Phys.*, September 2020.

[52] Thiago Junqueira de Castro Bezerra. *Improvement of θ_{13} Measurement in the Double Chooz Experiment and the First Effective Δm^2_{31} measurement from Reactor Neutrino Oscillation at Different Baselines*. PhD thesis, Tohoku University (Sendai, Japan), 2013.

[53] S. et al. Abe. Precision measurement of neutrino oscillation parameters with kamland. *Phys. Rev. Lett.*, 100:221803, Jun 2008.

[54] I. Esteban, M. Gonzalez-Garcia, and M. et al. Maltoni. 2020 global reassessment of the neutrino oscillation picture. *J. High Energ. Phys.*, February 2021.

[55] Yoichiro Suzuki. The super-kamiokande experiment. *The European Physical Journal C*, 79, 04 2019.

[56] R. Abbasi et al. The design and performance of icecube deepcore. *Astroparticle Physics*, 35(10):615–624, 2012.

[57] M. G. et al. Aartsen. Determining neutrino oscillation parameters from atmospheric muon neutrino disappearance with three years of icecube deepcore data. *Phys. Rev. D*, 91:072004, Apr 2015.

[58] Douglas Michael. The minos experiment. *Nuclear Physics B - Proceedings Supplements*, 118:189–196, 2003. Proceedings of the XXth International Conference on Neutrino Physics and Astrophysics.

[59] P. el al. Adamson. Measurements of atmospheric neutrinos and antineutrinos in the minos far detector. *Phys. Rev. D*, 86:052007, Sep 2012.

[60] I. Sokalski and for Collaboration. The antares experiment: past, present and future, 02 2005.

[61] S. et al. Adrian-Martinez. Measurement of Atmospheric Neutrino Oscillations with the ANTARES Neutrino Telescope. *Physics Letters B*, 714:224–230, Aug 2012. 9 pages, 5 figures.

[62] M. H. Ahn et al. Measurement of neutrino oscillation by the k2k experiment. *Phys. Rev. D*, 74:072003, Oct 2006.

[63] L.H. Whitehead. Neutrino oscillations with minos and minos+. *Nuclear Physics B*, 908:130–150, 2016. Neutrino Oscillations: Celebrating the Nobel Prize in Physics 2015.

[64] P. et al. Adamson. Precision constraints for three-flavor neutrino oscillations from the full minos+ and minos dataset. *Phys. Rev. Lett.*, 125:131802, Sep 2020.

[65] K. Abe et al. The t2k experiment. *Nuclear Instruments and Methods in Physics Research Section A: Accelerators, Spectrometers, Detectors and Associated Equipment*, 659(1):106–135, 2011.

[66] M. A. et al. Acero. First measurement of neutrino oscillation parameters using neutrinos and antineutrinos by nova. *Phys. Rev. Lett.*, 123:151803, Oct 2019.

[67] I. Esteban et. al. Global analysis of three-flavour neutrino oscillations: synergies and tensions in the determination of θ_{23}, δ_{CP} and the mass ordering. *J. High Energ. Phys.*, January 2019.

[68] E. Majorana. Teoria simmetrica dell'elettrone e del positrone. *Nuovo Cim.*, 1937.

[69] Ettore Majorana and Luciano Maiani. *A symmetric theory of electrons and positrons*. Springer Berlin Heidelberg, Berlin, Heidelberg, 2006.

[70] Stefano Dell'Oro, Simone Marcocci, Matteo Viel, and F. Vissani. Neutrinoless double beta decay: 2015 review. *Advances in High Energy Physics*, 2016:1–37, 01 2016.

[71] Michelle J. Dolinski, Alan W.P. Poon, and Werner Rodejohann. Neutrinoless double-beta decay: Status and prospects. *Annual Review of Nuclear and Particle Science*, 69(1):219–251, 2019.

[72] M. et al. Aker. Improved upper limit on the neutrino mass from a direct kinematic method by katrin. *Phys. Rev. Lett.*, 123:221802, Nov 2019.

[73] S F King. Neutrino mass models. *Reports on Progress in Physics*, 67(2):107–157, dec 2003.

[74] Steen Hannestad and Thomas Schwetz. Cosmology and the neutrino mass ordering. *Journal of Cosmology and Astroparticle Physics*, 2016(11):035–035, nov 2016.

[75] Stephen F. King. Neutrino mass and mixing in the seesaw playground. *Nuclear Physics B*, 908:456–466, 2016. Neutrino Oscillations: Celebrating the Nobel Prize in Physics 2015.

[76] A. Abusleme et. al. Juno physics and detector. *Progr. Part. Nucl. Phys. (2021) 103927*, April 2021.

[77] B. et al. Abi. Long-baseline neutrino oscillation physics potential of the DUNE experiment. *Eur.Phys.J.C*, 80(10):978, 2020.

[78] S. et al. Aiello. Determining the neutrino mass ordering and oscillation parameters with km3net/orca. *Eur. Phys. J. C*, 2022.

[79] K. et al. Abe. Hyper-kamiokande design report, 2018.

[80] Amol S. Dighe and Alexei Yu. Smirnov. Identifying the neutrino mass spectrum from a supernova neutrino burst. *Phys. Rev. D*, 62:033007, Jul 2000.

[81] Kate Scholberg. Supernova signatures of neutrino mass ordering. *Journal of Physics G: Nuclear and Particle Physics*, 45(1):014002, dec 2017.

[82] R. N. Mohapatra and A. Y. Smirnov. Neutrino Mass and New Physics. *Ann. Rev. Nucl. Part. Sci.*, 56:569–628, 2006.

[83] Dominic Brailsford. DUNE: Status and Perspectives. In *Prospects in Neutrino Physics*, pages 4–12, 4 2018.

[84] K. Abe et al. Letter of Intent: The Hyper-Kamiokande Experiment — Detector Design and Physics Potential —, 9 2011.

[85] J. H. Christenson, J. W. Cronin, V. L. Fitch, and R. Turlay. Evidence for the 2π decay of the k_2^0 meson. *Phys. Rev. Lett.*, 13:138–140, Jul 1964.

[86] H.A. Tanaka. Hyper-kamiokande: a next generation neutrino observatory to search for cp violation in the lepton sector. *Nuclear and Particle Physics Proceedings*, 273-275:1902–1908, 2016. 37th International Conference on High Energy Physics (ICHEP).

[87] Mayumi Aoki, Kaoru Hagiwara, and Naotoshi Okamura. Measuring the cp-violating phase by a long base-line neutrino experiment with hyper-kamiokande. *Physics Letters B*, 554(3):121–132, 2003.

[88] Carlo Giunti and Marco Laveder. Statistical significance of the gallium anomaly. *Phys. Rev. C*, 83:065504, Jun 2011.

[89] G. Mention, M. Fechner, Th. Lasserre, Th. A. Mueller, D. Lhuillier, M. Cribier, and A. Letourneau. Reactor antineutrino anomaly. *Phys. Rev. D*, 83:073006, Apr 2011.

[90] Sebastian Böser et al. Status of light sterile neutrino searches. *Progress in Particle and Nuclear Physics*, 111:103736, 2020.

[91] K. N. Abazajian et al. Light Sterile Neutrinos: A White Paper, 4 2012.

[92] F. Richard Stephenson and David A. Green. *Historical Supernovae and their Remnants*. Oxford Scholarship Online, 2002.

[93] W. Baade and F. Zwicky. On Super-novae. *Proceedings of the National Academy of Science*, 20(5):254–259, May 1934.

[94] P. Frank Winkler, Gaurav Gupta, and Knox S. Long. The SN 1006 remnant: Optical proper motions, deep imaging, distance, and brightness at maximum. *The Astrophysical Journal*, 585(1):324–335, mar 2003.

[95] Oliver Krause et al. Tycho brahe's 1572 supernova as a standard type ia as revealed by its light-echo spectrum. *Nature*, 456(7222):617–619, dec 2008.

[96] E M Schlegel. X-ray emission from supernovae: a review of the observations. *Reports on Progress in Physics*, 58(11):1375–1413, nov 1995.

[97] A. Burrows and D. Vartanyan. Core-collapse supernova explosion theory. *Nature*, 589(7840):29–39, jan 2021.

[98] K. et al. Hirata. Observation of a neutrino burst from the supernova sn1987a. *Phys. Rev. Lett.*, 58:1490–1493, Apr 1987.

[99] R. M. et al. Bionta. Observation of a neutrino burst in coincidence with supernova 1987a in the large magellanic cloud. *Phys. Rev. Lett.*, 58:1494–1496, Apr 1987.

[100] E.N. Alexeyev, L.N. Alexeyeva, I.V. Krivosheina, and V.I. Volchenko. Detection of the neutrino signal from sn 1987a in the lmc using the inr baksan underground scintillation telescope. *Physics Letters B*, 205(2):209–214, 1988.

[101] Dipankar Bhattacharya. Supernova 1987A - A review. *Bulletin of the Astronomical Society of India*, 16:57–66, June 1988.

[102] Stephen W. Bruenn. Neutrinos from sn1987a and current models of stellar-core collapse. *Phys. Rev. Lett.*, 59:938–941, Aug 1987.

[103] Karolina Rozwadowska, Francesco Vissani, and Enrico Cappellaro. On the rate of core collapse supernovae in the milky way. *New Astronomy*, 83:101498, 2021.

[104] Hans-Thomas Janka. Explosion mechanisms of core-collapse supernovae. *Annual Review of Nuclear and Particle Science*, 62(1):407–451, nov 2012.

[105] H. Janka. Neutrino emission from supernovae, 02 2017.

[106] Wick Haxton, R. Robertson, and Aldo Serenelli. Solar neutrinos: Status and prospects. *Annual Review of Astronomy and Astrophysics*, 51, 08 2012.

[107] Chinami Kato et al. Neutrino emissions in all flavors up to the pre-bounce of massive stars and the possibility of their detections. *The Astrophysical Journal*, 848(1):48, oct 2017.

[108] Takashi Yoshida, Koh Takahashi, Hideyuki Umeda, and Koji Ishidoshiro. Presupernova neutrino events relating to the final evolution of massive stars. *Phys. Rev. D*, 93:123012, Jun 2016.

[109] Hui-Ling Li, Yu-Feng Li, Liang-Jian Wen, and Shun Zhou. Prospects for presupernova neutrino observation in future large liquid-scintillator detectors. *Journal of Cosmology and Astroparticle Physics*, 2020(05):049–049, May 2020.

[110] Imre Bartos and Marek Kowalski. *Multimessenger Astronomy*. 2399-2891. IOP Publishing, 2017.

[111] Nirmal Raj, Volodymyr Takhistov, and Samuel J. Witte. Presupernova neutrinos in large dark matter direct detection experiments. *Phys. Rev. D*, 101:043008, Feb 2020.

[112] Freeman J. Dyson. Ground-State Energy of a Finite System of Charged Particles. *Journal of Mathematical Physics*, 8, 1967.

[113] W. Pauli. Über den Zusammenhang des Abschlusses der Elektronengruppen im Atom mit der Komplexstruktur der Spektren. *Zeitschrift für Physik*, 1925.

[114] S. E. Woosley, A. Heger, and T. A. Weaver. The evolution and explosion of massive stars. *Rev. Mod. Phys.*, 74:1015–1071, Nov 2002.

[115] William A. Fowler and F. Hoyle. Neutrino Processes and Pair Formation in Massive Stars and Supernovae. *Astrophysical Journal Supplement*, 9:201, December 1964.

[116] Thomas W. Baumgarte, H. Thomas Janka, Wolfgang Keil, Stuart L. Shapiro, and Saul A. Teukolsky. Delayed Collapse of Hot Neutron Stars to Black Holes via Hadronic Phase Transitions. *Astrophysical Journal*, 468:823, September 1996.

[117] Jia-Shian Wang, Jeff Tseng, Samuel Gullin, and Evan P. O'Connor. Nonradial neutrino emission upon black hole formation in core collapse supernovae. *Phys. Rev. D*, 104:104030, Nov 2021.

[118] Samuel Gullin, Evan P. O'Connor, Jia-Shian Wang, and Jeff Tseng. Neutrino echos following black hole formation in core-collapse supernovae. *The Astrophysical Journal*, 926(2):212, feb 2022.

[119] Bruno Peres. *Transport de neutrinos dans les supernovas gravitationnelles*. Theses, Observatoire de Paris, July 2013.

[120] Anthony Mezzacappa. Ascertaining the core collapse supernova mechanism: The state of the art and the road ahead. *Annual Review of Nuclear and Particle Science*, 55(1):467–515, 2005.

[121] Hans-Thomas Janka. Explosion mechanisms of core-collapse supernovae. *Annual Review of Nuclear and Particle Science*, 62(1):407–451, 2012.

[122] B. Müller. The status of multi-dimensional core-collapse supernova models. *Publications of the Astronomical Society of Australia*, 33:e048, September 2016.

[123] H. A. Bethe and J. R. Wilson. Revival of a stalled supernova shock by neutrino heating. *Astrophys. J*, 295:14–23, August 1985.

[124] John M. Blondin, Anthony Mezzacappa, and Christine DeMarino. Stability of standing accretion shocks, with an eye toward core collapse supernovae. *Astrophys. J.*, 584:971–980, 2003.

[125] Hans-Thomas Janka. Neutrino emission from supernovae. *Handbook of Supernovae*, page 1575–1604, 2017.

[126] Irene Tamborra, Bernhard Müller, Lorenz Hüdepohl, Hans-Thomas Janka, and Georg Raffelt. High-resolution supernova neutrino spectra represented by a simple fit. *Phys. Rev. D*, 86:125031, Dec 2012.

[127] T. Totani, K. Sato, H. E. Dalhed, and J. R. Wilson. Future detection of supernova neutrino burst and explosion mechanism. *The Astrophysical Journal*, 496(1):216–225, mar 1998.

[128] Ken'ichiro Nakazato, Kohsuke Sumiyoshi, and Hajime Togashi. Numerical study of stellar core collapse and neutrino emission using the nuclear equation of state obtained by the variational method. *Publications of the Astronomical Society of Japan*, 73(3):639–651, 05 2021.

[129] Sean M. Couch, MacKenzie L. Warren, and Evan P. O'Connor. Simulating turbulence-aided neutrino-driven core-collapse supernova explosions in one dimension. *The Astrophysical Journal*, 890(2):127, Feb 2020.

[130] Irene Tamborra, Florian Hanke, Bernhard Müller, Hans-Thomas Janka, and Georg Raffelt. Neutrino signature of supernova hydrodynamical instabilities in three dimensions. *Phys. Rev. Lett.*, 111:121104, Sep 2013.

[131] Tuguldur Sukhbold, T. Ertl, S. E. Woosley, Justin M. Brown, and H.-T. Janka. CORE-COLLAPSE SUPERNOVAE FROM 9 TO 120 SOLAR MASSES BASED ON NEUTRINO-POWERED EXPLOSIONS. *The Astrophysical Journal*, 821(1):38, apr 2016.

[132] B. Müller. Neutrino emission as diagnostics of core-collapse supernovae. *Annual Review of Nuclear and Particle Science*, 69(1):253–278, 2019.

[133] Scott M. Adams, C. S. Kochanek, John F. Beacom, Mark R. Vagins, and K. Z. Stanek. OBSERVING THE NEXT GALACTIC SUPERNOVA. *The Astrophysical Journal*, 778(2):164, nov 2013.

[134] Markus Ahlers, Philipp Mertsch, and Subir Sarkar. Cosmic ray acceleration in supernova remnants and the fermi/pamela data. *Phys. Rev. D*, 80:123017, Dec 2009.

[135] Huaiyu Duan, George M. Fuller, and Yong-Zhong Qian. Collective neutrino oscillations. *Annual Review of Nuclear and Particle Science*, 60(1):569–594, 2010.

[136] K. Abe et al. Supernova model discrimination with hyper-kamiokande. *The Astrophysical Journal*, 916(1):15, jul 2021.

[137] Jackson Olsen and Yong-Zhong Qian. Prospects for distinguishing supernova models using a future neutrino signal. *Phys. Rev. D*, 105:083017, Apr 2022.

[138] Lorenz Hüdepohl. *Neutrinos from the formation, cooling, and black hole collapse of neutron stars*. PhD thesis, Munich University of Technology, Germany, January 2014.

[139] G. Martínez-Pinedo, T. Fischer, A. Lohs, and L. Huther. Charged-current weak interaction processes in hot and dense matter and its impact on the spectra of neutrinos emitted from protoneutron star cooling. *Phys. Rev. Lett.*, 109:251104, Dec 2012.

[140] H. T. Janka and W. Hillebrandt. Neutrino emission from type II supernovae : an analysis of the spectra. *Astronomy and Astrophysics*, 224:49–56, October 1989.

[141] Bernhard Müller and Hans-Thomas Janka. A NEW MULTI-DIMENSIONAL GENERAL RELATIVISTIC NEUTRINO HYDRODYNAMICS CODE FOR CORE-COLLAPSE SUPERNOVAE. IV. THE NEUTRINO SIGNAL. *The Astrophysical Journal*, 788(1):82, may 2014.

[142] Evan O Connor and Christian D. Ott. THE PROGENITOR DEPENDENCE OF THE PRE-EXPLOSION NEUTRINO EMISSION IN CORE-COLLAPSE SUPERNOVAE. *The Astrophysical Journal*, 762(2):126, dec 2012.

[143] G. Pagliaroli, F. Vissani, M.L. Costantini, and A. Ianni. Improved analysis of sn1987a antineutrino events. *Astroparticle Physics*, 31(3):163–176, 2009.

[144] Kate Scholberg. Supernova neutrino detection. *Annual Review of Nuclear and Particle Science*, 62(1):81–103, nov 2012.

[145] A Oralbaev, Mikhail Skorokhvatov, and O Titov. The inverse beta decay: a study of cross section. *Journal of Physics: Conference Series*, 675:012003, 02 2016.

[146] William J Marciano and Zohreh Parsa. Neutrino–electron scattering theory. *Journal of Physics G: Nuclear and Particle Physics*, 29(11):2629–2645, oct 2003.

[147] John F. Beacom, Will M. Farr, and Petr Vogel. Detection of supernova neutrinos by neutrino-proton elastic scattering. *Phys. Rev. D*, 66:033001, Aug 2002.

[148] P. Vogel and J. F. Beacom. Angular distribution of neutron inverse beta decay, $\overline{\nu}_e + \vec{p}\, e^+ + n$. *Phys. Rev. D*, 60:053003, Jul 1999.

[149] Alessandro Strumia and Francesco Vissani. Precise quasielastic neutrino/nucleon cross-section. *Physics Letters B*, 564(1-2):42–54, jul 2003.

[150] Francis Halzen and Georg G. Raffelt. Reconstructing the supernova bounce time with neutrinos in icecube. *Phys. Rev. D*, 80:087301, Oct 2009.

[151] Aiello, S. et al. The km3net potential for the next core-collapse supernova observation with neutrinos - km3net collaboration. *Eur. Phys. J. C*, 81(5):445, 2021.

[152] E. Aprile et al. The XENON1t dark matter experiment. *The European Physical Journal C*, 77(12), dec 2017.

[153] E. Aprile et al. Projected WIMP sensitivity of the XENONnT dark matter experiment. *Journal of Cosmology and Astroparticle Physics*, 2020(11):031–031, nov 2020.

[154] J. Aalbers et al. DARWIN: towards the ultimate dark matter detector. *Journal of Cosmology and Astroparticle Physics*, 2016(11):017–017, nov 2016.

[155] S Al Kharusi et al. SNEWS 2.0: a next-generation supernova early warning system for multi-messenger astronomy. *New Journal of Physics*, 23(3):031201, mar 2021.

[156] John G. Learned, Stephen T. Dye, Sandip Pakvasa, and Robert C. Svoboda. Determination of neutrino mass hierarchy and θ_{13} with a remote detector of reactor antineutrinos. *Phys. Rev. D*, 78:071302, Oct 2008.

[157] Liang Zhan, Yifang Wang, Jun Cao, and Liangjian Wen. Determination of the neutrino mass hierarchy at an intermediate baseline. *Phys. Rev. D*, 78(11):111103, December 2008.

[158] Liang Zhan, Yifang Wang, Jun Cao, and Liangjian Wen. Experimental requirements to determine the neutrino mass hierarchy using reactor neutrinos. *Phys. Rev. D*, 79(7):073007, April 2009.

[159] F. P. et al. An. Observation of Electron-Antineutrino Disappearance at Daya Bay. *Phys. Rev. Lett.*, 108(17):171803, April 2012.

[160] Y. et al. Abe. Indication of Reactor Electron Antineutrinos Disappearance in the Double Chooz Experiment. *Phys. Rev. Lett.*, 108(13):131801, March 2012.

[161] J. K. et al. Ahn. Observation of Reactor Electron Antineutrinos Disappearance in the RENO Experiment. *Phys. Rev. Lett.*, 108(19):191802, May 2012.

[162] Fengpeng et al. An. Neutrino physics with JUNO. *J. Phys. G: Nucl. Part. Phys.*, 43(3):030401, March 2016.

[163] N. Chau et al. Neutrino mass ordering determination through combined analysis with JUNO and KM3net/ORCA. *Journal of Instrumentation*, 16(11):C11007, nov 2021.

[164] M. G. et al. Aartsen. Combined sensitivity to the neutrino mass ordering with JUNO, the icecube upgrade, and PINGU. *Phys. Rev. D*, 101:032006, Feb 2020.

[165] Anatael et al. Cabrera. Synergies and prospects for early resolution of the neutrino mass ordering. *Scientific Reports*, 12, 03 2022.

[166] K. Schreckenbach, H.R. Faust, F. von Feilitzsch, A.A. Hahn, K. Hawerkamp, and J.L. Vuilleumier. Absolute measurement of the beta spectrum from 235u fission as a basis for reactor antineutrino experiments. *Physics Letters B*, 99(3):251–256, 1981.

[167] F. von Feilitzsch, A.A. Hahn, and K. Schreckenbach. Experimental beta-spectra from 239pu and 235u thermal neutron fission products and their correlated antineutrino spectra. *Physics Letters B*, 118(1):162–166, 1982.

[168] K. Schreckenbach, G. Colvin, W. Gelletly, and F. Von Feilitzsch. Determination of the anti-neutrino spectrum from u-235 thermal neutron fission products up to 9.5 mev. *Phys. Lett. B*, 160:325–330, 1985.

[169] M. R. Bhat. Evaluated nuclear structure data file (ensdf). In Syed M. Qaim, editor, *Nuclear Data for Science and Technology*, pages 817–821, Berlin, Heidelberg, 1992. Springer Berlin Heidelberg.

[170] M. Fallot, S. Cormon, M. Estienne, A. Algora, V. M. Bui, A. Cucoanes, M. Elnimr, L. Giot, D. Jordan, J. Martino, A. Onillon, A. Porta, G. Pronost, A. Remoto, J. L. Taín, F. Yermia, and A.-A. Zakari-Issoufou. New antineutrino energy spectra predictions from the summation of beta decay branches of the fission products. *Phys. Rev. Lett.*, 109:202504, Nov 2012.

[171] Yasushi et al. Kino. Positron annihilation in liquid scintillator for electron antineutrino detection. *Journal of Nuclear and Radiochemical Sciences*, 1:63–68, 01 2000.

[172] D. Franco, G. Consolati, and D. Trezzi. Positronium signature in organic liquid scintillators for neutrino experiments. *Phys. Rev. C*, 83:015504, Jan 2011.

[173] Angel et al. Abusleme. Radioactivity control strategy for the JUNO detector. *Journal of High Energy Physics*, 2021, 11 2021.

[174] A. Fengpeng et al. Neutrino physics with JUNO. *J. Phys. G: Nucl. Part. Phys. 43, (2016) 030401*, February 2016.

[175] Angel et al. Abusleme. Sub-percent precision measurement of neutrino oscillation parameters with juno. `https://arxiv.org/abs/2204.13249`, 2022.

[176] Marco et al. Aglietta. On the event observed in the mont blanc underground neutrino observatory during the occurrence of supernova 1987a. *EPL (Europhysics Letters)*, 3:1315, 07 2007.

[177] Alessandro et al. Mirizzi. Supernova neutrinos: Production, oscillations and detection. *Rivista del Nuovo Cimento*, 39, 07 2016.

[178] B. Abi et al. Supernova neutrino burst detection with the deep underground neutrino experiment. *The European Physical Journal C*, 81(5), may 2021.

[179] Basudeb Dasgupta and John F. Beacom. Reconstruction of supernova ν_μ, ν_τ, $\overline{\nu}_\mu$, and $\overline{\nu}_\tau$ neutrino spectra at scintillator detectors. *Phys. Rev. D*, 83:113006, Jun 2011.

[180] Jia-Shu Lu, Yu-Feng Li, and Shun Zhou. Getting the most from the detection of galactic supernova neutrinos in future large liquid-scintillator detectors. *Phys. Rev. D*, 94:023006, Jul 2016.

[181] Steven Weinberg. Effects of a neutral intermediate boson in semileptonic processes. *Phys. Rev. D*, 5:1412–1417, Mar 1972.

[182] Ranjan Laha, John F. Beacom, and Sanjib Kumar Agarwalla. New power to measure supernova ν_e with large liquid scintillator detectors, 2014.

[183] M. Fukugita, Y. Kohyama, and K. Kubodera. Neutrino reaction cross-sections on c-12 target. *Phys. Lett. B*, 212:139–144, 1988.

[184] C. Volpe, N. Auerbach, G. Colò, T. Suzuki, and N. Van Giai. Microscopic theories of neutrino-^{12}C reactions. *Phys. Rev. C*, 62:015501, May 2000.

[185] L. B. et al. Auerbach. Measurements of charged current reactions of ν_e on ^{12}C. *Phys. Rev. C*, 64:065501, Nov 2001.

[186] Chinami Kato, Milad Delfan Azari, Shoichi Yamada, Koh Takahashi, Hideyuki Umeda, Takashi Yoshida, and Koji Ishidoshiro. Pre-supernova neutrino emissions from ONe cores in the progenitors of core-collapse supernovae: Are they distinguishable from those of Fe cores ? *The Astrophysical Journal*, 808(2):168, jul 2015.

[187] John F. Beacom. The diffuse supernova neutrino background. *Annual Review of Nuclear and Particle Science*, 60(1):439–462, 2010.

[188] M. et al. Malek. Search for supernova relic neutrinos at super-kamiokande. *Phys. Rev. Lett.*, 90:061101, Feb 2003.

[189] K. et al. Bays. Supernova relic neutrino search at super-kamiokande. *Phys. Rev. D*, 85:052007, Mar 2012.

[190] H. Zhang et al. Supernova relic neutrino search with neutron tagging at super-kamiokande-iv. *Astroparticle Physics*, 60:41–46, 2015.

[191] K. et al. Abe. Diffuse supernova neutrino background search at super-kamiokande. *Phys. Rev. D*, 104:122002, Dec 2021.

[192] JUNO Collaboration and Angel et al. Abusleme. Prospects for detecting the diffuse supernova neutrino background with juno, 2022.

[193] Mark Vagins Yufeng Li and Michael Wurm. Prospects for the detection of the diffuse supernova neutrino background with the experiments SK-gd and JUNO. *arXiv:2201.12920*, January 2022.

[194] M. et al. Agostini. Comprehensive measurement of *pp*-chain solar neutrinos. *Nature*, 562(7728):505–510, 2018.

[195] M. Agostini et al. Experimental evidence of neutrinos produced in the CNO fusion cycle in the Sun. *Nature*, 587:577–582, 2020.

[196] Angel et al. Abusleme. Feasibility and physics potential of detecting ^{8}b solar neutrinos at JUNO. *Chin.Phys.C*, 45(2):023004, 2021.

[197] T. K. Gaisser and M. Honda. Flux of atmospheric neutrinos. *Ann. Rev. Nucl. Part. Sci.*, 52:153–199, 2002.

[198] A Kumar et al. Invited review: Physics potential of the ICAL detector at the india-based neutrino observatory (INO). *Pramana*, 88(5), apr 2017.

[199] M G Aartsen et al. PINGU: a vision for neutrino and particle physics at the south pole. *Journal of Physics G: Nuclear and Particle Physics*, 44(5):054006, apr 2017.

[200] Angel et al. Abusleme. JUNO sensitivity to low energy atmospheric neutrino spectra. *Eur.Phys.J.C*, 81:10, 2021.

[201] M. Honda, M. Sajjad Athar, T. Kajita, K. Kasahara, and S. Midorikawa. Atmospheric neutrino flux calculation using the nrlmsise-00 atmospheric model. *Phys. Rev. D*, 92:023004, Jul 2015.

[202] E. et al. Richard. Measurements of the atmospheric neutrino flux by super-kamiokande: Energy spectra, geomagnetic effects, and solar modulation. *Phys. Rev. D*, 94:052001, Sep 2016.

[203] Christoph Berger et al. A Study of atmospheric neutrino oscillations in the FREJUS experiment. *Phys. Lett. B*, 245:305–310, 1990.

[204] Matteo et al. Agostini. Comprehensive geoneutrino analysis with borexino. *Physical Review D*, 101, 01 2020.

[205] A. et al. Gando. Partial radiogenic heat model for earth revealed by geoneutrino measurements. *Nature Geoscience*, 4:647–651, 08 2011.

[206] Howard Georgi and S. L. Glashow. Unity of all elementary-particle forces. *Phys. Rev. Lett.*, 32:438–441, Feb 1974.

[207] Pran Nath and Pavel Fileviez Pérez. Proton stability in grand unified theories, in strings and in branes. *Physics Reports*, 441(5):191–317, 2007.

[208] D H Perkins. Proton decay experiments. *Annual Review of Nuclear and Particle Science*, 34(1):1–50, 1984.

[209] F. Reines, C. L. Cowan, and M. Goldhaber. Conservation of the number of nucleons. *Phys. Rev.*, 96:1157–1158, Nov 1954.

[210] M. Miura. Search for nucleon decay in super-kamiokande. *Proceedings of the 44th Rencontres de Moriond - 2009 Electroweak Interactions and Unified Theories, EW 2009*, 273-275:525–530, 01 2009.

[211] E. Baussan et al. The neutrino oscillation OPERA experiment Target Tracker. *Nucl. Instrum. Meth. A*, 581(1-2):465–468, 2007.

[212] Angel et al. Abusleme. Mass testing and characterization of 20-inch pmts for juno, 2022.

[213] Chuanya et al. Cao. Mass production and characterization of 3-inch PMTs for the JUNO experiment. *Nucl.Instrum.Meth.A*, 1005:165347, 2021.

[214] J.B Birks. *The Theory and Practice of Scintillation Counting*. International Series of Monographs in Electronics and Instrumentation. Pergamon, 1964.

[215] Hai-Bo et al. Yang. Light attenuation length of high quality linear alkyl benzene as liquid scintillator solvent for the juno experiment. *Journal of Instrumentation*, 12, 03 2017.

[216] Dewen Cao et al. Light absorption properties of the high quality linear alkylbenzene for the juno experiment. *Nuclear Instruments and Methods in Physics Research Section A: Accelerators, Spectrometers, Detectors and Associated Equipment*, 927:230–235, 2019.

[217] P. Lombardi et al. Distillation and stripping pilot plants for the juno neutrino detector: Design, operations and reliability. *Nuclear Instruments and Methods in Physics Research Section A: Accelerators, Spectrometers, Detectors and Associated Equipment*, 925:6–17, 2019.

[218] Abusleme Angel et. al. The design and sensitivity of juno's scintillator radiopurity pre-detector osiris. *Eur. Phys. J. C*, 81, 3 2021.

[219] A. B. Arons and M. B. Peppard. Einstein's proposal of the photon concept, a translation of the annalen de physik paper of 1905. *American Journal of Physics*, 33, May 1965.

[220] Hamamatsu Photonics K.K. Photomultiplier tubes - basics and applications. `https://www.hamamatsu.com/content/dam/hamamatsu-photonics/sites/documents/99_SALES_LIBRARY/etd/PMT_handbook_v3aE.pdf`, 2007.

[221] Hamamatsu Photonics K.K. R12860 datasheet. `https://www.hamamatsu.com/jp/en/product/optical-sensors/pmt/pmt_tube-alone/head-on-type/R12860.html`.

[222] Ling Ren et al. Study on the improvement of the 20-inch microchannel plate photomultiplier tubes for neutrino detector. *Nuclear Instruments and Methods in Physics Research Section A: Accelerators, Spectrometers, Detectors and Associated Equipment*, 977:164333, 2020.

[223] M. Bellato et al. Embedded readout electronics r&d for the large pmts in the juno experiment. *Nuclear Instruments and Methods in Physics Research Section A: Accelerators, Spectrometers, Detectors and Associated Equipment*, 985:164600, 2021.

[224] Yu-Feng Li, Jun Cao, Yifang Wang, and Liang Zhan. Unambiguous determination of the neutrino mass hierarchy using reactor neutrinos. *Phys. Rev. D*, 88:013008, Jul 2013.

[225] X. Qian, D. A. Dwyer, R. D. McKeown, P. Vogel, W. Wang, and C. Zhang. Mass Hierarchy Resolution in Reactor Anti-neutrino Experiments: Parameter Degeneracies and Detector Energy Response. *Phys. Rev. D*, 87(3):033005, 2013.

[226] Francesco Capozzi, E. Lisi, and A. Marrone. Neutrino mass hierarchy and neutrino oscillation parameters with one hundred thousand reactor events. *Physical Review D*, 89, 09 2013.

[227] Y. et al. Abe. Improved measurements of the neutrino mixing angle θ_{13} with the Double Chooz detector. *Journal of High Energy Physics*, 10(2014):86, 2014. 43 pages, 24 figures, submitted to JHEP.

[228] J. H. et al. Choi. Observation of energy and baseline dependent reactor antineutrino disappearance in the reno experiment. *Phys. Rev. Lett.*, 116:211801, May 2016.

[229] D. Adey et al. A high precision calibration of the nonlinear energy response at daya bay. *Nuclear Instruments and Methods in Physics Research Section A: Accelerators, Spectrometers, Detectors and Associated Equipment*, 940:230–242, 2019.

[230] Yang Han. *Dual Calorimetry for High Precision Neutrino Oscillation Measurement at JUNO Experiment*. PhD thesis, Université de Paris, 2020.

[231] Selma et al. Conforti. CATIROC: an integrated chip for neutrino experiments using photomultiplier tubes. *Journal of Instrumentation*, 16(05):P05010, 2021.

[232] Y. P. et al. Zhang. The development of ^{222}rn detectors for juno prototype. *Radiation Detection Technology and Methods*, 2(1), Jan 2018.

[233] L.F. et al. Xie. Developing the radium measurement system for the water cherenkov detector of the jiangmen underground neutrino observatory. *Nuclear Instruments and Methods in Physics Research Section A: Accelerators, Spectrometers, Detectors and Associated Equipment*, 976:164266, Oct 2020.

[234] I. M. Frank and I. E. Tamm. Coherent visible radiation of fast electrons passing through matter. *Compt. Rend. Acad. Sci. URSS*, 14(3):109–114, 1937.

[235] Teerapat Payupol, Narumon Suwonjandee, and Burin Asavapibhop. Shielding the earth magnetic field using spherical coils. *Journal of Physics: Conference Series*, 1144:012092, 12 2018.

[236] Christoph et al. Genster. Muon reconstruction with a geometrical model in juno. *Journal of Instrumentation*, 13:T03003–T03003, 03 2018.

[237] Kun Zhang, Miao He, Weidong Li, and Jilei Xu. Muon tracking with the fastest light in the juno central detector. *Radiation Detection Technology and Methods*, 2, 03 2018.

[238] Tijjani et al. Adam. Juno conceptual design report, 08 2015.

[239] Angel Abusleme et al. Calibration Strategy of the JUNO Experiment. *JHEP*, 03:004, 2021.

[240] Jiaqi Hui et al. The automatic calibration unit in JUNO. *JINST*, 16(08):T08008, 2021.

[241] Yuanyuan et al. Zhang. Cable loop calibration system for jiangmen underground neutrino observatory. *Nuclear Instruments and Methods in Physics Research Section A: Accelerators, Spectrometers, Detectors and Associated Equipment*, 988:164867, Feb 2021.

[242] Guo-Lei Zhu, Jiang-Lai Liu, Qi Wang, Meng-Jiao Xiao, and Tao Zhang. Ultrasonic positioning system for the calibration of central detector. *Nucl. Sci. Tech.*, 30(1):5, 2019.

[243] Yuhang Guo, Qingmin Zhang, Feiyang Zhang, Mengjiao Xiao, Jianglai Liu, and Eryuan Qu. Design of the Guide Tube Calibration System for the JUNO experiment. *JINST*, 14(09):T09005, 2019.

[244] K. Feng, D. Li, Y. Shi, K. Qin, and K. Luo. A novel remotely operated vehicle as the calibration system in juno. *Journal of Instrumentation*, 13:T12001–T12001, 12 2018.

[245] Y. Zhang, J. Liu, Mengjiao Xiao, F. Zhang, and T. Zhang. Laser calibration system in juno. *Journal of Instrumentation*, 14:P01009–P01009, 01 2019.

[246] The EPICS Collaboration. Experimental physics and industrial control system (2021). https://epics-controls.org/.

[247] J. Zou, Xiang-Jie Huang, W.D. Li, Tao Lin, T. Li, Kiki Zhang, Z. Deng, and G. Cao. Sniper: an offline software framework for non-collider physics experiments. *Journal of Physics: Conference Series*, 664:072053, 12 2015.

[248] Kaijie Li, Zhengyun You, Yumei Zhang, Jiang Zhu, Tao Lin, Ziyan Deng, and Weidong Li. GDML based geometry management system for offline software in JUNO. *Nucl. Instrum. Meth. A*, 908:43–48, 2018.

[249] Z. You, K. Li, Y. Zhang, J. Zhu, T. Lin, and W. Li. A ROOT Based Event Display Software for JUNO. *JINST*, 13(02):T02002, 2018.

[250] Jiang Zhu, Zhengyun You, Yumei Zhang, Ziyuan Li, Shu Zhang, Tao Lin, and Weidong Li. A method of detector and event visualization with Unity in JUNO. *JINST*, 14(01):T01007, 2019.

[251] Tao Lin, Jiaheng Zou, Weidong Li, Ziyan Deng, Xiao Fang, Guofu Cao, Xingtao Huang, and Zhengyun You and. The application of SNiPER to the JUNO simulation. *Journal of Physics: Conference Series*, 898:042029, oct 2017.

[252] Angel et al. Abusleme. Tao conceptual design report: A precision measurement of the reactor antineutrino spectrum with sub-percent energy resolution, 05 2020.

[253] Hangkun et al. Xu. Calibration strategy of the juno-tao experiment, 2022.

[254] OMEGA, centre de microelectronique (UMS3605). https://portail.polytechnique.edu/omega/fr.

[255] AMD - Xilinx, inc. https://en.wikipedia.org/wiki/Xilinx.

[256] Ken'ichiro Nakazato, Kohsuke Sumiyoshi, Hideyuki Suzuki, Tomonori Totani, Hideyuki Umeda, and Shoichi Yamada. Supernova Neutrino Light Curves and Spectra for Various Progenitor Stars: From Core Collapse to Proto-neutron Star Cooling. *Astrophys. J. Suppl.*, 205:2, 2013.

[257] Irene Tamborra, Georg Raffelt, Florian Hanke, Hans-Thomas Janka, and Bernhard Müller. Neutrino emission characteristics and detection opportunities based on three-dimensional supernova simulations. *Phys. Rev. D*, 90:045032, Aug 2014.

[258] Rampp, M. and Janka, H.-T. Radiation hydrodynamics with neutrinos - variable eddington factor method for core-collapse supernova simulations. *A&A*, 396(1):361–392, 2002.

[259] Lorenz Hüdepohl. *Neutrinos from the Formation, Cooling, and Black Hole Collapse of Neutron Stars*. PhD thesis, Fakultät für Physik, Munichen, 2014.

[260] Data and structural profiles from Garching group simulation. www.mpa-garching.mpg.de/ccsnarchive.

[261] H. Shen, H. Toki, K. Oyamatsu, and K. Sumiyoshi. Relativistic equation of state of nuclear matter for supernova and neutron star. *Nuclear Physics A*, 637(3):435–450, 1998.

[262] James M. Lattimer and F. Douglas Swesty. A generalized equation of state for hot, dense matter. *Nuclear Physics A*, 535(2):331–376, 1991.

[263] Tingxuan Zeng, Fei Li, and Kejun Zhu. Juno daq readout and event building research. *IEEE Transactions on Nuclear Science*, 66(7):1217–1221, 2019.

[264] Abdel Rebii. Gcu-abc data format. JUNO-DocDB-7799.

[265] Clément Bordereau. Catiroc's time measurement on the abc. JUNO-DocDB-6109.

[266] Ziyuan Li, Yumei Zhang, Zhengyun You, Guofu Cao, Ziyan Deng, Guihong Huang, Weidong Li, Tao Lin, Liangjian Wen, Miao Yu, Jiaheng Zou, and Wuming Luo. Event vertex and time reconstruction in large volume liquid scintillator detector, 01 2021.

[267] H Wan Chan Tseung and N Tolich. Ellipsometric measurements of the refractive indices of linear alkylbenzene and EJ-301 scintillators from 210 to 1000 nm. *Physica Scripta*, 84(3):035701, August 2011.

[268] Zhaopeng Meng, Xiaoyu Zhai, Jianguo Wei, Zhiyang Wang, and Hanzhong Wu. Absolute measurement of the refractive index of water by a mode-locked laser at 518 nm. *Sensors*, 18:1143, 04 2018.

[269] Pickover Clifford. *The Math Book: From Pythagoras to the 57th Dimension, 250 Milestones in the History of Mathematics*. Sterling Publishing Company, Inc., 2009. ISBN 9781402757969.

[270] I S Yeo et al. Measurement of the refractive index of the LAB-based liquid scintillator and acrylic at RENO. *Physica Scripta*, 82(6):065706, nov 2010.

[271] Susan F. Marseken Lambert M. Surhone, Miriam T. Timpledon. *Snell's Law*. VDM Publishing, June 2010. ISBN 6130516401, 9786130516406.

[272] M.Born et. al. *Principles of optics: electromagnetic theory of propagation, interference and diffraction of light*. Pergamon press, Cambridge University Press, October 1999. ISBN 9780521642224, 0521642221.

[273] Cristiano Galbiati and Kevin McCarty. Time and space reconstruction in optical, non-imaging, scintillator-based particle detectors. *Nuclear Instruments and Methods in Physics Research Section A Accelerators Spectrometers Detectors and Associated Equipment*, 568, 03 2005.

[274] Glen Cowan. *Statistical Data Analysis*. Clarendon press, 1998. ISBN 0198501552, 9780198501558.

[275] Brun et. al. Tminuit class reference. https://root.cern.ch/doc/master/classTMinuit.html.

[276] Rene Brun and Fons Rademakers. Root — an object oriented data analysis framework. *Nuclear Instruments and Methods in Physics Research Section A: Accelerators, Spectrometers, Detectors and Associated Equipment*, 389(1):81–86, 1997. New Computing Techniques in Physics Research V.

[277] Zhen Qian et al. Vertex and energy reconstruction in juno with machine learning methods. *Nuclear Instruments and Methods in Physics Research Section A: Accelerators, Spectrometers, Detectors and Associated Equipment*, 1010:165527, 2021.

[278] A. Abusleme et al. Optimization of the juno liquid scintillator composition using a daya bay antineutrino detector. *Nuclear Instruments and Methods in Physics Research Section A: Accelerators, Spectrometers, Detectors and Associated Equipment*, 988:164823, 2021.

[279] U Fano. Penetration of protons, alpha particles, and mesons. *Annual Review of Nuclear Science*, 13(1):1–66, 1963.

[280] P. Lecoq. *Scintillation Detectors for Charged Particles and Photons*. Springer International Publishing, Cham, 2020.

[281] P. Kampmann, Y. Cheng, and L. Ludhova. A semi-analytical energy response model for low-energy events in JUNO. *Journal of Instrumentation*, 15(10):P10007–P10007, oct 2020.

[282] F. Zhang, R. Li, J. Hui, J. Liu, Y. Meng, and Y. Zhang. A precise method to determine the energy scale and resolution using gamma calibration sources in a liquid scintillator detector. *Journal of Instrumentation*, 16(08):T08007, aug 2021.

[283] Yaoguang Wang. Understanding of the new energy resolution in detsim. JUNO-DocDB-8412.

[284] P. Kampmann. *Energy scale non-linearity and event reconstruction for the Neutrino Mass Ordering measurement of the JUNO experiment*. thesis, Aachen University, Aachen, Germany, 2020.

[285] von Krosigk, B., Neumann, L., Nolte, R., Röttger, S., and Zuber, K. Measurement of the proton light response of various lab based scintillators and its implication for supernova neutrino detection via neutrino-proton scattering. *Eur. Phys. J. C*, 73(4):2390, 2013.

[286] S Schmitt. TUnfold, an algorithm for correcting migration effects in high energy physics. *Journal of Instrumentation*, 7(10):T10003–T10003, oct 2012.

[287] The tunfold package: user manual, 2014. https://docplayer.net/213662486-The-tunfold-package-user-manual-stefan-schmitt-desy-notkestrasse-85-hamburg.html.

[288] G. D'Agostini. Improved iterative bayesian unfolding. [Online]. Available from: `https://arxiv.org/abs/1010.0632`, 2010.

[289] Georgios Choudalakis. Fully bayesian unfolding. [Online]. Available from: `https://arxiv.org/abs/1201.4612`, 2012.

[290] A. N. Tikhonov. Solution of incorrectly formulated problems and the regularization method. *Soviet Mathematics Doklady*, 4:1035–1038, 1963.

[291] Per Christian Hansen. The l-curve and its use in the numerical treatment of inverse problems. *Computational Inverse Problems in Electrocardiology*, 4:119–142, 01 2001.

[292] Andreas Höcker and Vakhtang Kartvelishvili. SVD approach to data unfolding. *Nuclear Instruments and Methods in Physics Research Section A: Accelerators, Spectrometers, Detectors and Associated Equipment*, 372(3):469–481, apr 1996.

[293] TSVDUnfold Class Reference. https://root.cern.ch/doc/master/classTSVDUnfold.html.

L’air est rance. Bientôt l’errance... ?

DOCTORAT MATIERE BRETAGNE MOLECULES LOIRE ET MATERIAUX

Nantes Université

Titre : Vers la Détection des Neutrinos issus de l'Explosion des Supernovae à Effondrement de Coeur avec les système PMT 3 pouces du détecteur JUNO

Mot clés : Neutrinos ; Supernovae ; JUNO ; PMT ; Détection ; Neutrinos des Supernovae

Résumé : Les supernovae à effondrement de coeur (SNEC) sont des explosions gigantesques qui se produisent à la fin de la vie d'une étoile massive. Il y a trente-cinq ans, pour la première fois, deux douzaines de neutrinos provenant d'une SNEC (SN1987A) ont été détectés, marquant le début d'une nouvelle air dans l'études des SNEC. JUNO est un détecteur à liquide scintillant (LS) actuellement en construction en Chine. Deux systèmes de tubes photomultiplicateurs (PMT), le premier constitué de $\sim$18,000 PMT de 20 pouces et le second constitué de $\sim$26,000 PMT de 3 pouces, collecteront la lumière produite par les interactions des neutrinos avec le LS. Les objectives primaires de JUNO sont de déterminer l'ordre des masses des neutrinos et de mesurer précisément trois paramètres d'oscillation. Grâce à son immense volume de détection, JUNO devrait également détecter une salve de quelques centaines à quelques milliers de neutrinos provenant de la prochaine SNEC galactique. Cette thèse se concentre sur divers aspects de la détection des neutrinos des SNEC avec le système PMT 3 pouces de JUNO. Basé sur des données de simulation, les performances de lecture du système sont évaluées, les algorithmes de reconstruction de la position et de l'énergie des évènements dévelopés ainsi qu'une analyse pour la reconstruction des spèctres en énergie sont présentés.

Title: Towards the Detection of Core-Collapse Supernovae Burst Neutrinos with the 3-inch PMT System of the JUNO Detector

Keywords: Neutrinos; Supernovae; JUNO; PMT; Detection; Supernovae Neutrinos

Abstract: Core-Collapse Supernovae (CCSN) are gigantic explosions that occur when a massive star comes to death. Thirty-five years ago, for the first time, two dozens of neutrinos from a CCSN (SN1987A) were detected, marking the beginning of a new era in the study of CCSN. JUNO is a 20 kton liquid scintillator (LS) detector currently under construction in China. Two photomultiplier tube (PMT) systems, the first one made of $\sim$18,000 20-inch PMTs and the second one made of $\sim$26,000 3-inch PMTs, will collect the light produced by the neutrino interactions in the LS. JUNO primary objectives are to determine the neutrino mass ordering and to precisely measure three oscillation parameters. Thanks to its huge detection volume, JUNO is also expected to detect a burst of a few hundreds to a few thousands of neutrinos from the next galactic CCSN. The present thesis focuses on various aspects of the detection of CCSN neutrino using the 3-inch PMT system of JUNO. Based on simulation data, the rate capabilities of the system are assessed, the events vertex and energy reconstruction algorithms developed as well as an analysis for energy spectra reconstruction are presented.